

**Development of a fuzzy expert system for detailed land cover mapping
in the Dra catchment (Morocco) using high resolution satellite images**

Dissertation

zur

Erlangung des Doktorgrades (Dr. rer. nat.)

der

Mathematisch–Naturwissenschaftlichen Fakultät

der

Rheinischen Friedrich–Wilhelms–Universität Bonn

vorgelegt von

Michael Schmidt

aus

Gebhardshain

Bonn, Mai 2003

Angefertigt mit Genehmigung der Mathematisch–Naturwissenschaftlichen Fakultät
der Rheinischen Friedrich–Wilhelms–Universität Bonn

1. Referent: Prof. Dr. G. Menz
2. Referent: Prof. Dr. D. Klaus

Tag der Promotion: 11.06.2003

” And if I know of a flower which is unique in the world and grows nowhere other than on my planet and that a small sheep can destroy it with a single bite, just like that, without realising what it is doing, is that not important?”

The Little Prince, Antoine de Saint-Exupéry, 1944

Acknowledgements

I would like to thank kindly all those who have helped, supported and encouraged me to do this work. They are surely in the first instance my parents, family and friends.

Scientifically I would like to thank Prof. Dr. G. Menz for fruitful discussions and prosperous ideas, especially for the support during the difficult final stage. Prof. Dr. R. Goossens had a high impact on the content of the work due to our intensive and successful collaboration, which involved common field trips and long discussions. I would also like to thank him for helping to improve this text.

I would also like to thank the members of the RSRG starting with Dr. H.-P. Thamm for motivation and enthusiasm in scientific topics, also for sharing and reducing the project administration. Jan Richters for many discussions, technical advices and IDL solutions. Doris Klein for critical and intellectual discussions. Special thanks to Peter Poete for the outstanding common organised field course for last year students; and to the students who stayed with us for two weeks in M'hamid and contributed to the extraordinary group atmosphere resulting in very good field data, namely: Marc Altena, Sandra Amlang, Matthias Bellinghausen, Jana Borgwardt, Roland Goetzke, Robin Girmes, Michael Haass, Vanessa Heinzl, Kerstin Lehmann, Matthias Müller, Bettina Ostwald, Christina Prien, Christian Sebaly, Thorsten Sellheim, Michael Sondermann and Christoph Lauber.

I would like to thank Ouns Kissyar and Julia Rörig as desk neighbours for a good working environment. Dr. M. Canty for a scientific exchange and common programming projects during the whole period. Dr. A.A. Nielson for assistance in Figure 5.2.

Dr. M. Christoph for the sometimes unbureaucratic handling of administration within the project. Dr. Finckh, Frank Gresens and M. Staudinger for the uncomplicated and good collaboration within the sub-project B3.

The students, who were employed in the sub-project B3 did extraordinary work, especially at the final stage of this work: Christoph Lauber, Michael Klapproth, Roland Goetzke and Dominik Vogt. I like also thank the other members of the RSRG for making the stay pleasant.

O. Abellaoi made things easier for me in Ouarzazate with the local administration, thanks for him for this. I also thank K. Goldnick and J. Werner for the good and

efficient common work in Zagora.

Very special thanks to Birte Schöttker for patience, motivation, critical thematic discussions, figure and text editing support.

Thanks to Dr. M. McCabe for reading few chapters at an early stage of the writing process. Many thanks for the enormous work of Dr. E. King for the help in improving the text, editing and laying out of the final version and to my housemates Cath, Emily and Duncan for the warm welcome in Canberra. And thanks to all the people that I forgot to mention at this stage but helped or supported me in any way.

Contents

1	Introduction	1
1.1	Project framework of this study	3
1.2	Central objectives and research goals of this study	6
1.3	Structural composition of the work	8
2	Regional settings	11
2.1	The Dra catchment	11
2.2	Fieldwork and ground truth data	20
2.3	Conclusions	27
3	Low, Medium, High or Very High Resolution for land cover mapping?	28
3.1	Scale in land cover mapping	29
3.2	Vegetation mapping	32
3.3	Classification schemes and implications for this study	34
3.4	Conclusions and discussion	40
4	Remote sensing in 2, 3 and 4 dimensions	41
4.1	Photogrammetric background	43
4.2	3D Remote Sensing	47
4.2.1	Data	48
4.2.2	Methods	50
4.2.3	Results	53
4.2.4	Post-processing	55
4.2.5	Co-registration	56
4.3	Multi-temporal 3D analysis - or 4D remote sensing?	57
4.4	Discussion and Conclusions	58

5	Pre-processing - How much is necessary?	60
5.1	Satellite data	60
5.2	Geometric correction	62
5.2.1	Reference system	62
5.2.2	Geometric correction of (very-) high resolution Satellite Data .	64
5.3	Radiometric correction	67
5.3.1	Relative radiometric normalisation	68
5.3.2	Absolute calibration	79
5.4	Illumination and terrain correction	86
5.5	Discussion	88
5.6	Conclusion	90
6	Vegetation classification in an arid environment	91
6.1	Methods	93
6.1.1	Combined classification approach and materials	93
6.1.2	Spectral Mixture Analysis	96
6.1.3	Spectral Angle Mapper	100
6.1.4	Fuzzy classification and knowledge based decision rules	101
6.1.5	Post-processing	103
6.1.6	Validation	103
6.2	Results from the Dra catchment - South Morocco	105
6.2.1	Basin of Tazenakht	105
6.2.2	The Dra valley	113
6.2.3	High Atlas	128
6.2.4	Basin of Ouarzazate	130
6.2.5	Crystalline Anti-Atlas	132
6.2.6	Sedimentary Anti Atlas	135
6.3	Discussion and outlook	136
6.4	Conclusion	139
7	Change Detection: what to detect?	140
7.1	Data	141
7.2	Methods and results	142
7.2.1	Visual interpretation and object digitalisation	142
7.2.2	Analysis of multitemporal NDVI data	146

7.2.3	Post classification change detection	147
7.2.4	Multivariate Alternate Detection	162
7.3	Discussion and conclusion	164
8	Biophysical analysis and land use derivation	166
8.1	Biophysical analysis	166
8.1.1	Leaf area index derivation from IKONOS-2 data	167
8.1.2	Interpretations of the LAI density information	169
8.1.3	Transfer of LAI measurements	172
8.2	An integrated approach: the Basin of Fezuata	174
8.3	Discussion and Conclusions	182
9	Overall Discussion, Conclusions and Outlook	185
9.1	Conclusions	185
9.2	Outlook and recommendations for further research	190
	References	194
10	Appendix	215

List of Figures

1.1	Interrelations and structure of the CLIMBER earth system model . . .	2
1.2	Schematic overview of the IMPETUS project structure	5
1.3	Flow chart of the satellite data used and the processing steps applied	10
2.1	Location and overview of the Dra catchment	13
2.2	Annual average precipitation of Ouarzazate and Zagora	13
2.3	Sub-regions of the Dra catchment based on the PMU mapping	16
2.4	Landscape examples of the six sub-regions of the Dra catchment . . .	20
2.5	GCP documentation for the very high resolution CORONA data . . .	24
2.6	Ground truth data stored in a GIS (ArcView) database	25
2.7	The real time GPS link of ERDAS imagine in the field	26
2.8	Position shift of the ground truth data due to geo-location errors . . .	27
3.1	Spatial and temporal resolution of satellite data	31
3.2	Estimated size of a LANDSAT pixel in an oblique terrestrial photo .	36
3.3	Schematic relation of pixel size, numbers of classes and estimated accuracy dependent on the classification level	37
4.1	Relief displacements	42
4.2	Parallax displacements	45
4.3	Image orientation process	47
4.4	Coverage of derived photogrammetric products	48
4.5	Sensor geometry of CORONA and ASTER	49
4.6	Image pre-orientation along the flight-line	50
4.7	Processing steps	51
4.8	Lines of equal parallax difference	52
4.9	Image drape of CORONA data	53

4.10 Mosaiced DEM of three processed ASTER scenes	54
4.11 Image swipe of an ASTER orthoimage and a topographic map	56
4.12 Co-registered CORONA and IKONOS image	57
5.1 Overview of the IKONOS-2 and LANDSAT data coverage	62
5.2 PIFs regression of LANDSAT data from 1999 and 2000	74
5.3 MAD regression of 1999 on 2000 using training pixels	76
5.4 LANDSAT ETM+ image mosaic from May 2000	78
5.5 Example of an image mosaic of two adjacent LANDSAT ETM+ scenes	80
5.6 Unnormalised and normalised mean pixel intensities for six Landsat TM images	83
5.7 Examples of NDVI composites from AVHRR and MODIS data	85
5.8 Examples of NDVI composites from MODIS and ETM+ data	86
5.9 Example of an illumination correction approach	88
6.1 Flow chart of the combined classification procedure	94
6.2 Concept of spectral mixtures	96
6.3 Concept of linear spectral unmixing	99
6.4 Principle of spectral angle mapping	100
6.5 Schematic representation of the membership functions in LSU and in SAM	102
6.6 Distribution of the validation data within the Dra catchment used in the classification approach	104
6.7 LANDSAT ETM+ false colour composite of the Basin of Tazenakht .	106
6.8 Abundance channels of the endmembers	108
6.9 Knowledge based fuzzy decision rules for land cover class differentia- tion in the Basin of Tazenakht	109
6.10 Two example images of an RGB FCC, the corresponding classification and a ground truth image	110
6.11 Classification rules for the class 1120 - discontinuous urban fabric . .	110
6.12 Land cover/land use classification for the Basin of Tazenakht	112
6.13 Overview of the mapping area	115
6.14 Visual comparison of the overlaid classification polygon on a RGB FCC and NDVI image subset of IKONOS-2 data	116
6.15 Visual comparison of the Quarzite mask and the geological map . . .	117
6.16 Endmember spectra used in the image decomposition of the Dra valley	118

6.17	Examples of the background influence on the NDVI	118
6.18	Reference spectra used in the SAM on the vegetation pixels	120
6.19	Flow chart of the land cover classification decision rules for the Dra valley	121
6.20	Examples of the classification result in the Dra valley	122
6.21	Object oriented post-classification decision tree	123
6.22	Example of object oriented post-classification	124
6.23	Flow chart of the land cover classification decision rules for the High Atlas	129
6.24	Flow chart of the land cover classification decision rules for the Basin of Ouarzazate	131
6.25	Flow chart of the land cover classification decision rules for the Crystalline Anti-Atlas	133
6.26	Flow chart of the land cover classification decision rules for the Sedimentary Anti-Atlas	135
7.1	LANDSAT MSS and ETM+ RGB image subsets of the region around the Lac Iriki	143
7.2	Photos of the region around the Lac Iriki in 1969	143
7.3	Photos of the region around the Lac Iriki in 2000	144
7.4	The size of the town M'hamid in 2001, 1972 and 1964	145
7.5	Test area of the ORMVAO in a LANDSAT ETM+ subset	146
7.6	Comparison of NDVI values inside and outside the testplot at different time steps	147
7.7	Example of an oasis protection against mobile sand	148
7.8	Image displacements by CORONA and IKONOS satellite viewing geometry	150
7.9	Example of the tamarisk coverage of 1972 and 2001	151
7.10	Endmember spectra used in the LSU	153
7.11	Visualisation of change in the vegetation abundance displayed as a RGB image	154
7.12	Representative vegetation abundance values of the three time steps of investigation	156
7.13	Irrigation area near the town of Zagora	156
7.14	Flow chart of the post classification change detection approach	158

7.15	Classification of the Basin of Tazenakht from LANDSAT TM5, April 1987	159
7.16	RGB FCC and classification example of the Basin of Tazenakht, from May 2000 and April 1987	160
7.17	MAD based changes April 1987 - May 2000	162
8.1	Regression between field measured LAI and NDVI values derived from IKONOS-2 data	168
8.2	LAI values as derived from IKONOS-2 data	168
8.3	Example of disturbed tamarisk trees	169
8.4	Interpolated LAI values derived from IKONOS-2 data	172
8.5	Regression between field measured LAI and vegetation abundance . .	173
8.6	Overview of the Basin of Fezuata	175
8.7	Visualisation of three binary classifications for the Basin of Fezuata .	178
8.8	Examples of a cultivated and saline field	180
8.9	Vicious circle of nomadic people in the Basin of Fezuata	181
8.10	Example of field size and intensity of land use from Fejia and Tiguida	182

List of Tables

2.1	DGPS points obtained during field observations	25
3.1	Land use/land cover classification scheme	37
4.1	Characteristics of CORONA and ASTER stereo images.	49
4.2	Errors in the photogrammetric restitution - CORONA	54
4.3	Errors in the photogrammetric restitution - ASTER	55
5.1	Characteristics of the utilised and processed multispectral satellite data	61
5.2	Attributes of Lambert Conical Conform projection	63
5.3	Geometrically corrected LANDSAT images within the Dra catchment	66
5.4	Pseudo-invariant features chosen for normalisation to the 1999 scene .	69
5.5	Ordinary least squares regression on training PIFs	73
5.6	Comparison of mean intensities of PIF test pixels	75
5.7	Comparison of variances of PIF test pixels	75
5.8	Regression of the MAD approach of LANDSAT data from 1999 and 2000	75
5.9	Comparison of mean intensities of MAD test pixels	76
5.10	Comparison of variances of MAD test pixels	77
5.11	Regression of test pixels of the image mosaicing	79
5.12	Coefficients for DN to at sensor radiance for 11 <i>bit</i> IKONOS-2 data . .	81
5.13	Calibration coefficients for LANDSAT ETM+ data	81
5.14	Coefficients for the exoatmospheric irradiance for LANDSAT ETM+ .	82
6.1	Confusion matrix of ground truth pixels and the classified image of the Basin of Tazenakht, in percent and in pixels	111
6.2	Meta information of the two IKONOS-2 image tiles used in this study	114

6.3	Confusion matrix of the IKONOS-2 mapping	116
6.4	Confusion matrix of the LANDSAT ETM+ land cover classification in the Dra valley	124
6.5	Validation data of the intersection of the classes 3261, 3262 and 3263 with the vegetation mask	127
6.6	Land cover classification accuracies of the High Atlas with 6 validated classes (next page)	129
6.7	Land cover classification accuracies of the Basin of Ouarzazate with 9 validated classes	132
6.8	Land cover classification accuracies of the Crystallin Anti-Atlas with 8 validated classes	134
6.9	Land cover classification accuracies of the Sedimentary Anti-Atlas with 6 validated classes	136
6.10	Classification accuracies of the six sub-regions of the Dra catchment .	137
7.1	Meta information of CORONA KH4B (26.05.1972) and IKONOS-2 (23.11.2001) data used in this study	150
7.2	Land cover changes as mapped with CORONA and IKONOS-2 data .	152
7.3	Accuracy assessment for the three classification time steps	155
7.4	Correlations of the relative radiometric normalisation of TM (April 1987) towards ETM+ (May 2000)	157
7.5	Class coverages [%] of 1987 and 2000 of the Basin of Tazenakht, ac- cording to the post classification	161
7.6	Correlation coefficients for the MADs of the change pixels and the image DNs	163
8.1	Land cover changes and mean LAI values mapped with CORONA and IKONOS-2 data	170
8.2	Validation of the binary classification	177
8.3	Colour representation in the additive colour scheme	178
9.1	Classification accuracies of the six sub-regions of the Dra catchment .	188

Abbreviations

ADEDRA	Association de Développement de la Vallée du Dra
AVHRR	Advanced Very High Resolution Radiometer
ASTER	Advanced Spaceborne Thermal Emission and Reflection Radiometer
BAHC	Biospheric Aspects of the Hydrological Cycle
DEM	Digital Elevation Model
ETM+	Enhanced Thematic Mapper
CORINE	Coordinated Information on the Environment
DGPS	Differential Global Positioning System
EARSeL	European Association of Remote Sensing Laboratories
FCC	False Colour Composite
FAO	Food and Agricultural Organisation
ftp	file transfer protocol
GCP	Ground Control Point
GSD	Ground Sampling Distance
GPS	Global Positioning System
GTZ	German Technical Cooperation
GUI	Graphical User Interface
HASL	Height Above Sea Level
HRPT	High Resolution Picture Transmission
IFOV	Instantaneous Field Of View
IGBP	International Geosphere-Biosphere Programme
IMPETUS	Integratives Management-Projekt für einen Effizienten und Tragfähigen Umgang mit Süßwasser in Westafrika
ISPRS	International Society for Photogrammetry and Remote Sensing
LAI	Leaf Area Index
LAC	Local Area Coverage
LST	Land Surface Temperature
LSU	Linear Spectral Unmixing
LUCC	Land Use and Cover Change
MAD	Multivariate Alteration Detection
MLC	Maximum Likelihood Classifier
MODIS	Moderate Resolution Imaging Spectroradiometer
MSS	Multi Spectral Scanner

NASA	National Aeronautics and Space Administration
NIR	Near Infrared
MISR	Multiangle Imaging SpectroRadiometer
NDVI	Normalised Differenced Vegetation Index
NDSI	Normalised Differenced Snow Index
NOAA	National Oceanic and Atmospheric Administration
OLS	Ordinary Least Square
ORMVAO	Office Régional de Mise en Valeur Agricole Ourazazate
PIF	Pseudo Invariant Feature
Pixel	Picture element
PMU	PhotoMorphic Units
RAD	at sensor RADiance
REF	ground REFlectance
RMS	Root Mean Square
SAA	Satellite Active Archive
SAM	Spectral Angle Mapper
SI	SpaceImaging
SMA	Spectral Mixture Analysis
SRTM	Shuttle Radar Topograph Mission
SST	Sea Surface Temperature
tif	tagged image file
TM	Thematic Mapper
UTM	Universal Transverse Mercator
USGS	United States Geological Survey
VA	Vegetation Abundance
VI	Vegetation Index
VNIR	Visible Near Infrared

1 Introduction

”Sustainable development at local, regional and global scales represents perhaps the most daunting challenge that humanity has ever faced.”

Global Change Newsletter, 2002

One of the most obvious changes during the last three centuries is the direct human modification and conversion of land cover (Richards, 1990; Ramankutty et al., 2001). During this time period, for example, the amount of land used for agriculture has increased five-fold. Furthermore, large areas have been lost to degradation. Agricultural yields have increased due to the application of fertilisers, pesticides and irrigation techniques for the benefit of humankind, with negative consequences for the Earth system. The global population exceeded 6 billion in October 1999 (UN, 1999) and increased from the pre-industrial phase by a factor of about twelve (see Klaus, 1994). The supply of the basic needs for the increasing population as well as the rising living standards resulted in a major interaction with the natural environment. Global energy consumption increased by 84% between 1970 and 1997 (von Weizäcker et al., 1997). The implications of human activities on the earth system become apparent when the enormous amounts of small human-driven changes are aggregated globally over a long time period. Although human-driven changes are not easy to identify and attribute in a cause-effect paradigm, they are superimposed on, and usually interact with, natural patterns of variability within the earth system (Hulme, 2000). The world actually faces changes in the human-nature relationship at a speed that exceeds the natural changes and variability (Trenberth et al., 1996; IPCC, 2001). Environmental problems due to these changes are: shortages of clean and accessible freshwater, degradation of terrestrial and aquatic ecosystems, increases in soil erosion, loss of biodiversity, changes in chemistry of the atmosphere, declines in fisheries, and the possibility of significant changes in climate (Steffen and Tyson, 2001).

In order to understand the complex feedback mechanisms of the Earth system and

to identify potential sources of these problems interacting sub-systems of the earth are usually examined (Houghton, 1997). Environmental systems are characterised by multiple non-linear internal interactions and external forcing; as a consequence they do not behave predicably on long terms (Lorenz, 1963; Klaus, 1999). The chaotic behavior of the dynamic Earth system might, by exceeding certain thresholds led, the system to another state (see Klaus et al., 1994, for further discussion) with environmental conditions that can only be estimated. The description and modelling of potential scenarios of changes for the Earth system as a whole is thus a surpassing challenge. Figure 1.1 shows an example of the linkages between different components within an earth system model (Petoukhov et al., 2000).

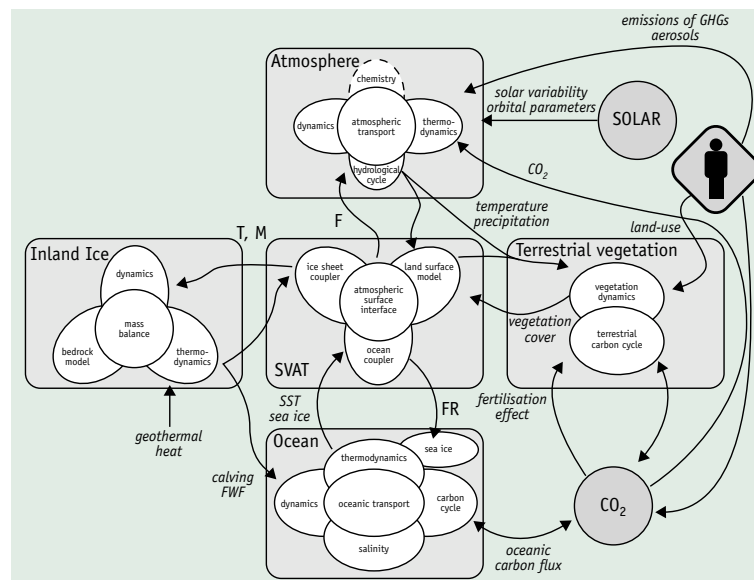


Figure 1.1: Interrelations and structure of the CLIMBER earth system model (Petoukhov et al., 2000)

During the last decade, research in the International Geosphere-Biosphere Programme (IGBP), the project Biospheric Aspects of the Hydrological Cycle (BAHC) investigated the role of biophysical and biogeochemical feedbacks of the terrestrial biosphere to the climate system. "This understanding has allowed the importance of feedbacks of land use and land cover change to the physical climate system to be understood in ways not appreciated a decade ago." (Kabat et al., 2002). So, it was understood that the biosphere and land cover are 'active players' in the Earth system (Steffen and Tyson, 2001) and that these contribute importantly to the description of the hydrological cycle and the quality of climate models (Crossley et al.,

2000).

The amount of available fresh water is controlled by the hydrological cycle. Fresh water has already become critically scarce in many regions of the world. It is projected for the first quarter of the 21st century, that about one-quarter of the world population will suffer from severe water shortage (IMPETUS, 2003).

Actual conflicts about the freshwater resource and existing potentials for further conflicts show a demand for management strategies. Population pressure will inevitably increase and therefore the aim of research projects should be to contribute not only to an understanding of the complex feedback mechanisms (especially with respect to ecological and human constraints) but also to establish a decision support system for food and water supply, and a better land and resource management.

Earth observation from space has revolutionised human perspectives and understanding of the planet (Steffen and Tyson, 2001). With data from the successful CORONA missions in 1960 and the initiation of the LANDSAT program in the early 1970's, satellite data are globally available and deliver an extraordinary amount of information about the Earth surface and the biosphere, thereby opening enormous monitoring potential (Botkin et al., 1984; Campbell, 1996; Jensen, 2000). To identify and monitor changes, in the first instance the state of the monitored object must be known at a specific time. From this point onwards or backwards hot spots of changes are interpretable. For this reason an image classification as a thematic interpretation of the satellite data recorded is a very useful mapping product. Image classifications from different time steps can reveal, by the application of the same classification technique, changes in the thematic maps. This detailed and potentially validated source of information can be used to initiate and validate environmental models describing and projecting changes to the Earth system. Integrated studies and analysis for regional adjusted development on the basis of sustainable use of resources are necessary to manage the expected changes in the Earth system.

1.1 Project framework of this study

The German federal ministry of education and research (BMBF) announced the GLOWA projects in 2000. "The aim of GLOWA is the development of strategies for sustainable and future-oriented water management on a regional level while taking into account global environmental changes and socio-economic framework condi-

tions. The programmatic orientation of GLOWA focuses on case studies for large river catchment areas (i.e. some 100000km^2), where simultaneous research is done in a collaborative research programme on interrelations between changes in the hydrological cycle and the large-scale climate and precipitation variability, changes in the biosphere (in particular caused by changes in land use) as well as the effects on water availability and related conflicts of use" (GLOWA, 2002). Within GLOWA, five large cluster projects have been promoted. Two of them are located in Germany (Danube, Elbe), while the others are investigating river catchment areas in North and West Africa (Dra, Queme, Volta) as well as in the Near East (Jordan) (see GLOWA, 2002, for further reading).

In Northwest and West Africa since the early 1970's an increased occurrence of years of drought resulted in serious problems related to the supply of fresh water (IMPETUS, 2003). The general precipitation decline in subtropical Northwest Africa and tropical West Africa are probably related. Investigation with an integrated approach including several aspects of the hydrological cycle is performed within the IMPETUS project: an integrated approach to the efficient management of scarce water resources in West Africa.

Two study areas north and south of the Sahara desert were chosen for intensive investigation by means of a transect between the High Atlas mountains and the Gulf of Guinea. This transect contains two reasonably-sized river catchments, representative in the sense that the Dra catchment, in the south east of Morocco, exhibits a typical gradient from humid/subhumid subtropical mountains to the arid foothills. The Oueme basin in Benin is typical of an alternating subhumid climate of the outer tropics. West Africa was chosen because (i) it has experienced the most pronounced interdecadal variability of climate in the world during the 20th century, (ii) relations to the climates of Europe might exist via complex atmosphere ocean interactions, and (iii) the regions north and south of the Sahara might be linked via atmospheric teleconnection processes with regard to precipitation anomalies (IMPETUS, 2003).

During the first project phase (May 2000 - May 2003) factors influencing the hydrological cycle have been identified and analysed. Different global change scenarios (IPCC, 2001) will, in the second phase (June 2003- June 2006), be used to project the bandwidth of consequences and feedback mechanisms regarding the fresh water supply on the local and regional scale. Therefore, in the IMPETUS-project an interdisciplinary approach was chosen. In addition to the scientists from the basic physical sciences, such as geology, hydrology, biology, remote sensing, etc. anthro-

pologists are working within the project group (Thamm et al., 2000). The variability of the hydrological cycle and environmental consequences are monitored, including social-economic impacts. Figure 1.2 shows the structure of the interdisciplinary approach within the IMPETUS project from Benin (A) and Morocco (B).

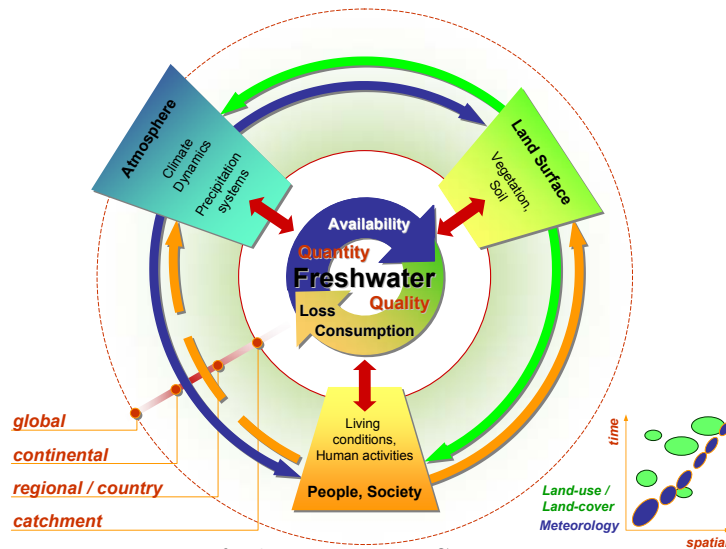


Figure 1.2: Schematic overview of the IMPETUS project structure (IMPETUS, 2001)

The different components and their interactions are considered in individual sub-projects: the atmospheric variability in subprojects A1/ B1, the continental hydro-sphere in subprojects A2/ B2 and the land surface processes in subprojects A3/ B3. Human activities related to fresh water are investigated in subprojects A4/ B4 and A5 (IMPETUS, 2001). The investigations are performed in different spatial and temporal scales. The spatial scales range from local- over regional- to subcontinental scale. It is a challenging task to build up interfaces between the different operational scales, such as integration of micrometeorological measurements in a mesoscale climate model or the linkage of biomass production of a single field with vegetation parameters derived by remote sensing techniques. The temporal scales investigated range from minutes for the measurements of runoff and meteorological parameters to more than three decades for the detection of changes in land cover with remote sensing data. Underlying the analysis of climatological and hydrological parameters (e.g. precipitation, runoff), the documentation of changes in land cover/land use with remote sensing is one of the main topics of the project.

With regard to the assembled knowledge about the hydrological cycle, a management scheme and the installation of operational tools for the decision making process, a "Decision Support System" for the use of fresh water in the study areas is aimed to be established in 2006. An estimate of the effects of changes in the variability of the hydrological cycle and a related risk assessment are other research goals.

Local project partners are principally the Office Régional de Mise en Valeur Agricole Ourazazate (ORMVAO) and the Association de Développement de la Vallée du Dra (ADEDRA), Zagora (for further details see IMPETUS, 2003).

1.2 Central objectives and research goals of this study

Electromagnetic energy, as emitted from the sun in form of photons, reaches the Earth's surface after travelling through the atmosphere and interacting with surface components. Reflection of the photons and interaction with surface components results in information that, after the second passage through the atmosphere, reaches a satellite sensor and is recorded as intensity values. These intensity values are stored in 2-dimensional data arrays for each recorded spectral band. Analysis and interpretation of these data can contribute to extracting useful thematic information - thus transforming data into information. The extraction of the specific information of interest requires an understanding of the radiation interactions with those elements that characterize the surface conditions. To make use of this information it is necessary to locate the data exactly. This leads to the requirement of the geometric registration of the obtained data. During their passage through the atmosphere, photons interact with the atmospheric constituents (aerosols and gases). These interactions make direct comparisons of satellite data that are not obtained at the same atmospheric conditions difficult. Algorithms that minimise these effects within multi-temporal datasets are thus required. Once these steps are performed, multi-temporal analysis of satellite data can commence.

The derivation of different thematic information from satellite data requires the use of different techniques and data (see chapter 3), so a multi-sensor approach was chosen. In accordance with the thematic focus of the IMPETUS sub-projects are four main topics identified and addressed:

1. **The generation of a land cover classification in high spatial detail.** For

the Dra catchment, one of the biggest oasis systems in Saharian North Africa (Pletsch, 1971), no land cover or vegetation map presently exists. Some parts of the Dra catchment are mapped with varying approaches, data, thematic focus and quality levels. Zillbach (1984), for example, mapped the Basin of Ouarzazate (see chapter 2) on the basis of geo-ecological characteristics, Zouri (1992) used SPOT satellite images for a local vegetation study, Ben-nouna et al. (2000) described the vegetation within the Basin of Tazenakht by a pedological surface characterisation on the basis of SPOT data. In the Basin of Ouarzazate and near Zagora, unpublished local studies on the basis of SPOT and LANDSAT data were performed by ORMVAO and the German Technical Cooperation (GTZ), but not with focus on vegetation or land cover classification.

Within this study, a land cover classification of the Dra catchment with high heterogeneity of the land surface as well as in the vegetation associations, with $28419km^2$ is performed with focus on a detailed description of vegetation associations. This work aims not only to assess the oasis systems, but also the rangeland vegetation, which implies a dedicated approach to assess the often sparse vegetation coverage (see chapter 6). The high heterogeneity in the vegetation associations and the complex landscape implied that, for a detailed land cover analysis, standard classification procedures need to be extended or adjusted for this application. To access and classify the sparsely vegetated rangelands, fuzzified sub-pixel information were utilised to implement classification decision rules in an expert system based on terrain observations (Wharton, 1994; Hung and Ridd, 2002).

Due to this discussion, the following research question was formulated : *Is it possible to map this large and heterogeneous catchment using sub-pixel information by means of an expert classification system of high resolution data and gain a high thematic content with high classification accuracy?*

- 2. The detection and analysis of changes in land cover.** Change detection techniques suitable for the analysis of specific land cover changes are purpose-dependent to identify and to evaluate. The research question is: *Is it possible to establish an automatic, operational change detection system for high resolution satellite data without loss of thematic content?*

3. **Analysis of the dynamic behaviour of vegetation associations or land cover classes.** A prerequisite for the analysis of dynamic behaviour is a data time series suitable for the identification of changes in the objects of interest. The research question pursued in this context is: *Is it possible to analyse the dynamic behaviour of land cover classes and vegetation associations on the basis of daily satellite data in the Dra catchment?*
4. **The derivation of bio-physical parameters.** Biophysical parameters are of major importance for the estimation of biomass or net primary productivity and are input parameters for environmental models (see chapter 8). The research question followed is: *Is it possible to derive bio-physical parameters on the basis of single species or vegetation associations with satellite data?*

To achieve these main goals several intermediate research steps need to be achieved. These steps were followed with the objective to automate processing as much as possible.

- **establishment of a transferable classification scheme for the whole catchment**
- **elaborated fieldwork and data storage in a GIS**
- **automatic generation of base material of satellite imagery in high geometric accuracy (DEM and ortho-photomap)**
- **automatic radiometric normalisation of (multitemporal) satellite images**
- **generation of a radiometrically correct satellite image mosaic of the Dra catchment**
- **development of decision rules for a hybrid classification system**

1.3 Structural composition of the work

Chapter 2 introduces the study area and describes field observation techniques and the assessment of validation data. In chapter 3, land cover classification schemes are discussed and the specifications of the land cover classification scheme used within

this study are described. Chapter 4 introduces techniques of modern photogrammetry applied to remote sensing satellite images for the automatic generation of cartographically correct base material. Chapter 5 discusses the pre-processing techniques applied to the satellite images in order to obtain data with low calibration errors as a prerequisite for data interpretation and comparison. In the data processing emphasis was put on the geometric and radiometric accuracy of the processed data. Different processing steps for very high (CORONA KH4B, IKONOS-2), high (ASTER, LANDSAT MSS/TM/ETM+) and low resolution data (NOAA/AVHRR) are outlined. With chapter 6 the thematic interpretations begin in the form of the generation of a land cover map. The theoretical background and applied methods are discussed. In chapter 7, purpose dependent change detection techniques for the comparison of historic and recent satellite data are discussed. Chapter 8 discusses the derivation of a locally obtained bio-physical parameter and the transfer to the Dra catchment. A change detection application to the Basin of Fezuata reviews the complex social and economic interactions of human-induced land cover change and outlines the possibility of using historical land cover information and change detection to derive land use information.

Figure 1.3 shows a flow chart of the work structure and the interrelation of processed satellite data (next page).

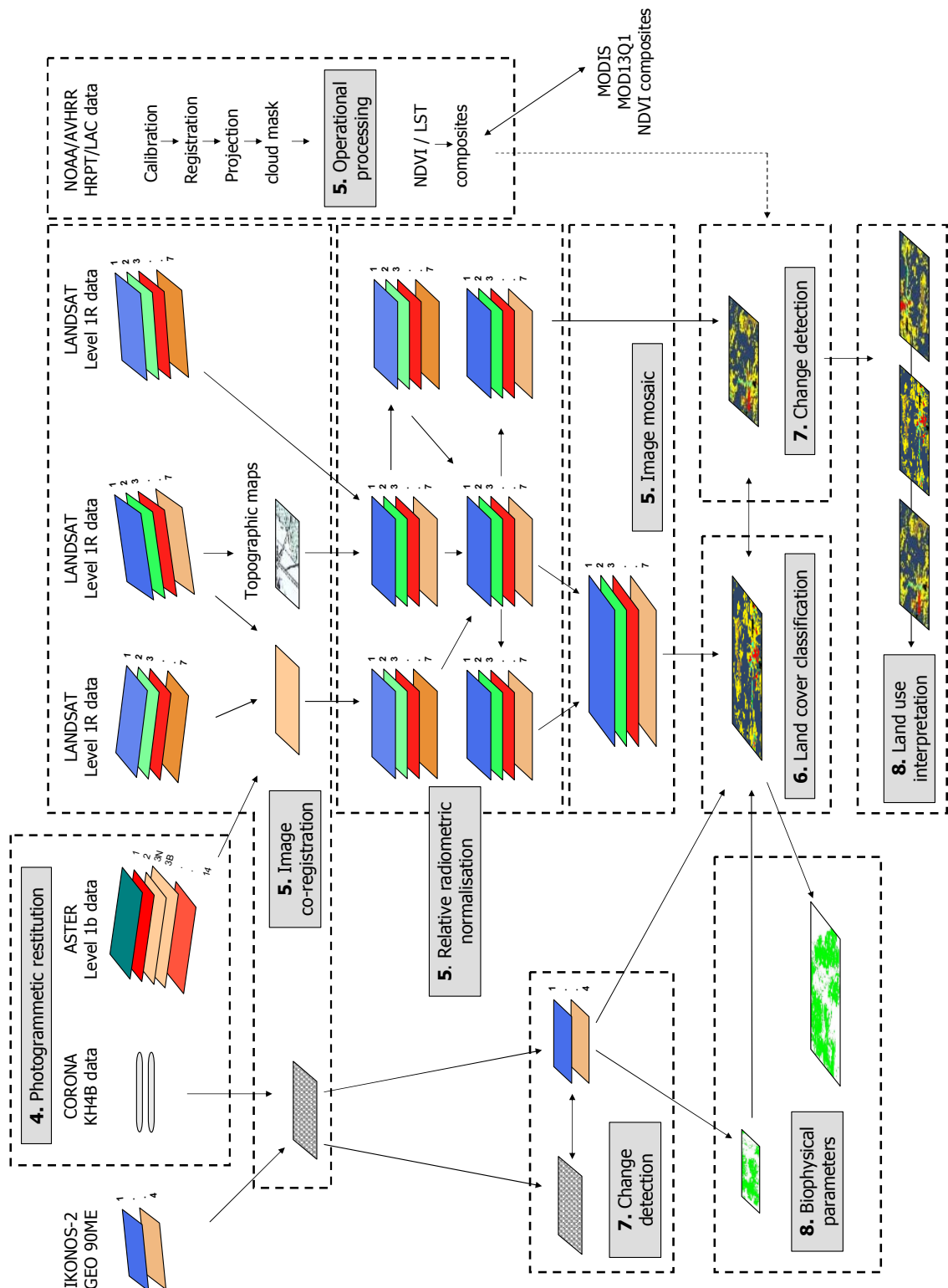


Figure 1.3: Flow chart of the satellite data used and the processing steps applied within this study. The numbered text boxes correspond directly to the chapters within this thesis.

2 Regional settings

”Desertification means a long term change in the characteristics of a biome. Plant life, vegetation and soil changed and impoverished, and so desertification should not be confused with short term drought; although drought can be a causal factor.”

S. Mayhew, 1997

Dryland areas cover approximately one third of the solid earth surface. Arid and semiarid regions belong to drylands, which are permanently, seasonally or temporarily subject to deficit in moisture availability. These regions are especially vulnerable to natural climatic and man made changes and are identified as areas at risk in the global climate change discussion. The importance of monitoring the desertification dynamics in these areas has long been recognised (see e.g. Hill, 2000).

Considering the spatial extent, the need to observe some areas frequently, and the difficulty of access it is clear that a ground survey alone would be incapable for a monitoring process. Graetz (1987) postulates that, in order to obtain information of the surface ”in the Australian semi-arid rangelands remote sensing provides the only possibility in a reasonable temporal resolution”. Due to the generally low cloud coverage in arid areas, optical remote sensing data is well suited for land cover/land use analysis (Hill, 2000).

2.1 The Dra catchment

The Dra catchment appears extremely heterogeneous with more than 4000m of elevation in the High Atlas, compared to the lowest region of the project area of Lac Iriki, 300km distant, at an elevation about 450m. The northern and southern parts not only have different geologic and geo-morphologic regimes, but also differ in climate conditions (Mediterranean and Saharan), thus affecting the vegetation distribution, characteristics, and their annual seasonal behavior. Houérou

(2001) describes the study area generally as part of the semi-arid steppeland north of the Sahara, with a more propitious regime for perennial species due to a bimodal climate regime with higher amounts of precipitation in March/April and October/November. The catchment itself is located in a transition zone with mediterranean influenced subhumid steppeforest and the mountain-ecosystem vegetation associations in the northern parts, semi-arid vegetation in the central parts, and the arid desert ecosystems of the pre-saharan vegetation types in the southern parts (Finckh and Staudinger, 2002).

The scarcity of water and the temporal and spatial distribution of this limited resource determines vegetation growth and agricultural production to a large extent. Runoff from the High Atlas mountain chain, which acts as an orographic barrier, is drained by two major river systems: the Qued Dades and the Qued Ouarzazate, which join in the Basin of Ouarzazate. From this point, one river system transports water further south to the Dra valley (see Figure 2.1). In recent times water from the Atlas mountains rarely reaches the southernmost oasis of the Dra valley, the oasis of M'hamid. Figure 2.1 shows the catchment area of $28419km^2$ size with assumed sink of the Lac Iriki.

The system of the river Dra, at the fringe of the Sahara desert, with potential evapotranspiration of about $2000mm$ per year and $70mm$ of annual precipitation at Zagora (Pletsch, 1971), depends to a high extent on water runoff from the High Atlas mountain chain, as well as on the highly variable local precipitation. The bimodal annual precipitation regime peaks in spring and autumn but there is a significant amount of summer precipitation about 10-20% (Houérou, 2001). The mean annual precipitation values differ regionally from $54mm$ in the region of the Lac Iriki (Hnichi, 1989) to $150mm$ in Ouarzazate (see Figure 2.2). The mean annual precipitation estimations in the High Atlas mountains vary: Messerli (1967) describes measurements from the 1950's to 1960's of $550mm$ annual precipitation on the southern slope of the Jebel Mgoun. (Youbi, 1990) describes $518mm$ of annual precipitation. The climate station installed by the IMPETUS project at the Jebel Mgoun recorded from October 2001 until October 2002 $520mm$ (pers. comm., O. Schultz, University of Bonn). The highest temperatures in the southern parts during the summer months range between $40^{\circ}C$ and $55^{\circ}C$, creating an evaporation rate that far exceeds the precipitation (see IMPETUS, 2001, for further discussion).

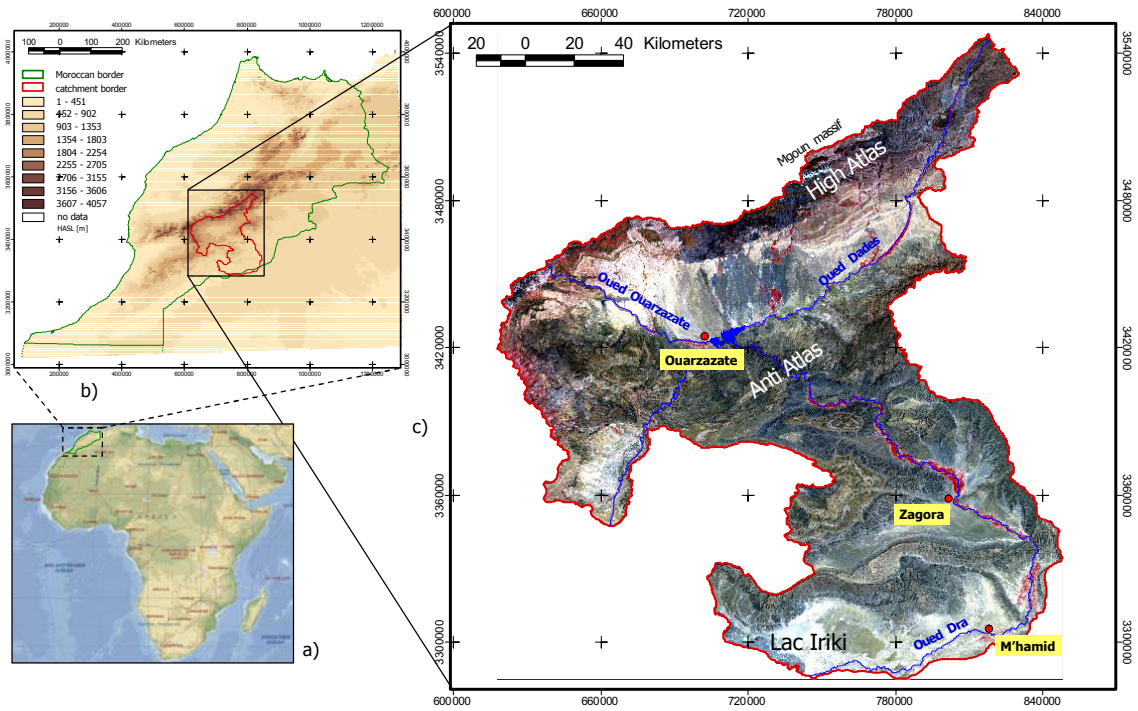


Figure 2.1: Zoom to the Dra catchment in Morocco b) (background GTOPO30 digital elevation model (USGS, 2003a) in height above sea level (HASL)) from a continental view a) (source Encarta) to the location of the catchment in an LANDSAT image mosaic false color composite (FCC - RGB 432) c). (The dotted green lines represent the border of the West-Sahara)

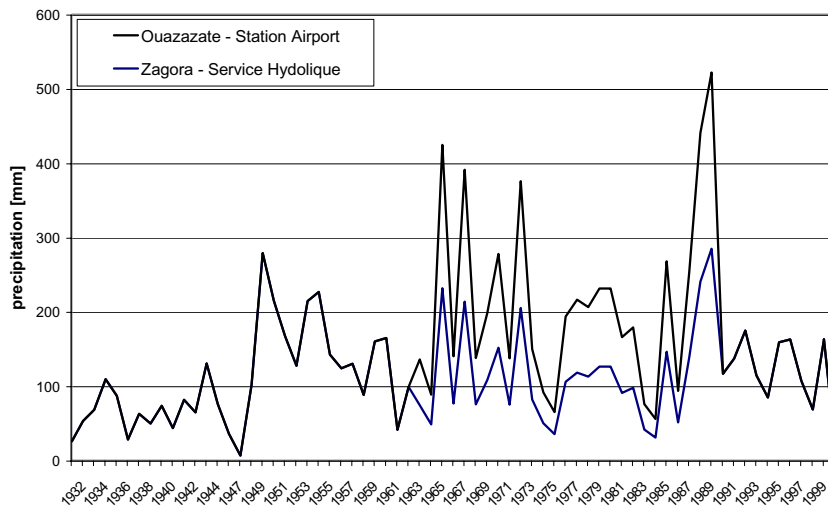


Figure 2.2: Annual average precipitation of Ouarzazate and Zagora (data were provided by P. Knippertz, University Cologne and M. Sabbar, Service Hydrolique in Ouarzazate)

The runoff from the High Atlas mountains since 1972 is retained in an artificial lake near Ouarzazate by the dam Al Mancour ad Dehbi. Since 1972, the water flow has been regulated, so that floods in the river Dra after snow melt or intensive precipitation events are controlled. Water is released at certain periods according to an agricultural and water management plan, to optimize production and guarantee water availability in the growing town of Ouarzazate (Bencherifa, 1990). Before the dam was constructed, the major water loss for agricultural production was that water drained in the ground aquifers during periods of high discharge. Nowadays the major loss is due to evaporation of lake water. The hydrological system of the Dra valley has changed since 1972 when the dam was constructed. Most wells have lower water levels as the groundwater table dropped, due to increased irrigation and water consumption and less re-filling of the aquifers (M. Sabbar, Servicé Hydrique Ouarzazate, pers comm.; K. Goldnick, GTZ Zagora, pers. comm.). The Dra catchment generally drains into the Atlantic ocean. Since human interference was made to the hydrologic system in 1972 spring floods were regulated, water only reached the region south of the Lac Iriki in 1989 (O. Abellaoi pers. comm, ORM-VAO, Ouarzazate). Currently the relevant hydrological processes and major land cover changes take place in the upper part of the Dra catchment. This part of the catchment, with the assumed sink of the Lac Iriki, is referred to as the study area or Dra catchment (see Figure 2.1).

The oasis systems oriented along rivers in mountainous areas with small artificial terrace systems have a width of few meters (Spaeth, 1997), while in the less elevated parts in the Qued Dra, wider oasis up to 6km (near Zagora) exist. In the northern Atlas Mountain oasis, major agricultural communities are influenced by mediterranean vegetation associations consisting of: poplar, ash, maple, fruit trees (such as apple, almond, olive, peach, walnut, figs, pomegranate) and crops (including maize, wheat, oats, radish, potatoes, alfalfa, carrots). In the southern oasis of the Dra valley the classical production method includes the use of different agricultural levels (Müller-Hohenstein, 1997). The palm trees (*Phoenix dactylifera*) produce not only dates, but also protect the lower vegetation from direct sunlight, thereby reducing evaporation. In the shade of the palms, olive trees, pomegranate, figs or grapes are cultivated. The third layer consists mostly of vegetables and crops such as potatoes, maize, wheat, henna or alfalfa (Pletsch, 1971).

The vegetation coverage is sparse, apart from the river oasis or irrigated areas. Pastoral nomadism in the rangelands has been a traditional and sustainable form of

land-use over several centuries (Hammoudi, 1985; Zainabi, 1989). Some nomads still practice a certain form of transhumance (Pletsch, 1971; Hou  rou, 2001), staying in the mountainous areas during the hot summer months and migrating to the lower elevations in winter. Due to overgrazing and fuel-wood extraction, the inhabitants are interfering intensively with the natural environmental system. Herds of goats and sheep further degrade the landscape. Population growth and land use conflicts between sedentary and nomadic people additionally increase the degradation pressure by reducing the vegetation coverage (see section 8.2). The extreme climate and varieties of geomorphology have assisted in developing a significant diversity of landscapes and habitats that are adapted to the semi-arid conditions. Despite the human impact, even in areas of extreme climate conditions (less than 70mm annual precipitation), natural wood and shrub vegetation types such as *Acacia raddeana* and *Tamarix aphylla* still exist within the catchment.

The high surface heterogeneity within the catchment led to the decision to divide the Dra catchment into sub-regions of similar geological and ecological characteristics for the purposes of conducting a vegetation and land cover description. The first step towards this was to digitise the borders of the catchment on the basis of existing topographic maps on a scale of 1:100000. Lac Iriki was considered as the lowest point or sink in the catchment (see Figure 2.3). Reflection of soil material was considered to discriminate the background information into units. The method applied for this differentiation of image units is referred to as photomorphic unit (PMU) mapping (Daels and Antrop, 1977). The PMUs are described by 1) dominating tonality or colour, 2) patterns (dots, lines, patches etc.) and c) texture. Landscape elements are characterised by combinations of similar colour, shape, sizes and patterns. This is represented in the PMUs (Daels and Antrop, 1977). The mapping and the mapping criteria of the PMUs depend on the scale and resolution of the image and need to be adapted for each purpose. For each type of analysis an interpretation key is necessary. What in a courser resolution is described as texture, might in a finer resolution become a pattern, or even a single object. PMUs or sub-units of the catchment were digitized on the basis of the colour differences, texture and pattern of a LANDSAT ETM+ mosaic (section 5.3). This mapping was also guided by the use of field data, topographic maps at a scale of 1:100000 and a geological map at a scale of 1:500000.

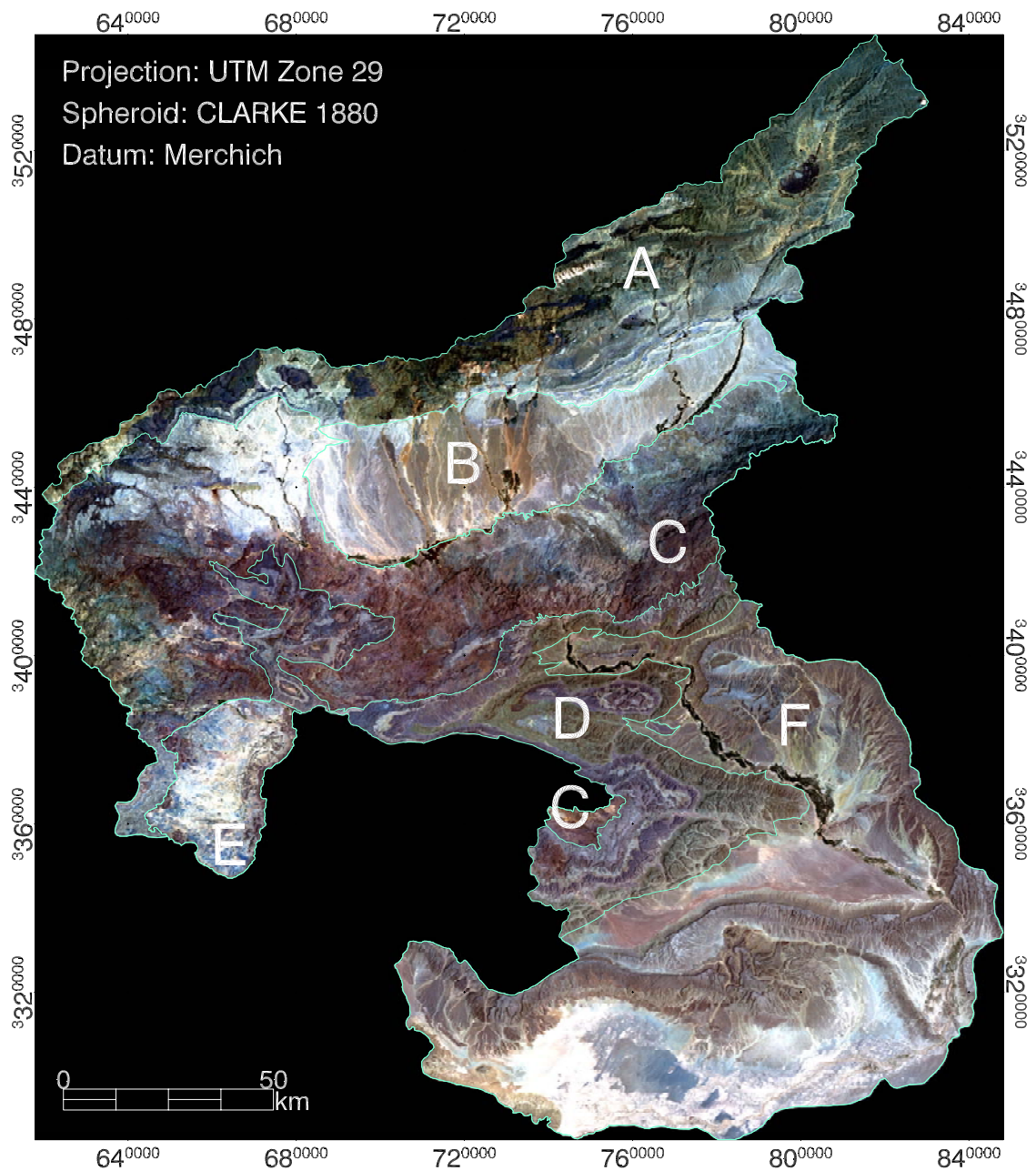


Figure 2.3: Sub-regions of the Dra catchment based on the PMU mapping displayed in a LANDSAT ETM+ true colour mosaic

From north to south, the sub-regions (see Figure 2.3) are described below with respect to geological origin and the dominant (rangeland) vegetation types (M. Finckh, M. Staudinger pers. comm, 2000-2003). For further reading on the vegetation composition of the catchment see Emberger (1939); Ozenda (1977); Fennane and Tattou

(1998); Hou  rou (2001).

A High Atlas (4643km^2), with Jebel Mgoun as the highest mountain at 4058m , has a variscan mountain basement with overlying, mesozoic carbonate dominated layers. The High Atlas is an ancient rift system which formed in a plate tectonic driven orogeny that resulted in a complex structure (Froitzheim et al., 1988; IMPETUS, 2001) with a variety of rock types (Abdeljali et al., 1959). The dominant vegetation types in this region are comprised of characteristic species such as:

Tall shrubs or trees: *Juniperus phoenicea*, *Juniperus thurifera*, *Juniperus oxycedrus*, *Fraxinus xanthoxyloides*, *Quercus rotundifolia*, *Pinus halepensis*.

Bushes and shrubs: *Ephedra nebrodensis*, *Tamarix africana*, *Nerium oleander*, *Buxus balearica*.

Dwarf shrubs: *Convolvulus trabutianus*, *Zilla spinosa*, *Hammada scoparia*, *Artemisia herba-alba*, *Artemisia atlantica*, *Launaea acanthoclada*, *Salvia aegyptiaca*, *Marrubium desertii*, *Cytisus balansae*, *Astragalus spinosus*, *Astragalus ibrahimianus*, *Genista scorpius*, *Ormenis scariosa*, *Erinacea anthyllis*, *Bupleurum spinosum*, *Ribes uva-crispa*, *Teucrium malenconianum*, *Alyssum spinosum*, *Ormenis scariosa*, *Adenocarpus bacquei*, *Helianthemum ellipticum*, *Hertia maroccana*, *Thymus spec.*, *Vella mairei*

Grasses and herbs: *Stipa barbata*, *Stipa parviflora*, *Stipa tenacissima*, *Lygeum spartum*, *Dactylis hispanica*, *Scorzonera pygmaea*, *Carduncellus pinnatus*, *Jurinea humilis*, *Festuca hystrix*, *Arenaria pungens*

B Basin of Ouarzazate (2651km^2) is a basin of up to 3000m thick tertiary sediments with origins in the High Atlas mountains. The elevation ranges from 1200m - 1500m (IMPETUS, 2001). The dominant vegetation types in this region are comprised of characteristic species such as:

Bushes and shrubs: *Ziziphus lotus*

Dwarf shrubs: *Convolvulus trabutianus*, *Zilla spinosa*, *Hammada scoparia*, *Antirrhinum ramosissimum*, *Artemisia herba-alba*, *Gaillonia reboudiana*, *Launaea arborescense*, *Farsetia hamiltonii*, *Gymnocarpus decander*, *Salvia aegyptiaca*, *Marrubium desertii*, *Astragalus spinosus*, *Genista scorpius*, *Helianthemum ellipticum*, *Teucrium polium*, *Zygophyllum gaetulum*

Grasses and herbs: *Stipa retorta*, *Stipa parviflora*, *Stipagrostis obtusa*, *Peganum harmala*, *Cymbopogon schoenanthus*

C Crystalline Anti-Atlas (2651km²), consists of mainly Precambrian crystalline formations of volcanic and magmatic origin. Elevations range from 1100m up to 2900m (IMPETUS, 2001). The dominant vegetation types in this region include characteristic species such as:

Tall shrubs or trees: *Juniperus thurifera*

Bushes and shrubs: *Atriplex glauca*, *Tamarix africana*, *Nerium oleander*, *Ziziphus lotus*, *Withania adpressa*, *Vitex agnus-casti*, *Burus balearica*

Dwarf shrubs: *Anvillea radiata*, *Convolvulus trabutianus*, *Zilla spinosa*, *Hammada scoparia*, *Antirrhinum ramosissimum*, *Artemisia herba-alba*, *Artemisia atlantica*, *Gaillonia reboudiana*, *Launaea arborescens*, *Launaea acanthoclada*, *Lavandula mairei*, *Lavandula tenuisecta*, *Farsetia hamiltonii*, *Gymnocarpus decander*, *Salvia aegyptiaca*, *Marrubium desertii*, *Cytisus balansae*, *Astragalus spinosus*, *Genista scorpius*, *Ormenis scariosa*, *Erinacea anthyllis*, *Bupleurum spinosum*, *Ribes uva-crispa*, *Helianthemum ellipticum*

Grasses and herbs: *Stipa barbarta*, *Stipa parviflora*, *Lygeum spartum*, *Dactylis hispanica*, *Scorzonera pygmaea*, *Carduncellus pinnatus*

D Sedimentary Anti Atlas (3706km²) rocks are mainly deposits of the late Proterozoic at elevations up to 2600m (Emran et al., 1996). The dominant vegetation types in this region are comprised of characteristic species such as:

Bushes and shrubs: *Atriplex glauca*, *Tamarix africana*, *Nerium oleander*, *Ziziphus lotus*, *Withania adpressa*, *Acacia raddiana*, *Vitex agnus-casti*

Dwarf shrubs: *Anvillea radiata*, *Convolvulus trabutianus*, *Zilla spinosa*, *Hammada scoparia*, *Antirrhinum ramosissimum*, *Artemisia herba-alba*, *Gaillonia reboudiana*, *Launaea arborescens*, *Launaea acanthoclada*, *Lavandula mairei*, *Lavandula tenuisecta*, *Farsetia hamiltonii*, *Gymnocarpus decander*, *Carthamus fruticosus*, *Salvia aegyptiaca*, *Marrubium desertii*, *Ormenis scariosa*, *Genista scorpius*, *Teucrium malenconianum*, *Adenocarpus bacquei*, *Withania adpressa*

E Basin of Tazenakht, (920km²) with a mean elevation of 1500m is a region embedded in the Anti-Atlas. The surrounding rocks are predominantly Cambrian

and carbonatic. In the interior of the basin are outcrops of pre-cambrian crystalline and magmatitic rocks with quaternary deposits (Abdeljali et al., 1959). The dominant vegetation types in this region are comprised of characteristic species such as:

Bushes and shrubs: *Atriplex glauca*, *Ziziphus lotus*, *Withania adpressa*, *Vitex agnus-casti*

Dwarf shrubs: *Convolvulus trabutianus*, *Zilla spinosa*, *Hammada scoparia*, *Antirrhinum ramosissimum*, *Artemisia herba-alba*, *Gaillonia reboudiana*, *Lau-naea acanthoclada*, *Farsetia hamiltonii*, *Gymnocarpus decander*, *Salvia aegyptiaca*, *Marrubium desertii*, *Astragalus spinosus*, *Genista scorpius*, *Helianthemum ellipticum*, *Helianthemum croceum*, *Teucrium polium*

Grasses and herbs: *Stipa retorta*, *Stipa parviflora*, *Stipagrostis obtusa*, *Peganum harmala*

F Dra Valley (9286km²). At the northern limit, where the river Dra breaks through the crystalline Anti Atlas, the elevation is 850m, compared with the lowest point in the south near Lac Iriki of about 450m. The landscape is dominated by quartzite lineaments of up to 1150m height with quaternary basin fillments. Since 2000, the Qued Dra has been part of the UNESCO World Heritage Program: Man and Biosphere (UNESCO, 2003). The dominant vegetation types in this region comprise characteristic species such as:

Tall shrubs or trees: *Maerua crassifolia*, *Acacia ehrenbergiana*, *Tamarix aphylla*, *Acacia raddiana*.

Bushes and shrubs: *Tamarix africana*, *Nerium oleander*, *Ziziphus lotus*, *Calligonum comosum*, *Retama raetam*, *Retama monosperma*, *Rhus tripartita*, *Withania adpressa*, *Randonia africana*, *Callotropis procera*, *Salsola tetragona*, *Anabasis articulata*

Dwarf shrubs: *Ephedra alata*, *Anvillea radiata*, *Convolvulus trabutianus*, *Zilla spinosa*, *Hammada scoparia*, *Nitraria retusa*, *Fagonia zilloides*, *Anabasis articulata*, *Antirrhinum ramosissimum*, *Zygophyllum gaetulum*

Grasses and herbs: *Panicum turgidum*, *Pennisetum dichotomum*, *Pergularia tomentosa*, *Pulicaria crispa*

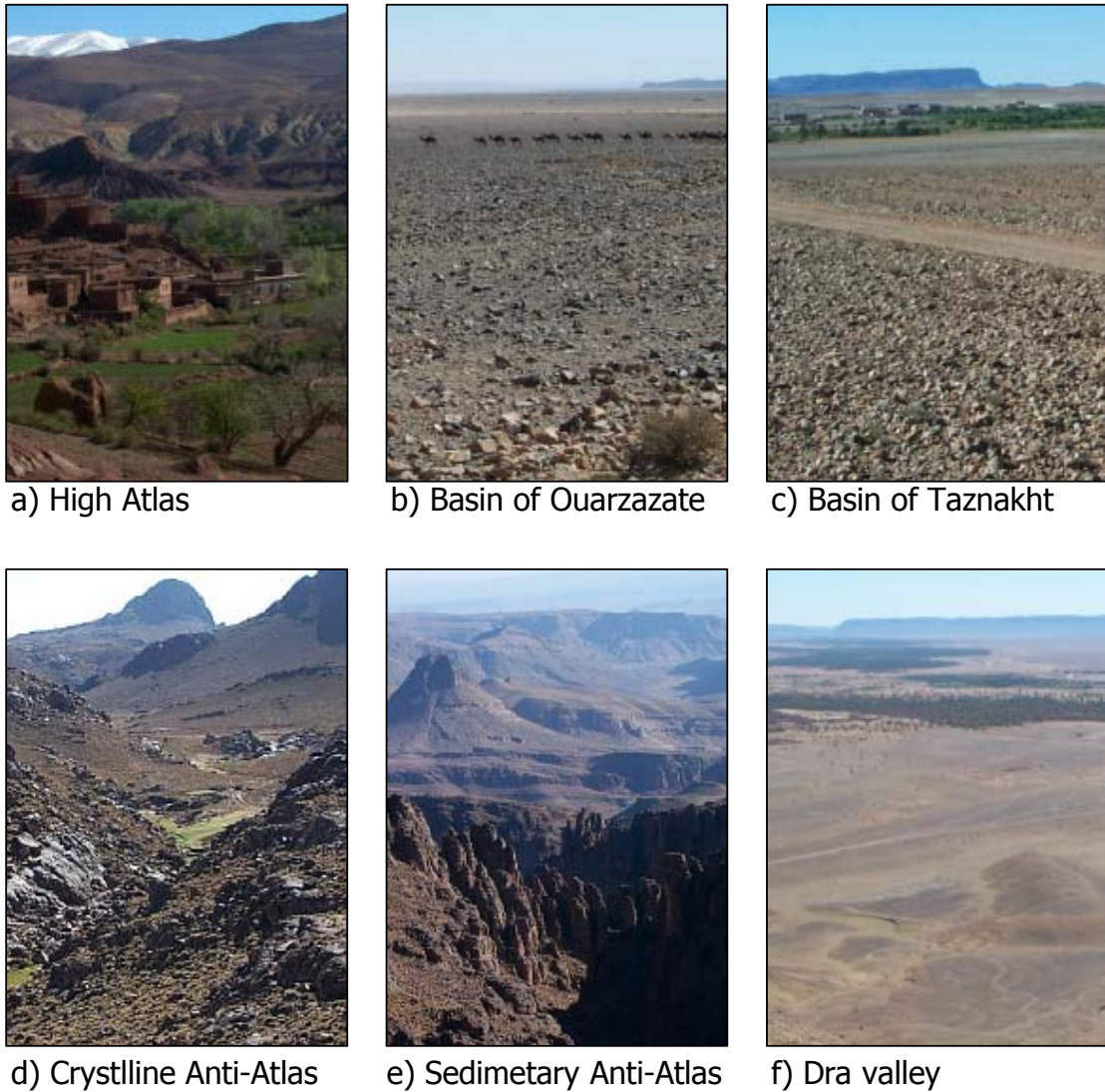


Figure 2.4: Landscape examples of the six sub-regions of the Dra catchment (Photos: M. Schmidt, 2000-2002)

2.2 Fieldwork and ground truth data

”Remote Sensing is nothing without ground truth and ground truth is nothing without remote sensing”

G. Konecny, 2000

The quality of a classification result is not only dependent on the skills and ex-

periences of an operator, but also to a high degree on the knowledge of the terrain and the eco-system interactions and feedback mechanisms. Lillesand and Kiefer (2000) state that "The acquisition of reference data involves collecting measurements or observations about the objects, areas, or phenomena that are being sensed remotely." Reference data, including training and test data, are of great importance in a supervised classification: without training pixels no supervised classification is possible and without validation a classification is useless. Prior to the collection of a large amount of field data, the identification of the potential land cover/land use classes and the thematic content that a classification can or should incorporate is required. In fact a classification should be the thematic interpretation of the landscape (Jensen, 1996a). For the establishment of such an interpretation factors that influence and determine the appearance of objects or phenomena need to be identified and understood. For this purpose, field observations are necessary for a supervised and knowledge based classification approach (Richards and Jia, 1999). If the thematic content, and thus a classification scheme, is defined, field data can be obtained and assigned for the classification purposes. For this reason three field campaigns were conducted in the years 2000 (October 9 - November 11), 2001 (March 10 - April 19) and 2002 (February 2 - April 9). Spring and autumn were chosen to observe the vegetation at different phenological stages. Field data of the different vegetation states were obtained, although the vegetation onset in the mountainous areas and the lower areas are slightly different.

Vegetation analysis

The first field trip in October/November 2000 served to identify the vegetation cover and composition and to identify the potential land cover and land use classes. Vegetation data were obtained for the purpose of:

- identification of vegetation associations;
- identification of the physical plant properties/requirements;
- to obtain vegetation density information.

Within the interdisciplinary approach of the IMPETUS subproject B3, a close collaboration with botanists (N. Jürgens, M. Finckh and M. Staudinger) was established. This collaboration resulted in the identification of vegetation associations, and finally the definition of a classification scheme (see chapter 3). As a standard,

for every field observation, in addition to site and vegetation descriptions, at least one GPS point and one digital image was taken. Botanic vegetation reveals, obtained during the project, of representative $10m \times 10m$ rasters (IMPETUS, 2001; Finckh and Staudinger, 2002) could be used as independently obtained data.

The time consuming Leaf Area Index (LAI) measurements were concentrated on one vegetation class to test whether this approach is suitable in this environment. Measurements were performed with a hand-held digital plant canopy imager (CI-110) device from CID, INC. Species of *Tamarix aphylla* individuals were chosen as a suitable study class, due to the extended coverage within the Dra valley and the importance of the species e.g. in fixing mobile sand. LAI measurements, estimations of plant coverage, and density for the individuals in different test plots were performed (see subsection 8.1.1). The amount of accumulated sand beneath the Tamarisks was estimated due by measurements of the length, height and width of the Tamarisk hills (see subsection 8.1.1).

Soil/background analysis

The main focus of this study is a vegetation description. Therefore a categorisation of the soil/background information in five classes was found to be sufficient: 1. *sand*, which describes all kinds of loose sands including dunes and surface components associated with the arabic terms "Nebkha" and "Erg". 2. *Desert Crust*, which is a description of sandy materials fixed by a calcium carbonate crust. 3. *Playa* describes areas of high clay content, which are often also saline. 4. *Gravel/pediment* includes the arabic terms "Reg" or "Hammada", which describe (weathered) loose stone material. 5. *Rock*, representing all kinds of solid outcrops.

Analysis of the soil was performed for the purpose of identifying different surface components and their spectral response pattern. The presence of a calcium carbonate ($CaCO_3$) crust was tested in the field with a HCl reaction test for the identification of desert crust (Press and Siever, 1995). The existence of desert varnish and the amount of gravel were parameters used to differentiate between pediment/gravel, rock and sand. Electrical conductivity of some wells and the top-soils was used as proxy information on soil salinity (see e.g. Fogarty et al., 1993). This was measured with an Eijkelkamp L17p device. Clay content and salinity information were used to identify areas grouped as playa.

Interrelation of geo-factors

Analysis of the environmental conditions in terms of soil information, water availability and quality, elevation etc. contributed to the identification and formulation of interrelations that determine the vegetation distribution. The incorporation of these rules is important for the detailed class differentiation and the classification approach. These rules were formulated by close collaboration within the sub project B3 and are discussed for each sub-region within chapter 6.

Ground Control Points

During the field campaigns Ground Control Points (GCPs) were obtained for a number of purposes:

- to locate ground truth data
- for the photogrammetrical restitution of CORONA and ASTER data
- geo-coding LANDSAT and IKONOS-2 data

The polygon, line and point data were recorded, depending on purpose, by different GPS systems and devices. The accuracy of the GPS systems is dependent on the availability, distribution and signal intensity of satellites in the sky. A Leica 300 and a TRIMBLE PATHFINDER Pro XS differential GPS were used to meet the requirements for high geometric accuracy GCPs in x, y and z coordinates (see chapter 4). The different GPS systems used are:

- a *LEICA 300* system requires a ground based reference station for the differential correction of the GPS signal from the satellites. The position must either be known or measured over a certain time interval (e.g. 2h). The relative accuracy of the receiver signal is in the range of centimeters, while the absolute point accuracy is dependent on the accuracy of the reference station. A high GCP accuracy is necessary for the photogrammetrical restitution of CORONA data (see chapter 4).
- a *TRIMBLE PATHFINDER Pro XS* system uses a geo-stationary satellite for the differential correction of the position signal and has a signal accuracy of less than 1m (Trimble, 2003). This accuracy was necessary for the geometric correction of IKONOS-2 data and the photogrammetric restitution of ASTER data (see chapter 4 and chapter 5).

- a *Garmin III plus* GPS with an accuracy of 4 – 10m (Garmin, 1999) was used for obtaining GCPs for geo-referencing and ground truth data for the analysis with LANDSAT data (see chapter 5).

The identification of GCPs is scale dependent and requires good documentation, otherwise the information is imprecise, or even useless, for later applications. Figure 2.5 shows a documentation example of a GCP obtained on 17.04.2000, near Zagora for the restitution of CORONA data. Full documentation requires the storage of meta information such as the cartographic and the observation datum and the measurement accuracy.

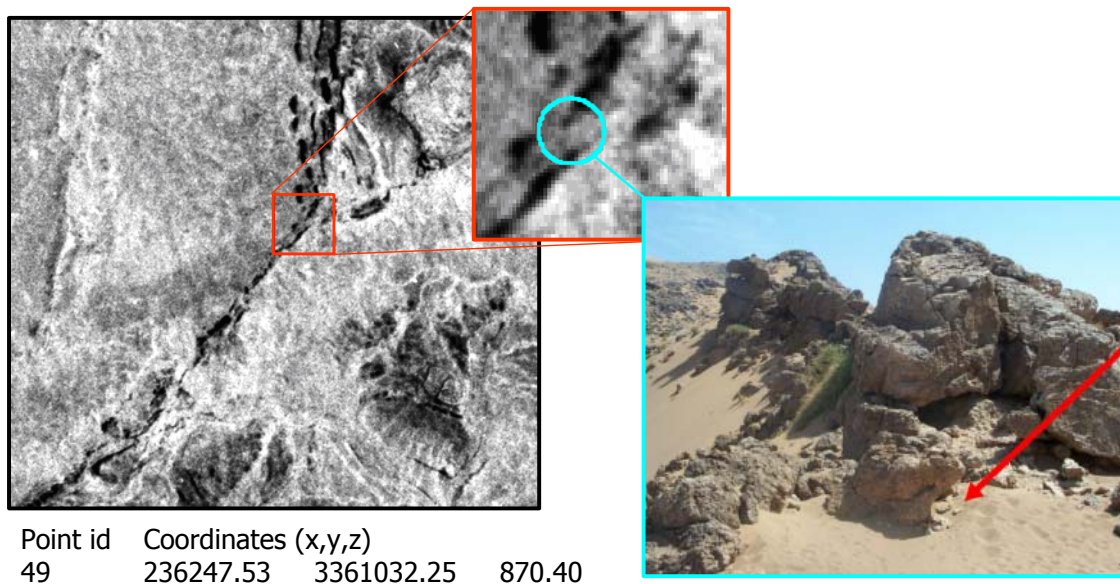


Figure 2.5: Example of a GCP documentation for the very high resolution CORONA data (displayed coordinates are in UTM WGS84), the location of the GCP is indicated

Table 2.1 shows the region, number and overall accuracy (in x, y and z) of the differential GPS (DGPS) points obtained during the field campaigns.

Although the DGPS points in the region of Toundoute were obtained with high precision ($< 0.5m$), due to an insufficient documentation, the quality of the data was reduced. Due to interference of the GPS signal by sandstorms, leading to inconsistent and inaccurate results, measurements in the K'tauer area were repeated. Besides GCPs terrain check points were recorded.

Table 2.1: DGPS points obtained during field observations

Region	No. of GCPs	accuracy	device
Zagora	19	< 0.5m	Leica
Toundoute	18	< 3m	Leica
K'tauer	15	< 1m	Trimble
Basin of Ouarzazate	31	< 1m	Trimble

The field derived point data or line segments were downloaded from the GPS devices, transformed into vector data, re-projected (if necessary) and stored in a GIS database together with digital images and a short description of the area (see Figure 2.6). Polygons obtained as points were recorded as fixed time interval, fixed distance interval or manually.

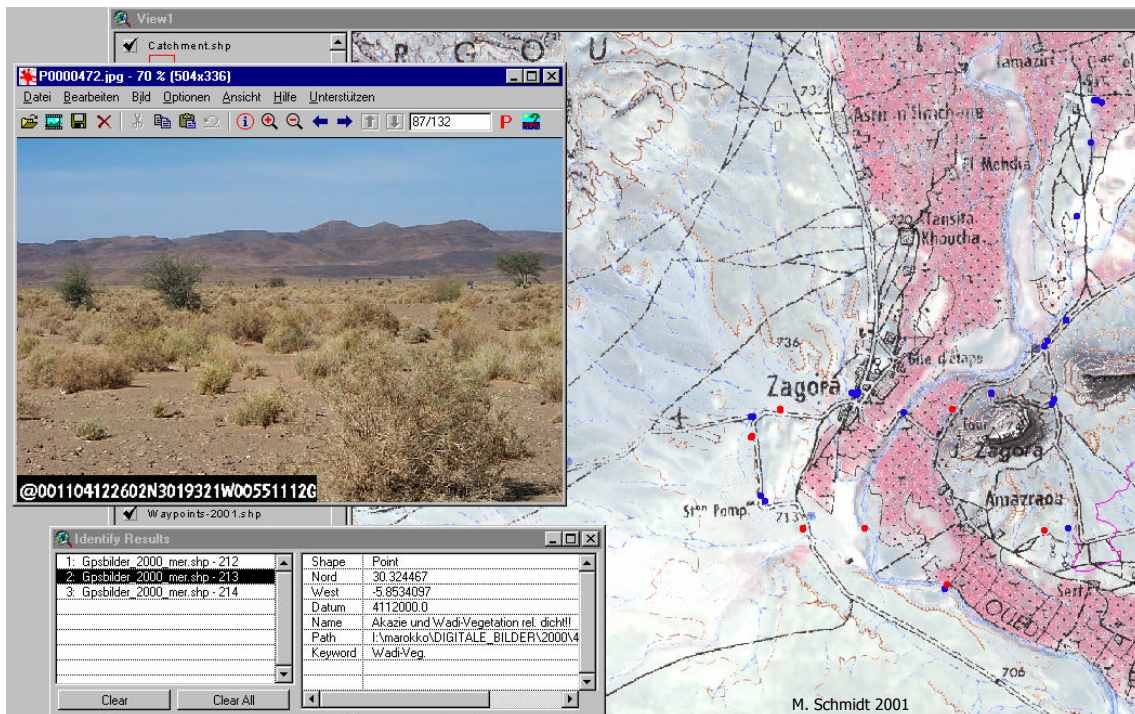


Figure 2.6: Ground truth data stored in a GIS (ArcView) database (screen-print)

In combination with geo-referenced datasets, the GPS link in ERDAS Imagine and ENVI/IDL was a useful and efficient tool to locate the positions within the

dataset of interest in real time and store the ground truth information directly in a vector layer, together with field notes (see Figure 2.7).



Figure 2.7: Example of the real time GPS link of ERDAS imagine in the field (adapted from Thamm and Schmidt, 2001)

Information from the GPS tracks was used to compile a road network and superimpose this on the classification, as all major sealed routes within the catchment were recorded.

For the orientation in the field and object identification LANDSAT and ASTER data were used. The very high resolution CORONA KH4B mission DS-1117 data from 1972 were used for visual identification of sub-pixel objects, such as species of *Acacia raddiana*. The data were scanned and archived for the whole catchment (for further descriptions on CORONA see chapter 4).

Post-processing and problems

The ground truth information from the field trips were integrated and used for defining the land cover/land use classification scheme. Ground truth information were assigned either in the field, or in a post-processing step, to the specific land cover class. Experience after the first field trip showed that the reference polygons are better for object identification in the context of the terrain as, especially in the rugged terrain, deviations of map and GPS data are often evident. Incorrect or inaccurate geo-location polygons that it was not possible to correct by reference to the contextual situation, or that were ambiguous, were removed. Consequently on

the reliable fraction of the ground truth data were used as either test or validation data in the image classification (see chapter 6). Figure 2.8 shows an example of a polygon shift.



Figure 2.8: Position shift of the ground truth data due to geo-location errors. The yellow points represent the data obtained in the field, the green polygon represents the shifted dataset. Coordinates of the photo (UTM): 809370/3348542

A homogeneous distribution of the validation data within the catchment was hampered by the large catchment size and variable accessibility to some areas, especially in the rugged mountain terrains.

2.3 Conclusions

Field observations underpin the understanding of the complex ecosystem interactions and driving forces for the occurrence of vegetation patterns and their changes. Due to the size and heterogeneity of Dra catchment, six sub-regions were identified according to similar ecological and geological constraints, which were delimited into PMUs. Field measurements and ground truth data were stored in a GIS database for later use. The GIS database of the ground truth data served as data source of the compilation of the test and validation dataset used in the image classification in chapter 6.

3 Low, Medium, High or Very High Resolution for land cover mapping?

”The higher a land cover classification is in resolution the more specific it is and lesser the possibility of transfer is given.”

G. Menz, 2003

Land cover and land use information of the earth surface is a key source of information for many scientific, resource management and policy purposes (Jensen, 1996a; Cihlar et al., 2000). Critical biophysical parameters that determine ecosystem functionality, hydrological processes and interactions between surface and atmosphere can be derived from land use and land cover information. This information of the earth surface is therefore of strong interest for studies aiming at interaction, dynamics and feedback mechanisms of terrestrial processes, at all scales from regional to global (Cihlar et al., 2000). Loveland et al. (2000) denotes that land cover data are among the most important terrestrial data. While the term land cover relates to the type of features on the earth surface, it also relates to human activity on surface areas (Lillesand and Kiefer, 2000). Usually supplementary information is needed to determine land use information. In land cover classification spectral information are generally transferred into thematic information. Ideally a classification process should be operator-independent running objectively according to pre-defined rules and a prescribed taxonomy: a classification scheme.

Land cover analysis can be performed either by classical cartography, interpretations of aerial pictures, as introduced by the German geographer Troll (1939), or since the launch of the early LANDSAT 1 satellite in 1972, by satellite data. Land cover mapping has become probably the most widely applied in remote sensing studies (Cihlar, 2000). In terms of cost-effectiveness satellite data provides the most efficient alternative (Konecny, 1999).

3.1 Scale in land cover mapping

”The question of scale is one that bedevils all spatial analysis”

P.Mather, 1999

As environmental planning and management became attractive the demand for land cover information increased, and thus this topic became probably the most widely applied in remote sensing (Cihlar, 2000). Large area observations with reasonable repetition intervals allows multispectral and multitemporal analysis without physical contact with the 'sensed' objects. In certain areas this might be the only rational observing possibility (Hill, 2000). The concept of land cover is not standardised in terms of parameters or units and in reality a land cover classification is always operator-dependent (Foody, 2002). Thus the planning of a land cover mapping needs careful attention. Based on Cihlar (2000) there are certain considerations that need to be made:

- *Purpose.* Resource management, land planning, policy, and/or science use different levels of information depending on the required content and detail.
- *Thematic content.* It is necessary to define the degree of generalization and thematic clusters in which the surface components can be classified.
- *Scale.* Differing operational scales, from global to regional can not impart the same level of detail. A classification should therefore be hierarchical and scale dependent (Lillesand and Kiefer, 2000).
- *Data.* Data with the appropriate information content should be chosen, dependent on scale, purpose and content.
- *Processing and Analysis.* Techniques to derive the desired information need to be identified. The accuracy level required should be defined.
- *Environmental conditions.* The physical and ecological settings depend on the choice of data, methods and level of detail. For example, tropical environment mapping during the wet season would require atmospheric independent data such as radar, while in an arid environment hyperspectral data would serve best for geologic mapping.

Purpose and thematic content help to define the land cover classes that need to be differentiated i.e. the mapping legend. The scale and the legend point out the spatial and spectral resolution of the remote sensing data. Data from different sensors are widely available, the choice of which is primarily dependant on the purpose. Data and algorithms need to be sufficient for the desired scale and legend in the area of investigation. Over-determined data might introduce even an inner class variability (Atkinson and Curran, 1997; Nagendra, 2002). The terms are not disjunct and might overlap in their meaning. Data availability, not only due to budget constraints, is usually also a part of the decision making process.

Temporal Resolution

Land cover changes over time. Therefore, it is the temporal aspect which is of most interest in data identification - with regard to the purpose. Some information cannot be obtained by the classification of one single scene. The dynamics or changes over time are often the only way to differentiate classes if spectral information is not sufficient. Region A in Figure 3.1 displays satellite data with high temporal and low spatial resolution. Sensors such as NOAA/AVHRR, TERRA/MODIS, SPOT VEG, SeaWifs record daily scenes of the earth surface. This is possible due to a large swath width and thus large area coverage (Richards and Jia, 1999). Data from the sensors in Region B, like LANDSAT, ASTER, IKONOS or Quickbird cover a smaller area with higher spatial but lower temporal resolution. The term medium high resolution data describes usually sensors in the resolution between high and low (spatial) resolution, such as the instrument MISR (Multiangle Imaging SpectroRadiometer).

Optical data in Region B are obtained once every 14-16 days, but because of cloud coverage, scenes are more often available on a monthly time scale. The advantage of higher spatial resolution is due to the smaller sensor's swath angle. However there are some draw-backs: for example, large areas are usually covered by a mosaic of several scenes at different times, potentially including images with vegetation at different phenological stages. Data of Region A cover large areas with one single scene, but the larger the observed area the higher is the probability of cloud contamination. The generation of composites from daily cloud masked images over periods of 5-16 days is achieved by methods such as the maximum (pixel) value composite or spatio-temporal interpolation (Addink and Stein, 1999). Earth observation data from Region D are not available, being primarily the domain of government and military

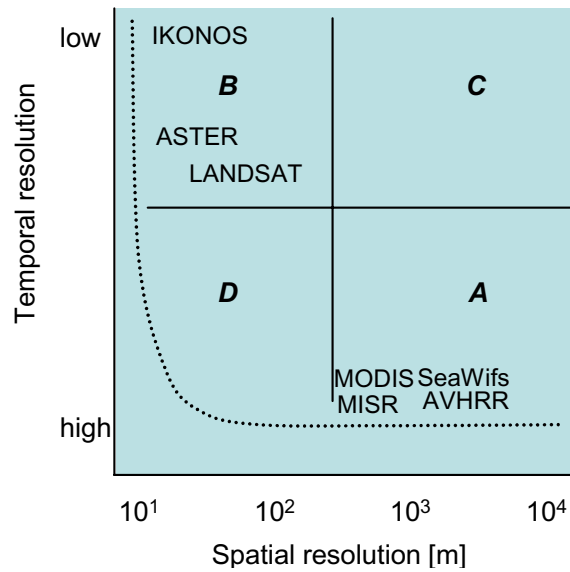


Figure 3.1: Relationship between spatial and temporal resolution of satellite data (Cihlar, 2000)

operations. Small satellites might overcome this scale gap in the near future and give the opportunity of a new land cover mapping age. The commercial company RapidEye promises to do this by monitoring daily multispectral information at $6.5m$ pixel resolution (Scherer and Krischke, 2001).

Spatial Resolution

The amount of information in a remotely sensed scene is to a certain extent determined by the spatial resolution. The spatial resolution should be such that the desired objects can be identified using the least amount of data; if the spatial resolution is too low, objects of interest cannot be identified. If the spatial resolution is too high, inter and intra class variability might increase and decrease the classification accuracy (Atkinson and Curran, 1997; Nagendra, 2002).

Spectral Resolution

Individual images are separately recorded in discrete spectral bands. The position and the width of the spectral bands is determined by the degree to which certain targets can be distinguished in the multispectral image space. Multispectral imagery can lead to a higher degree of discrimination power than a single band (Mather, 1999). The draw-back is that with narrow bands the signal to noise ratio decreases (Smith et al., 1996). Multispectral information can be used for classification, product

derivation (albedo etc.) or for sub-pixel analysis. The latter is discussed in chapter 6.

To incorporate the best available information content, data from Regions A and B (see Figure 3.1) can be used in a synergetic way (Cihlar, 2000) for an improved data analysis. This is possible either by integrating products from Region A with data of Region B or to improve classifications of Region B by incorporating temporal/dynamical aspects recorded by sensors in Region A (e.g. see Graetz, 1987).

For land cover mapping five processing steps are usually applied:

1. data acquisition,
2. pre-processing,
3. analysis and classification,
4. product generation,
5. validation and documentation.

Apart from step 1, these topics are discussed in the following chapters. According to project and scientific requirements NOAA/AVHRR, MODIS, LANDSAT (MSS, TM, ETM+), ASTER, CORONA and IKONOS data were used in various analysis throughout this research.

3.2 Vegetation mapping

The identification of surface vegetation in the remote sensing literature is often described by Vegetation Indices (VI). The most prominent of these is the Normalised Differenced Vegetation Index (NDVI), being sensitive to the photosynthetic active biomass (Jensen, 2000). Thresholding a VI is a simple binary decision to classify the earth surface as either vegetated or non-vegetated. Any further vegetation differentiation requires a more detailed knowledge of the vegetation characteristics. The existence of any type of vegetation in a specific region is determined by the bio-physical environment and the ecological conditions. These conditions can be seen as a sum of different ecological factors like geological subsoil, soil type, irradiation, temperature, precipitation, nutrient supply or salinity, all of which contribute to the allocation of species over the land surface. Each species shows, due to its evolutionary history, a certain reaction to resources and the physical environment, called the

fundamental niche (Hutchinson, 1957) or the species ecological amplitude. If species overlap in their fundamental niches (in their abilities to exist under certain environmental conditions), they will compete with each other and their fundamental niche is reduced to a realised niche (Hutchinson, 1957). This multidimensional niche is what we can detect in the three dimensions of the land surface (see Braun, 1996). Knowledge about the autecology of the vegetation composing species (i.e. the physiological and the ecological optima) is an important contribution to improve satellite derived vegetation or land-cover classifications. Pure spectral differentiation is not always possible and thus combinations with knowledge-based discrimination rules can serve to better optimise results. This knowledge can either be implemented in a post processing step or incorporated directly in the classification scheme (see chapter 6). In reverse, remote sensing by mapping vegetation distribution has the potential to identify habitats in remote areas and contribute to identifying the species' tolerances i.e. *Zygophyllum gaetulum* as a salt tolerant species.

The appearance of the multidimensional realised niche on the earth's surface has for a long time, but most severely during the last decades, been influenced by a particular species; the humans.

Grazing, and potentially overgrazing, with herds of sheep, goats and camels has led to the vegetation appearance of single species, or even vegetation associations, to be altered significantly. Degradation is a potential result of this process, but also accounts for the natural causes of degradation such as drought (see Thomas and Middleton (1994); Nicholson et al. (1998); Katyal and Vleck (2000) for further reading).

The term landscape ecology was introduced by Troll (1939) using mapping approaches of aerial pictures and accounts for the human impact on the landscape. The potential of vegetation mapping contributing to landscape ecology in remote areas was outlined by Naveh and Liebermann (1984) and Leser (1991). The discipline of qualitative landscape ecology formed during the 1980's and 1990's. North American ecologists Forman and Godron (1986) defined landscape ecology as: "exploring how a heterogeneous combination of ecosystems - such as woods, meadows, marshes, corridors and villages - is structured, functions and changes. From wilderness to urban landscape, our focus is on a) the distribution patterns of landscape elements or ecosystems b) the flows of animals, plants, energy, mineral nutrients, and water among these elements and c) the ecological changes in the landscape mosaic over time".

Within this framework the mapping of vegetation and their spatial distribution, especially in combination with change detection, can be interpreted as applied landscape ecology.

3.3 Classification schemes and implications for this study

”If a reputable classification system already exists, it is foolish to develop an entirely new system that will probably only be used by ourselves.”

J. R. Jensen, 1996

Classification schemes

Every land cover classification is performed according to a classification scheme. For the purpose of comparability and data homogeneity attempts were made to initiate a common classification system that the remote sensing community could use. These schemes were designed usually with differing thematic or spatial (resolution) focus. Hierarchical classification schemes have the advantage of a homogeneous structure and different levels of class detail. The level of detail can then be adapted to the desired scale of the mapping product. US Geological Survey (USGS) together with the European Joint Research Center, in the framework of the IGBP, established a global land cover classification scheme and a global land cover map compiled from 1992-1993 Advanced Very High Resolution Radiometer (AVHRR) data in $1.1km$ pixel size (Belward et al., 1999; Scepan, 1999). On a quarterly basis the MODIS Land Cover Product supplies a land cover classification with 17 classes based on the IGBP system, globally, in $1km$ resolution (Strahler et al., 1999). Global land cover data are important for purposes such as, global change research. For some purposes land cover data in finer resolution are necessary, as within several sub-projects of the IMPETUS project of which this study is a part. Applications are eg regionalised climate models which require more detailed input data.

The hierarchical USGS land use/land cover classification system (Anderson et al., 1976) for mapping with high resolution data was developed for the United States with scale dependent levels of classes. Level one and two are pre-defined, levels three and four can be user defined according to the hierarchical structure and require higher resolution information, like aerial photography (Lillesand and Kiefer,

2000; Jensen, 1996a). The Coordinated Information on the Environment (CORINE) land cover classification scheme from the European Environment Agency is also an example of a hierarchical classifier, designed for European countries by using LANDSAT TM/ETM+ data focusing on agricultural and forested areas. The first level differentiates five general cover types: 1. artificial surfaces, 2. agricultural areas 3. forest and semi-natural areas, 4. wetlands and 5. water bodies. The second, more detailed level with 15 classes is designed for scales between 1:500000 and 1:1000000. The third level incorporates 44 levels and is designed for mapping scales of 1:100000. Although the structure of the CORINE classification scheme was designed for European countries, most coastal parts of Morocco and Tunisia are mapped using this classification scheme.

The land cover classification system of the Food and Agricultural Organisation (FAO) of the United Nations, as part of the IGBP land use and cover change (LUCC) imitative AFRICOVER, developed a highly flexible scheme of several environmental layers including soil, lithology, climate, plant physiology etc., with the overall aim of establishing an environmental database. This scheme seems to be a prosperous initiative, despite that "The land cover is mainly derived from visual interpretation of recent high resolution satellite images digitally enhanced". (Africover, 2003).

Discussions concerning the Dra catchment

The heterogeneous vegetation patches of the often sparsely vegetated rangelands require, for an adequate mapping, high or very high resolution images. Requirements of the related meteorological models and botanic arguments led to a similar decision, that precise mapping with multispectral high resolution data would be necessary. The only reasonable option at the beginning of the project was to use LANDSAT ETM+ due to the higher spectral resolution in comparison to SPOT images (ASTER data was, at this stage, not available). A great advantage is the good calibration, geometrical accuracy and availability of the MSS, TM and ETM+ satellite data, over three decades. Parts of Morocco are already mapped with LANDSAT data based on the CORINE land cover scheme, including the coastal areas, also also the nearby Sous valley which has comparable environmental conditions to those in parts of the Dra catchment. These circumstances led to the decision to adopt the nationally recognised CORINE classification scheme with modifications (Jensen, 1996a). As already stated, the CORINE land cover classification scheme was designed for European surfaces. Thus certain modifications were necessary to adopt this scheme

to the arid environment of the Dra valley of South Morocco. Three new units were introduced on the third level: steppe vegetation, savanna vegetation and riparian vegetation. The level two class, shrub and/or herbaceous vegetation, was extended by the first two, while riparian vegetation was introduced as supplement of the level two class, inland wetlands. Thus the originally 44 CORINE level three classes were expanded to 47. This was found to be useful as the arid character of the existing classes was not found to be sufficient, as revealed by field observation. Following the concept of the USGS system, a major change was the introduction of a fourth level to further differentiate land cover. This would imply either the use of higher resolution data (e.g. 10m) or the use of more dedicated classification methods. In order to produce a land cover map with the highest possible detail, and due to sub-pixel object size (Figure 3.2), sub-pixel analysis methods were applied to increase the spatial interpretation possibilities of the LANDSAT TM/ETM+ data.

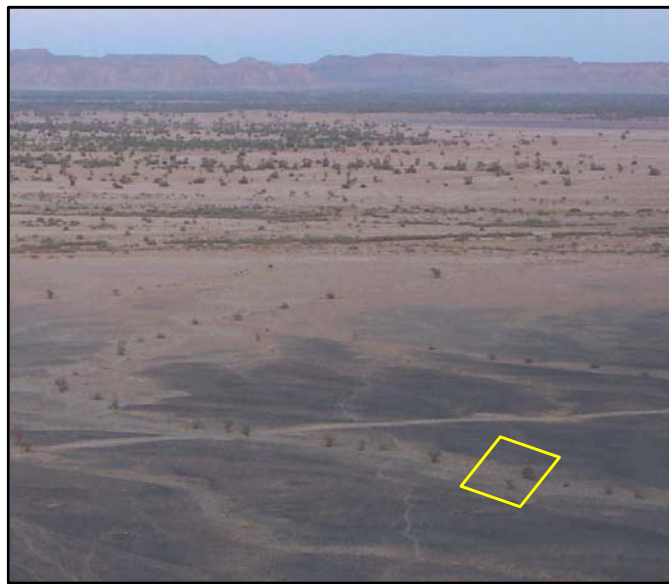


Figure 3.2: Estimated size of a LANDSAT pixel in an oblique terrestrial photo. Trees of *Acacia raddiana* in the valley of pediment fields (Photo: M. Schmidt, 2000), coordinates of the rectangle center (in UTM): 829045/3314167

It should be recognised that with this step not only were the number of possible classes enlarged to 64 (see Table 3.1), and so the probability of misclassification increased, but also that sub-pixel analysis additionally incorporates a source of uncertainty itself. Figure 3.3 depicts this relationship schematically.

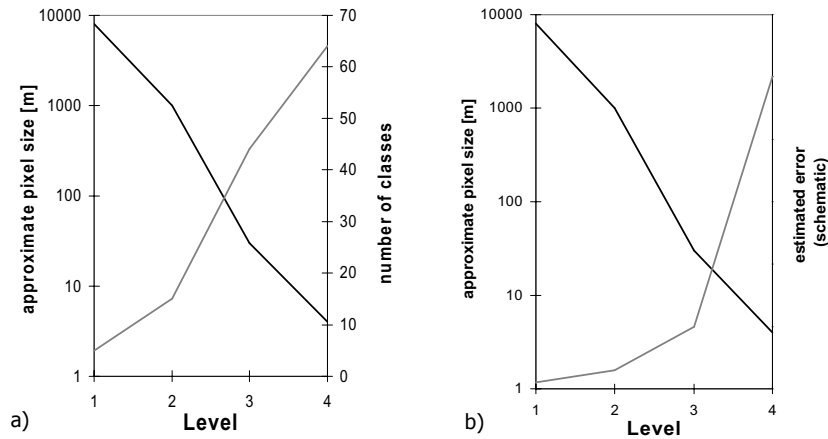


Figure 3.3: Schematic relation of pixel size, numbers of classes and estimated accuracy dependent on the classification level

Figure 3.3 a) indicates the increasing number of classes with increasing level of classification detail in relation to the necessary pixel size. Figure 3.3 b) shows a similar relationship but with a schematic representation of the expected error increase by increasing classification level with respect to the sub-pixel analysis of LANDSAT TM/ETM+ data.

The extension of the existing CORINE land cover classification scheme up to the fourth level was performed in close collaboration within the IMPETUS sub-project B3. Profound knowledge of the terrain allowed this approach by incorporating supplement information of plant properties. The level four classes can be merged to the higher levels due to the hierarchic structure of the classification scheme (see Table 3.1). Modifications on level three can also be merged with the existing classes of level three in order to contribute to land-cover mappings on the basis of CORINE in Morocco. The complete classification scheme is shown in Table 3.1. The vegetation classes within this land cover/land use classification scheme usually represent plant associations. These are detailed in Appendix A.

Table 3.1: Land use/land cover classification scheme used within this study, based on CORINE land cover (next page)

3 Low, Medium, High or Very High Resolution for land cover mapping?

Level 1	Level 2	Level 3	Level 4	
1000 - ARTIFICIAL SURFACES	1100 - urban fabric	1110 - continuous urban fabric 1120 - discontinuous urban fabric		
	1200 - industrial, commercial and transport	1210 - industrial or commercial units 1220 - road and rail networks and associations 1230 - port areas 1240 - airport areas		
	1300 - mine, dump and construction sites	1310 - mineral extraction sites 1320 - dump sites 1330 - construction sites		
	1400 - artificial non-agricultural vegetation	1410 - green urban areas 1420 - sport and leisure facilities		
	2100 - arable land	2110 - non-irrigated arable land 2120 - permanently irrigated land 2130 - rice fields 2210 - vineyards 2220 - fruit trees and berry plantations 2230 - olive groves	2111 - rain fed agriculture 2121 - irrigated farmland	
	2200 - permanent crops	2310 - annual crops associated with permanent 2320 - complex cultivation patterns 2330 - land principally occupied by agriculture 2340 - agro-forestry areas	2341 - palm oasis 2342 - mountainous oasis	
	2300 - heterogeneous agricultural areas			
	2400 - pastures			
	3100 - forest	3110 - broad-leaved forest 3120 - coniferous forest 3130 - mixed forest 3210 - natural grassland 3220 - moors and heathland 3230 - sclerophyllous vegetation 3240 - transitional woodland shrub	3221 - oromediterranean vegetation 3241 - Juniperus thurifera - Buxus shrubland 3242 - Juniperus phoeniceae shrubland 3243 - Buxus balearica	
	2000 - ARABLE LAND			
	3000 - FOREST AND SEMI- NATURAL AREAS			

3.3 Classification schemes and implications for this study

3000 - FOREST AND SEMI-NATURAL AREAS	3200 - shrub and/or herbaceous vegetation	3250 - steppe vegetation	3251 - Hammada scoparia - Artemisia steppe 3252 - tussock-grass steppe 3253 - rocksteppe vegetation 3254 - dwarf bush steppe 3255 - Pulicaria steppe 3256 - Anvillea - Convolvulus steppe 3257 - Hammada scoparia steppe	
		3260 - savanna vegetation	3261 - Acacia raddiana - Ziziphus - Mearua 3262 - Acacia raddiana - Retama 3263 - Acacia raddiana - Panicum - Zilla 3264 - Tamarix aphylla	
	3300 - open spaces with little or no vegetation	3310 - beaches, dunes and sand plains	3311 - sand 3312 - desert crust	
		3320 - bare surfaces	3321 - gravel/pediment 3322 - rock 3323 - playa	
		3330 - sparsely vegetated areas	3331 - sanddune vegetation 3332 - Zygochloa gaetulum	
		3340 - burnt areas		
		3350 - glaciers and perpetual snow		
		4110 - inland marshes		
	4000 - WETLANDS	4100 - inland wetlands	4120 - peat bogs	4131 - Atriplex glauca 4132 - Tamarix africana - Oleander 4133 - riparian shrublands
			4130 - riparian vegetation	
		4200 - coastal wetlands	4210 - salt marshes	
			4220 - salines	
		5000 - WATER BODIES	5100 - inland waters	4230 - intertidal flats
	5110 - water courses			
5120 - lakes				
5200 - marine waters	5210 - coastal lagoons			
	5220 - estuaries			
	5230 - sea and ocean			

3.4 Conclusions and discussion

Large catchment-wide mapping was performed in the late 1960s and early 1970s resulting in the presently used topographic maps in the study area. Recent studies involving satellite data are either locally used or never integrated into a common GIS database system. For the vegetation mapping approach LANDSAT ETM+ data were found to be suitable with respect to spatial and spectral resolution. The level of detail to be mapped was identified in accordance with project requirements and ecological characteristics. It seemed appropriate to adopt and refine the existing CORINE land cover classification scheme as large parts of Morocco have already been mapped with this scheme. This way the whole catchment can be mapped according to one classification scheme, even if, due to surface heterogeneity, sub units needed to be classified separately. Nevertheless, related to the enlarged number of classes, the probability for mis-classifications potentially rises.

The integration of the classification products/results with different methodological origin and local modifications and accuracy is a difficult task and is a question of database homogeneity and management. The additional classes can be merged and incorporated in the standard CORINE system.

New environmental satellite data, such as ASTER or SPOT 5, which have increased resolution (spatial and/or spectral), also increase the expected classification detail and accuracy. Consequently a fourth classification level of the CORINE land cover scheme might well become standard in the near future, especially if classifications of very high resolution data, such as IKONOS or QUICKBIRD were to be incorporated. Otherwise these mappings would be performed with different, more flexible and/or more detailed classification schemes.

4 Remote sensing in 2, 3 and 4 dimensions

”A mind that is stretched by a new experience can never go back to its old dimensions.”

O. W. Holmes, 1841-1935

Satellite images appear as two dimensional maps with pixels organised in regular grided 2D data array. Across track scanners provide this data recorded by a rotating mirror or a linear detector array in an across track direction of the swath (Richards and Jia, 1999). The size of a pixel is determined by the focal length, the flight height and the view angle, and the Instantaneous Field Of View (IFOV) of the recording system (Mikhail et al., 2001). The projection of a pixel to the earth surface, referred to as the Ground Sampling Distance (GSD), is influenced by the local relief. Thus, only in rare occasions truly a 2D image information obtained if e.g. a LANDSAT satellite would fly along the center of an ideal shaped valley with the valley walls curved in the same angle as the recording mirror of the sensor moves. In all other instances, elevation effects and thus the third dimension, is image inherent by incorporating larger GSD off NADIR (Richards and Jia, 1999) or relief displacements of the pixels (Mikhail et al., 2001; Schmidt et al., 2003a). Image displacements, d , are a function of the view angle α , object height Δh , and, in the case of mountains, dependent on slope and aspect (Mikhail et al., 2001). Figure 4.1 shows this principle. Point P of an object with height h above the reference plane, is recorded in the image plane at position p . Distances can be expressed from similar triangles (Goossens, 2002):

$$\frac{pp'}{pw} = \frac{d}{OP''} = \frac{h}{H}$$

or

$$h = H \frac{pp'}{OP''}$$

If the points p and p' are clearly to be identified in the image plane and the flight height above the same datum as the object is known, then the object height can be calculated.

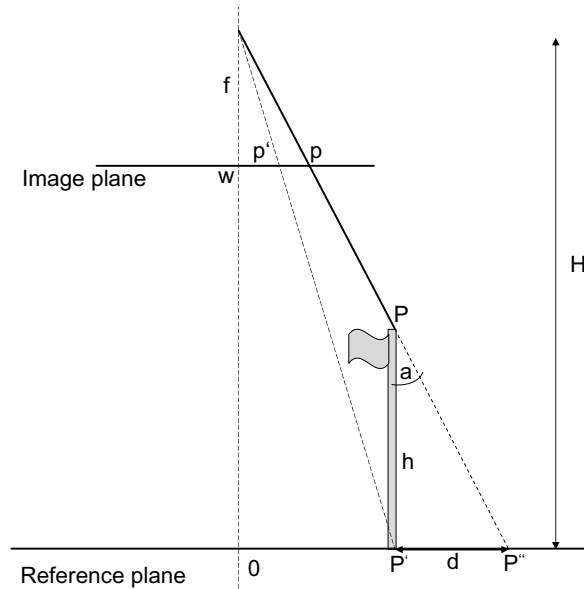


Figure 4.1: Relief displacements (Goossens, 2002, modified)

The interrelation between the object height and view angle α and image displacements is expressed as:

$$d = \Delta h * \tan(\alpha)$$

In rugged terrains, such as the High Atlas Mountains with $\Delta h = 1500m$ the displacements even for satellites with narrow swath e.g. LANDSAT with $\alpha = 7.7^\circ$ at the image edges, can contribute to displacements of more than $200m$ (equating to 6-7 pixels). The problems of image displacements are ubiquitous for satellite data as for aerial pictures recorded in conic projection. These basic photogrammetric principles became with the advent of the very high resolution data, such as IKONOS-2 or Quickbird-2 particularly important to the remote sensing community (Konecny, 2001; Andresen et al., 2001; Kim and Muller, 2001; Lohmann, 2001). The very high resolution sensors were built to record images oblique with certain view angles (Figure 4.1). The displacement increases non-linearly with increasing view angle due to the hyperbolic behavior of the Tangents function (Schmidt et al., 2003a).

Image displacements of an monoscopic IKONOS-2 scene are in a case study in South Morocco with $\Delta h = 300m$ and $\alpha = 27.9^\circ$ at $d = 158m$, which is in the case of

IKONOS-2 panchromatic 158 pixels. The dilemma of this situation is that not only maps on the necessary scale are missing, but also that the data can not be rectified to real world coordinates simply by recording GCPs in the field. In working monoscopically the operator only has the chance to indicate the correct GCP coordinate to the displaced point in the image. So that the Root Mean Square (RMS) error is in fact an estimator of the mean image displacement at these points within the image, plus the registration error in finding the corresponding pixel position (Schmidt et al., 2003a). A solution is, as applied in most studies, to work with ortho-rectified products like topographic maps or true ortho-photos section 4.4. Within this cartographic document the 3D information is provided by the use of a Digital Elevation Model (DEM) and is employed to correct the distortions resulting from the view geometry. Jensen (1996b) stated that the "geometric accuracy (x,y) of a photogrammetrically terrain corrected orthoimage is superior to the normal remote sensing image rectification". Often orthorectified base material is not at an adequate scale, or more generally, is just not available. In cases where such data does exist, it is often high in errors - especially in the case of areas close to political borders e.g. in developing countries or where borders are (still) under discussion as in Morocco/Algeria. The demand for adequate and correct map products with displacement free x and y coordinates is not only from the geometric and cartographic aspects of remote sensing height. Mapping with remote sensing data is cost and time efficient (Konecny, 1999) and, due to stereo coverage of sensors as CORONA, SPOT or ASTER, possible.

This, and the following discussion and the basic trigonometric context (explained below), immediately demonstrates the potential for what was recently called *photogrammetric remote sensing* or *3D remote sensing* (Goossens et al., 2002a, Goossens, pers. comm.) and the necessity to be able to apply methods and knowledge of photogrammetry to stereo data of satellite images. These methods were basically developed for use with aerial photography when remote sensing and photogrammetry were one discipline (Goossens et al., 2002a).

4.1 Photogrammetric background

Projective geometry was introduced by renaissance artists as Filippo Brunelleschi (1377-1446) and later by Leonardo da Vinci in his image the 'last supper' and Albrecht Dürer. Photogrammetric methods are based on the principles of projective

geometry (McGlone, 1996). A traditional definition of photogrammetry is "the process of deriving (usually) metric information about an object through measurements made on photographs of the object" (Mikhail et al., 2001). This includes the stereo viewing of image pairs and the derivation of an ortho-projection out of two conic projections (Goossens, 2002). Sensing techniques provided images in multispectral ranges with a broader pixel resolution in the early 1970s. Photogrammetrists followed the framework of projective geometry and worked with aerial photographs, while operation with satellite images and their interpretation is called remote sensing. The evolution of photogrammetry can basically be divided in three successive stages; the analog stage, the analytical stage and the digital stage (Zhang et al., 1996). The analog stage, started about 1900, was determined by the utilisation of the optical-mechanical instrument: the stereo-plotter. Aerial pictures were oriented to a perspective center according to the flight line and the rotation angles κ , ϕ and ω of the recording system. The stereo-view allowed the operator to draw contour lines and to generate analog topographic maps. The analytical stage, which arose in the 1970s (Goossens, 2002), allowed manual drawings and elevation information be stored directly in a computer, although the analysis was still dependent on the operator and his/her interpretation. The advent of the digital stage in the late 1990s changed the possibilities tremendously. Automatic photogrammetric analysis is now also possible with scanned and digital recorded non-metric images. The major advantage is that labour, time, and thus, cost intensive analysis can be performed automatically, and to a greater extent, independent from human interpretation (Zhang et al., 1996; Mikhail et al., 2001).

Modern photogrammetry deals with several types of digital images, including both classical metric images and non-metric images (Mikhail et al., 2001). The major progress was the reliable processing of automatic image matching and orientation procedures (Zhang et al., 1996; Heipke, 1997; Wang, 1998). With the launch of the IKONOS-2 satellite in 1999 and the availability of $1m$ pixel resolution (potentially stereoscopic) the scale gap between remote sensing and photogrammetry was bridged: scientists from formerly disparate disciplines worked again with the same actual data on similar topics. The release of the CORONA data in 1995 is another important step towards the intersection of these disciplines and will surely lead to the incorporation of methods from both to maximise the usage of the inherent information.

Parallax and stereo view

Applications in classical photogrammetry incorporate the use of stereo-image pairs and the principle of parallax. Parallax refers to the relative position change of a stationary object due to the position shift of the observer (Lillesand and Kiefer, 2000; Mikhail et al., 2001). Figure 4.2 shows this graphically. Images as taken from the points o and o' display the points A and B different in the image space as a and b . The parallax p_a of point A is the sum of the measured x coordinate x_a of the left image of the stereo-pair and the measured x coordinate x'_a of the right image. Which can due to the negative sign of x'_a be expressed as:

$$p_a = x_a - x'_a$$

The parallax difference on vertically overlapping photographs is shown in Figure 4.2.

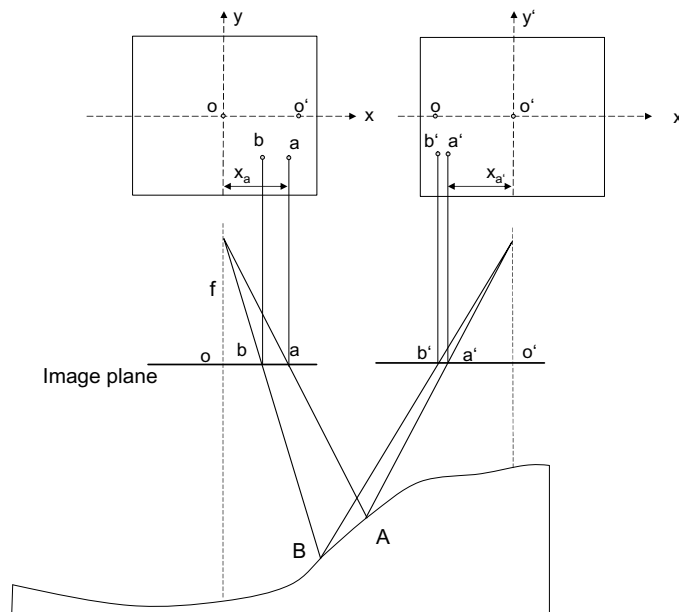


Figure 4.2: Parallax displacements on overlapping vertical photographs (Lillesand and Kiefer, 2000, modified)

The principle of parallax and floating points (Mikhail et al., 2001) allows the calculation of object heights within stereo models with known focal length of the observing camera system. Ideally, and as shown in Figure 4.2, with a flight line along the x and x' axis, the distance between o and o' is called the photogrammetrical

base. A non stable platform is additionally moving in three possible directions as described usually with the angles κ , ϕ and ω (Mikhail et al., 2001). So that in reality the base also has a y component, with a y parallax resulting from y movement of the platform plus the recoding distortions due to κ , ϕ and ω . The base to height ratio, as the distance between the obtained images and their recording height above the ground determines the amount of parallax and consequently the precision of the object height that can be obtained. Relative model orientation incorporates estimation of the parameters κ , ϕ and ω (McGlone, 1996). Conjugate image points allow the image orientation along so called epipolar lines and the elimination of the image y parallax (Mikhail et al., 2001). These orientations were classically performed with a stereo-plotter. With the absolute model orientation an operator could measure distances and heights and analog topographic maps can be produced. This was a manual and labor intensive process. With these concepts, using stereoscopic data, relief or object displacements can be resolved.

Digital photogrammetry

The concepts of analog and analytical techniques were transferred to digital photogrammetric software systems, which was a major step in automation of the information extraction of stereo data (Baltsavias, 1996; Mikhail et al., 2001). Fundamental to the digital stereo-image analysis is the image matching process (Schenk, 1996; Wang, 1998; Mikhail et al., 2001) within which conjugate points are found in the corresponding image. Matching algorithms can generally be categorised into (Schenk, 1996):

- *area based matching* works on matching of grey level distributions by image correlation on small windows (Schenk, 1996)
- *feature based matching* matches image derived primitives, e.g. grey level contour lines (Li et al., 1997)
- *structural matching* or relational matching establishes a correspondence between image primitives and their interrelationships (Wang, 1998)

Combinations of these algorithms are mostly applied, with respect to pyramid layers (Heipke, 1996; Baltsavias, 1996). Due to image matching algorithms the process of relative orientation runs fully automatically and parameter free, even with non-metric recorded images (Wang, 1998; Zhang et al., 1996). This relative orientation

of the stereo images and the relative DEM of the so called image space can be transferred into the object space of real coordinates (Figure 4.3). To solve the transformation problem three GCPs in x,y,z and two planimetric GCPs are necessary (Jacobsen, 2001).

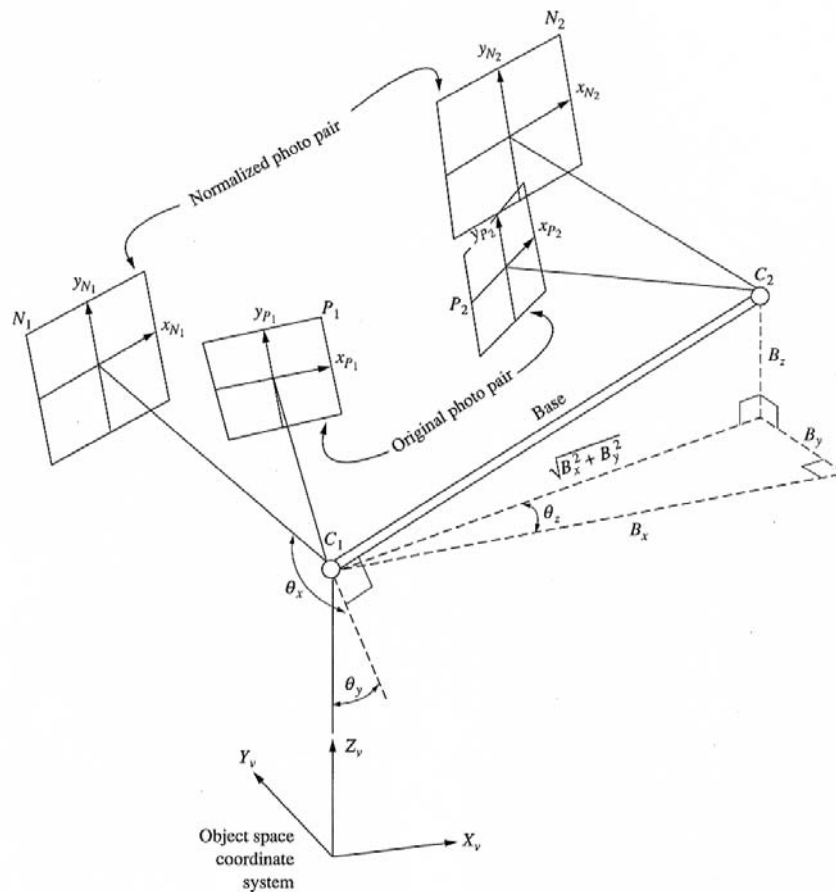


Figure 4.3: Image orientation process (Mikhail et al., 2001)

4.2 3D Remote Sensing

Remotely sensed images usually have no fiducial marks, unlike aerial photographs, as most sensors record images pixel-wise line after line. These images are recorded in the so called non-metric way (Mikhail et al., 2001). Camera parameters of satellite observing systems are often not available or remain secret as in the case of CORONA (by the United States Central Intelligence Agency (Ruffner, 1995)) or in the case

of IKONOS and SPOT by their companies SpaceImaging (SI) and EURIMAGE respectively. Recent developments allow image matching and relative orientation of non-metric recorded images without an internal orientation (Zhang et al., 1996). With this achievement the camera information is no longer necessary for the generation of 3D corrected products and satellite data serve as an effective data-source for DEM generation.

4.2.1 Data

For orthographic mapping and DEM generation stereo-image pairs of CORONA KH4B recordings (mission DS-1117) dating from 26 May 1972 were used in test and evaluation areas. First approaches were conducted at an area near the town of Zagora while the evaluation took place near the town of Toundoute. ASTER data were also evaluated first in the area of K'tauer and applied then to three adjoining ASTER scenes of April 12, 19 and July 6, 2001 of the basin of Ouarzazate (Figure 4.4).

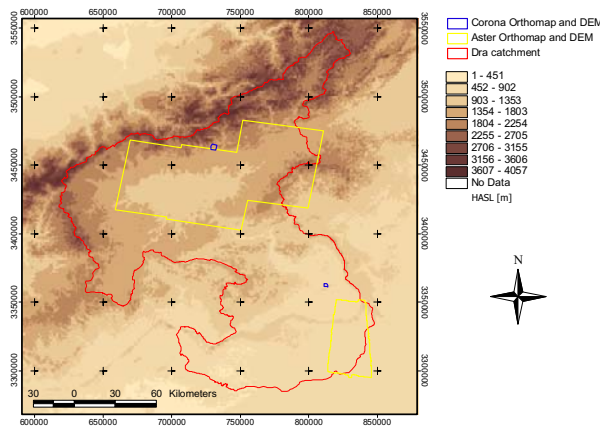


Figure 4.4: Coverage of CORONA and ASTER derived photogrammetric products

Both satellites observe overlapping images due to two recording systems on-board. While CORONA has two panchromatic cameras forward and a backwards viewing each 15° off NADIR (Campbell, 1996), ASTER records 14 spectral bands at NADIR and additionally has a backwards viewing camera in the VNIR with a view angle of 27.9° (NASA, 2002a). The geometry of the image recording systems are shown in Figure 4.5.

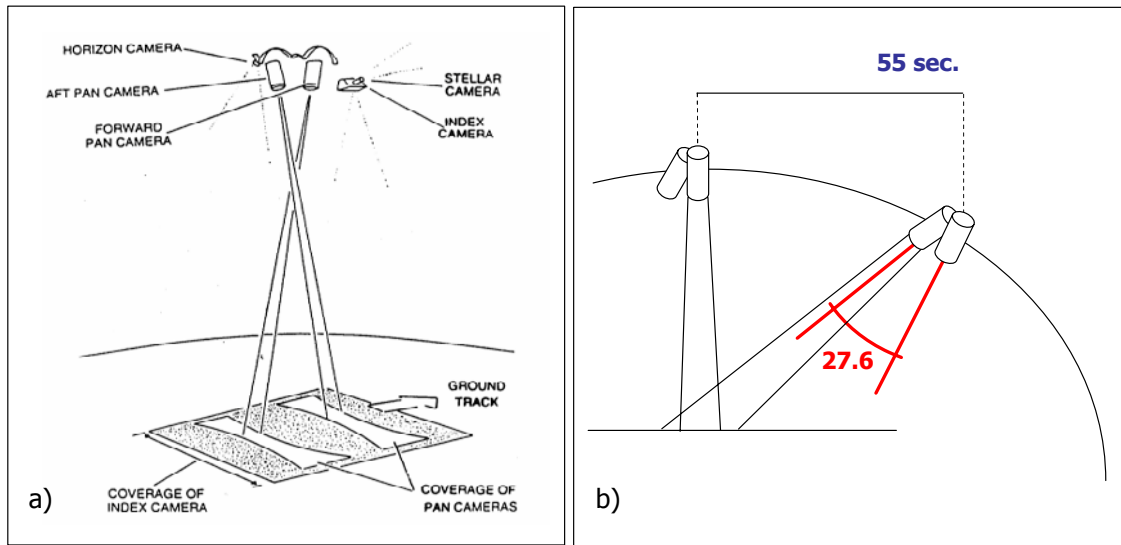


Figure 4.5: Sensor geometry of a) CORONA (Campbell, 1996) and b) ASTER satellite

The characteristics of the data are displayed in Table 4.1 and are discussed in further detail, e.g. by Ruffner (1995); MacDonald (1995); Campbell (1996); Goossens et al. (2003).

Table 4.1: Characteristics of CORONA and ASTER stereo images.

	CORONA	ASTER
Ground resolution	$\approx 1.8m$ (in the center)	15m
Operation time	1960-1972	since 1999
Spectral properties	panchromatic	VNIR (760-860 nm)
Camera type	Panorama (KH4B)	CCD
Spatial coverage	$\approx 14km \times 188km$	$60km \times 60km$
Storage	Film (black and white)	Digital

The CORONA images were scanned with a Z/I (Zeiss/Integrph) imaging Photo-Scan scanner with absolute position accuracy of 2μ at resolution of 7μ , at the Institute of Photogrammetry, University of Bonn, Germany, for further digital analysis. The position accuracy and thus distortion reduction compared to a desktop scanner is about a factor of 100 higher (K.H. Ellenbeck, University of Bonn, 2003, pers.

comm). First tests were performed by photographic enlargement of the CORONA strips on photo-paper and scanning afterwards which resulted in less accurate products (Schmidt et al., 2001b,a).

4.2.2 Methods

The photogrammetric software package VirtuoZo requires aerial pictures to be oriented along the flight line L_p , which is in this case defined as an E-W direction. CORONA and ASTER are mounted on satellites with a N-S flight direction, L_s . Thus it is necessary to rotate the images 90° anti-clockwise (Figure 4.6a). This is important because the component along the flight line contains the parallax and thus the height information. The the left image in the stereo model must be the forward image of CORONA and the nadir image of ASTER (n) (Figure 4.6b) while the backwards image (b) must be the right image.

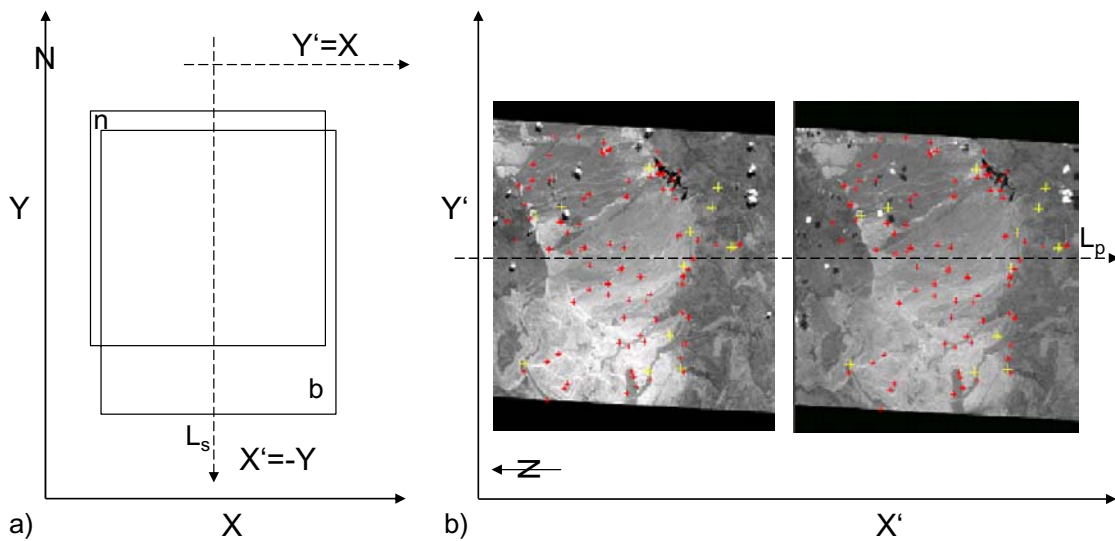


Figure 4.6: ASTER image pre-orientation along the E/W flight-line

The image rotation implies a rotation of the object coordinate system. All analysis is then performed in the new coordinate system spanned by X' and Y' . The re-transformation to real world coordinates can be performed in a GIS system during post-processing. Figure 4.7 outlines the processing steps which are necessary to produce an orthoimage and DEM using VirtuoZo (Version 3.2).

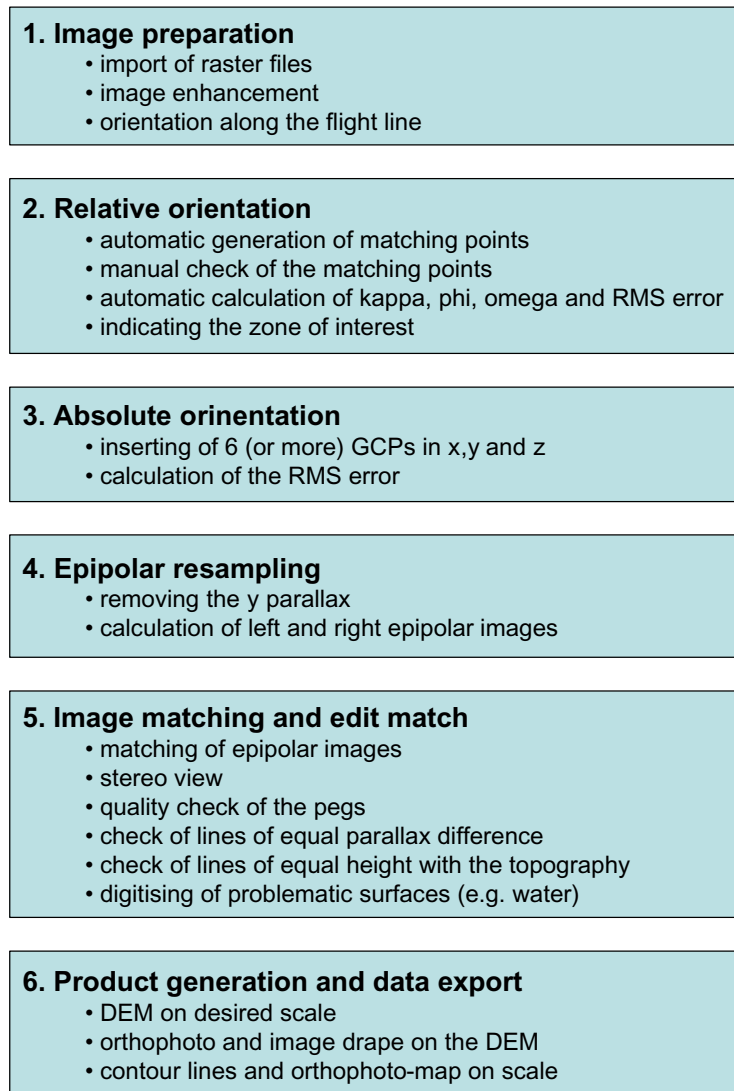


Figure 4.7: Processing steps within Virtuoso

VirtuoZo applies a combination of image matching based on area correlation within moving windows of 9×9 pixel size (Baltsavias et al., 1996), and feature based matching using probability relaxation and neuronal network techniques (see Zhang et al., 1996, for further discussion) for the automatic generation of matching points (red points in Figure 4.6b) in pyramid layers. A minimum of 6 GPS in x,y and z coordinate are required by Virtuoso for the absolute orientation (yellow points in Figure 4.6b). The accuracy in x,y and z of the GCPs is crucial for the resulting DEM accuracy. Therefore the GCPs need to be recorded in the field at

sub-pixel level. For the CORONA restitution a Leica 300 differential Global Positioning System (GPS) with an accuracy of less than half a meter was used. In the case of the ASTER data, a TRIMBLE Pathfinder PRO XRS differential GPS with an accuracy of less than one meter provided a sufficient retrieval accuracy (see section 2.2). These points should be evenly distributed over the image overlapping area in the three dimensions (Baltsavias et al., 1996; Mikhail et al., 2001). Epipolar resampling creates left and right epipolar images and contributes by the use of the matching points and the inserted GCPs to the calculation of epipolar planes and the removal of the image y parallax. VirtuoZo offers the ability to check matching quality of the epipolar images by the gridded 'pegs' in which coefficients from the matching algorithm are displayed (Zhang et al., 1996). For every peg is the parallax calculated and lines of equal parallax difference are interpolated. Problematic areas, such as water bodies, can be edited by polygon digitising and assigning a constant elevation value. Figure 4.8 shows the calculated lines of equal parallax difference of an ASTER scene and the digitised lake near Ouarzazate.

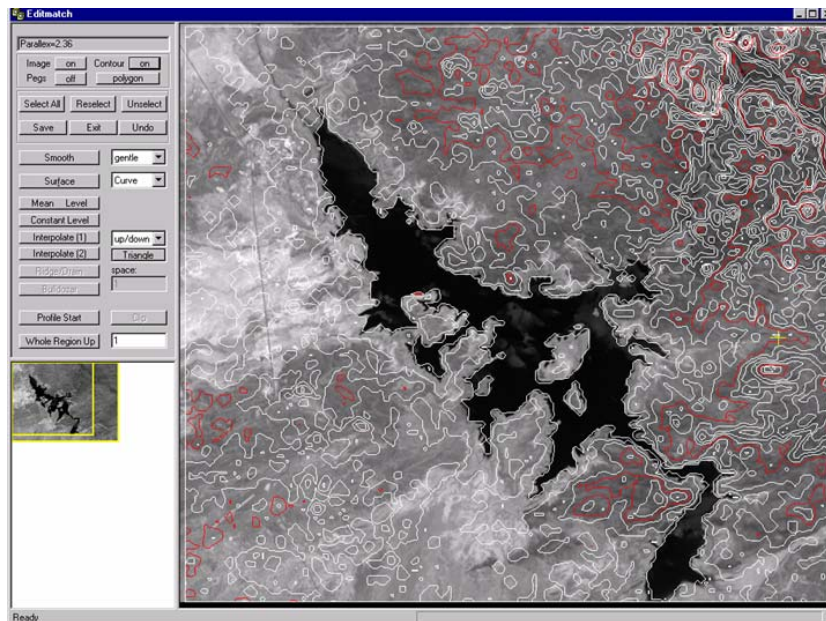


Figure 4.8: Lines of equal parallax difference in an ASTER scene near Ouarzazate.

The collinearity equations (Mikhail et al., 2001, see e.g.) transform lines of equal parallax difference to contour lines of the surface elevation. The fitting of the contour lines with the relief should finally be controlled with polarisation glasses in a 3D view

(Zhang et al., 1996).

4.2.3 Results

DEM

DEMs were generated with CORONA images (Figure 4.9) and with ASTER data and represent the terrain surface. In the areas of the river oasis with dense and high vegetation, an elevation greater than the true relief is to be expected.

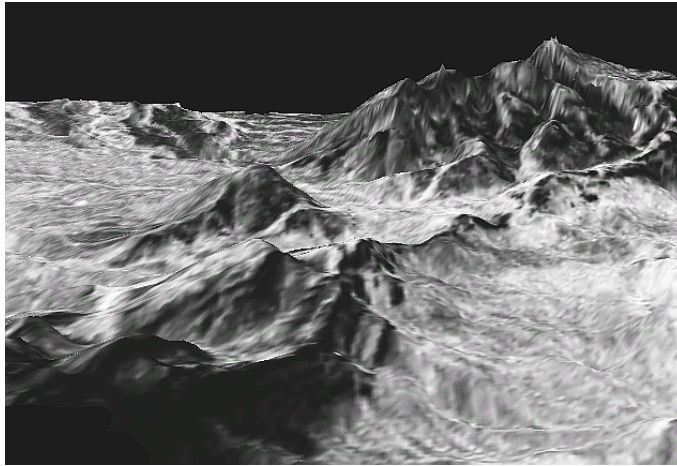


Figure 4.9: Image drape of CORONA data, near the town of Zagora

The first tests of the CORONA restitution were performed in a $5km \times 5km$ area near Zagora Figure 4.4. The RMS errors from the relative and absolute orientation are shown in Table 4.2. The DEM accuracy was evaluated with 49 field measured GPS points which resulted in a mean vertical accuracy $\Delta z = 9.54m$ and with a standard-deviation $\sigma = 13.74m$. The sandy test area (Figure 4.9) not only resulted in a rather poor image matching due to lack of image contrast, but also there were few infrastructure lines existing for reliable GCP recording. The best mean vertical accuracy of a CORONA derived DEM was obtained in a subset of roughly $10km \times 10km$ near Toundoute (Table 4.2), with $\Delta z = 3.6m$ and $\sigma = 13.2m$ according to 146 GCPs.

Table 4.2: Errors in the photogrammetric restitution - CORONA

Area	Zagora	Toundoute
Relative orientation		
Number of points	58	98
RMS error (<i>m</i>)	0.0189	0.008
Absolute orientation		
RMS x (<i>m</i>)	9.83	8.87
RMS y (<i>m</i>)	9.17	2.18
RMS xy (<i>m</i>)	13.45	9.14
RMS z (<i>m</i>)	3.38	0.70
Number of GCPs	8	7

This high standard deviation can potentially be reduced with more identifiable and better documented GCPs. The possibility of using ASTER data for DEM and orthoimage generation was tested in the area of K'tauer with an area of $30km \times 60km$ and verified in the basin of Ouarzazate Figure 4.4, where three full ASTER scenes were processed independently by the use of 29 GCPs and merged afterwards (Figure 4.10).

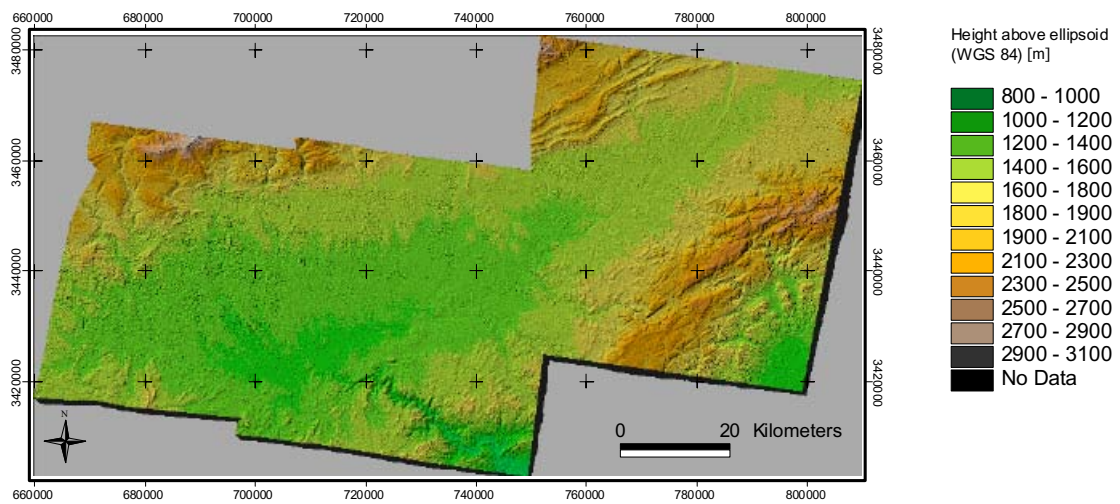


Figure 4.10: Mosaiced DEM of three processed ASTER scenes from the basin of Ouarzazate on scale 1:10000

The relative error estimation of the restitutions are shown in Table 4.3. For

K'tauer, were 15 check points were available with $\Delta z = 3.6m$ and $\sigma = 7.8m$. The mean height difference of the ASTER DEM in the basin of Ouarzazate to 1439 validation points was $\Delta z = 1.6m$ with $\sigma = 11.9m$, while the DGPS points were obtained in a small hilly region and were interpolated to a $5m$ grid.

Table 4.3: Errors in the photogrammetric restitution - ASTER

Data	K'tauer	East	West	Middle
Relative orientation				
Number of points	89	158	231	246
RMS error	0.0079	0.0064	0.0049	0.0049
Absolute orientation				
RMS x (<i>m</i>)	17.81	12.77	13.54	9.32
RMS y (<i>m</i>)	22.02.18	18.38	16.81	11.21
RMS xy (<i>m</i>)	28.33	22.38	21.59	14.58
RMS z (<i>m</i>)	4.76	5.44	10.40	5.87
Number of GCPs	7	12	10	11

Ortho-image

Orthoimages, as displacement free and cartographic correct products, could be generated at a scale of 1:10000 (keeping in the case of ASTER, the original resolution of $15m$). The orthoimages from CORONA, as well as of the ASTER data, could be superimposed with contour lines of desired interval generated from the DEMs and thus be utilised as topographic-orthophoto maps. These maps offer more detailed information than the best available topographic maps at scale of 1:100000 and on smaller scale. The only drawback is that the user of these documents must be able to interpret the black and white ortho-images, or in the case of ASTER, even a VNIR image.

4.2.4 Post-processing

To make use of the generated data the products need to be exported and re-transformed to a real world coordinate system Figure 4.6. The products were further processed with other software packages; ERDAS imagine was used to mosaic

the individual ASTER ortho-photomaps. The ortho-image mosaic was the basis for digitising clouds and their shadows. The DEM was imported to ArcView and manually cloud masked. The three 'cleaned' DEMs were merged and converted to one grid file, removing some corner effects in the DEMs. These products are available for validation and further analysis. The ortho-images were compared with scanned and geo-referenced topographic maps at scale of 1:100000. Visual inspection indicated very good matching with topographic maps (Figure 4.11).

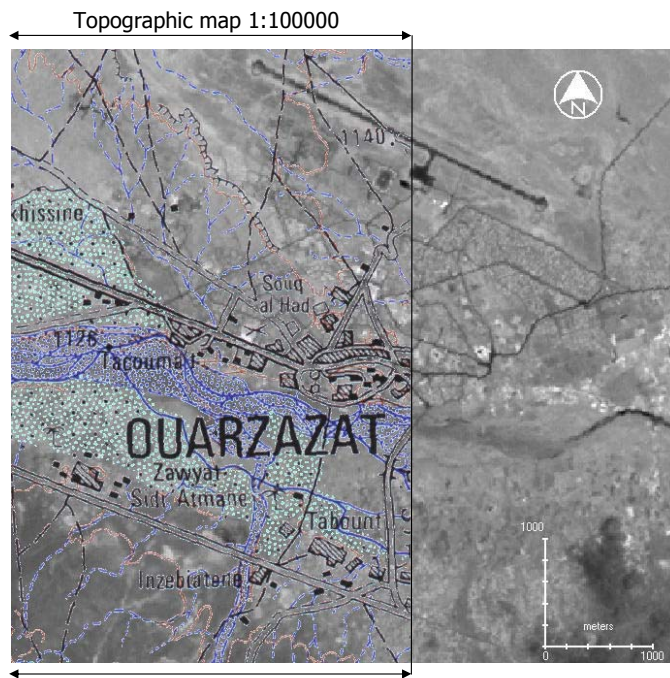


Figure 4.11: Image swipe of an ASTER orthoimage overlaid on the topographic map Ouarzazate on scale 1:10000

4.2.5 Co-registration

Constructed orthoimages served as a basis for image co-registration. This is especially important for the very high resolution data as recorded obliquely. Figure 4.12 shows an example of an IKONOS-2 image, with a large view angle (chapter 4), and therefore strong relief displacement (Schmidt et al., 2003a). An orthophoto of CORONA data was produced (subsection 4.2.3) and was used as a cartographic basis due to the lack of orthographic material at the desired scale.

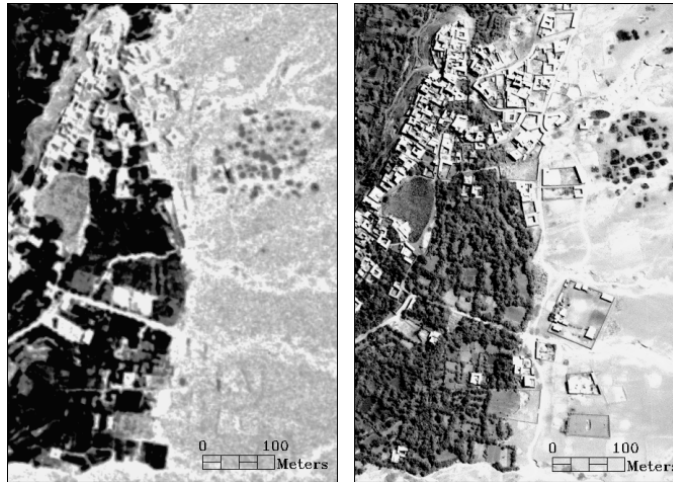


Figure 4.12: Co-registered CORONA (26.05.1972) and IKONOS (24.06.2001) panchromatic image - pixel size 1m near Toundoute

The images were co-registered with 90 control points and a high RMS error (44.3 pixel), as the terrain difference is about 150m in this area, which served to a good matching. As discussed in chapter 4, in this case error estimations need to be introduced other than the classical RMS error.

4.3 Multi-temporal 3D analysis - or 4D remote sensing?

Incorporating a DEM is a 3D analysis and provides very useful data for many applications. The integration of time series data recorded in 2D, such as images of NOAA-AVHRR or LANDSAT, would result in an analysis with a dimension higher than 3. Real 4D analysis by the incorporation of DEMs over time is certainly possible: DEMs and orthophotos of large areas can be generated in almost real time after a stereo-satellite overpass using a set of updated GCPs. Monitoring surfaces with DEMs can improve early warning systems, e.g. in vulcanology or geo-morphology. Especially with very high resolution, combining the elevation information with multispectral information, can serve to better identify and predict hazard events.

4.4 Discussion and Conclusions

High quality DEMs are important for several environmental applications, e.g. hydrology, botany, illumination correction in remote sensing etc. Recent progress in remote sensing as well as in Photogrammetry allows one to generate DEMs from non-metric data and to produce up-to-date cartographic base material. Solution of the photogrammetrical equations in VirtuoZo requires the insertion of a minimum of 6 GCPs in x,y and z coordinate within a stereo data-set. The quality of the ASTER DEM was checked in a small test area, with good results, where a GCP for the photogrammetric restitution was used in the neighborhood. Further field work in the remote areas can only serve to improve the overall validation of the derived DEM and ortho-product. The incorporation of additional GCPs in the existing VirtuoZo projects is possible so that the automatic product generation is not time consuming. The quality of the photogrammetrically results is dependent on the quality of the input GCPs and the image matching based on the image contrast.

Images co-registered to orthographic base material permit further analysis and image interpretations, change detection or object recognition applications e.g. see Mueller and Segl (1999). The interface to other software systems and the export of products into GIS systems is an important component of the photogrammetric packages necessary to make the information available to users.

A methodology was proposed, in which the use of CORONA satellite images, available globally between the years 1960-1972, is possible. In difficult terrains, such as mountainous or urban areas, if very high resolution oblique data such as IKONOS or Quickbird are integrated in mapping activities, a correction for image displacement is necessary if the result is to have accurate geo-information.

It was and is possible to combine SPOT P images of 10m pixel size obtained from different orbits (and dates) to use for DEM generation. This was in historic times only possible for companies with knowledge of the camera parameters for an internal orientation. These camera parameters are no longer needed and historical satellite data, as well as recent data, can, with digital photogrammetric methods, now also be used for a DEM and orthophoto generation of non-metric images. Modern sensors, such as ASTER, provide satellite data with which a 3D remote sensing analyst can produce his/her own cartographic base material together with a DEM of high quality and potentially multispectral channels for image interpretation. The great advantage of the recording system of ASTER is that both images are recorded

with a time interval of only 55 seconds under effectively the same environmental conditions. Consequently surface changes and atmospheric variations can in most cases be disregarded; the author can only propose considering this advantage for future satellite missions, as the so called 3D remote sensing becomes, with finer spatial resolution, more and more important.

5 Pre-processing - How much is necessary?

”A good player never makes more effort than he needs to win”

- old arabic wisdom

According to Mather (1999) the term pre-processing is understood as the correction of geometric and radiometric deficiencies and the removal of data errors. It seems natural that errors within the data are removed, if possible, before image interpretations start. The choice of methods to do so is always purpose dependent. If, for instance, a check of a certain land cover or object with an satellite image is the purpose, visual interpretation might be sufficient and even geometric correction not necessary (Jensen, 1996b). In our opinion the operator should define precisely the demands on the data and chose the necessary processing steps to achieve his specific task. The importance of pre-processing methods becomes obvious in change detection or monitoring applications, where the operator must be able to distinguish data noise, pre-processing and data handling errors from real changes. Song et al. (2001) discuss this topic in more detail.

For high and very high spatial resolution data are currently no automatic or fully operational pre-processing programs available as there are for high temporal resolution data such as NOAA/AVHRR and TERRA/MODIS. One emphasis of this work outlined in the following sections was an attempt to automate pre-processing steps for high resolution data (LANDSAT TM/ETM+) as much as possible and to integrate these routines in standard software packages.

5.1 Satellite data

The data to be processed, within this study, have a variety of different resolutions and characteristics (Table 5.1).

Table 5.1: Characteristics of the utilised and processed multispectral satellite data

Satellite Sensor	NOAA AVHRR	TERRA MODIS	LANDSAT MSS/TM/ETM+	TERRA ASTER	IKONOS	CORONA KH4B/KH4A
Pixel size [m]	1100	250/500/1000	79/28.5/28.5 (25)	15/30/90	4	~1.8/~4
Spectral channels	5	36	4/7/7+pan	14	4+pan	pan
Flight height [km]	860	705	706	705	680	180
Satellite	14,16	1	1,3,4,5,7	1	2	18/14
Data Distributor	SAA	NASA	RADARSAT/USGS	NASA	SI	USGS
Processing level	1b	MOD13Q1	1R/1G	1b	Geo	raw
Delivery media	ftp	ftp	Cdrom	ftp	CDrom	filmstrips
Storage	10bit	16bit	8bit	8bit	11bit	64 lines/mm
Dataformat	LAC/HRPT	HDF	(geo-) tif/NLAPS	HDF	(geo-) tif	dia-positive

AVHRR level 1b data from NOAA 14 and 16 in local area coverage (LAC) and high resolution picture transmission-station (HRPT) format were obtained by the NOAA satellite active archive (SAA). The data are delivered daily by file transfer protocol (ftp). NOAA records daily data for a crop monitoring project in north Africa. The Dra valley is located at the edges of the recorded coverage, resulting in a data coverage less than daily.

The MODIS MOD13Q1 product (USGS, 2003b) of the MODIS Level 3 16-day composite of NDVI at 250m resolution were downloaded (USGS, 2003a) and re-projected for the comparison with NOAA/AVHRR data (NASA, 2003b).

LANDSAT level 1R data are radiometrically corrected, while 1G data are radiometrically and systematically corrected. Level 1R and 1G data undergo a two-dimensional resampling according to user-specified parameters including output map projection, rotation angle and pixel size (NASA, 2001).

ASTER data were obtained (NASA, 2002b), the level 1b data are systematically corrected and transformed to a map projection. All available level 1b data for the Dra valley were downloaded and stored.

The IKONOS product GEO is radiometrically and systematically corrected and delivered as map product in a user-specified map projection. The product specification 90ME guarantees a horizontal map accuracy of 90% of all pixels with a accuracy of 25m (SpaceImaging, 2002). It is also guaranteed, that the view angle is less than 27°, which happens often to be not the case in the delivered products (see e.g. subsection 6.2.2).

Figure 5.1 shows the coverage of IKONOS-2 data and the LANDSAT path and row values necessary for the catchment coverage, according to the world reference

system II. The LANDSAT data were in a first step roughly cut to the extent of the Dra catchment to reduce the data volume.

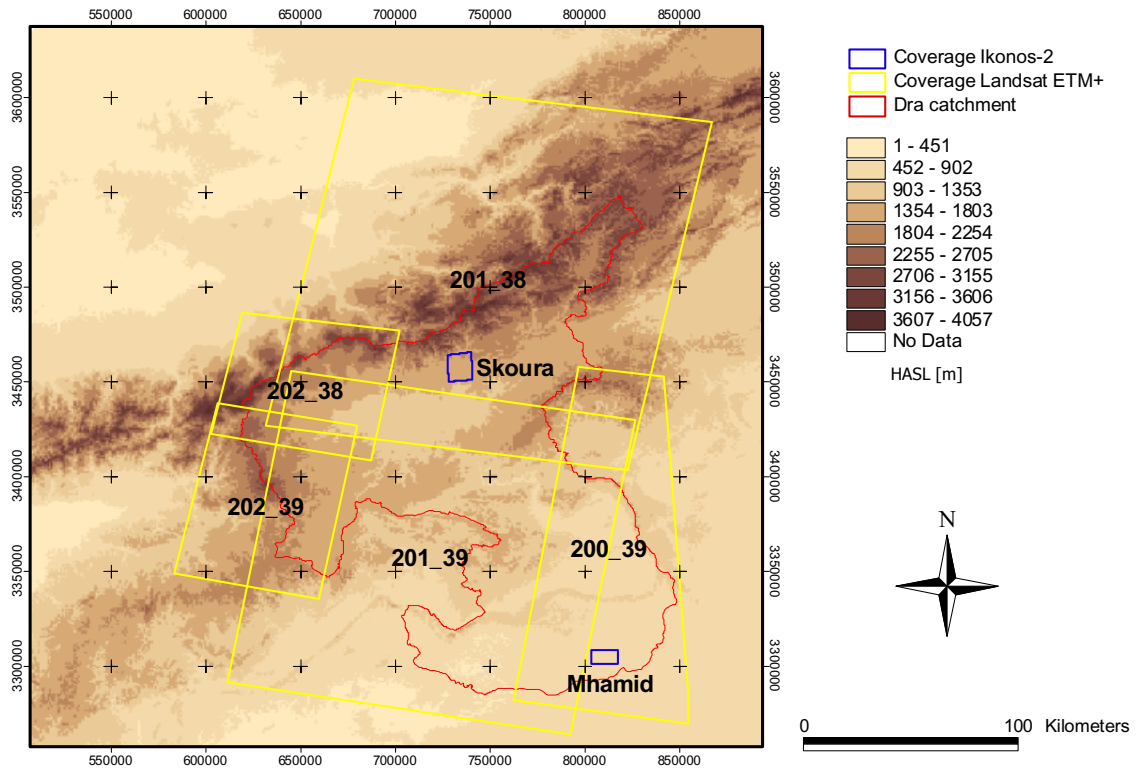


Figure 5.1: Overview of the IKONOS-2 and LANDSAT (WRS2) data coverage within the Dra catchment, overlaid on GTOPO30 DEM (Projection: UTM)

CORONA satellite images were transferred into digital data in tagged image file (tif) format, as described in chapter 4. The data coverage includes 38 image strips for the whole catchment in forward and afterward view.

5.2 Geometric correction

5.2.1 Reference system

Integration of data from various sources, such as topographic maps, GPS data from field survey, satellite images etc. require that this data are stored in the same reference system. This is essential for the use of a homogeneous and operational GIS

database. Prior to the geo-correction of the satellite data a cartographic reference system was defined. The available topographical maps are in a Lambert Conic Conformal projection (Mugnier, 1999) with spheroid CLARKE 1880 and datum Merchich. The Dra catchment is located within two different projections the Zones: Maroc Nord and Maroc Sud. Table 5.2 shows the projection parameters.

Table 5.2: Attributes of Lambert Conical Conform projection, for Zone Maroc Nord and Maroc Sud

Attribute	Zone Maroc Nord (35.55° – 31.05°)	Zone Maroc Sud (31.05° – 27.45°)
1st standard parallel	31.785°	28.107°
2nd standard parallel	34.875°	31.293°
Central meridian	−5.4°	−5.4°
Latitude of projection origin	33.3°	29.7°
False easting	500 000	500 000
False northing	300 000	300 000
Scale factor at origin	0.9996	0.9996

For the delivery of a final map product of the whole catchment the mapping with two different projections not found to be a satisfactory solution. For this reason a **Universal Transverse Mercator (UTM)** metric projection was chosen. The whole catchment was mapped within the **Zone 29** with -9° as central meridian and $500000m$ as false easting. To simplify the data exchange spheroid and datum of the local reference systems were chosen: **CLARKE 1880** and **Merchich**.

Topographic maps on scale 1:100000 are available for the whole catchment (IMPE-TUS, 2001). The scanned maps ($300dpi$) were geo-referenced with ERDAS Imagine to the corresponding Lambert Conic Conformal projection and projected to UTM. The topographic maps served as orthographic base material for further mapping and display purposes.

For the purpose of data integration and GIS analysis, all raster and GIS data with related geo-information within this work were registered in this projection.

5.2.2 Geometric correction of (very-) high resolution Satellite Data

Raw digital images obtained by air- or spacecraft usually contain geometric distortions so significant that they need subsequent processing before usage (Lillesand and Kiefer, 2000). These distortions can either be *systematic* and induced by factors, such as panoramic effects, earth rotation, change in platform velocity etc. (for further discussion see Jensen, 1996b) or *non systematic*. Non systematic distortion include platform variations in altitude and attitude, with changes in kappa, phi, omega and the image scale, or terrain induced effects (see chapter 4). Confusion of terms geo-rectification, geo-registration, geo-coding, geometric correction in literature is not discussed here. In the following the term geometric correction will be used.

Geometric correction is usually a two step process, where the systematic errors can be reduced directly after image recording by modelling the sources of errors mathematically (Lillesand and Kiefer, 2000). Most data are distributed as systematic corrected products. Non systematic distortions are corrected by the co-registration to an orthographic reference map or, in the case of a moderate or flat terrain, by field measured GCPs. The different satellite data require different treatment.

CORONA images can due to the availability of stereo-coverage serve by a photogrammetrical restitution to generate orthophoto-maps which can is a distortion free base material e.g. for image to image co- registration, as discussed in detail in chapter 4. A prerequisite of this approach is the availability of accurate GCPs in x,y and z. The acquisition of GCPs is a crucial analysis step and is at historic images sometimes a difficult task. *CORONA* orthophotos were generated for two test regions within the study area, as shown in Figure 4.4.

One way to derive a geometric corrected image, even in a rugged terrain, of *IKONOS-2* data is an image to image/map co-registration to an orthographic product, as proposed in chapter 4. This approach was followed in the study area near Skoura (see Figure 5.1). Within a study area located near the town of M'hamid (see Figure 5.1), in a sand dune dominated landscape was in absence of any infrastructure the identification of GCPs within the *CORONA* images not possible. The terrain is generally flat, so that the multispectral image of a $10km \times 10km$ were geometrically corrected by an affine transformation, as proposed by Baltsavias et al. (2001). They propose that a set of 3 GCPs is sufficient. 20 GCPs were collected

in the field with an accuracy of less than one meter (Trimble, 2003). 5 GCPs were used for the affine transformation, while 15 GCPs were used as test points. The RMS error in the 15 test points was less than one pixel.

ASTER data within this study are only used for the generation of DEMs and ortho-photos as discussed in detail in chapter 4. The ortho-photos can, in a second step, be used for the co registration of the multispectral bands to the ortho-photo. The base material can be generated from the same data source as the multispectral bands which has great advantages for image matching algorithms to perform an automated image co-registration.

The topographic maps in UTM projection served as base material for an image to map registration of *LANDSAT TM/ETM+* data covering the Dra catchment (see Figure 5.1). A set of *LANDSAT TM/ETM+* data available at the beginning of the project were registered and mosaiced to a master image used for the image co-registration (see Table 5.3). Problems arose due to the difficult identification of GCPs in rugged terrain, especially in areas close to the Algerian border. The cause of this effect is most probably lack of readily identifiable infrastructure lines, but might potentially be due to inaccurate maps at the border for military purposes. These circumstances led to the decision to integrate an *ASTER* panchromatic ortho-image of this region K'tauer, see subsection 4.2.3. The co-registration to this ortho-image resulted in a better fitting with the ground truth data.

An image matching algorithm for the automatic and independent matching points generation due to Li et al. (1997) was used for GCP identification at the image to image registration of *LANDSAT* data to the *LANDSAT* mosaic. The contour based image matching algorithm is based on a Laplacian-of-Gaussian filter (Li et al., 1997) where a chain encoding of closed contour lines is used to identify matching points (Canty, 2002). This algorithm is implemented within the freeware package *CDSAT* as described in Canty (2002). The matching point generation as performed in *CD-SAT* was integrated in *ERDAS Imagine*, where the potential matching points were imported and checked for plausibility. In image areas with poor GCP representation GCPs were manually inserted. The image matching algorithm identifies matching points in mountainous areas better than in flat terrains (Li et al., 1997). This is especially of advantage in the Dra catchment as in the remote mountainous areas GCPs accuracy was in this way improved in comparison to the operator dependent identification. The images were registered with a nearest neighbour resampling with a second order polynomial transformation. Table 5.3 shows the number of points

5 Pre-processing - How much is necessary?

and the RMS error used for the image geometric corrections.

Table 5.3: Geometrically corrected LANDSAT images within the Dra catchment, the scenes displayed in bold letters represent the data used to generate the initial LANDSAT mosaic. The pixel size describes the output resampling (see text)

sensor	path/row WRS I	path/row WRS II	date	pixel size	GCPs			RMS error
					manual	automatic	total	
MSS	216-38		08.09.1972	28.5m	21		21	0.3264
MSS	216-39		08.09.1972	28.5m	48		48	0.3500
MSS	216-38		25.01.1974	28.5m	26		26	0.2943
MSS	216-39		25.01.1974	28.5m	52		52	0.3400
MSS		201-39	05.04.1987	28.5m	51		51	0.4322
TM		201-38	18.08.1984	28.5m	23		23	0.4423
TM		201-39	18.08.1984	28.5m	23		23	0.4423
TM		200-39	27.08.1984	28.5m	50		50	0.4656
TM		200-39	08.01.1987	28.5m	46	86	132	0.4209
TM		200-39	09.02.1987	28.5m	23	103	126	0.4934
TM		201-39	05.04.1987	28.5m	14	33	47	0.3200
TM		202-38	17.07.1987	28.5m	10		10	0.2227
TM		200-39	07.10.1987	28.5m	49	92	141	0.4000
TM		201-38	14.10.1987	28.5m	37	59	96	0.3985
ETM+		201-38	24.11.1999	28.5m	28		28	0.2913
ETM+		201-39	10.12.1999	28.5m	20		20	0.4374
ETM+		200-39	19.12.1999	28.5m	88		88	0.4604
ETM+		200-39	18.10.2000	28.5m	18	98	116	0.4875
ETM+		201-39	25.10.2000	28.5m			38	0.3921
ETM+		201-38	02.05.2000	25m	28		28	0.3576
ETM+		201-39	02.05.2000	25m	40	125	165	0.3989
ETM+		202-38	25.05.2000	25m			28	0.4596
ETM+		202-39	25.05.2000	25m	18		18	0.2848
ETM+		200-39	27.05.2000	25m	55	77	132	0.4583

A catchment coverage of LANDSAT ETM+ data in 25m resolution was obtained from the Canadian company RADARSAT. For the image to image registration of this 25m resolution data the 28.5m image mosaic was resampled to 25m in order to use the automatic GCP generation and maintain the higher resolution.

Data processing of NOAA/AVHRR data was performed with the software package TERASCAN. Parameter files of orbital elements provide in a first positional image

estimate as a starting point for the geo-rectification algorithm. This algorithm works without GCPs and integrates a feature based matching technique (see section 4.1) to existing vector information. For example coastlines are used for matching purposes and can be chosen either from Digital Chart of the World or from the World Database II (Seaspace, 2000). Each image is, within this algorithm, segmented in predefined boxes within which the matching is performed. The number of boxes used is dependent on the cloud coverage. This is done to make registration possible even with a high cloud content. A check of each processed scene accompanied with modifications in the box size is advisable if no matching was found and often results in a registration improvement. The geometric image correction and projection to UTM projection performed for a bounding box (N-S $37^{\circ} - 27^{\circ}N$, W - E $0 - 15^{\circ}E$) in $1.1km \times 1.1km$ pixel resolution. Depending on the distance to the coastline, the registration accuracy ranges usually from sub-pixel up to 2.5 pixels (Dech, 1997). Areas recorded with high zenith angles (greater than 55°) were excluded as proposed by Cracknell (1997).

5.3 Radiometric correction

Absolute radiometric correction of multi-temporal satellite imagery requires atmospheric corrections associated with the atmospheric properties at the time of the image acquisition. Data for the characterisation of the relevant atmospheric processes modulating the incoming radiation at the satellite sensor require auxiliary data of parameters, such as the content of aerosols, ozone or water vapor in different atmospheric layers (see e.g. Kaufmann, 1989; Mitchell and O'Brien, 1993, for further discussion). For historic satellite data such data are often difficult or impossible to obtain. Whenever atmospheric parameters are not available and/or absolute surface radiances are not necessary, a relative normalisation of the satellite images to a master scene, based on the radiometric information intrinsic to the images, is an alternative (Furby and Campbell, 2001). This is especially true in land cover classifications and post classification change detection applications (Song et al., 2001). Radiometric normalisation, either relative or absolute, of imagery is important for many other applications, such as image mosaicing or tracking vegetation indices over time etc. (see Yang and Lo, 2000, and chapter 7). Furthermore, if change detection procedures, such as image differencing or change vector analysis, is preferred it must

generally be preceded by radiometric normalisation (either absolute or relative).

5.3.1 Relative radiometric normalisation

Several methods as of Schott et al. (1988); Hall et al. (1991); Moran et al. (1995); Furby and Campbell (2001); Du et al. (2002) have been proposed for the relative radiometric normalisation of multispectral images taken under different conditions at different times. All proceed under the assumption that the relationship between the at-sensor radiances recorded at two different times from regions of constant surface reflection can be approximated by linear functions. The most difficult and time-consuming aspect of all of these methods is the determination of suitable time-invariant features upon which the normalisation is based.

Relative radiometric normalisation methods are not implemented in the standard software tools, such as ENVI 3.5 and ERDAS Imagine 8.5. This led to the decision to program two relative radiometric normalisation algorithms within the environment of ENVI/IDL. The methods were evaluated and tested on a bitemporal image pair of Landsat ETM+ data acquired over south Morocco on December 19, 1999 and October 18, 2000. The images were subset with dimensions 729×754 pixels. The first method follows the approach of Schott et al. (1988) and is based on the selection of so called pseudo-invariant features, which need to be selected manually from the image. The pseudo-invariant features are assumed to undergo no changes in the interval between the acquisition of the images. The pseudo-invariant features are used for a stochastic estimation of regression coefficients for an image to image radiometric normalisation (see Equation 5.1). The second algorithm is new and fully automatic, although the principle is similar: invariant pixels are used in an regression approach. The main progress is the automatic identification of "no change pixels", that are homogeneously distributed over the entire image and different surface types.

5.3.1.1 Pseudo-Invariant Feature approach

Schott et al. (1988) proposed that in the case of the availability of a large amount of homogeneously distributed invariant pixels, a regression of would produce the best results, but assumed that these pixels are not identifiable. This would be satisfied if ground truth data of the true invariant pixel were available, which is rarely the case. Thus their idea was to introduce the term pseudo-invariant feature (PIF). PIFs are areas, assumed to be invariant but potentially exhibit some change pixels. PIFs need

to be identified manually within bi- or multi-temporal images. Schott et al. (1988) proposed the usage of band ratios, Hall et al. (1991) a tasseled cap transformation to identify potential no-change pixels a priori (Crist and Cicone, 1984). The approach of Schott et al. (1988) is based on the assumption that PIFs are used to estimate a linear regression for the relative radiometric image normalisation. The 'master' image is denoted with DN_1 , the image that is normalised to the master image is DN_2 , and DN'_2 the normalised image; i represents the spectral bands. The following expression from Schott et al. (1988) was used for a radiometric normalisation:

$$DN'_{2i} = \frac{\sigma_{1i}}{\sigma_{2i}} DN_{2i} + \overline{DN_{1i}} - \frac{\sigma_{1i}}{\sigma_{2i}} \overline{DN_{2i}} \quad (5.1)$$

where $\overline{DN_{1i}}$ and $\overline{DN_{2i}}$ are the means of the pseudo-invariant pixels of image 1 and 2. σ_{1i} and σ_{2i} are the respective standard-deviations.

This formula can be reduced to a simplified expression of an independent variable x and a dependent variable y in the sense:

$$y = ax + c, \quad (5.2)$$

with slope $a = \frac{\sigma_{1i}}{\sigma_{2i}}$ and intercept $c = \overline{DN_{1i}} - \frac{\sigma_{1i}}{\sigma_{2i}} \overline{DN_{2i}}$. PIFs were manually selected from the ground truth data of non-vegetated surfaces. Table 5.4 shows the number of pixels distributed across different the surface types to obtain the best regression estimation.

Table 5.4: Pseudo-invariant features chosen for normalisation to the 1999 scene

Feature	No. pixels	appearance
playa	213	bright
sand	183	bright
desert crust	9347	medium
gravel	301	medium
quartzite	117	medium
pediment	365	dark
dark stones	233	dark

5.3.1.2 Multivariate Alteration Detection

This section is the result of a close collaboration with M. Canty, KFA, Jülich (Germany) and A.A. Nielson, School of Mathematics, Copenhagen (Denmark). Results of this work can be found in Canty et al. (2003, for further reading).

Selecting invariant pixels

Nielsen et al. (1998) recently proposed a change detection technique, called multivariate alteration detection (MAD), which is invariant to radiometric linear and affine scaling. Thus, if one uses MAD for change detection applications, preprocessing by linear radiometric normalization, whether absolute or relative, is superfluous. However, in this application are the no-change pixels in a bitemporal scene of interest. Therefore are first linear combinations formed of the intensities for all N channels in the two images, acquired at times t_1 and t_2 . Representing the intensities by the random vectors \mathbf{F} and \mathbf{G} , respectively, we have

$$\begin{aligned} U &= \mathbf{a}^\top \cdot \mathbf{F} = a_1 F_1 + a_2 F_2 + \dots a_N F_N \\ V &= \mathbf{b}^\top \cdot \mathbf{G} = b_1 G_1 + b_2 G_2 + \dots b_N G_N, \end{aligned}$$

where \mathbf{a} and \mathbf{b} are constant vectors. Nielsen et al. (1998) suggest determining the transformation coefficients so that the positive correlation between U and V is minimized. This means that the difference image $U - V$ will show maximum spread in its pixel intensities. If we assume that the spread is primarily due to actual changes that have taken place in the scene over the interval $[t_1, t_2]$, then this procedure will enhance those changes as much as possible.

Specifically we seek linear combinations such that

$$\text{var}(U - V) = \text{var}(U) + \text{var}(V) - 2\text{cov}(U, V) \rightarrow \text{maximum}, \quad (5.3)$$

subject to the constraints

$$\text{var}(U) = \text{var}(V) = 1 \quad (5.4)$$

and with $\text{cov}(U, V) > 0$. Note that under these constraints

$$\text{var}(U - V) = 2(1 - \rho), \quad (5.5)$$

where ρ is the correlation of the transformed vectors U and V ,

$$\rho = \text{corr}(U, V) = \frac{\text{cov}(U, V)}{\sqrt{\text{var}(U)\text{var}(V)}}.$$

For multivariate normally distributed data the combined random vector for the bitemporal scene is distributed as

$$\begin{pmatrix} \mathbf{F} \\ \mathbf{G} \end{pmatrix} \sim N \left[\begin{pmatrix} 0 \\ 0 \end{pmatrix}, \begin{pmatrix} \boldsymbol{\Sigma}_{ff} & \boldsymbol{\Sigma}_{fg} \\ \boldsymbol{\Sigma}_{gf} & \boldsymbol{\Sigma}_{gg} \end{pmatrix} \right],$$

where

$$\text{var}(U) = \mathbf{a}^\top \boldsymbol{\Sigma}_{ff} \mathbf{a}, \quad \text{var}(V) = \mathbf{b}^\top \boldsymbol{\Sigma}_{gg} \mathbf{b}, \quad \text{cov}(U, V) = \mathbf{a}^\top \boldsymbol{\Sigma}_{fg} \mathbf{b}.$$

Extremalising the covariance $\text{cov}(U, V)$ under the constraints Equation 5.4 is equivalent to extremalising the unconstrained function

$$L = \mathbf{a}^\top \boldsymbol{\Sigma}_{fg} \mathbf{b} - \frac{\nu}{2} (\mathbf{a}^\top \boldsymbol{\Sigma}_{ff} \mathbf{a} - 1) - \frac{\mu}{2} (\mathbf{b}^\top \boldsymbol{\Sigma}_{gg} \mathbf{b} - 1),$$

where ν and μ are Lagrange multipliers. This leads to the coupled generalized eigenvalue problems

$$\begin{aligned} \boldsymbol{\Sigma}_{fg} \boldsymbol{\Sigma}_{gg}^{-1} \boldsymbol{\Sigma}_{gf} \mathbf{a} &= \rho^2 \boldsymbol{\Sigma}_{ff} \mathbf{a} \\ \boldsymbol{\Sigma}_{gf} \boldsymbol{\Sigma}_{ff}^{-1} \boldsymbol{\Sigma}_{fg} \mathbf{b} &= \rho^2 \boldsymbol{\Sigma}_{gg} \mathbf{b}. \end{aligned} \tag{5.6}$$

Thus the desired projections $U = \mathbf{a}^\top \mathbf{F}$ are given by the eigenvectors $\mathbf{a}_1 \dots \mathbf{a}_N$ corresponding to the generalized eigenvalues

$$\rho_1^2 \geq \dots \geq \rho_N^2$$

of $\boldsymbol{\Sigma}_{fg} \boldsymbol{\Sigma}_{gg}^{-1} \boldsymbol{\Sigma}_{gf}$ with respect to $\boldsymbol{\Sigma}_{ff}$. Similarly the desired projections $V = \mathbf{b}^\top \mathbf{G}$ are given by the eigenvectors $\mathbf{b}_1 \dots \mathbf{b}_N$ of $\boldsymbol{\Sigma}_{gf} \boldsymbol{\Sigma}_{ff}^{-1} \boldsymbol{\Sigma}_{fg}$ with respect to $\boldsymbol{\Sigma}_{gg}$ corresponding to the *same* eigenvalues. Nielsen et al. (1998) refer to the N difference components

$$MAD_i := U_i - V_i = \mathbf{a}_i^\top \mathbf{F} - \mathbf{b}_i^\top \mathbf{G}, \quad i = 1 \dots N, \tag{5.7}$$

as the *multivariate alteration detection* (MAD) components of the combined bitemporal image. The covariances of the MAD components are given by

$$\text{cov}(U_i - V_i, U_j - V_j) = 2\delta_{ij}(1 - \rho_j),$$

where δ_{ij} denotes Kronecker's delta,

$$\delta_{ij} = \begin{cases} 1 & \text{for } i = j \\ 0 & \text{for } i \neq j \end{cases}$$

The components are orthogonal (uncorrelated) with variances

$$\text{var}(U_i - V_i) = \sigma_{MAD_i}^2 = 2(1 - \rho_i). \quad (5.8)$$

The last MAD component has maximum spread in its pixel intensities and, ideally, maximum change information. The second-to-last component has maximum spread subject to the condition that the pixel intensities are statistically uncorrelated with those in the first MAD component, and so on.

The MAD components are invariant under linear transformations of the original image intensities. We can see this as follows. Suppose the second image \mathbf{G} is transformed according to some linear transformation $\mathbf{H} = \mathbf{T}\mathbf{G}$. The relevant covariance matrices are then

$$\begin{aligned} \Sigma'_{fg} &= \langle \mathbf{F}\mathbf{H}^\top \rangle = \Sigma_{fg}\mathbf{T}^\top \\ \Sigma'_{gf} &= \langle \mathbf{H}\mathbf{F}^\top \rangle = \mathbf{T}\Sigma_{gf} \\ \Sigma'_{ff} &= \Sigma_{ff} \\ \Sigma'_{gg} &= \langle \mathbf{H}\mathbf{H}^\top \rangle = \mathbf{T}\Sigma_{gg}\mathbf{T}^\top. \end{aligned}$$

The eigenvalue problems (4) are therefore equivalent to

$$\begin{aligned} \Sigma_{fg}\mathbf{T}^\top(\mathbf{T}\Sigma_{gg}\mathbf{T}^\top)^{-1}\mathbf{T}\Sigma_{gf}\mathbf{a} &= \rho^2\Sigma_{ff}\mathbf{a} \\ \mathbf{T}\Sigma_{gf}\Sigma_{ff}^{-1}\Sigma_{fg}\mathbf{T}^\top\mathbf{c} &= \rho^2\mathbf{T}\Sigma_{gg}\mathbf{T}^\top\mathbf{c}, \end{aligned}$$

where \mathbf{c} is the desired projection for \mathbf{H} . These in turn are equivalent to

$$\begin{aligned} \Sigma_{fg}\Sigma_{gg}^{-1}\Sigma_{gf}\mathbf{a} &= \rho^2\Sigma_{ff}\mathbf{a} \\ \Sigma_{gf}\Sigma_{ff}^{-1}\Sigma_{fg}(\mathbf{T}^\top\mathbf{c}) &= \rho^2\Sigma_{gg}(\mathbf{T}^\top\mathbf{c}), \end{aligned}$$

which are identical to Equation 5.6 with $\mathbf{b} = \mathbf{T}^\top\mathbf{c}$. Therefore the MAD components in the transformed situation are

$$\mathbf{a}_i^\top\mathbf{F} - \mathbf{c}_i^\top\mathbf{H} = \mathbf{a}_i^\top\mathbf{F} - \mathbf{c}_i^\top\mathbf{T}\mathbf{G} = \mathbf{a}_i^\top\mathbf{F} - (\mathbf{T}^\top\mathbf{c}_i)^\top\mathbf{G} = \mathbf{a}_i^\top\mathbf{F} - \mathbf{b}_i^\top\mathbf{G}$$

as before. Given this scale invariance, we can select for radiometric normalisation all pixel coordinates which satisfy

$$\sum_{i=1}^N \left(\frac{MAD_i}{\sigma_{MAD_i}} \right)^2 < t,$$

where t is a decision threshold. Under the hypothesis of no-change, the above sum of squares of standardized MAD variables is approximately chi-square distributed with

N degrees of freedom. We therefore choose $t = \chi_{N,P=0.01}^2$ where P is the probability of observing that value of t or lower.

The pixels thus selected should correspond to truly invariant features so long as the overall radiometric differences between the two images can be attributed to linear effects. Since this method usually identifies quite a large number of no-change pixels we can, without serious penalty, reserve some fraction of for subsequent testing and use the remaining pixels for performing the actual linear regressions.

Comparison of the methods

Schott et al. (1988) do not use ordinary linear regression, but rather assume a direct (error-free) estimated linear relation between digital numbers recorded from man-made features at two times (see Figure 5.2). The regression coefficients are compared to a linear regression with the PIF pixels (see Equation 5.3.1.2), which represent the PIF pixels best. Figure 5.2 shows the point distribution and a regression line of a ordinary least square regression (OLS), based on 2/3 of the no-change pixels (referred to henceforth as "training pixel") determined from the pseudo-invariant features (see Table 5.4). The fitted intercepts (c) and slopes (a) are shown in Table 5.5 for the 7200 training pixels.

Table 5.5: Ordinary least square regression on training PIF pixels c is the fitted intercept, a is the fitted slope, r is the correlation and RMSE the root mean square error. In comparison the regression estimated by Schott et al. (1988)

Band	OLS regression				regression by Schott et al. (1988)	
	a	c	r	RMSE	a	c
1	1.081	8.60	0.818	2.019	1.297	-4.843
2	1.184	-3.00	0.928	1.845	1.264	-7.730
3	1.198	-7.09	0.947	2.761	1.256	-11.867
4	1.258	-6.37	0.961	2.020	1.203	-9.115
5	1.081	4.76	0.927	2.891	1.162	-1.546
7	1.077	5.31	0.910	2.870	1.178	-2.079

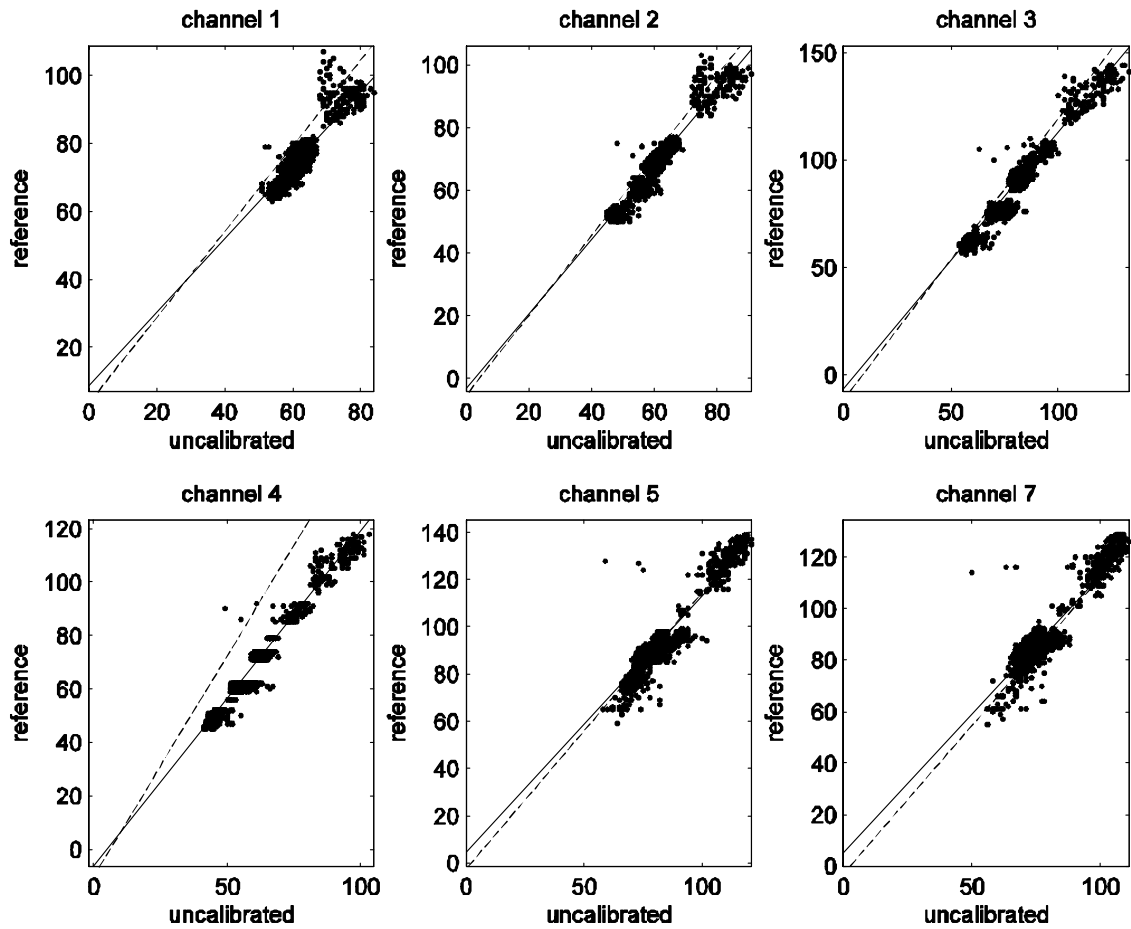


Figure 5.2: Regression of the 1999 reference scene on the 2000 target (uncalibrated) scene using manually selected training pixels. The dotted lines show the regression followed Schott et al. (1988)

Table 5.6 and Table 5.7 show, respectively, the means and variances of the 1999 scene before and after normalisation to the 2000 scene with the approach of Schott et al. (1988). The means and variances were determined with the 3600 holdout test pixels.

Table 5.6: Comparison of mean intensities of hold-out test PIF pixels for the 2000 scene before and after normalisation to the 1999 scene with OLS regression

TM Band	1	2	3	4	5	7
Uncorrected(2000)	62.080	59.898	81.975	62.612	77.989	72.898
Normalised(2000)	75.720	67.969	91.143	72.400	89.117	83.820
Reference(1999)	75.650	67.969	91.115	72.455	89.114	83.771
Difference	-0.069	0.000	-0.027	0.055	-0.003	-0.049

Table 5.7: Comparison of variances of hold-out test PIF pixels for the 2000 scene before and after normalisation to the 1999 scene with OLS regression

TM Band	1	2	3	4	5	7
Uncorrected(2000)	6.96	14.48	44.93	29.60	40.692	31.70
Normalised(2000)	8.14	20.34	64.52	46.85	47.60	36.77
Reference(1999)	10.88	22.09	68.98	49.16	54.16	43.27

In contrast with the PIF data, Figure 5.3 displays least squares regressions for normalisation of the two Morocco images based on 11260 no-change training pixels derived from the MAD procedure. Table 5.8 through Table 5.10 give the corresponding information on regression statistics and on the comparisons of means and variances with 5630 test pixels.

Table 5.8: OLS regression on training MAD pixels for the two scenes

Band	a	c	r	RMSE
1	1.230	-1.56	0.966	1.074
2	1.191	-4.68	0.978	1.372
3	1.194	-8.88	0.983	2.109
4	1.265	-8.31	0.987	1.546
5	1.148	-2.22	0.981	2.244
7	1.146	-1.33	0.976	1.983

Table 5.9: Comparison of mean intensities of hold-out test MAD pixels for the 2000 scene before and after normalisation to the 1999 scene with OLS regression

TM Band	1	2	3	4	5	7
Uncorrected(2000)	62.734	61.544	83.894	64.573	88.128	80.094
Normalised(2000)	75.577	68.621	91.319	73.345	98.936	90.441
Reference(1999)	75.576	68.595	91.279	73.323	98.905	90.414
Difference	-0.001	-0.026	-0.039	-0.022	-0.032	-0.027

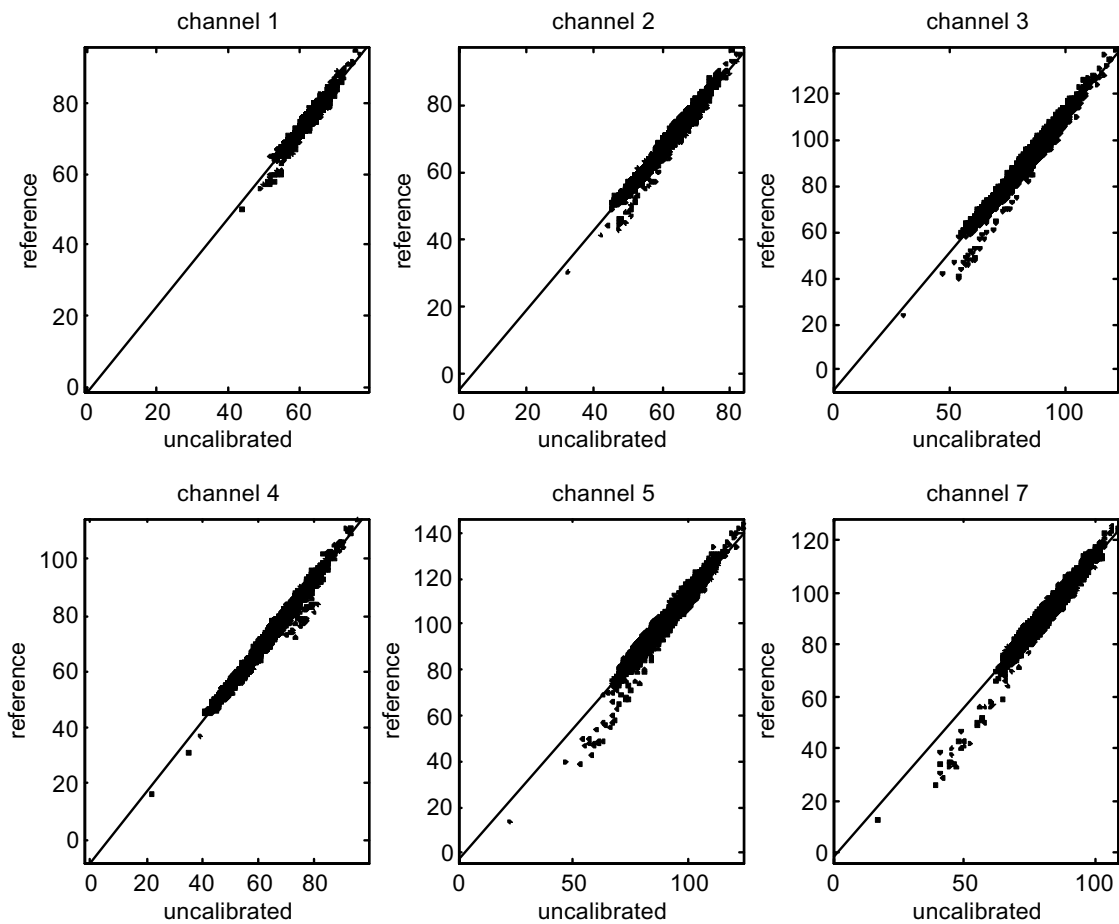


Figure 5.3: Regression of the 1999 reference scene on the 2000 target (uncalibrated) scene using the MAD training pixels.

Table 5.10: Comparison of variances of hold-out test MAD pixels for the 2000 scene before and after normalisation to the 1999 scene with ordinary least squares regression

TM Band	1	2	3	4	5	7
Uncorrected(2000)	10.58	28.71	86.99	54.45	95.67	59.79
Normalised(2000)	15.99	40.72	124.11	87.06	126.05	78.50
Reference(1999)	16.92	42.43	128.44	89.26	131.27	82.86

The MAD based regression of the no-change pixels shows for all image bands of the two LANDSAT scenes higher regression coefficients and lower RMSE values than regression line based on the PIF pixels, as Table 5.5 and Table 5.8 show. The mean pixel intensities of the no change pixels for the PIF and MAD approach are shown in Table 5.6 and Table 5.9. Generally the mean values after the image normalisation in both approaches are well represented. The variances of the no change pixels in both normalisation approaches are slightly underestimated.

Comparison of the plots in Figure 5.2 and Figure 5.3 clearly show a more scatter in the no-change pixels for the PIF method corresponding to lower correlations as seen in Table 5.5 and Table 5.8.

The MAD based normalisation and the PIF based normalisation technique generally produce comparable results. The regression parameters on the no change pixels are slightly better represented in the MAD based approach. Due to its completely automatic operation, and because it is parameter free and fast, the MAD based normalisation technique was favored. All relative radiometric normalisations with this work were performed with this technique. Since an OLS assumes that one parameter is independent and the other is dependant, which is in the case of a relative normalisation not given, (Canty et al., 2003) the MAD based normalisation procedure is improved with an orthogonal regression approach.

The reliable normalisation offers numerous advantages in change detection or consistent time series analysis (see chapter 7).

Image mosaic

An image mosaic of 5 different LANDSAT ETM+ scenes with 25m pixel resolution, each acquired in May 2000 (see Table 5.3), was generated for the Dra catchment and used as basis for an image classification (as shown in Figure 2.1). The images

were chosen within the same month (May 2000) and to minimise cloud coverage and atmospheric noise. The center scene of path/row 201/39 was used as the master scene in the image normalisations. Areas in the image overlap zones of the adjacent scenes (see Figure 5.1) were used to calculate regression coefficients, that were applied in a second step to the whole sub-scene. The overlapping areas were chosen to represent the the surface variability within the image scenes.

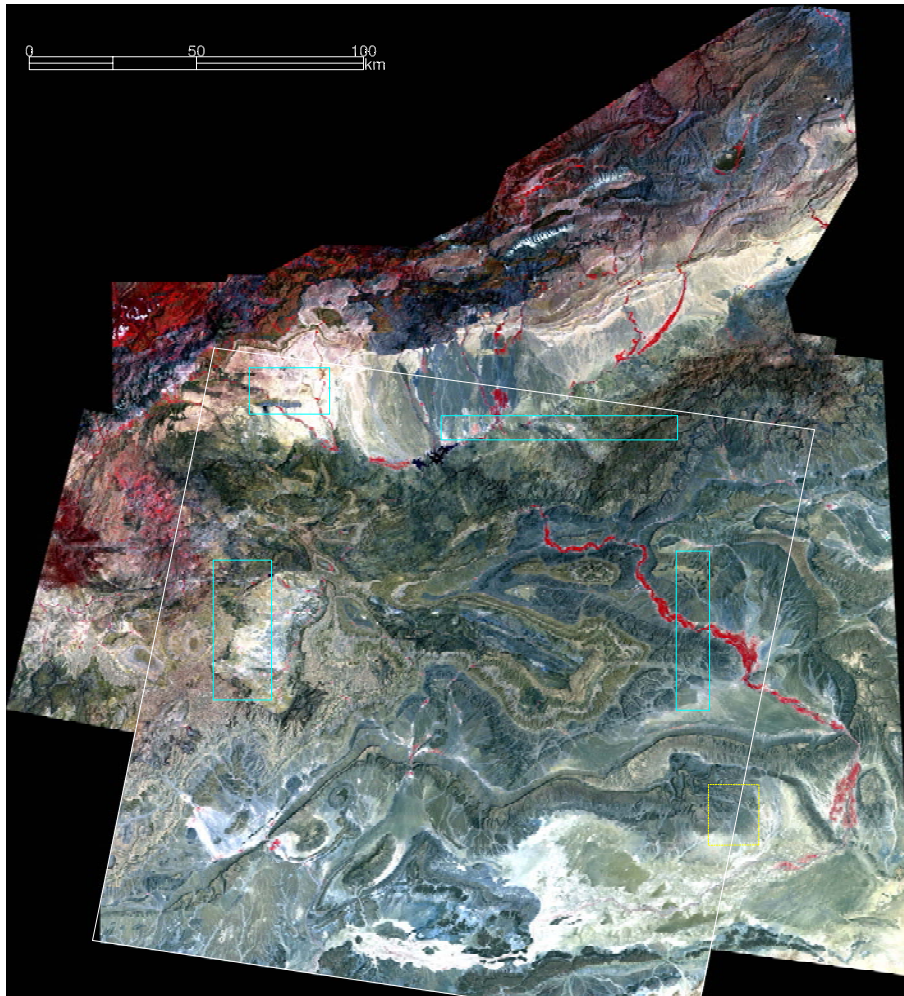


Figure 5.4: LANDSAT ETM+ mosaic from May, 2000. The cyan rectangles indicate the overlap areas used for the relative radiometric normalisation, in white is the extent of the center scene 201-39 displayed. In yellow is an example area marked as shown in Figure 5.5

Regression coefficients of $1/3$ of the MAD based no change test pixels and the size

of the overlap areas are shown in Table 5.11.

Table 5.11: Regression of test pixels of the MAD normalisation within the representative overlap areas with scene 201/39 of the image mosaicing

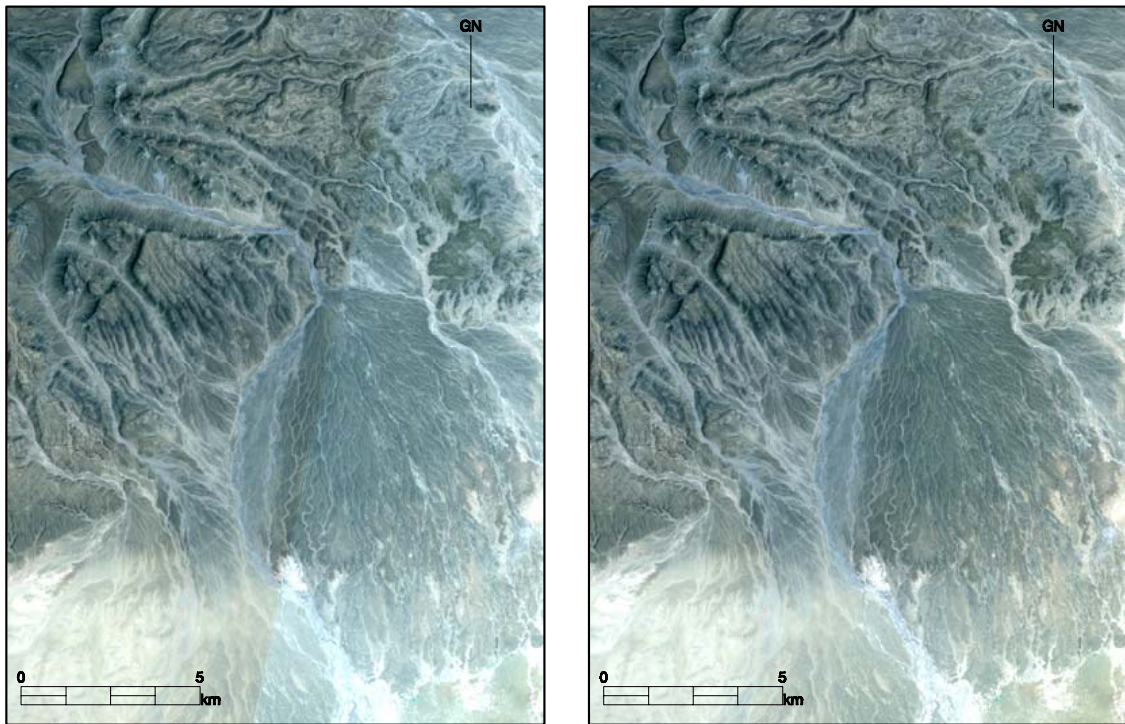
scene	200/39	201/38	202/38	202/39
band 1	0.9880	0.9995	0.9841	0.9880
band 2	0.9882	0.9999	0.9879	0.9882
band 3	0.9878	0.9998	0.9901	0.9878
band 4	0.9888	0.9997	0.9921	0.9888
band 5	0.9810	0.9997	0.9610	0.9810
band 6	0.9531	0.9999	0.9862	0.9531
band 7	0.9817	0.9996	0.9845	0.9817
overlap area	412×1907	2831×295	961×559	412×1907
nr. of test pixels	4571	69550	8887	4571

The regression coefficients of the single scenes with the master scene (201/39) are generally high, indicating a good fit especially with the scene 201/38. Both images were recorded at the same overpass, but delivered with different gain and offset values.

Figure 5.5 (next page) shows an example of two adjacent paths (201-39 and 200-39) dating from May 02, 2000 and May 25, 2000. In the left image the non-normalised scenes were mosaiced; in the right image a normalisation was performed prior to the mosaicing. Real changes in the surface reflectance result from rainfall prior to the recording of the 2nd scene.

5.3.2 Absolute calibration

Dimensionless DNs of satellite imagery represent the radiation recorded at the sensor. The calculation of parameters where absolute values, or the multitemporal comparison are of interest, such as the NDVI or other indices and band ratios, require that the data are transformed to the same units e.g. at-sensor radiance (referred to as RAD) in units of $\frac{W}{m^2 sr}$. The conversion from DNs to RAD is usually possible by applying a linear formula (Richards and Jia, 1999; Lillesand and Kiefer, 2000).



a) Image mosaic without normalisation

b) Image mosaic with normalisation

Figure 5.5: Example of an image mosaic of two adjacent LANDSAT ETM+ scenes: paths-row 201-39 and 200-39 dating from May 02, 2000 and May 25, 2000. The image examples are both stretched linear.

The conversion to unitless planetary reflectance (referred to as REF) or albedo requires the consideration of atmospheric effects at the time of the image acquisition (Kaufmann, 1989; Rahman and Dedieu, 1994). A method to derive REF values for relatively clear LANDSAT or IKONOS scenes is outlined in the following, based on NASA (2001); Fleming (2001). The path through the atmosphere is, within this approach, assumed to be without modulation. This huge simplification of the photon interactions and the complex atmospheric physics can be interpreted as a simple estimation of the surface reflectance. For a more accurate derivation of surface parameters is a calibration including the atmospheric conditions necessary. The conversion was applied to IKONOS-2 data and a test data-set of LANDSAT TM/ETM+ data in order to reduce the inter-scene spectral differences due to varying illumination conditions in different days of the year.

IKONOS

Coefficients for the calculation of RAD were in the case of 11 bit IKONOS-2 data applied, as proposed by SI (SpaceImaging, 2002):

$$RAD_i = \frac{DN_i}{calcoef_i}$$

where i stands for the spectral bands (Table 5.12).

Table 5.12: Coefficients for DN to at sensor radiance for 11bit IKONOS-2 data (SpaceImaging, 2002)

Band	1 (blue)	2 (green)	3 (red)	4 (near infrared)
Value [$\frac{W}{m^2sr}$]	72.8	72.7	94.9	84.3

LANDSAT

In the case of LANDSAT data the formula for calculation of RAD is generally (see e.g. Lillesand and Kiefer, 2000):

$$RAD_i = gain_i \cdot DN_i + offset_i$$

The gain and offset values are sensor specific and change with sensor age and over different recoding intervals. Values for gain and offset are either delivered with the data itself or can be found at the web-pages of the EROS data center, or for LANDSAT ETM+ from for the specific scene meta files. The USGS delivers the coefficients for the conversion of LANDSAT ETM+ scenes with LMIN and LMAX values NASA (2001), as shown in Table 5.13. The calibration expression is:

$$RAD_i = \left(\frac{LMAX_i - LMIN_i}{255} \right) \cdot DN_i + LMIN_i \quad (5.9)$$

Table 5.13: Calibration coefficients for LANDSAT ETM+ data [$\frac{W}{m^2sr}$] (from NASA, 2001)

Band	Before July 1, 2000				After July 1, 2000			
	Low Gain		High Gain		Low Gain		High Gain	
	LMIN	LMAX	LMIN	LMAX	LMIN	LMAX	LMIN	LMAX
1	-6.20	297.50	-6.20	194.30	-6.20	293.70	-6.20	191.60
2	-6.00	303.40	-6.00	202.40	-6.40	300.90	-6.40	196.50
3	-4.50	235.50	-4.50	158.60	-5.00	234.40	-5.00	152.90
4	-4.50	235.00	-4.50	157.50	-5.10	241.10	-5.10	157.40
5	-1.00	47.70	-1.00	31.76	-1.00	47.57	-1.00	31.06
6	0.00	17.04	3.20	12.65	0.00	17.04	3.20	12.65
7	-0.35	16.60	-0.35	10.93	-0.35	16.54	-0.35	10.80
8	-5.00	244.00	-5.00	158.40	-4.70	243.10	-4.70	158.30

NASA (2001); Fleming (2001) describe a correction of the differing illumination and reflectance conditions for images acquired on different dates of the year. Their approach to the conversion to REF is:

$$REF_i = \frac{\pi \times RAD_i d^2}{E_{sun_i} \times \cos(\varphi_s)} \quad (5.10)$$

with d = earth-sun distance in astronomical units (see Iqbal, 1983), E_{sun_i} = mean solar exoatmospheric irradiances as shown in Table 5.14 φ_s = solar zenith angle in degrees.

Table 5.14: Coefficients for the exoatmospheric irradiance for LANDSAT ETM+

Band	1	2	3	4	5	7
Value [$\frac{W}{m^2 sr}$]	1969.00	1840.00	1551.00	1044.000	225.70	82.07

Canty et al. (2003) have demonstrated with a time series of LANDSAT TM data acquired over Nevada, that the relative normalisation of the multitemporal data results in a better comparability as with the absolute calibration formula as proposed by NASA (2001); Fleming (2001). The TM data used in their study were recorded with identical gain settings, so that for purposes of comparison Equation 5.9 was not applied and only the earth sun distance and the solar zenith angle were considered, which simplifies the conversion formula to

$$DN'_i = DN_i \times \frac{d^2}{\cos(\varphi_s)}. \quad (5.11)$$

Figure 5.6 shows a plot of the mean DN values averaged over all non-thermal image channels.

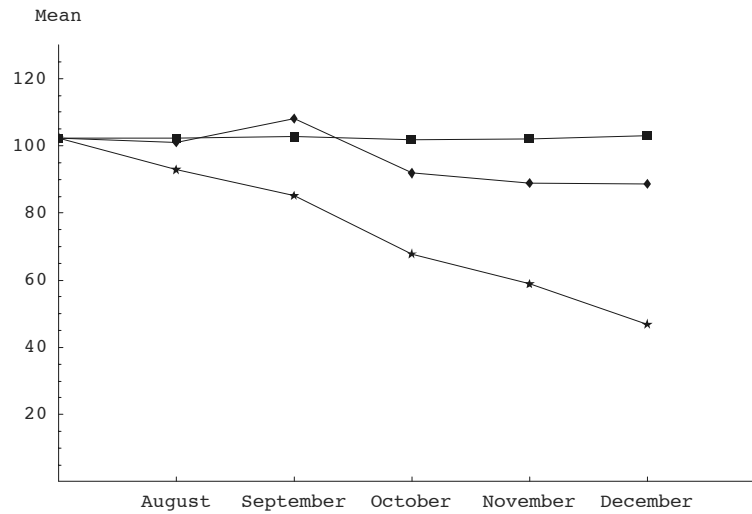


Figure 5.6: Unnormalised (stars) and normalised (boxes) mean pixel intensities (in DN) for six Landsat TM images over Nevada from July to December, 1991. The July image was taken as reference. The diamonds are the unnormalised mean values corrected for sun elevation and earth-sun distance (see text), adapted from (Canty et al., 2003)

Figure 5.6 clearly shows that the normalisation considering the earth sun distance has an effect on the data values towards a reduction of the illumination effects (diamonds), but the MAD based normalisation (boxes) results in an improved normalisation of this time series.

NOAA/AVHRR

Data, recorded from the AVHRR sensor, were converted to planetary reflectance and brightness temperature with built-in routines of TERASCAN (Seaspace, 2000). Cloud detection and the masking of the latter are based on the algorithm of Saunders and Kriebel (1988). Generally cloud detection can differentiate between, land, water and clouds/snow. Confusions of detected clouds and snow were of not relevance, therefore that both themes were masked out. NDVI datasets were produced on the basis of this geometric and radiometric corrected datasets. The NDVI data were reduced to 10 day and monthly composites using the maximum value composites (see e.g. Dech, 1997).

Following the approach of Sobrino and Raissouni (2000), who analyzed NOAA/AVHRR data of Morocco, the land surface temperature (LST) was calculated from brightness

temperature, with a standard error of $0.6K$ (due to their analysis) as follows:

$$LST = 1.40(T_4 - T_5) + 0.32(T_4 - 5_5)^2 + 0.83$$

where T_4 and T_5 are brightness temperatures recorded by the AVHRR channels 4 and 5.

The NOAA/AVHRR data processing is fully automatic, but inspection of the scenes is necessary as a quality control. With a developed processing chain of Terascan scripts organised in a UNIX c-shell environment products were generated that could be used for analysis. The data were used for the generation of a land cover map of Morocco on the basis of monthly composites. This study was performed in the framework of the IMPETUS project and was related to the Masters thesis of Dominik Vogt (Vogt, 2002). The resulting map is a regionalisation of the NOAA/AVHRR IGBP land cover classification. The generation of composites of less than monthly resulted, due to the infrequent data coverage, not in products suitable for analysis on sub-pixel level. The processed data were intended for the analysis of the vegetation dynamics of land cover types in the Dra valley. For this reason a time series of NDVI and LST data from January 01, 2000 to July 30, 2002 was processed. The Terascan processed data have an inherent positional accuracy between 0.5 and 2.5 pixels, but in extreme cloudy scenes even worse (see subsection 5.2.2).

Figure 5.7 shows an example of monthly NDVI data calculated from calibrated (RAD) AVHRR data and the positional shift in the time series data near the town of Zagora. For comparison an accurate geometrically corrected MODIS NDVI image product (see USGS, 2003b, for further description), as obtained from NASA (NASA, 2002b) and projected (see NASA, 2003b) to the UTM projection used in this study (see subsection 5.2.1), is displayed.

The width of the Dra oasis near the town of Zagora is at the widest $\approx 6km$ (see Figure 5.7). In this area, with a clear difference between vegetated and non-vegetated areas, a positional shift is visible in some months. This is unsuitable especially for a sub-pixel analysis of smaller vegetation patches. In the nine month shown only three (8/00, 3/01 and 4/01) have an adequate geometric correction. The higher cloud coverage in the winter month at the coastline, the distance of the Dra catchment from the coastline and the elevation of the High Atlas mountains all negatively influence the the position accuracy. Due to the low data coverage only a limited number of scenes were for the generation of composites available so

that dropping of poorly navigated scenes would have caused data gaps of almost the whole season (see Figure 5.7). These circumstances led to the decision that the data quality for was inadequate for an analysis of the dynamic behavior of land cover classes derived from a LANDSAT image classifications (see chapter 6). MODIS comprises with the 250m NDVI dataset, a highly accurate geometric corrected data with an positional accuracy of about 50m at nadir (Wolfe et al., 2002). This data seems more suitable for the integration of spatial high resolution data and potentially for a subpixel analysis. Figure 5.8 demonstrates the spatial relationship between NDVI data calculated from calibrated (RAD) LANDSAT ETM+ and MODIS data.

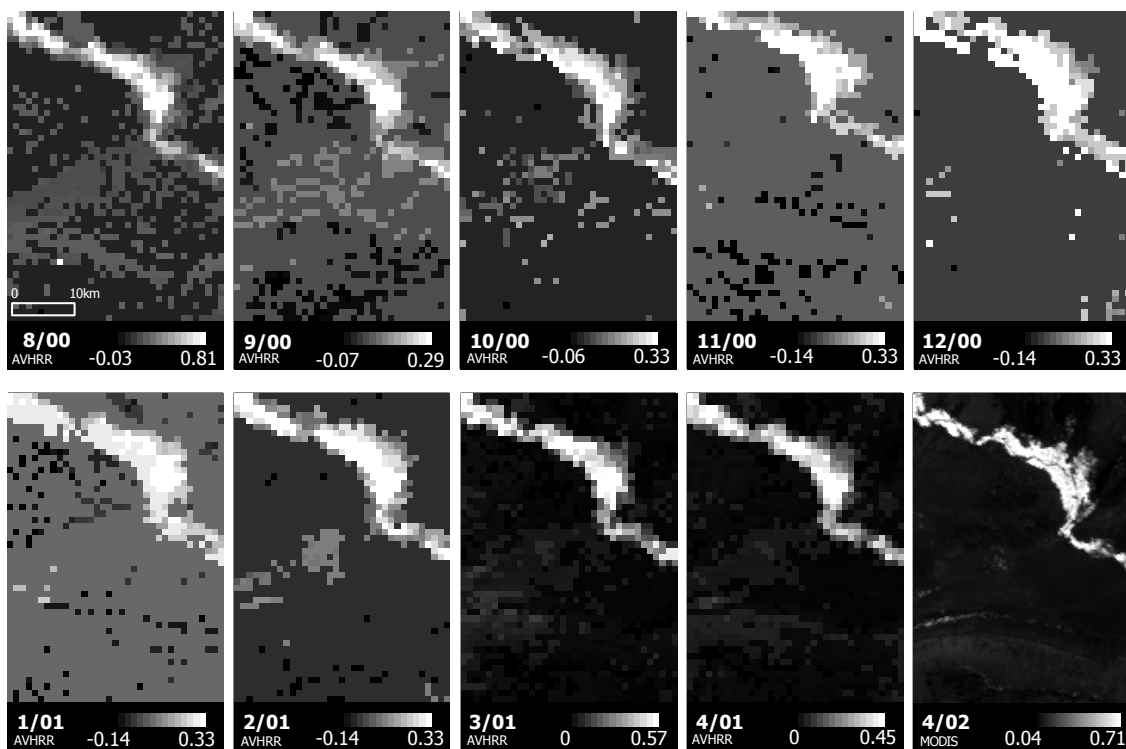


Figure 5.7: Examples of NDVI MVC composites of the oasis of Zagora from monthly AVHRR and 16 day MODIS data (indicated is month/year)

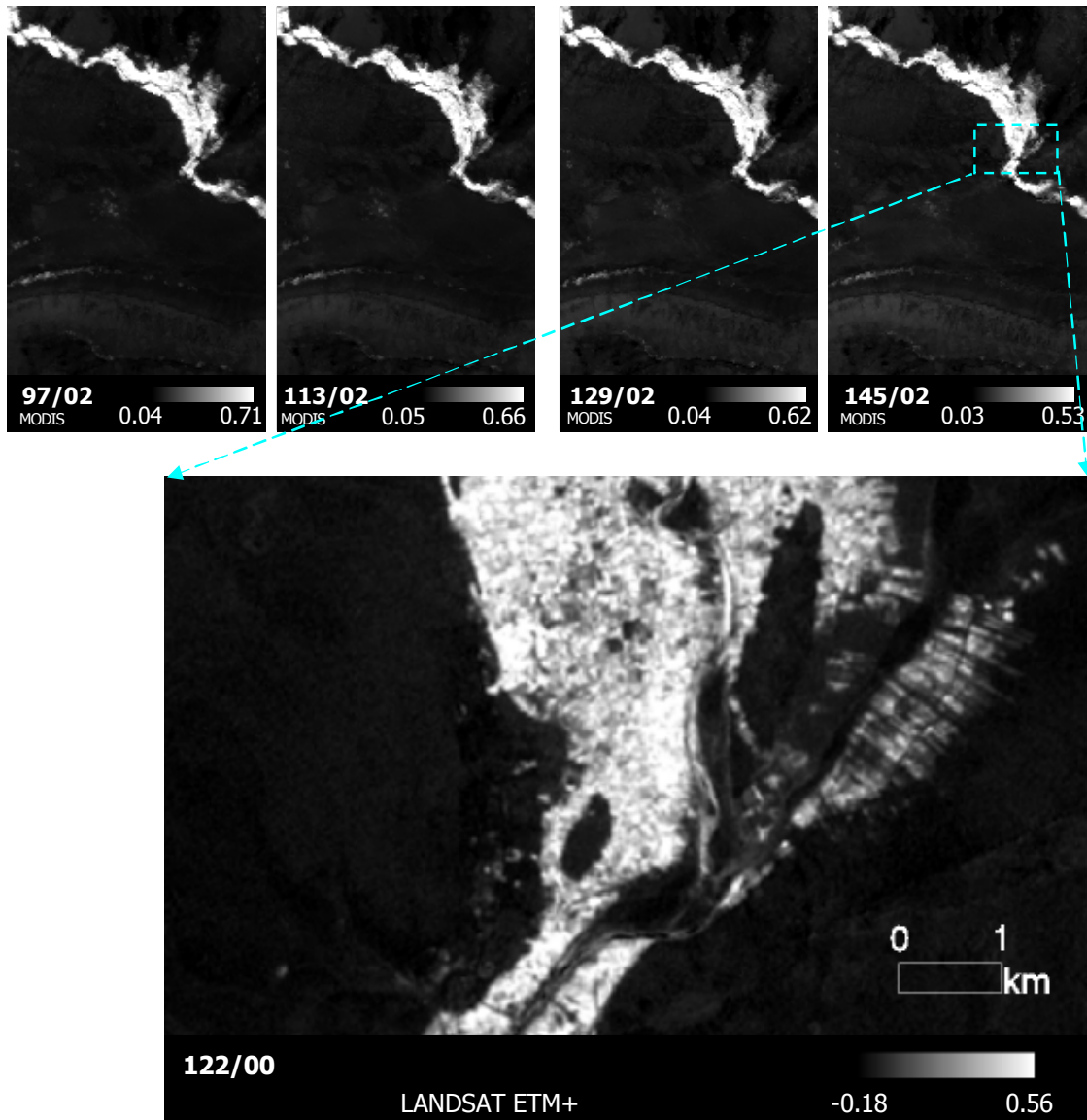


Figure 5.8: Examples of NDVI MVC composites of the oasis of Zagora from 16 day MODIS data and a single day NDVI image of the ETM+ sensor (indicated is the day/year)

5.4 Illumination and terrain correction

In flat areas with lambertian surfaces reflectance properties represent the pixel intensities of the surface. Reality shows that this ideal condition are the exception (Leroy and Roujean, 1994). Different surfaces types result in different mostly non-

lambertian surface reflectances, so that the varying illumination conditions need consideration. Bidirectional reflectance distribution functions (BRDF) are an attempt to model these effects (Deering, 1989). While BRDF effects are less pronounced with high resolution data such as LANDSAT due to the low swath angle. With increasing image resolution terrain induced modulations become more important. Relief effects are severe and directly visible in the satellite image if parts of the image are shaded. The correction of topographic induced shade requires a DEM in the same (or even better) pixel size than the satellite image. A DEM of insufficient quality causes a correction algorithm to introduce errors in these image areas. Several approaches to correct for relief effects have been used (Smith et al., 1980; Civco, 1989; Parlow, 1991; Banko, 1997; Gu and Gillespie, 1998; Fahsi et al., 2000; Herold et al., 2000). These algorithms are based on the cosine, c , Mincart correction or the approach of Civco (1989) and modifications of these. All of which utilise correction factors based on slope and aspect values of a DEM (Mather, 1999). These corrections work in moderate reliefs. Figure 5.9 shows an example where the algorithm of Civco (1989) was applied. The approach corrects for terrain induced illumination differences due to the integration of the shaded relief as calculated from slope and aspect values of a DEM under the same sun illumination as the satellite data are acquired:

$$DN'_{\lambda ij} = DN_{\lambda ij} + DN_{\lambda ij} \frac{MS - X_{ij}}{MS}$$

,

where X = pixel value of the shaded relief, MS = mean value of the entire illumination model (see Civco (1989)). λ represents the wavelength and ij the pixel position in a 2D image array. Figure 5.9 shows the result of this approach in the area where the Dra breaks through the Crystalline Anti Atlas.

The correction alters the pixel values in the center of the shaded area, see Figure 5.9 b). The image parts where the shadow reaches the sun faced slope on the opposite wall are not further corrected. This is due to the circumstance, that these areas are not considered as shaded by the shaded relief or any other algorithm that only used slope and aspect values (see 3D view in Figure 5.9). Thus are these areas not corrected adequate. Shaded image parts with low slopes seem with the applied coefficients to underestimate the correction. Civco (1989) introduced for this reason a correction coefficient C_λ , which was not generated after the general lack of the method became obvious. This example shows the need for improved illumination

correction algorithms in steep terrains, such as the Crystallin Anti-Atlas and the High Atlas Mountains. An integration of the true shaded relief including parameterisations of diffuse and direct radiation seems in this case more promising, as recently proposed by Schmidt (2003). The development of improved correction algorithms was not further preserved, because that no DEM in adequate quality was available for the whole catchment.

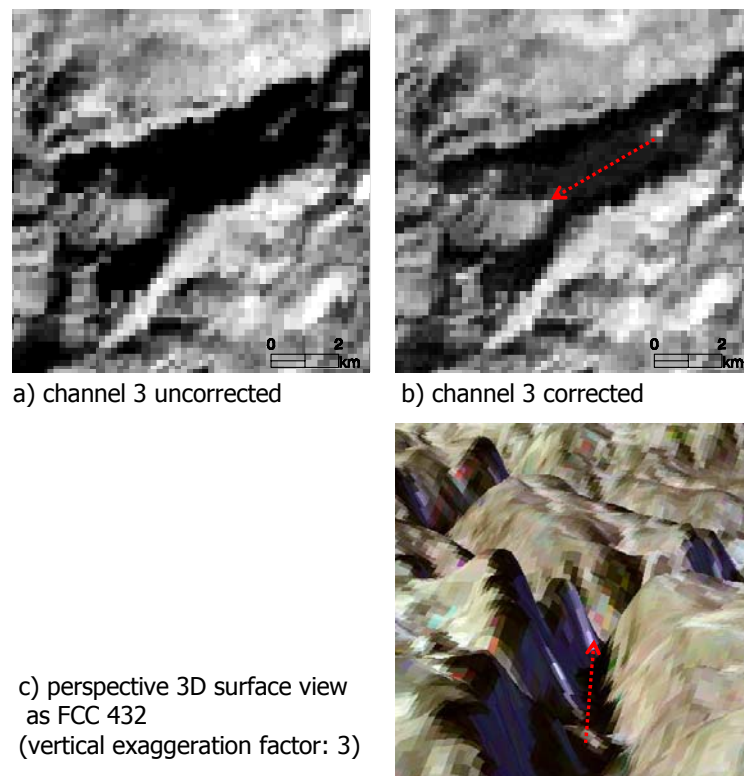


Figure 5.9: Raw a) and illumination corrected b) LANDSAT ETM+ channel 3 with the approach of Civco (1989). The arrow in c) indicates the view direction indicated in b) in a 3D view

5.5 Discussion

In combination with the generated orthophoto-maps of ASTER data in chapter 4, the integration of an automatic algorithm for GCP generation and image matching algorithm is a big step forward toward the improvement of the geometric accuracy and automation of high resolution data. The implementation of these algorithms in

either the standard photogrammetric or remote sensing software packages would be advantageous.

The results of the relative radiometric normalisation obtained with the PIF approach are of high quality, because during field campaigns data were especially obtained for this purpose. This manual and time consuming process can be avoided by the new, reliable and fast MAD based algorithm for relative radiometric normalisation. This full automatic approach is sensor independent and works slightly better than the PIF approach, and is thus a significant improvement as it operates fully automatically and operator independent. This is especially an improvement if PIFs were not obtained carefully during field visits or not available for historic data.

For the overall project requirement to classify the land cover of the whole Dra catchment on the basis of a LANDSAT image classification was assumed, that either image classifications could be performed scene by scene and by merging the results afterwards or that this step could potentially be achieved with a decent radiometric normalisation in one step on one image mosaic. For this reason the generation of the radiometrical corrected image mosaic was a crucial improvement.

A further data improvement, especially of the relief induced shades, might be obtained by the incorporation of a better relief correction algorithm, potentially in combination with BRDF corrections as proposed by Gu and Gillespie (1998). A prerequisite for an operational algorithm is the availability of DEM in decent quality for the whole catchment. For the image classification process (see next chapter) were shaded pixels masked.

Due to the better geometric correction of the images, MODIS seems to be the better dataset compared to AVHRR data for the analysis of dynamic surface processes. But for historic data and long time series, NOAA/AVHRR data are valuable dataset. Improvements of the AVHRR data processing can potentially result from better navigation algorithms and a better data coverage of the Dra catchment. Data integration and the dynamic behavior of surface variables, such as vegetation coverage or salinisation processes are substance for further research in the follow up phase of the IMPETUS project starting in May 2003.

5.6 Conclusion

A precise geo-information of map products determines the quality of cartographic documents and is important for (geo-) data integration in a (GIS-) database. This goal could be achieved by the registration of topographic maps on scale 1:100000, the generation of CORONA and ASTER orthophoto-maps and co-registration of LANDSAT or IKONOS data to this base material. All spatial data were transformed and geometrically corrected to a common reference system: a UTM projection of Zone 29 with the local common spheroid CLARKE 1880 and datum Merchich. Multitemporal LANDSAT data were geometrically corrected and co-registered by the usage of an automatic GCP generation tool (CDSAT). The autonomously generated points were integrated in the geometric correction process in ERDAS Imagine and resulted in more reliable GCPs and better point distribution, especially in the rural areas.

In contrast to common image mosaicing algorithms, an image mosaic was generated where not e.g. the histograms were matched for a nice presentation: a radiometric consistent mosaic over large scale for further mapping and image classification was applied to 5 LANDSAT scenes. The MAD based relative radiometric calibration method makes a data calibration with linear values as gain and offset coefficients superfluous, which is not only convenient, but also makes scene comparison possible even if these values are not available or wrong. This normalisation technique can be applied for the generation and comparison of consistent data time series.

The discussed pre-processing steps for the high resolution LANDSAT data are a major improvement of the existing pre-processing techniques towards a (semi-) automatised image pre-processing in a high data quality.

6 Vegetation classification in an arid environment

”The overall objective of image classification procedures is to automatically categorize all pixels in an image into land cover classes or themes”
Lillesand and Kiefer, 2000

This study aims to derive a vegetation- and land cover/land use map. In order to achieve this the surface needs to be classified, which poses a problem for the sparsely vegetated rangelands. A question that inevitably arises when mapping vegetation using optical remote sensing data in arid or semi-arid regions is: to what degree is green vegetation detectable and how to distinguish it?

Siegel and Goetz (1977) have demonstrated that significant changes in the reflectance characteristics require a vegetation cover of more than 10% and that a vegetation signal tends to become more important than the soil signal with a vegetation coverage of more than 30%. Hill (2000) proposes that this does not mean that vegetation coverages of less than 30% are not detectable by remote sensing. They also state that ratio based vegetation indices do not provide the best estimates. Vegetation estimates under the spectral unmixing paradigm provide better estimates of the true vegetation coverage (Smith et al., 1996; Hurcom and Harrison, 1998; Hill, 2000).

Classification methods generally produce discrete information classes from input data. In remote sensing, spectral signatures of different materials in one or more spectral bands are recorded by a sensor and stored as image pixels. The spectral bands span the so called feature space, in which each pixel represents the spectral signal of an observed surface area. One assumption in the analysis is that similar surfaces induce a similar spectral response pattern (Campbell, 1996). Unsupervised classification algorithms identify autonomous clusters of signatures within the feature space. These methods can be used to locate areas with similar spectral

properties without *a priori* terrain knowledge. Supervised classification methods require *a priori* terrain knowledge and the specification of representative areas of the various land cover types in a scene (Lillesand and Kiefer, 2000). One advantage is that an operator can concentrate on the land-cover classes of a particular interest (Lillesand and Kiefer, 2000). Jensen (1996a) differentiates supervised classification methods into three categories:

- **hard classifiers** which are classically single stage classifiers with a one-pixel-one-class relation e.g. the Maximum Likelihood Classifier (MLC),
- **sub-pixel** or **soft classifiers** which compute one or more channels with fuzzy class membership grades e.g. with ranges [1..0]. In a second step the real (fuzzy) classification occurs due to a set of decision rules,
- **hybrid classification** which includes existing classifications as well as ancillary information e.g. hydrological maps or a DEM in the classification process.

Hard classifiers require that class memberships are clearly defined and that only one theme, either a land cover/land use class or an object, is allowed at one pixel (Maselli et al., 1996; Hung and Ridd, 2002). This is true if all pixels are smaller than the targets to be classified. In other cases the problems of mixed pixels arise (Lillesand and Kiefer, 2000). These problems are addressed by soft classifiers, through which further class differentiation is possible. Soft classifiers evaluate and utilise uncertainties in class differentiation (Eastman and Laney, 2002): the spectral information is first transformed into a set of membership grades or fuzzy sets rather than discrete classes, together with an error term (e.g. see Equation 6.2). These layers can potentially be interpreted as thematic information (see subsection 6.1.2). By incorporating knowledge based decisions, fuzzy rules can help to optimise the identification of the surface objects and land-cover classes by their grade memberships of different surface components (Eastman and Laney, 2002). Hybrid classifiers may combine all kinds of spatial GIS-information layers to derive, according to the knowledge of interdependence of the available information layers, a set of classification rules.

In hybrid classifications, satellite derived Vegetation Indices (VI) (see Purevdorj et al., 1998; Jensen, 2000, for further discussions), soil descriptions or band ratios are often used to assess certain surface components as information sources. The fact that either soil influences VIs, especially at low vegetation coverage, or that natural

vegetation can mask or significantly alter the spectral ground response, makes the development of separate vegetation and soil related indices difficult. It seems more natural and promising to utilise dedicated spectral decomposition techniques to derive this information in one step e.g. by spectral unmixing techniques (Hill, 2000). Spectral unmixing, like other (sub-pixel) classifiers, describes spectral data in terms of membership grades to a cluster or a reference spectrum. These membership grades can be interpreted as fuzzy sets (see Figure 6.5 for more details). A complex of rules that emulate the decision process of human experts in form of procedures are called **expert systems** (see Wharton, 1994, for further discussion). Expert systems generally include three major components: a knowledge base, a rules interpreter and a memory (Wharton, 1994). Hung and Ridd (2002) use if-then-else clauses in an expert system based on sub-pixel classifier information. Penaloza and Welch (1996); Metternicht (2001) use the term fuzzy expert system for image feature selection by implemented decision rules based on fuzzified descriptions of cloud and land surface parameters. According to this discussion, within this study an expert system was implemented based on fuzzy descriptions of the feature space derived by spectral unmixing, and including auxiliary information layers. The approach is discussed in detail in the following section.

6.1 Methods

6.1.1 Combined classification approach and materials

Figure 6.1 depicts an overview of the classification process used in this study, displayed in the form of a flow-chart. The individual methods referred to in the overall approach in Figure 6.1 are described in detail in the following subsections. The LANDSAT ETM+ image mosaic from May 2000 as described in section 5.3 was utilised as data source for the image classification of the Dra catchment.

The backbone of the classification procedure is a Linear Spectral Unmixing (LSU) technique (see subsection 6.1.2). If photons interact with only a single component (e.g. sand) then is this a pure spectrum within the IFOV. A set of "pure" spectra need to be identified to account for the image inherent surface variability. These pure spectra are referred to as endmembers (Adams et al., 1986, 1995; Roberts et al., 1998; Hill, 2000). Endmember spectra should potentially be identified at the edges of a multidimensional scatter-plot. Price (1994) also refers to spectral unmixing as

”end points analysis”. Linear combinations of this set of pure spectra are used in the LSU to model in a mixture space all other spectra in terms of fractions of the pure spectra. Figure 6.3 illustrates this concept theoretically while in Figure 6.16 an example of the Dra valley is given.

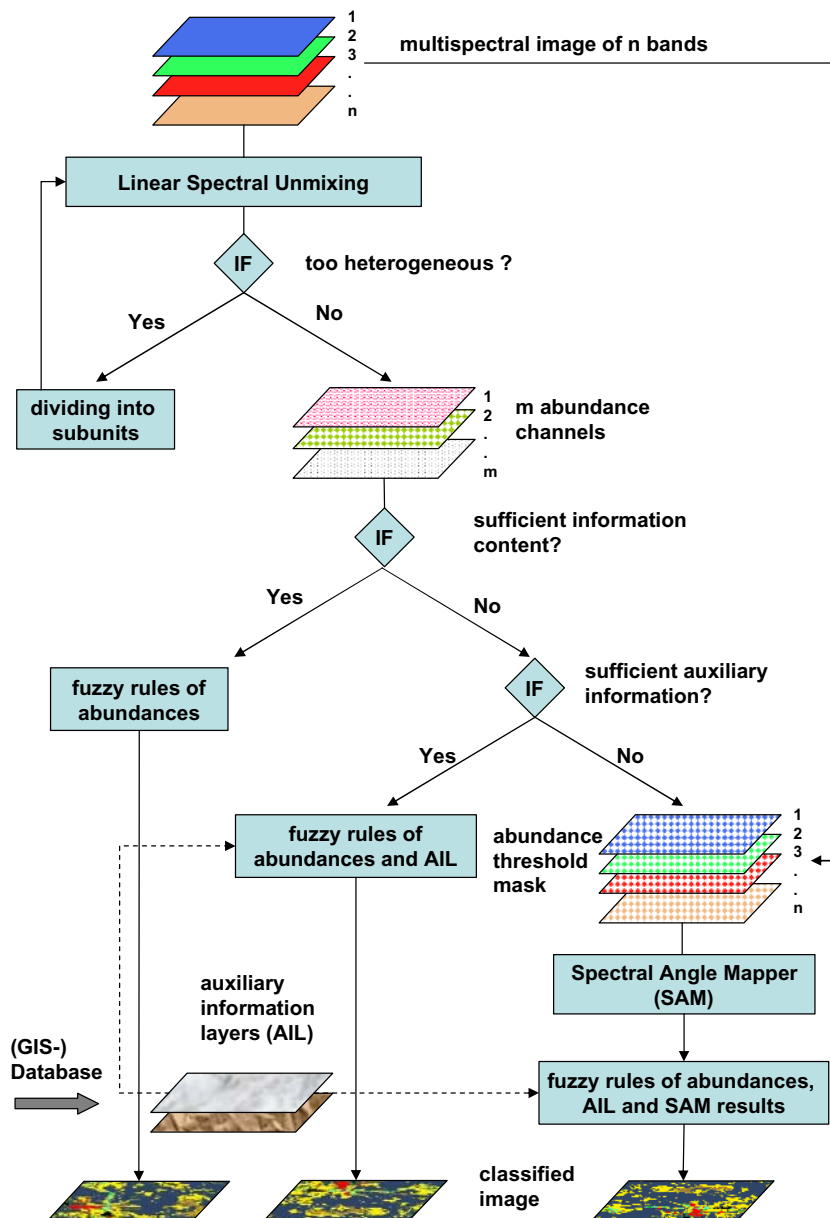


Figure 6.1: Flow chart of the combined classification procedure for the generation of a (monotemporal) land cover map of the Dra catchment (explanation in the text)

The number of endmember spectra normally can not exceed the number of bands plus one (Hill, 1998). Identifying a suitable set of endmembers for an acceptable image decomposition is a trial and error process. If the surface variability of the image to be classified is too high no suitable set of endmembers for an LSU can be identified, resulting in incorrect abundance values and high RMS errors (see subsection 6.1.2). In this case a reduction of the feature space was performed (e.g. see subsection 6.2.2). The catchment was, in a first step, segmented in sub-regions of similar geological and ecological conditions resulting in six PMUs of similar dominating tonality, patterns and texture (see section 2.1). The LSU of the individual sub-units resulted in improved surface descriptions. For the classification of the whole catchment separate classifications of the six sub-regions were performed and then merged afterwards. A prerequisite for a consistent classification of the catchment is a classification scheme for the whole catchment, as described in Table 3.1. If the heterogeneity within the sub-regions was still too high the sub-regions were further subset following the same principle (see first IF statement and loop in Figure 6.1).

If LSU resulted in a satisfying solution (expressed by a low RMS error) fuzzy decision rules for class discrimination were formulated and applied with programmed codes in ENVI/IDL (e.g. see subsection 6.2.1). Non-vegetation abundances were utilised to describe the soil layer (referred to as background information), according to the land-cover classification scheme (Table 3.1), while vegetation is referred to as foreground information.

If the information content of the LSU is (still) too high for the discrimination of the desired vegetation and land cover classes, the integration of auxiliary information sources was evaluated (second IF statement in Figure 6.1), such as a river network or elevation information. Due to the lack of a complete DEM of sufficient quality, riverbeds were, in some places, digitised manually. Elevation information was either extracted from the generated ASTER DEMs (see subsection 4.2.3) or from the GTOPO30 DEM which has a $1km$ resolution. Elevation information were used to formulate vegetation class differentiation rules e.g. that *Acacia raddiana* can not grow on elevations higher than $1000m$. Due to the coarse DEM resolution and in some places, imprecise elevation information, manual changes to the DEM derived contour lines in accordance to the terrain morphology were made. The auxiliary information layers contributed in most cases to the desired vegetation differentiation (see e.g. subsection 6.2.1). If the auxiliary information content was

not available or sufficient (e.g. subsection 6.2.2), the spectral information of the vegetated surface was utilised to differentiate further vegetation classes (third IF statement in Figure 6.1).

For this reason the vegetated pixels were extracted from the vegetation abundance channel by applying a vegetation mask, so that only pixels that contain vegetation fraction above a certain, empirically found threshold, remain (see Figure 6.17). As a consequence, a segmented multispectral image was retained with only the vegetated pixels. The spectral information of the vegetated pixels was further evaluated and classified with a *second supervised classification* method: the spectral angle mapper (SAM). Reference spectra of the vegetation classes, representing the spectral compound of the surface, serve in calculating the spectral similarity, by ignoring the intensity values (length of the vector). Information from SAM, LSU and supplementary sources can be used to derive the desired vegetation class differentiation followed by post-processing steps.

6.1.2 Spectral Mixture Analysis

The term "mixed pixels" describes an effect that occurs when different surface materials or land cover types comprise the spectrum measured within satellite's IFOV. Spectral mixture analysis is based on the assumption that the spectrum recorded from the satellite is a linear or non-linear combination of each of those components (Adams et al., 1986; Roberts et al., 1998). The decomposition of a surface area within the IFOV or a pixel, into proportional abundance of a finite number of endmembers assumes that most of the spectral variation in a multispectral image can be described, in a first approximation, by additive (linear) spectral mixtures (Hill, 2000). Figure 6.2 illustrates this concept.

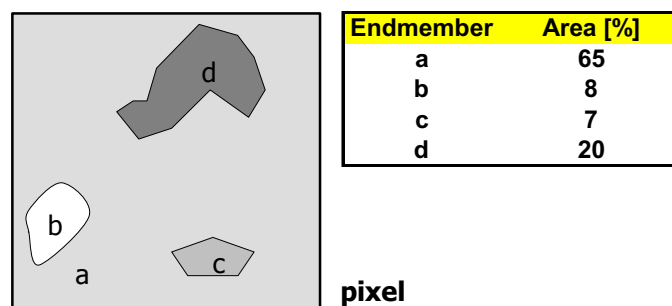


Figure 6.2: Concept of (linear) spectral mixtures

In the case of multiple scattering the mixture has the potential to be non-linear and the mixture would need non-linear mixture models (Roberts et al., 1998), which can be important for certain vegetation types (see Ray and Murray, 1996). In most applications of spectral mixtures, especially in arid and semi-arid regions, multiple scattering is assumed to be negligible (Smith et al., 1996; Adams et al., 1995; Ustin et al., 1996; Roberts et al., 1997; Hill, 2000; Elmore et al., 2000; Hung and Ridd, 2002). Gilabert et al. (2000) states that the mixture of vegetation and soil spectra tends to be more linear and that leaf spectra within a canopy have non-linear behavior. Based on these arguments, especially with respect to the sparsely vegetated areas, a linear spectral unmixing technique was used, as implemented in ENVI/IDL 3.5 with the 'sum to unity constraint', which means that the endmember fractions of each pixel sum to 1 (100%). The LSU is mathematically described by Equation 6.1 and Equation 6.2.

A mixed spectrum P_λ of a given pixel is modelled by the sum of the fractions f of the n endmembers E_i in the IFOV (Roberts et al., 1997):

$$P_\lambda = \sum_{i=1}^n f_i E_{i\lambda} + \varepsilon_\lambda \quad (6.1)$$

where λ represents a spectral band, n the number of endmembers and ε the residual term. Thus for a given set of endmembers their fractions within a pixel can be modelled. The model fit is expressed either as error in the fractions f or ε_λ at each wavelength or across all bands as global RMS error (Roberts et al., 1998).

$$RMS = \frac{1}{m} \sqrt{\sum_{i=1}^n \varepsilon_{i\lambda}} \quad (6.2)$$

where m is the number of bands. The process of the LSU creates the endmember fractions for every pixel in the image and each endmember, referred to as endmember abundance (see e.g. Hill, 1998; Eastman and Laney, 2002). The identification of potential endmembers and the choice of endmembers in this way, such that the spectra of most pixels are explained properly, is the key issue in spectral unmixing. The endmembers in the case of calibrated and atmospheric corrected satellite images can be extracted from spectral libraries data of ground measurements. An alternative to the usage of absolute calibrated data is to extract the spectra from the image itself, independent of image calibration or atmospheric correction (Adams et al., 1986). In hyperspectral data analysis, methods like the "pixel purity index" are

prominent for the identification of extreme spectra within the feature space (Boardman et al., 1995) to automatically provide an analyst with potential endmembers. Tompkins et al. (1997) propagates an endmember selection based on a principal component analysis and points out that difficulties might arise for a data scattered not in straight lines in the data space, such that an adequate endmember fit cannot be found. The reason for a manual endmember selection within this study was that if endmembers were selected automatically the decomposition did not result in endmembers that could be interpreted in a physical sense (Tompkins et al., 1997) or that were useful for the image classification. However, these tools to automatically provide potential endmembers were designed for hyperspectral data and are less useful for multispectral data (J. Hill, University Trier, pers. comm.). Therefore the endmembers were selected manually per sub-region based on terrain knowledge and extracted from the satellite image directly. The spectra were visually inspected to be at the edges of the data cloud of a multidimensional scatterplot (see Figure 6.16). The RMS error provides a measurement for how much the spectral variability was explained by the selected endmembers. Pixels with high RMS error help to identify which spectral components are not well represented in the model (Bateson and Curtiss, 1996). The quality of the LSU is dependent on the ability of the endmember spectra to represent each image pixel in a linear combination. The RMS error and ε_λ are important diagnostic tools, as Hill (2000) state that positive residuals occur when the sensor-measured spectra has higher reflectance than P_λ , indicating that P_λ contains absorption features which were lacking in the measured signature. Negative ε_λ indicate the presence of absorption features in the measured spectrum that are absent or less pronounced in the modelled spectrum P_λ . Figure 6.3 depicts an example of a three endmember modelling and the possible combination of materials in the mixture space within the LSU model concept.

Hill et al. (1994) propose a method that aims to optimise the number of endmembers, since it is not advisable in vegetation abundance estimates to simply add other background endmembers to compensate for RMS errors. Their approach is based on the assumption that the mixed spectrum of a pixel is conditioned by three primary components: "foreground" materials, "background" materials and shade. Vegetation is thus constantly the foreground material, while background materials may be different soil types, rocks or leaf litter or senescent vegetation.

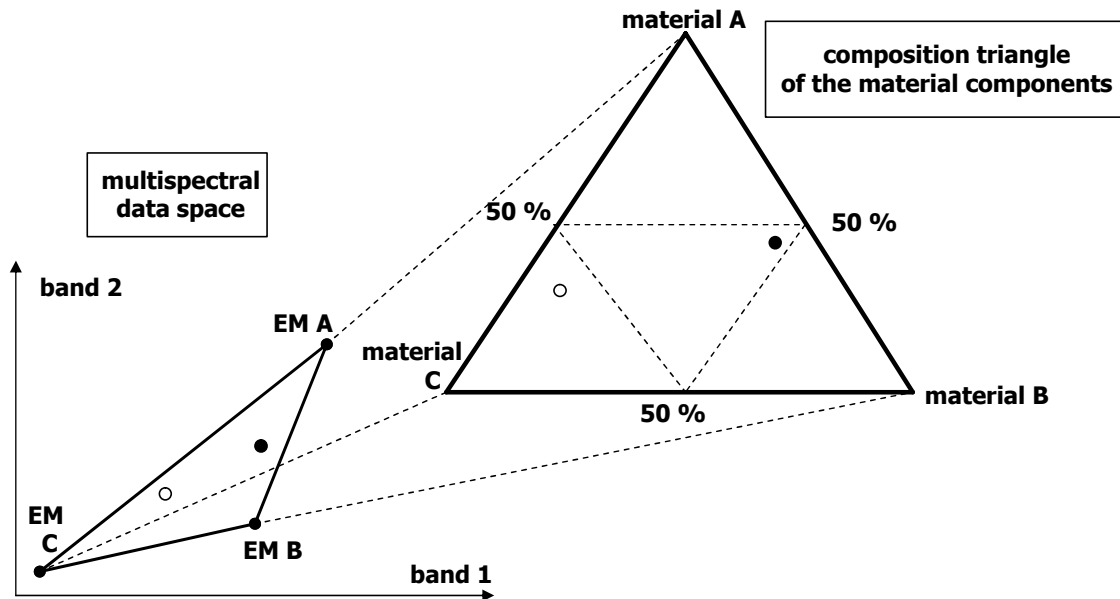


Figure 6.3: Concept of linear spectral unmixing with an example of two image bands and a three endmember (EM) mixture space. The dots represent pixels in the data and mixture space (adapted from Hill, 1998)

Following this concept a vegetation abundance channel was used as vegetation information and compared with vegetated areas as obtained during the ground truth campaigns. Endmembers were repeatedly selected and used in the LSU until the vegetation abundance matched best with the true vegetation coverage, as did the ground truth data of the background (see section 2.2). The vegetation abundance was used in combination with the non-vegetation abundances to discriminate the desired vegetation classes by formulating knowledge based decision rules e.g. by the knowledge that a species of *Tamarix aphylla* cannot grow on rock material. LSU can be used for the estimation of the abundances of certain materials within a spectrum, but it is not a classification procedure (Roberts et al., 1997; Hill, 1998). LSU decomposes the multispectral data space into layers of material abundances that can serve for a more physically based interpretation of the membership grades. For this reason decision rules were formulated based on field knowledge as shown in section 6.2.

6.1.3 Spectral Angle Mapper

The Spectral Angle Mapper (SAM) determines the spectral similarity between two spectra by calculating the angle Θ (in radians) between two spectra in the multi-dimensional data space. The angles between spectra v_1 and v_2 in an n-dimensional data space can be calculated as follows (Fischer, 1986):

$$\Theta = \cos^{-1}\left(\frac{v_1 v_2}{\|v_1\| \|v_2\|}\right) \quad (6.3)$$

Let v_1 denote the reference spectra and v_2 image spectra. By calculating the spectral angle between v_1 and v_2 smaller angles represent closer matches to the reference spectrum while the maximum angle is $\frac{\pi}{2}$. The length of the vectors is not taken into consideration (Figure 6.4). Following that the SAM is not sensitive to the signal intensity (Kruse et al., 1993), which was found to be useful in vegetation analysis due to varying vegetation density of specific classes. The reference spectra are either obtained from a spectral library in the case of calibrated data or extracted from the image itself. A 'rule image' per reference spectrum is calculated (RSI, 2002), containing per pixel the spectral angle to the reference spectrum. SAM does not require a normal distribution of training pixels, as the angle between a reference spectrum and image spectra is calculated.

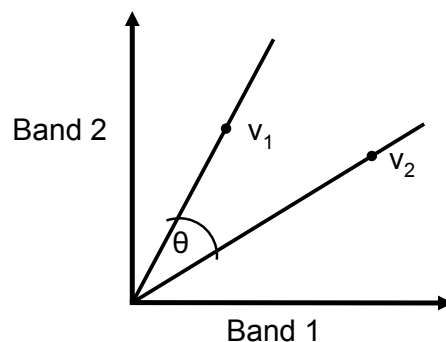


Figure 6.4: Principle of spectral angle mapping, (Kruse et al., 1993, modified)

Within this study SAM was used to differentiate between vegetated pixels. For this reason the vegetated pixels were extracted from the multispectral image by a vegetation mask and only these pixels were used in the supervised SAM classification (see subsection 6.2.2).

6.1.4 Fuzzy classification and knowledge based decision rules

”As its name implies, the theory of fuzzy sets is, basically, a theory of graded concepts - a theory in which everything is a matter of degree [..].”

H.-J. Zimmermann, 1996

The beginnings of fuzzy logic date back to the time of Plato (427-347 AC) who suspected that between the true or false of dual logic must lie a third possibility. These thoughts were later brought up by philosophers like Hegel (1770-1831). The Polish mathematician Lukasiewicz (1878-1956) developed the ”Lukasiewicz logic” in which between true=1 and false=0 additionally indifferent=0.5 is differentiated. His theories are seen as the precursors of fuzzy logic, in which he used later all real numbers in the interval [0,1]. Fuzzy sets were introduced by Zadeh (1965) to express ambiguous terms and based on inexact reasoning. (Zimmermann, 1996) defines a membership function as follows:

Definition 1: If X is a collection of objects denoted generally by x, then a fuzzy set A in X is a set of ordered pairs:

$$A = (x, \mu_A(x) | x \in X),$$

$\mu_A(x)$ is called the membership function or grade of membership of x in A that maps X to the membership space M. The range of the membership function is a subset of the non-negative real numbers whose supremum, $\sup_x \mu_A(x)$, is finite.

Thus the image abundances can be interpreted as the membership function and M can be interpreted as the mixture space. The terminology from fuzzy logic can generally be applied to the LSU results as Kruse (1993) generally stated that fuzzy logic can be applied to raster images. The constraint on the values of the membership function can be met by setting potential negative values of the LSU to zero. Definition 1 reveals that a membership function is not limited to values between 0 and 1. If $\sup_x \mu_A(x) = 1$ the fuzzy set is called normal (Zimmermann, 1996). A non-empty fuzzy set A, can always be normalised by dividing $\mu_A(x)$ by $\sup_x \mu_A(x)$. Thus, for convenience, in the following notation we generally assume we are working with normalised fuzzy sets.

A classification of the background information from the LSU was derived by applying the fuzzy ”AND” in from of the maximum operator to the background abundances (all except vegetation), while in some cases the membership function was

modified in such a way that values below a certain threshold were set to zero (see Figure 6.5 a)).

Definition 2: The membership function $\mu_C(x)$ of the union $C = A \cup B$ is defined pointwise by

$$\mu_C(x) = \max\{\mu_A(x), \mu_B(x)\} \quad x \in X).$$

In subsection 6.2.1 this concept is discussed in more detail with an example. With similar arguments results from the SAM can be interpreted as values in the interval $[0, \frac{\pi}{2}]$ are within the rule images (see subsection 6.1.3). The fuzzy "OR" or the minimum operator as defined in Definition 3 (Zimmermann, 1996), is used to assign the vegetated pixels to their respective class.

Definition 3: The membership function of the $\mu_D(x)$ of the intersection $D = A \cap B$ is pointwise defined by

$$\mu_D(x) = \min\{\mu_A(x), \mu_B(x)\} \quad x \in X).$$

The incorporation of the fuzzy theory provides the opportunity to incorporate other (fuzzy) layers of information and leads to a fuzzy classification approach as defined by Jensen (1996b). Knowledge based identification of image thresholds were used to modify the membership function, so that values above a certain threshold were set to zero (see Figure 6.5). The maximum angle up to which a vegetation spectrum should be assigned to a reference spectra was class dependently derived (see subsection 6.2.2). Figure 6.5 shows the types of membership functions used in this study and the modifications.

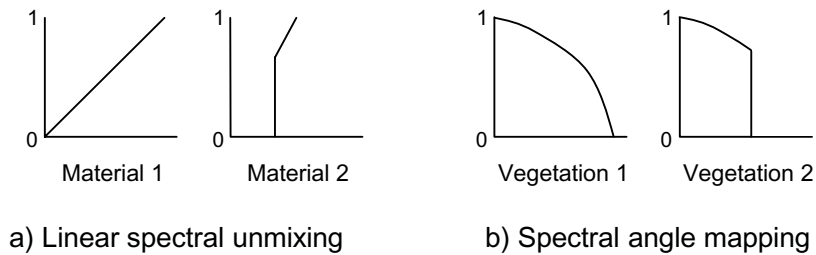


Figure 6.5: Schematic representation of the membership functions (left) and the modification (right) with a linear relationship in the LSU (a) and of vegetation spectra in SAM with a cosine-behavior (b)

6.1.5 Post-processing

The terms post processing or post classification is used here in the term of improving a classification result by the following techniques:

Object oriented class discrimination

In some cases classes are, by their pure spectral information, hard to differentiate. The neighbourhood of single pixels or their aggregation is often characteristic for class determination. For this post-classification analysis, the software package eCognition was used (Definiens, 2002). Objects as patches of a certain class can be described by fuzzy membership functions (common border length, shape/width etc.) and can be further differentiated by these attributes (Definiens, 2002; Ivits and Koch, 2002). This analysis is described in subsection 6.2.2.

Majority and minority filter

In situations where classes are lacking spatial coherence, a clumping or sieving procedures, such as a majority or minority filter, can be applied to either group neighbouring pixels or to remove isolated pixels (RSI, 2002). These procedures were only applied to non-vegetated classes such as settlements.

6.1.6 Validation

Validation of the classification is generally performed with ground truth polygons obtained during field campaigns, as described in section 2.2. The ground truth data consisting of about 2100 samples stored as point, line and polygon data were used to compile a set of 559 validation polygons according to the land cover classification scheme. Figure 6.6 shows the location of the polygons within the (sub-) catchment. Additionally 399 botanic vegetation reveals (see section 2.2 or Finckh and Staudinger (2002)) were assigned with the corresponding land cover class as an independent data source and could be incorporated in the validation dataset.

Foody (2002) briefly reviews the history of image classification accuracy assessment. In their opinion, at present the confusion matrix is the most objective way to validate remote sensing image classifications. Additionally they state that: "Indeed, the confusion matrix provides the basis on which to both describe classification accuracy and characterise errors, which may help to refine the classification or estimates derived from it.". For this reason the classified data were validated with a set of data compiled from the ground truth information in from of a confusion matrix.

6 Vegetation classification in an arid environment

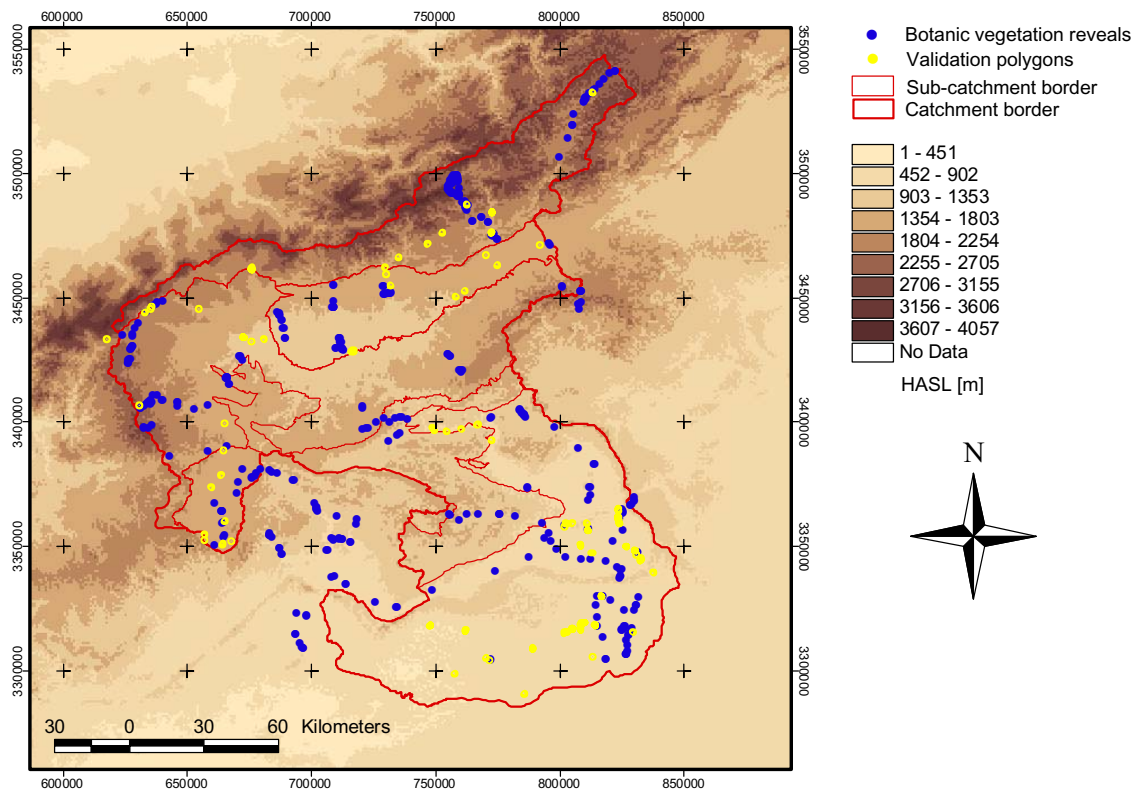


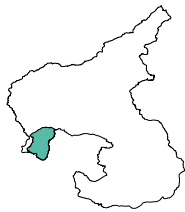
Figure 6.6: Distribution of the validation data within the Dra catchment used in the classification approach

After the first attempt at classification the confusion matrix indicated a low accuracy for the *Acacia raddiana* classes in the sparsely vegetated rangelands of the Dra valley. The growth of *Acacia raddiana* is controlled by the surplus water in linear depression lines and so they are distributed linearly rather than homogeneously. The polygons obtained during the field work were usually measured around the vegetated areas and were designed to incorporate natural variability of the vegetation. Thus, not all pixels within the validation polygons are purely vegetated and not all pixels within the polygons were identified as vegetated areas. Therefore an intersection of the vegetation mask and the validation polygons was used to derive the validation pixels in the quality assessment for classes where it is necessary e.g. the associations with thin, small leaves and low green vegetation content of the hardwood dominated *Acacia raddiana* classes (see subsection 6.2.2).

6.2 Results from the Dra catchment - South Morocco

The classifications of the sub-regions within the Dra catchment (as defined in section 2.1) are described within this section. Two sub-regions covering all methodological aspects are discussed in more detail. The Basin of Tazenakht (Region E) was chosen as an example where the abundance of information and supplementary information enabled the derivation of a land cover classification. The Dra valley (Region F) is an example of a large area mapping of a complex environment with a differentiated vegetation coverage, in which a combination of LSU and SAM was applied. The classification and validation results of all 6 sub-regions are discussed. The six classifications were merged to create one land cover classification map of the Dra catchment. The described classification was performed on the geometrically corrected (see subsection 5.2.1) and relative radiometric normalised LANDSAT ETM+ image mosaic, dating from May 2000 (see subsection 5.3.1.2). A shade mask was applied by removing pixels falling below a threshold (varying with sub-region) in band 4. In areas of bright surfaces, a saturation in channel 3 was recognised in the images and the corresponding pixels in this channel were masked out and assigned as unclassified.

6.2.1 Basin of Tazenakht



The Basin of Tazenakht is characterised by arid conditions: an annual average rainfall of 119mm , an annual average temperature of 20.3° , and potential evapotranspiration of 1600mm . With an average elevation of 1500m above sea level (Bennouna et al., 2000) the basin, with 920km^2 , is the smallest of the mapped sub-regions in the catchment. Land-use is characterised by areas of intensive agriculture, predominantly on loamy/sandy river terraces, irrigated agriculture and areas of rainfed agriculture. The rangelands are mostly overgrazed and sparsely vegetated (see section 2.1). Areas of potentially good growing conditions for natural vegetation are, in most cases, fields ploughed for seeding in case of rainfall for rainfed agriculture. The extensively used fields increase the grazing pressure for the natural vegetation on the remaining grazing ground, so that this type of agriculture is a forcing factor for land degradation. Often these fields are not used for several years in the absence of precipitation.

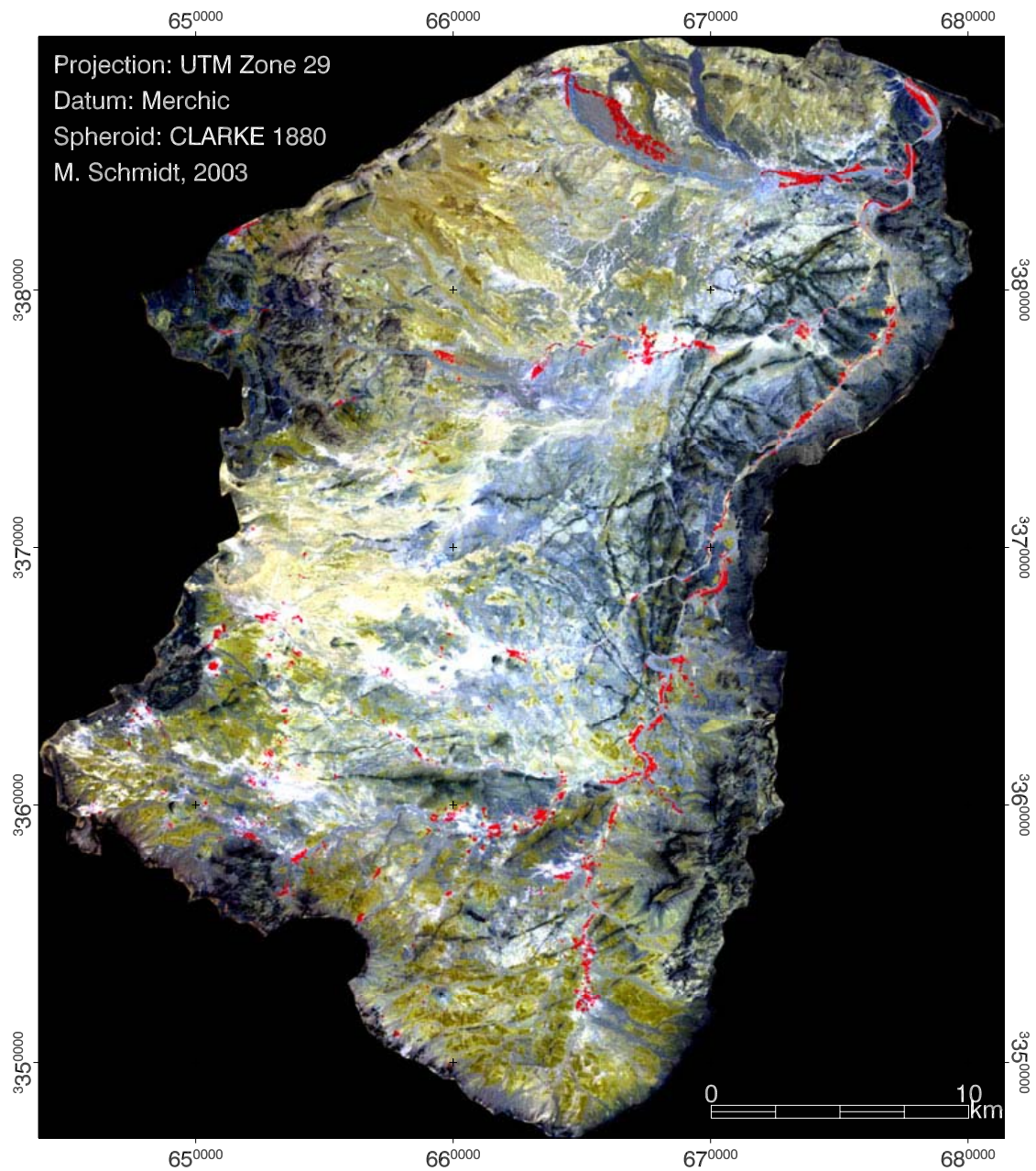


Figure 6.7: FCC of the Basin of Tazenakht with ETM+ (RGB 431) from May 2000

Land cover classes within this region are, according to the classification scheme defined in chapter 3: 1120 - discontinuous urban fabric, 1220 - road and rail networks and associations, 2111 - rainfed agriculture, 2342 - mountainous oasis, 3251 - Hammada scoparia - Artemisia steppe, 3312 - desert crust, 3322 - rock, 4131 -

Atriplex glauca, 4132 - *Tamarix africana* - Oleander, photos of which can be seen in Appendix A for a better surface impression.

The most recent vegetation mapping analysis in this region was performed by Bennouna et al. (2000), who tried to assess the surface vegetation by classifying pedologically homogenous regions within the Basin of Tazenakht using SPOT XS data (not mentioning the date of the image acquisition). Their approach is in fact more of a potential vegetation mapping based on morphological descriptions, which was improved by visual analysis. A broad landscape and vegetation characterization is given by Houérou (2001). Mappings to assess the actual vegetation distribution in this region, especially with respect to remote sensing, are not known to the author.

Figure 6.7 shows a False Colour Composite (FCC) of Basin of Tazenakht. The main features visible in the composite include the red areas which represent dense vegetated areas, rocks (grey/blue) and fields (brownish).

Linear Spectral Unmixing

In accordance with Figure 6.1, endmembers were selected and identified to explain the surface variability. An adequate solution, according to field observations, was found with a four endmember model consisting of vegetation, soil, desert crust and rock. Figure 6.8 shows the abundance channels and the RMS error as calculated from the image derived endmembers.

In the first step of the analysis the abundances of the background endmembers (subsection 6.1.2) were classified with the fuzzy AND as defined in subsection 6.1.4. In order to map the ploughed fields the membership function of the soil abundance was modified to be zero below an empirically derived threshold of 0.7 (Figure 6.9). Areas with high RMS errors contributed to the rock class. Vegetation abundance was differentiated by setting up and applying knowledge-based rules, incorporating the background information. Figure 6.9 reveals the applied rules in form of a diagram and the derivation of the classes 3322 (rock) and 3312 (desert crust). In this case the soil abundance was directly assigned to the land cover class 2111 (rainfed agriculture) as recent ploughed areas.

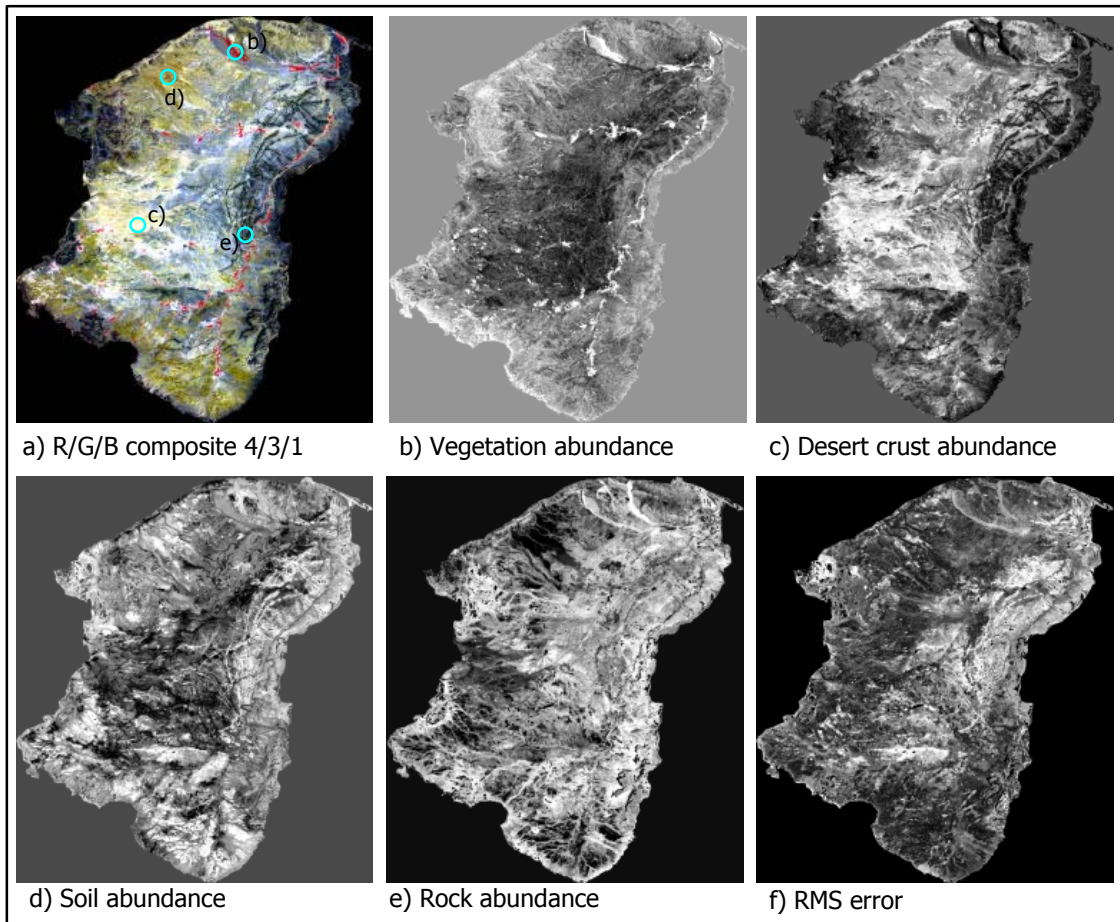


Figure 6.8: a) FCC of LANDSAT ETM+ (approximately indicating the location of the endmembers), b - e the abundance channels of the endmembers used in the decomposition and f) the RMS error (bright pixels refer to high abundance/RMS values)

The class 3251 (*Hammada scoparia* - *Artemisia* steppe) is derived if the vegetation abundance lies between 0.035 and 0.18, while the class 2342 (mountainous oasis) was derived by the abundance threshold of greater than 0.18. Due to the orientation of *Atriplex glauca* and riparian vegetation along the river network, stream-lines were identified as a useful source of information. The available GTOPO30 DEM (in 1km resolution) is too coarse for calculating this information on the required level of detail. Thus the main river-beds were digitised from the Tazenakht topographic map at a scale of 1:100000. *Atriplex glauca* is characterised by sandy/loamy soils on river terraces (M. Finckh, pers. comm, 2003). Figure 6.9 illustrates the decision

rules implemented to identify this vegetation class: potential terraces were identified by a 10 pixel buffer zone around the river network. A 5 pixel buffer zone was used to describe the potential areas for riparian vegetation. Materials present in the sandy and loamy terraces are similar to the surface areas classified as desert crust. Vegetation with an abundance threshold between 0.035 and 0.45 on desert crust in a potential terrace area is assigned to the class 4131 (*Atriplex glauca*). The class 4132 (*Tamarix africana* - *Oleander*) is derived from the condition of being on areas of potential riparian vegetation and on rocky ground with a vegetation abundance threshold between 0.035 and 0.30.

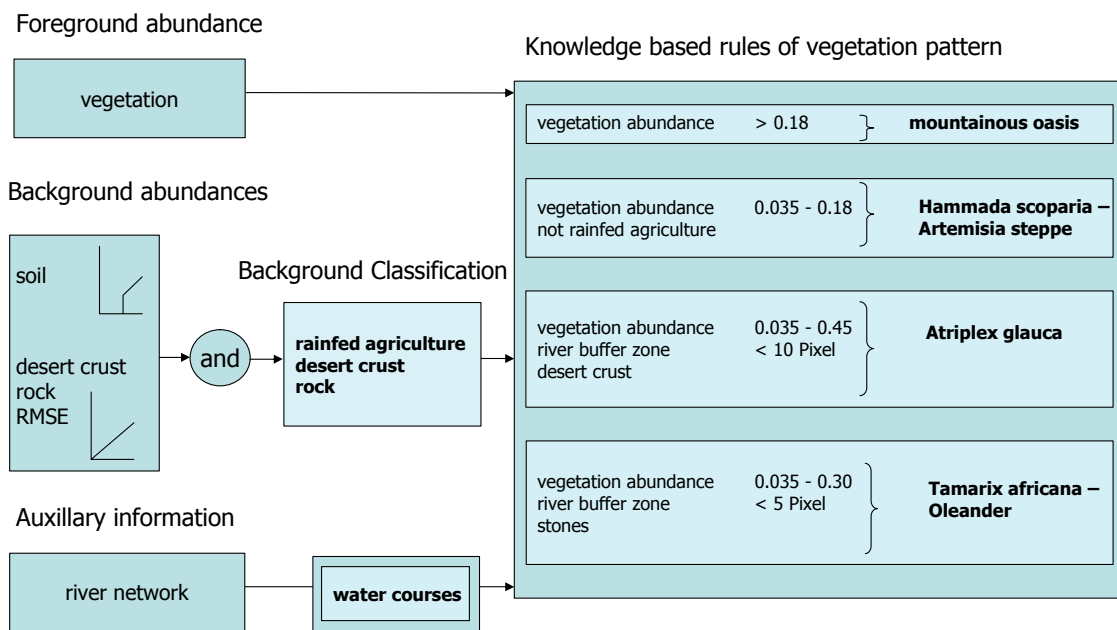


Figure 6.9: Knowledge based fuzzy decision rules for land cover class differentiation in the Basin of Tazenakht

Figure 6.10 shows two examples of the classification result: Example 1 of class 4131 (*Atriplex glauca*), the indicated photograph shows species of *Atriplex glauca* in the foreground on a river terrace. The photograph in Example 2 shows class 2111 (rainfed agriculture) with ploughed fields. The class 1120 (discontinuous urban fabric) describes within this study area exclusively the town of Tazenakht, built predominantly of modern stone houses. Most smaller and older settlements in rural areas are mostly traditionally built with clay and straw materials and these are much harder to detect and to differentiate from surface materials. They are also less aggregated. The complex mixture of urban pixels can be directly discriminated by

thresholds from the abundances channels. For the class 1120 (discontinuous urban fabric) a 3×3 majority filter was applied in a post processing step. The decision rules of the image classification are shown in Figure 6.11.

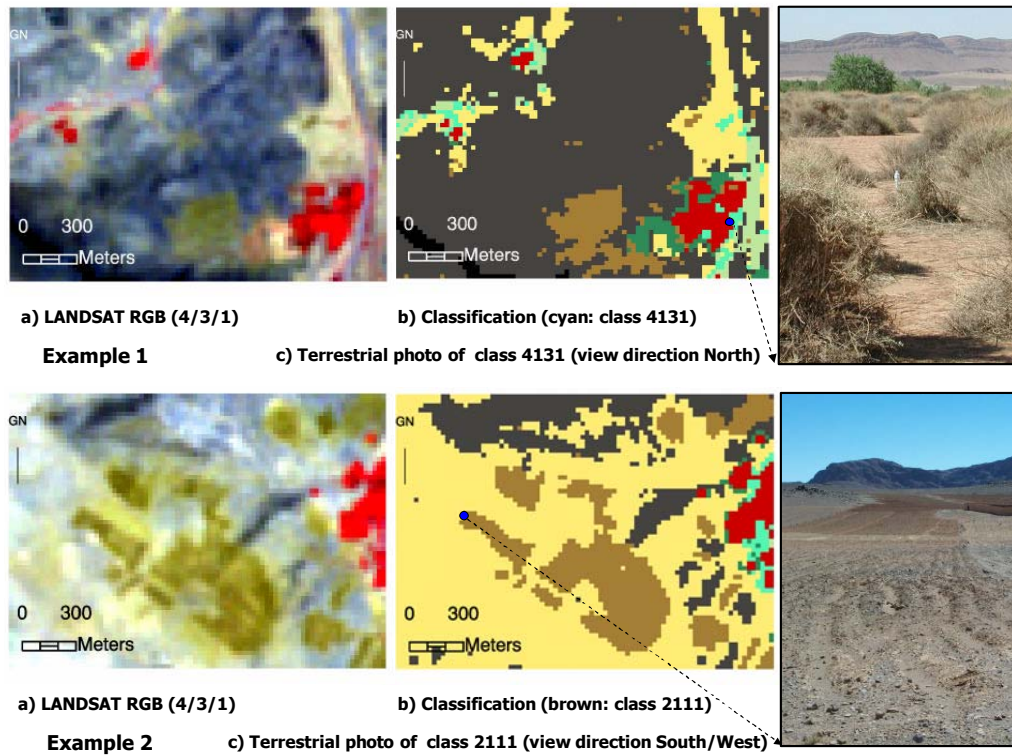


Figure 6.10: Two example images of an RGB FCC (a), the corresponding classification (b)(for the legend see Figure 6.11) and a ground truth image (c). Example 1: class 4131 (*Atriplex glauca*) coordinates of the photo-location: 665270/3362542 (UTM) and Example 2: class 2111 (rain-fed agriculture), coordinates of the photo-location: 677620/3379242 (UTM)

field abundance	< 0.1	} discontinuous urban fabric
sand abundance	0.3 - 0.8	
stone abundance	< 0.9	
RMSE	> 4.5	

Figure 6.11: Classification rules for the class 1120 - discontinuous urban fabric

Table 6.1 shows the confusion matrix of the image classification in percent. Training pixels were excluded in the validation.

Table 6.1: Confusion matrix of ground truth pixels and the classified image of the Basin of Tazenakht, in percent and in pixels

Class	Ground Truth (Percent)										Total
	3251	3312	3322	2111	2342	4132	4131	1120			
Uncl.	0.00	0.00	2.16	0.00	0.00	0.00	0.00	0.00			0.17
3251	93.73	0.00	2.16	0.00	2.80	0.00	0.00	0.00			14.79
3312	4.06	94.02	0.00	0.23	0.00	0.00	0.00	0.00			7.00
3322	2.21	5.98	95.68	0.23	0.00	0.00	0.00	9.55			9.50
2111	0.00	0.00	0.00	99.54	0.00	0.00	0.00	0.00			49.77
2342	0.00	0.00	0.00	0.00	96.26	0.00	7.69	0.00			5.92
4132	0.00	0.00	0.00	0.00	0.00	90.91	0.00	0.00			1.71
4131	0.00	0.00	0.00	0.00	0.93	9.09	92.31	0.00			0.91
1120	0.00	0.00	0.00	0.00	0.00	0.00	0.00	90.45			10.24
Total	100	100	100	100	100	100	100	100	100	100	100

Class	Ground Truth (Pixels)										Total
	3251	3312	3322	2111	2342	4132	4131	1120			
Uncl.	0	0	3	0	0	0	0	0			3
3251	254	0	3	0	3	0	0	0			260
3312	11	110	0	2	0	0	0	0			123
3322	6	7	133	2	0	0	0	19			167
2111	0	0	0	875	0	0	0	0			875
2342	0	0	0	0	103	0	1	0			104
4132	0	0	0	0	0	30	0	0			30
4131	0	0	0	0	1	3	12	0			16
1120	0	0	0	0	0	0	0	180			180
Total	271	117	139	879	107	33	13	199			1758

The overall accuracy of 96.53% and a Kappa coefficient of 0.951 (Jensen, 1996b) is remarkably high. 9.55% of the class 1120 (discontinuous urban fabric) was misclassified as 3322 (rock) because rock and concrete have similar spectra. Table 6.1 shows that for the two classes 4133 (*Tamarix africana* - Oleander) and 4131 (*Atriplex glauca*) the number of validation pixels is especially low, particularly for the latter. This class was only identified during the last days of the final field campaign with very localised ground truth measurements. Consequently a more thorough validation of this class needs to be performed during a future field campaign.

6 Vegetation classification in an arid environment

The final classification for the Basin of Tazenakht with 9 land cover classes is presented in Figure 6.12.

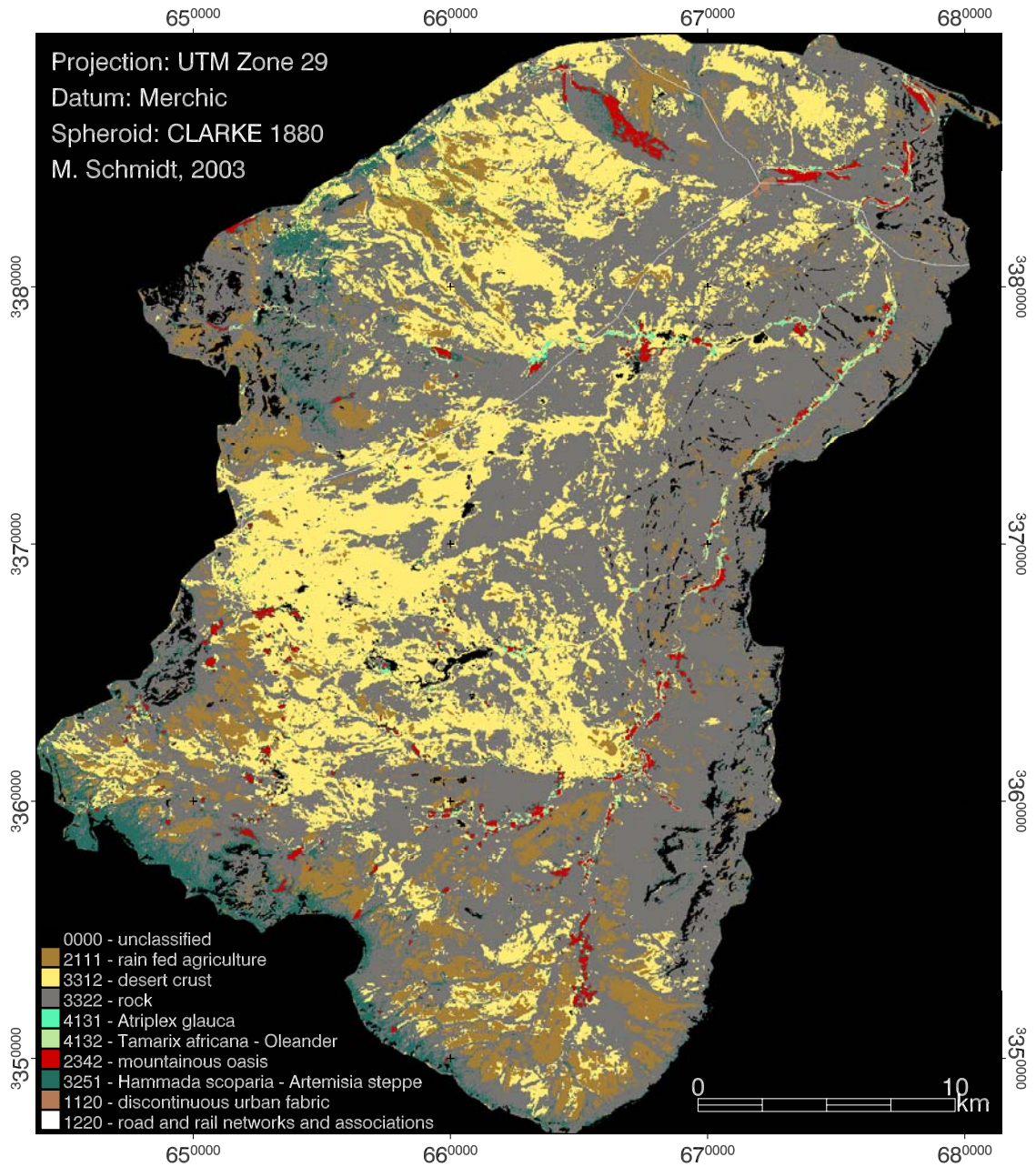
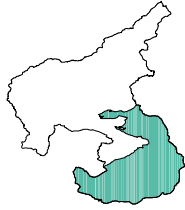


Figure 6.12: Land cover/land use classification for the Basin of Tazenakht on the basis of LANDSAT ETM+ data from May 2000

6.2.2 The Dra valley

Landscape



The Oued Dades and Oued Ouarzazate merge to Oued Dra, which gives the name for the landscape dominating river oasis downstream (Pletsch, 1971). Agricultural production in this arid environment, with an annual average precipitation of $70mm$ and annual potential evaporation of $2000mm$, is to a high degree dependent on the availability of freshwater. Water is taken either from the river and distributed with a historically evolved, complicated system of water rights and water channels (arabic "Seguia") or from the groundwater with wells and pumps (Müller-Hohenstein, 1997). This system often results in intensive socio-economic and ethnic complications and conflicts. For example the owner of the land is not necessarily the owner of the palm trees and in some instances, the owner of the water is another person (O. Abellaoui, ORMVAO Ouarzazate, pers. comm). Population growth combined with freshwater water scarcity, reinforces problems such as irrigation or an increased grazing pressure on the rangelands due to increased number of domestic animals.

The rangeland vegetation is characterised in section 2.1. Dominant vegetation associations were categorized according to the classification scheme as described in section 3.3 and displayed in Appendix A. Classes within the sub-region are: 3312 - desert crust, 3321 - gravel/pediment, 3311 - sand, 3323 - playa, 3322 - rock, 3332 - *Zygophyllum gaetulum*, 3331 - sanddune vegetation, 3264 - *Tamarix aphylla*, 3263 - *Acacia raddiana* - *Panicum* - *Zilla*, 3261 - *Acacia raddiana* - *Ziziphus* - *Mearua*, 4132 - *Tamarix africana* - *Oleander*, 3251 - *Hammada scoparia* - *Artemisia* steppe, 2341 - palm oasis, 5110 - water courses, 3262 - *Acacia raddiana* - *Retama*, 3255 - *Pulicaria* steppe, 1120 - discontinuous urban fabric, 3256 - *Anvillea* - *Convolvulus* steppe and 1220 - road and rail networks and associations .

The land cover classification was performed on the basis of LANDSAT ETM+ data. In a high resolution case study with IKONOS-2 data and an intensive field campaign in February 2002 results from the detailed mapping of one land cover class: 3264 (*Tamarix aphylla*) were integrated in the validation of the LANDSAT ETM+ land cover classification.

Case study with very high resolution data, near M'hamid

This section illustrates how very high resolution IKONOS-2 data were used to assess the coverage of one land cover class. Multispectral IKONOS-2 data were geometrically and radiometrically corrected as described in section 5.3 and subsection 5.2.1. The aim of this mapping is a detailed study of high spatial detail in a $10km \times 10km$ study area. The image was delivered in two tiles from November 23, 2001 (left image) and November 26, 2001 (right image). The meta information of the images are listed in Table 6.2.

Table 6.2: Meta information of the two IKONOS-2 image tiles used in this study

	left scene	scene right
Date of Acquisition	23.11.2001	26.11.2001
Collection Azimuth	347.2°	272.15°
View angle	21.8°	29.3°
Sun azimuth	164.3°	167.2°
Sun elevation	38.4°	38.3°

Figure 6.13 shows an image-subset of the study area. The town of M'hamid and five representative test plots from which validation data were obtained are indicated. In this case ground truth data were obtained on the basis of DGPS point measurements of single trees.

The vegetation coverage within this area consists, with the exception of the oasis, of the vegetation association grouped in class 3264 (*Tamarix aphylla*) and 4132 (*Tamarix africana* - *Oleander*) along the river Dra. Species of *Tamarix aphylla* usually build up and grow on sandy hills, which can be up to $10m$ in height. Their size varies from single tree examples to associations of more than $25m$ in diameter. Consequently in this case the objects to be mapped are mostly larger, or at least similar, to the size of the IKONOS-2 pixels. This forested area is basically flat and sandy and is located west of the town of M'hamid. (A photo of a healthy and undisturbed tamarix tree can be seen in the extended classification scheme in Appendix A).

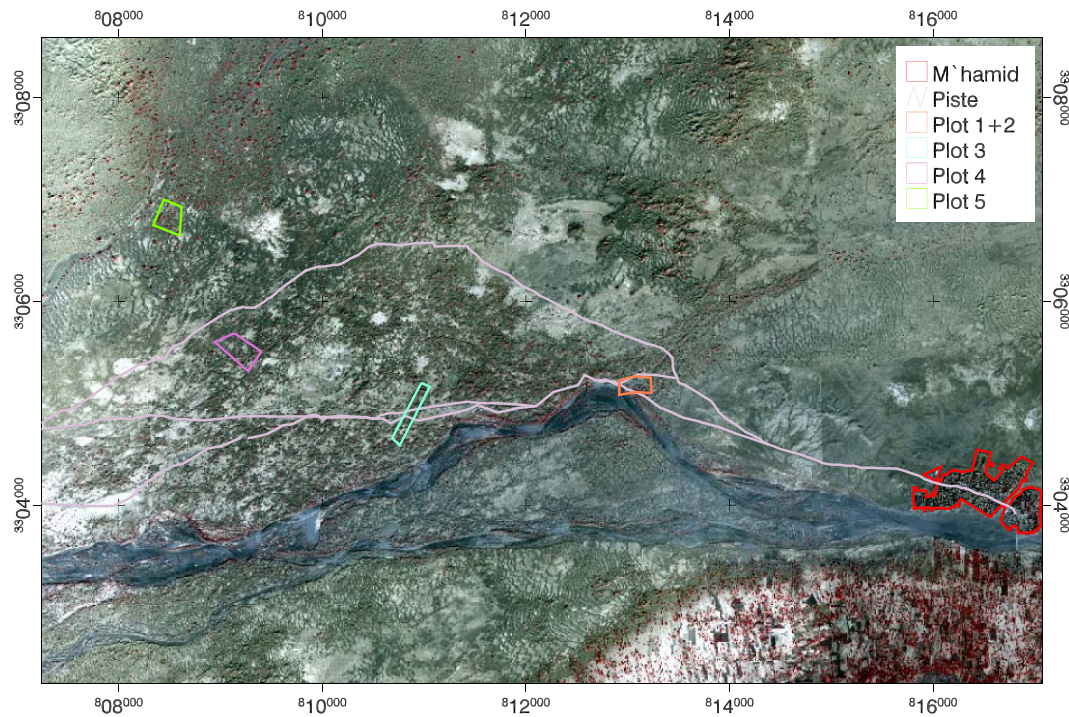


Figure 6.13: Overview of the mapping area

The vegetation distribution was determined by the NDVI as the objects of interest are in the order of the size of a pixel or larger. The NDVI was calculated from the third IKONOS channel in the red (RED) and the fourth channel in the near infrared (NIR) spectrum (The recoded wavelength in this bands is exactly the same as in the case of LANDSAT ETM+).

$$NDVI = \frac{RED - NIR}{RED + NIR}$$

Due to the recoding of view angle and azimuth angle, parts of the trees are covered by shade. Lillesand and Kiefer (2000) stated, that the NDVI in a shaded surface remains stable within the same vegetation cover type. Their explanation is that the pixel intensities for both bands are reduced similarly in the shade. As a consequence an index derived from band ratios should remain stable. NDVI was calculated from the IKONOS data and thresholded, resulting in an image classification. These pixels classified as 3264 (*Tamarix aphylla*) by applying an empirically derived NDVI threshold of greater than 0.05. The polygons with a common border to the digitised river Dra were assigned as individuals of *Tamarix africana* and excluded from the

classification and validation.

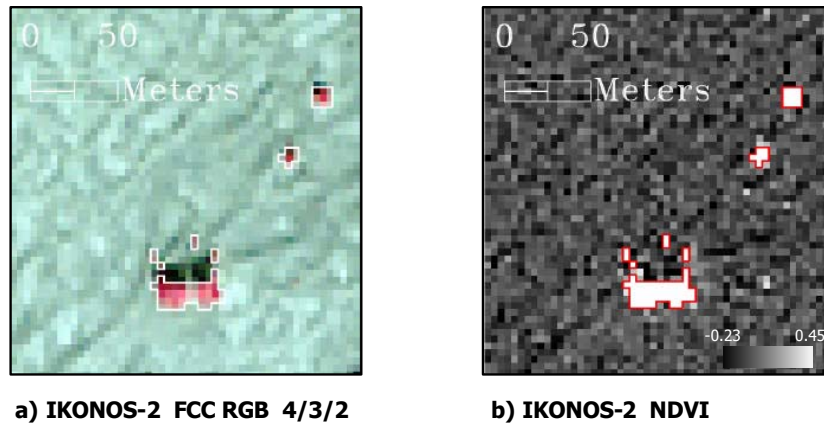


Figure 6.14: Visual comparison of the overlaid classification polygon on a RGB FCC and NDVI image subset of IKONOS-2 data

Minor amounts of grasses and herbs were excluded by the NDVI threshold. The classification was validated with 104 DGPS points (see section 2.2) obtained for single tamarisk trees. The validation points were taken without regard to the size of the individual trees. As a result small or degraded exemplars with a low NDVI signal resulted in classification errors. The validation points resulted in an overall accuracy of 94.2%, as shown in Table 6.3.

Table 6.3: Confusion matrix of the IKONOS-2 mapping, the horizontal axis is the ground truth data

Class	3264	Total
Unclassified	5.8	5.8
3264	94.2	94.2
Total	100.0	100.0

The classification result was exported as vector polygons to be utilised to enlarge the amount of validation data for the accuracy assessment of the LANDSAT ETM+ classification for the class 3264 (*Tamarix aphylla*) (see subsection 6.2.2).

Image processing and LSU of LANDSAT ETM+ data

For the sub-region as a whole no endmember combination was found to be satisfactory. A reduction of the feature space, as discussed in subsection 6.1.1, was a practical solution: a mask for the solid rocks, predominantly consisting of quartzites (Jebel Bani) and Precambrian sediments was generated on the basis of a regular MLC for one class (see Figure 6.15). Visual comparisons with the geologic map on a scale of 1:500000 indicated sufficient matching.

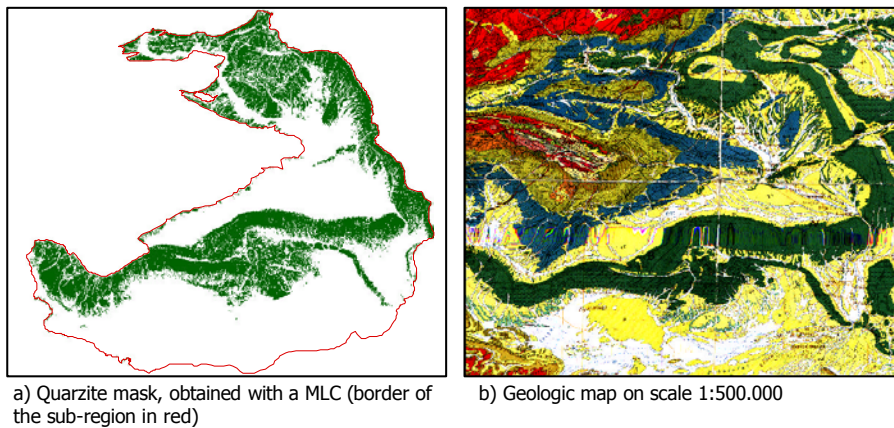


Figure 6.15: Visual comparison of the Quarzite mask and the geological map Abdeljali et al. (1959)

The masked image segments were treated separately with different endmember sets, resulting in improved abundance representations. The endmember combination used in the remaining "non-quarzite" image were spectra of vegetation, playa, desert crust, sand and pediment/gravel. Figure 6.16 shows the endmember spectra and locations at the corners of the scatterplot.

Vegetation types of sparsely vegetated areas could be identified as vegetation by the vegetation abundance information, which was difficult to achieve with the NDVI. The vegetation abundance was compared with ground truth information obtained during field campaigns (see section 2.2) and NDVI values. The correspondence between the NDVI and the vegetation abundance was generally high, but on some surfaces the NDVI appeared to be strongly influenced by the background. Figure 6.17 shows two image examples of surface vegetation representations derived from the NDVI (from calibrated data) and the vegetation abundance. In both examples the same threshold values were used, above which the image pixels appear colored: 0.022 for the vegetation abundance and -0.104 for the NDVI.

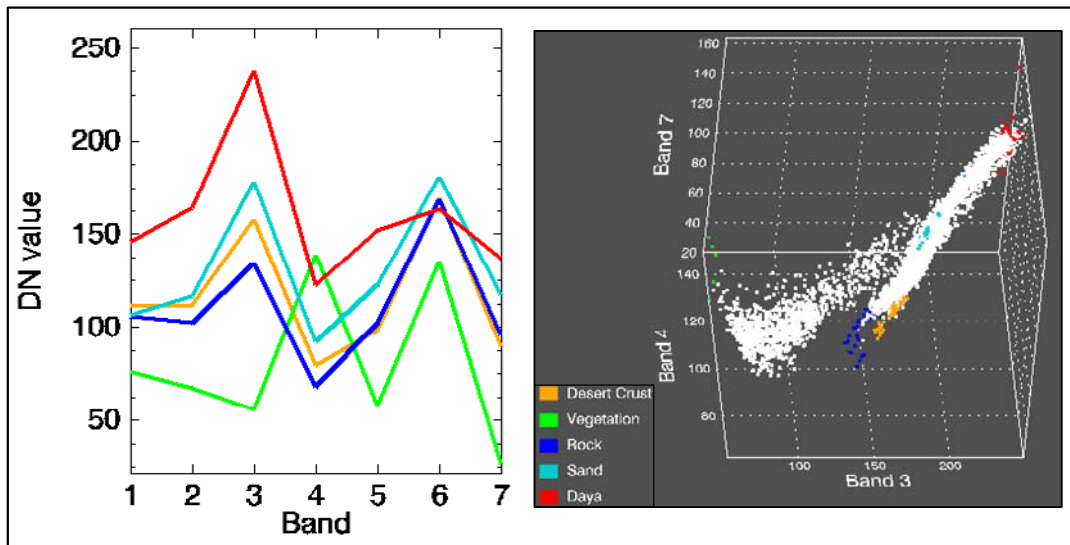


Figure 6.16: Endmember spectra used in the image decomposition of the Dra valley (white pixels represent samples of the feature space)

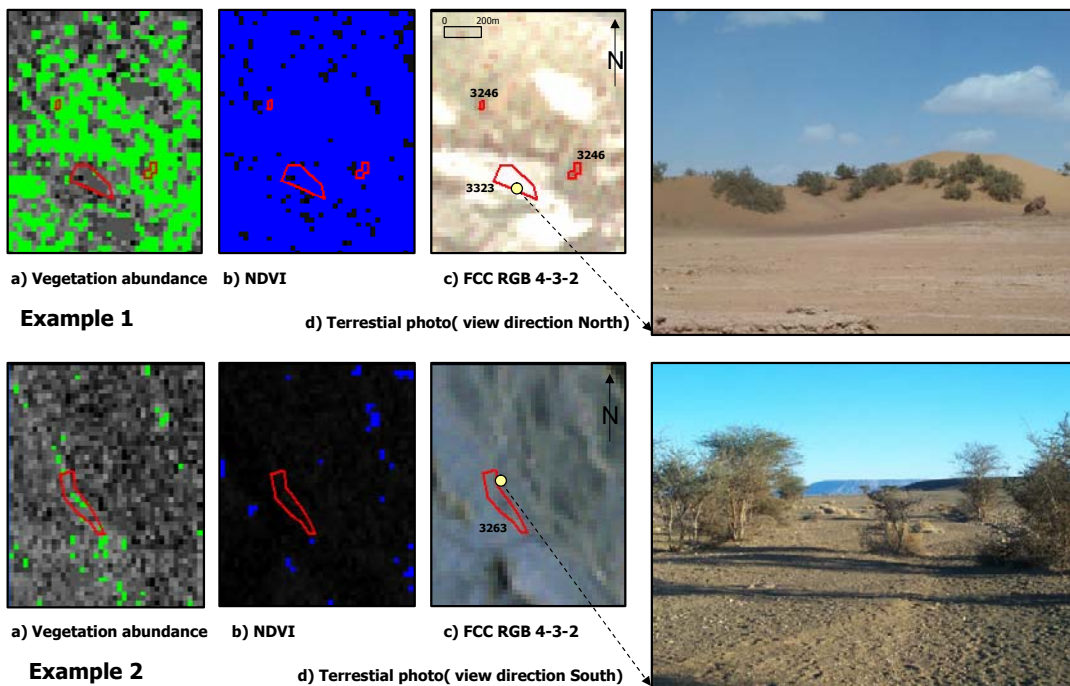


Figure 6.17: Examples of the background influence on the NDVI. The location of the photograph is indicated with the land cover class of the ground truth polygon Example 1 c) with coordinates (UTM): 817195/3308992 and Example 2 c): 827920/3355617.

Example 1 shows the NDVI bare surfaces as vegetated areas, while in Example 2 less vegetation is recognised. As a consequence of this the vegetation abundance was used for further analysis and vegetation differentiation.

In this ecological extreme most species are specialized in their growing conditions and well adapted to the physical environment. A differentiation of vegetation classes by their physical properties would be promising. Besides the soil information, the water availability and quality/salinity is a major factor that determines plant growth. For example *Acacia raddiana* can only survive with low salinity ground water while *Tamarix aphylla* and *Tamarix africana* grow better in more saline conditions (El-Addouni, 1989). The vegetation abundance of the two mentioned classes is similar, as is also the preferred sandy ground, so that on this basis a differentiation is not possible. A hydrological map of groundwater salinity would be very useful for the differentiation of these two, and some other vegetation classes. Pletsch (1971) refers to a groundwater salinity map, dating from 1968. This was before the dam near Ouarzazate was built, potentially changing the hydrologic system. As auxiliary information suitable to differentiate the land cover classes of this sub-region were not available, an attempt to differentiate the vegetation classes by their spectral properties was performed. SAM was applied to the original 7 channel spectral information of only the vegetated pixels (see subsection 6.1.1, subsection 6.1.3). The vegetated pixels were extracted from the multispectral LANDSAT ETM+ image by the identification on a minimum threshold value of 0.022 of the vegetation abundance above which all pixels contain vegetation information. These multispectral vegetation pixels were classified by choosing a set of reference spectra per class. The mean class value of the reference spectra is used in the SAM. The resultant membership function of each rule image from SAM can be modified by applying empirically identified threshold values for class differentiation. With the SAM a supervised classification is thus performed through the use of the fuzzy OR, as defined in subsection 6.1.4. The vegetation reference spectra and corresponding maximum threshold for the spectral angles $\Theta_i, i = [1..9]$ are shown in Figure 6.18.

The classification of the foreground layer vegetation is incorporated in a classification procedure based on decision rules and used for class discrimination as Figure 6.19 shows. The background information are obtained by LSU, resulting in a background classification by the use of the fuzzy AND operation of the abundance channels (see Figure 6.16). The membership functions of desert crust, playa and pediment were set to zero below 0.6, 0.6 and 0.5 respectively.

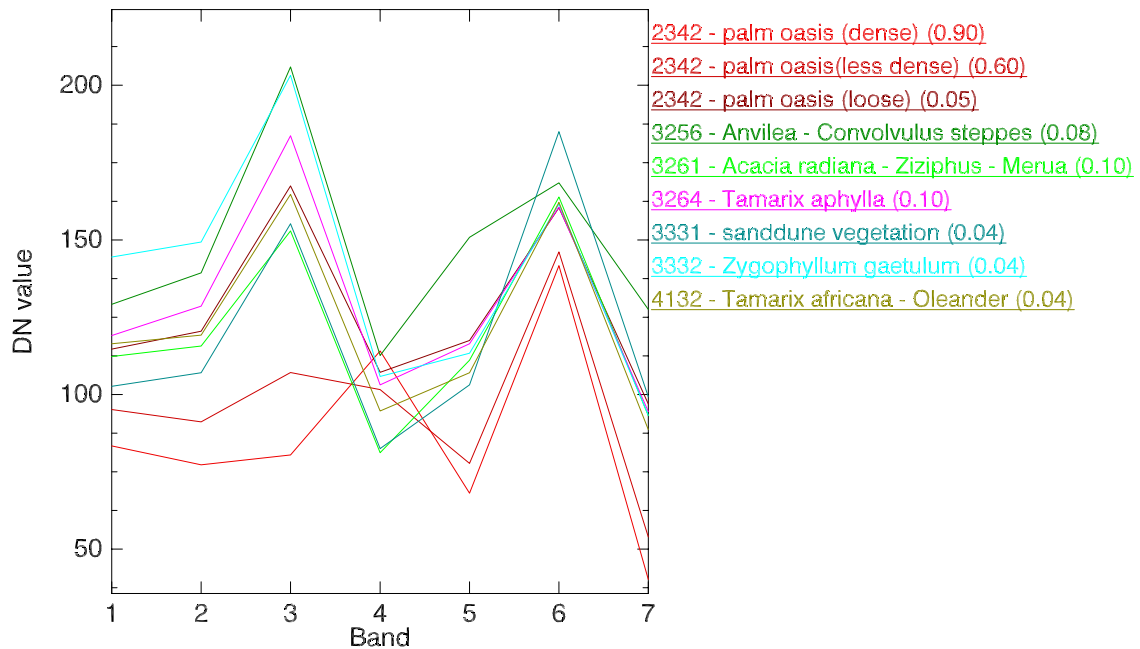


Figure 6.18: Reference spectra used in the SAM on the vegetation pixels with Θ_i values in brackets

The foreground and background classification can be superimposed resulting in a classified image of the sub-region.

A rainfall event and/or water outlet from the dam near Ouarzazate resulted in water within the riverbed of the Dra. Streamlines could not be calculated with sufficient quality from the GTOPO30 DEM of the sub-region. The varying water depth made a classification of the water pixels difficult. Consequently the river Dra was manually digitised and attributed to class 5110 (water courses). Pixels with vegetation abundance between 0.022 and 0.10 within a 3 pixel buffer zone were assigned to class 4132 (Tamarix africana - Oleander). Daya Chegaga is a depression 90km west of M'hamid, where rainfall water occasionally accumulates, resulting in specific growing conditions. The vegetation association in this area identified as 3255 (Pulicaria steppe). A polygon of this geographic region, indicated in the topographic map Zaouia Sidi abd en Nebi (on scale 1:100000) was used to assign pixels with vegetation abundance between 0.022 and 0.1 within the Daya Chegaga to the class 3255 (Pulicaria steppe). The 1120 (class discontinuous urban fabric) was derived with 21 reference spectral signatures due to the SAM with low angles Θ (less than 0.03).

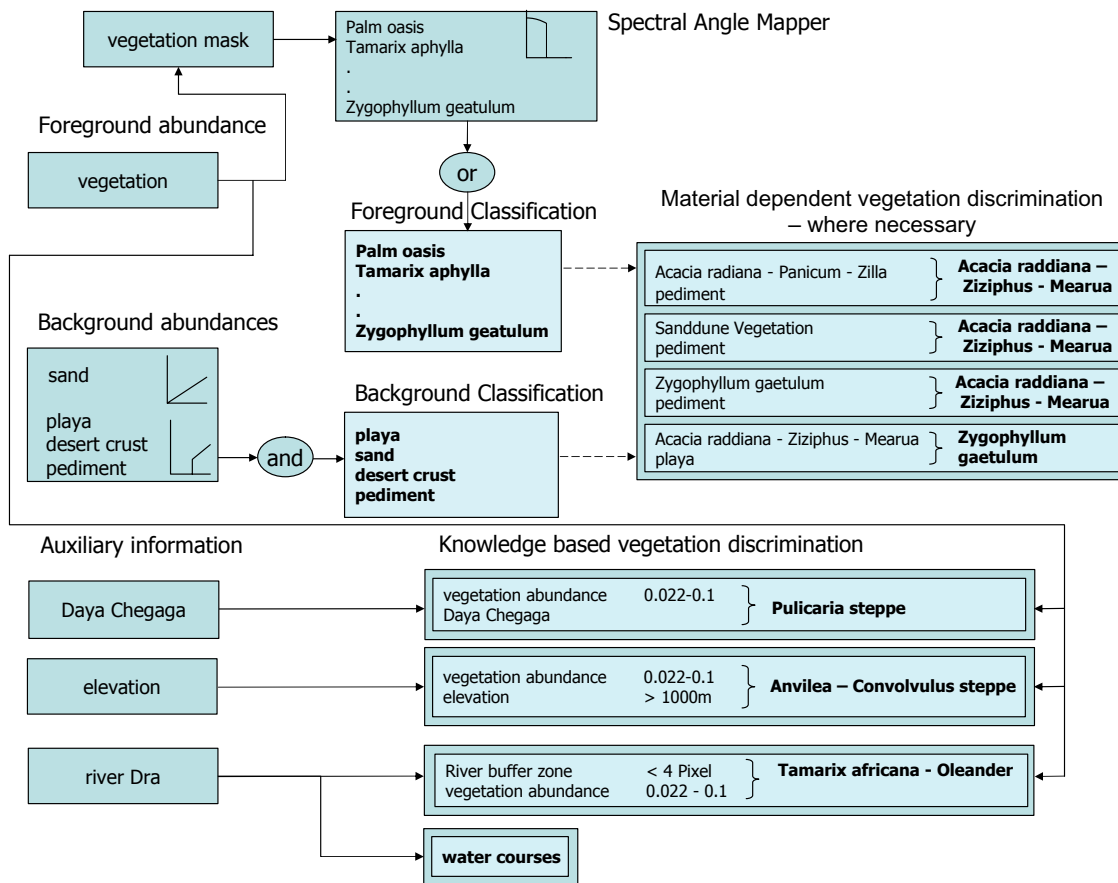


Figure 6.19: Flow chart of the land cover classification decision rules for the Dra valley (explanation in the text)

For the masked areas the background was already pre-classified as quarzitic rock. An endmember combination of vegetation (same spectrum as in the other Dra region), bright and dark rocks were selected for the LSU. Vegetation abundances greater than 0.035 were assigned to class 3262 (*Acacia raddiana* - *Retama*). Elevation information from the GTOPO30 DEM and from the Topographic map Zagora (scale 1:100000) served as base material to derive areas higher than 1000m elevation. Pixels classified as 3262 (*Acacia raddiana* - *Retama*) on elevations above 1000m were classified as 3256 (*Anvillea* - *Convolvulus* steppe) and superimposed on the background information. Figure 6.20 shows examples of the image classification.

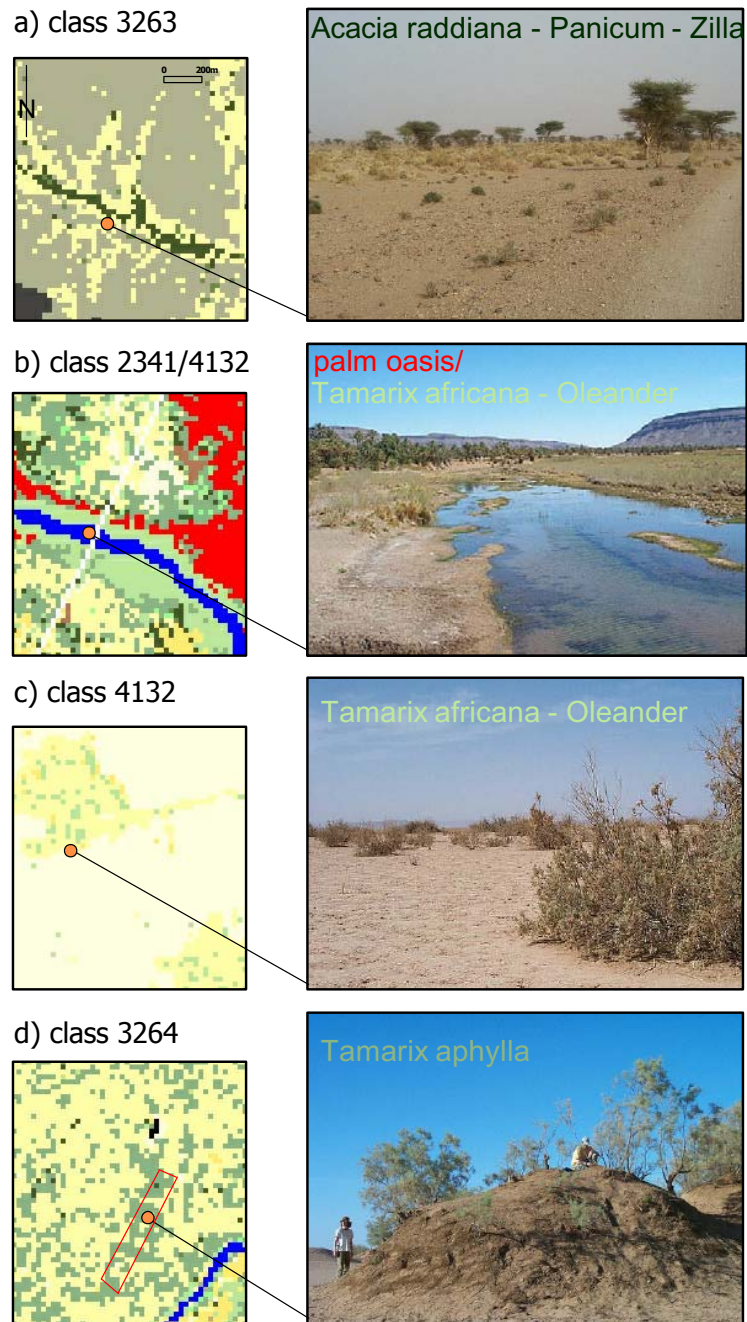


Figure 6.20: Examples of the classification result in the Dra valley (image size: 188×212 pixel), view direction in photo a) west (coordinates: 816520/3329536), view direction in photo b) south/west (coordinates: 829351/3344361), view direction in photo c) north (coordinates: 742514/3298805), view direction in photo d) north (coordinates: 810901/3305030)

Post classification

Confusions in a few classes were recognised, e.g. sanddune vegetation never grows on pediments. For this reason, an interactive IDL-based Graphical User Interface (GUI) tool was programmed for foreground class discrimination on certain surfaces. The applied rules are graphically shown in Figure 6.19.

In some areas close to the river Dra, *Tamarix africana* has ideal growing conditions, resulting in a dense coverage and thus in a high vegetation abundance. This is especially the case in some sinks of the riverbed with a high groundwater table and active salinisation processes. The spectral signatures of these dense coverage are similar to some signatures of agricultural areas and therefore hard to differentiate spectrally (Figure 6.22). These areas were mis-classified as palm oasis. Characteristic of these areas is that they are aligned linearly along rivers. This object characteristic was utilised for an object oriented post classification step within the software package e-Cognition (Definiens, 2002). As a first step the classified image was imported into e-Cognition. Objects were identified by image segmentation as connected pixels belonging to the same class. Objects were hierarchically selected and identified by certain attributes until the objects to discriminate were selected unequivocally. Rules for the differentiation of the objects are shown graphically in Figure 6.21.

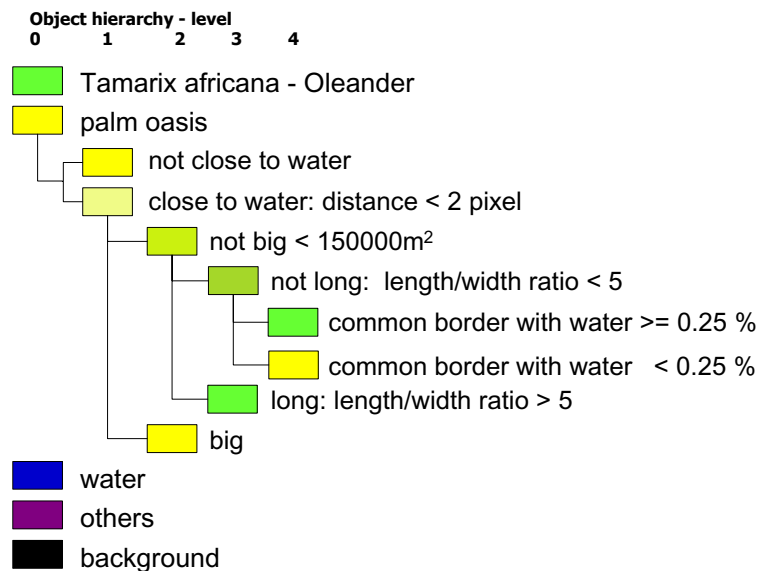


Figure 6.21: Object oriented post-classification decision tree for the differentiation of the classes 2341 (palm oasis) and 4132 (Tamarix africana - Oleander)

In the first level all objects of the class palm oasis were selected. In the second and third level of hierarchy objects that are close to water (less than 2 pixels) and smaller than $150000m^2$ are selected. The attribute that the riparian vegetation often grows in a linear manner was accounted for with the length/width ratio. So that on the next level objects with a length/width ratio > 5 were assigned to the class *Tamarix africana* - Oleander. Additionally objects with a large common border ($> 25\%$) with the object water were at the lowest hierarchy level assigned to the class *Tamarix africana* - Oleander. Figure 6.22 shows an example of the classification improvement near the river Dra.

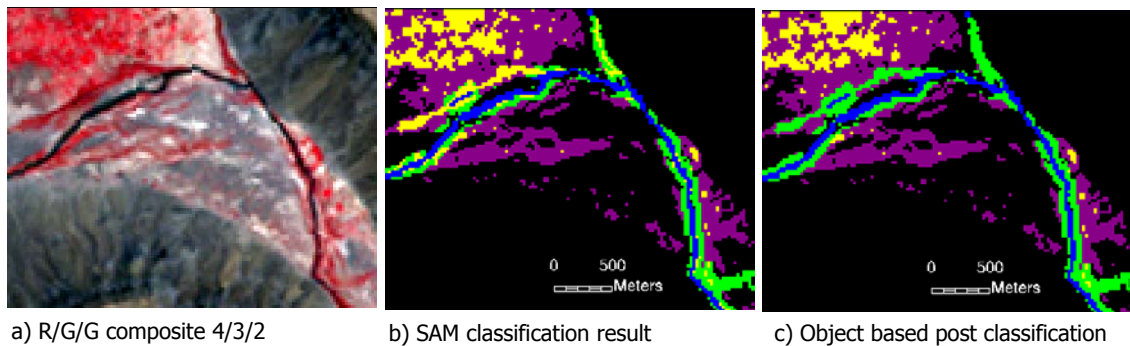


Figure 6.22: Example of object oriented post-classification improvement of the riparian vegetation association 4132 (*Tamarix africana* - Oleander), coordinates of the image center (UTM): 833770/3342792 (Legend as in Figure 6.21)

Validation

For a combined validation of the image classifications, the non-quarzite and quartzite areas were merged. Validation data (see subsection 6.1.6) were not included in the classification process as reference spectra or endmember. The overall accuracy of the classification approach is 82.24% with a Kappa coefficient of 0.795. Table 6.4 shows the confusion matrix of the image classification in the Dra valley in percent and in pixels.

Table 6.4: Confusion matrix of the LANDSAT ETM+ land cover classification in the Dra valley in percents and in pixels (next page)

6.2 Results from the Dra catchment - South Morocco

Class	Ground Truth (Percent)																Total	
	3312	3321	3311	3323	3322	3332	3331	3264	3263	3261	4132	3257	2341	3262	3255	1120		3256
Uncl.	0	0	0	0	0	0	0	0.16	0.08	0	0	0	0	0	0	0.26	0	
3312	94.31	0	0.99	0	0	0.35	2.22	0	4.25	0	0	0	0.11	0	2.63	18.81	0	
3321	0.32	95.09	0.4	0	1.9	0	0	6.34	34.05	0	0	0	0	0	0	4.38	0	
3311	5.21	1.34	97.81	2.63	0.63	0.35	5.56	0	16.29	17.6	0	1.64	0	0	0	2.84	0	
3323	0	0.89	0	97.37	0	4.51	0	0.04	1.44	1.44	0	0	0.22	0	5.26	0.52	0	
3322	0	2.68	0	0	97.46	0	0	0	0	0.14	0	0	0	33.33	0	0	33.33	
3332	0	0	0	0	0	80.21	0	5.33	0	0	0	6.56	0.11	0	0	0	0	
3331	0	0	0.8	0	0	0	71.11	0	0	0	0	0	0	0	0	0	0	
3264	0	0	0	0	0	9.03	17.78	92.17	0.32	0.14	4.93	1.64	1.09	0	0	0.26	0	
3263	0.16	0	0	0	0	3.13	3.33	1.67	52.73	0.87	0	4.92	0	0	0	1.29	0	
3261	0	0	0	0	0	1.74	0	0.04	18.46	45.45	0	0	0	6.67	0	1.03	0	
4132	0	0	0	0	0	0.35	0	0.4	0.08	0	92.96	0	0.44	0	0	0	0	
3257	0	0	0	0	0	0.35	0	0.08	0	0	0	85.25	0	0	0	0	0	
2341	0	0	0	0	0	0	0	0.12	0	0.14	2.11	0	98.03	0	0	0	0	
3262	0	0	0	0	0	0	0	0	0	0.14	0	0	0	60	0	0	0	
3255	0	0	0	0	0	0	0	0	0	0	0	0	0	0	92.11	0	0	
1120	0	0	0	0	0	0	0	0	0	0	0	0	0	0	0	70.62	0	
3256	0	0	0	0	0	0	0	0	0	0	0	0	0	0	0	0	66.67	
Total	100	100	100	100	100	100	100	100	100	100	100	100	100	100	100	100	100	100

Class	Ground Truth (Pixels)																Total
	3312	3321	3311	3323	3322	3332	3331	3264	3263	3261	4132	3257	2341	3262	3255	1120	
Uncl.	0	0	0	0	0	0	0	4	1	0	0	0	0	0	0	1	0
3312	597	0	5	0	0	1	2	0	53	0	0	0	1	0	1	73	0
3321	2	426	2	0	6	0	0	0	79	236	0	0	0	0	0	17	0
3311	33	6	492	3	2	1	5	0	203	122	0	2	0	0	0	11	0
3323	0	4	0	111	0	13	0	1	18	10	0	0	2	0	2	2	0
3322	0	12	0	0	307	0	0	0	0	1	0	0	0	15	0	0	2
3332	0	0	0	0	0	231	0	134	0	0	0	8	1	0	0	0	0
3331	0	0	4	0	0	0	64	0	0	0	0	0	0	0	0	0	0
3264	0	0	0	0	0	26	16	2318	4	1	7	2	10	0	0	1	0
3263	1	0	0	0	0	9	3	42	657	6	0	6	0	0	0	5	0
3261	0	0	0	0	0	5	0	1	230	315	0	0	0	3	0	4	0
4132	0	0	0	0	0	1	0	10	1	0	132	0	4	0	0	0	0
3257	0	0	0	0	0	1	0	2	0	0	0	104	0	0	0	0	0
2341	0	0	0	0	0	0	0	3	0	1	3	0	898	0	0	0	0
3262	0	0	0	0	0	0	0	0	0	1	0	0	0	27	0	0	0
3255	0	0	0	0	0	0	0	0	0	0	0	0	0	0	35	0	0
1120	0	0	0	0	0	0	0	0	0	0	0	0	0	0	0	274	0
3256	0	0	0	0	0	0	0	0	0	0	0	0	0	0	0	0	4
Total	633	448	503	114	315	288	90	2515	1246	693	142	122	916	45	38	388	6

Classification accuracies of the non-vegetated classes: 3311, 3312, 3321, 3322 and 3323 are generally high. The vegetation classes 2341, 3331, 3332, 3255, 3257 and

4132 are represented with relatively high classification accuracies. The class 3264 has high accuracies and with 2515 test pixels is a reliable statistic. The large number of test pixels results from the incorporation of classification polygons from the mapping with IKONOS-2 data within the Dra valley, as described in subsection 6.2.2. The classes 3256 and 3262 could only be validated with 6 and 45 test pixels respectively and thus with less reliability. Although for class 3255 only 38 pixels were used the result is more reliable due to the localised occurrence of the class 3255 (see Figure 6.19).

The classes 3261, 3262 and 3263 represent with of 45%, 60% and 53% low classification accuracies, with high errors of commission with the non-vegetated classes. The classes 3261, 3262 and 3263 summarise different, soil dependent, associations of *Acacia raddiana* with low amounts of green biomass. The growth of this association is oriented along little wadi systems with a surplus of non-saline water. Ground truth data were mostly obtained as polygons so that only single pixels within the test or validation polygons are true vegetation pixels, as shown in Figure 6.17. Non vegetated pixels within these polygons undermine the classification and validation accuracies. For this reason an intersection of the polygons and the vegetated pixels as derived from the vegetation abundance channel was performed. The overall accuracy was increased by this to 90.14%, with a Kappa coefficient of 0.884. The confusion matrix (in percent) of the of the class intersection is shown in Table 6.5 a).

The difference between the classes 3261 and 3263 is the amount of sand, stones and the resultant differing vegetation associations, but both classes are dominated by *Acacia raddiana*. These differences are often slight and represent transition examples which can be attributed of either of the two classes. With respect to the commission error of the classes 3261 and 3263, these two classes were merged. As a result the overall accuracy changed to 93.14% with a Kappa coefficient of 0.918. Table 6.5 b) shows the confusion matrix (in percent) with the merged classes 3261 and 3263.

Summarising it can be stated that the classification accuracies are generally high for all classes. the classes 3331 with 71.11% was mis-classified to 17.78% with class 3264 as both are growing on sandy substrate; the class 3265 has high confusion with rock background. The classes dominated by the species *Acacia raddiana* are caused by their growth along little linear depression lines and their low green biomass at the edge of detectability with this classification method. For this class it appeared to be not suitable to collect the ground truth and validation as polygon data.

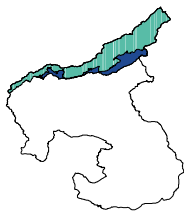
Table 6.5: a) Validation data of the intersection of the classes 3261, 3262 and 3263 with the vegetation mask, b) validation results from the intersection of the *Acacia raddiana* classes with the vegetation mask and the merged classes 3261 and 3263

Class	Ground Truth (Percent)																				Total
	3312	3321	3311	3323	3322	3332	3331	3264	3263	3261	4132	3257	2341	3262	3255	1120	3256	Total			
Uncl.	0.00	0.00	0.00	0.00	0.00	0.00	0.00	0.16	0.00	0.00	0.00	0.00	0.00	0.00	0.00	0.26	0.00	0.06			
3312	94.31	0.00	0.99	0.00	0.00	0.35	2.22	0.00	0.00	0.00	0.00	0.00	0.11	0.00	2.63	18.81	0.00	8.77			
3321	0.32	95.09	0.40	0.00	1.90	0.00	0.00	0.00	0.00	0.00	0.00	0.00	0.00	0.00	0.00	4.38	0.00	5.84			
3311	5.21	1.34	97.81	2.63	0.63	0.35	5.56	0.00	0.00	0.00	0.00	1.64	0.00	0.22	0.00	2.84	0.00	7.15			
3323	0.00	0.89	0.00	97.37	0.00	4.51	0.00	0.04	0.00	0.00	0.00	0.00	0.00	0.00	5.26	0.52	0.00	1.74			
3322	0.00	2.68	0.00	0.00	97.46	0.00	0.00	0.00	0.00	0.00	0.00	0.00	6.56	0.11	0.00	0.00	33.33	4.14			
3332	0.00	0.00	0.00	0.00	0.00	80.21	0.00	5.33	0.00	0.00	0.00	0.00	0.00	0.00	0.00	0.00	0.00	4.82			
3331	0.00	0.00	0.80	0.00	0.00	71.11	0.00	0.00	0.00	0.00	0.00	0.00	0.00	0.00	0.00	0.00	0.00	0.88			
3264	0.00	0.00	0.00	0.00	0.00	9.03	17.78	92.17	0.00	0.00	4.93	1.64	1.09	0.00	0.00	0.26	0.00	30.68			
3263	0.16	0.00	0.00	0.00	0.00	3.13	3.33	1.67	74.07	1.86	0.00	4.92	0.00	0.00	0.00	1.29	0.00	9.40			
3261	0.00	0.00	0.00	0.00	0.00	1.74	0.00	0.04	25.93	97.83	0.00	0.00	0.00	10.00	0.00	1.03	0.00	7.19			
4132	0.00	0.00	0.00	0.00	0.00	0.35	0.00	0.4	0.00	92.96	0.00	0.00	0.44	0.00	0.00	0.00	0.00	1.90			
3257	0.00	0.00	0.00	0.00	0.00	0.35	0.00	0.08	0.00	0.00	85.25	0.00	0.00	0.00	0.00	0.00	0.00	1.38			
2341	0.00	0.00	0.00	0.00	0.00	0.00	0.00	0.12	0.00	0.00	2.11	0.00	98.03	0.00	0.00	0.00	0.00	11.65			
3262	0.00	0.00	0.00	0.00	0.00	0.00	0.00	0.00	0.00	0.31	0.00	0.00	0.00	90.00	0.00	0.00	0.00	0.36			
3255	0.00	0.00	0.00	0.00	0.00	0.00	0.00	0.00	0.00	0.00	0.00	0.00	0.00	0.00	92.11	0.00	0.00	0.45			
1120	0.00	0.00	0.00	0.00	0.00	0.00	0.00	0.00	0.00	0.00	0.00	0.00	0.00	0.00	0.00	70.62	0.00	3.53			
3256	0.00	0.00	0.00	0.00	0.00	0.00	0.00	0.00	0.00	0.00	0.00	0.00	0.00	0.00	0.00	0.00	66.67	0.05			
Total	100	100	100	100	100	100	100	100	100	100	100	100	100	100	100	100	100	100			

Class	Ground Truth (Percent)																				Total
	3312	3321	3311	3323	3322	3332	3331	3264	3263	4132	3257	2341	3262	3255	1120	3256	Total				
Uncl.	0.00	0.00	0.00	0.00	0.00	0.00	0.00	0.16	0.00	0.00	0.00	0.00	0.00	0.00	0.26	0.00	0.00	0.06			
3312	94.31	0.00	0.99	0.00	0.00	0.35	2.22	0.00	0.00	0.00	0.00	0.00	0.11	0.00	2.63	18.81	0.00	8.77			
3321	0.32	95.09	0.40	0.00	1.90	0.00	0.00	0.00	0.00	0.00	0.00	0.00	0.00	0.00	0.00	4.38	0.00	5.84			
3311	5.21	1.34	97.81	2.63	0.63	0.35	5.56	0.00	0.00	0.00	1.64	0.00	0.00	0.00	2.84	0.00	0.00	7.15			
3323	0.00	0.89	0.00	97.37	0.00	4.51	0.00	0.04	0.00	0.00	0.00	0.00	0.22	0.00	5.26	0.52	0.00	1.74			
3322	0.00	2.68	0.00	0.00	97.46	0.00	0.00	0.00	0.00	0.00	0.00	6.56	0.11	0.00	0.00	0.00	33.33	4.14			
3332	0.00	0.00	0.00	0.00	0.00	80.21	0.00	5.33	0.00	0.00	0.00	0.00	0.00	0.00	0.00	0.00	0.00	4.82			
3331	0.00	0.00	0.80	0.00	0.00	71.11	0.00	0.00	0.00	0.00	0.00	0.00	0.00	0.00	0.00	0.00	0.00	0.88			
3264	0.00	0.00	0.00	0.00	0.00	9.03	17.78	92.17	0.00	0.00	4.93	1.64	1.09	0.00	0.00	0.26	0.00	30.68			
3263	0.16	0.00	0.00	0.00	0.00	4.86	3.33	1.71	99.92	0.00	4.92	0.00	10.00	0.00	2.32	0.00	0.00	16.59			
4132	0.00	0.00	0.00	0.00	0.00	0.35	0.00	0.40	0.00	92.96	0.00	0.44	0.00	0.00	0.00	0.00	0.00	1.90			
3257	0.00	0.00	0.00	0.00	0.00	0.35	0.00	0.08	0.00	0.00	85.25	0.00	0.00	0.00	0.00	0.00	0.00	1.38			
2341	0.00	0.00	0.00	0.00	0.00	0.00	0.00	0.12	0.00	0.00	2.11	0.00	98.03	0.00	0.00	0.00	0.00	11.65			
3262	0.00	0.00	0.00	0.00	0.00	0.00	0.00	0.00	0.00	0.00	0.00	0.00	0.00	90.00	0.00	0.00	0.00	0.36			
3255	0.00	0.00	0.00	0.00	0.00	0.00	0.00	0.00	0.00	0.00	0.00	0.00	0.00	0.00	92.11	0.00	0.00	0.45			
1120	0.00	0.00	0.00	0.00	0.00	0.00	0.00	0.00	0.00	0.00	0.00	0.00	0.00	0.00	0.00	70.62	0.00	3.53			
3256	0.00	0.00	0.00	0.00	0.00	0.00	0.00	0.00	0.00	0.00	0.00	0.00	0.00	0.00	0.00	0.00	66.67	0.05			
Total	100	100	100	100	100	100	100	100	100	100	100	100	100	100	100	100	100	100			

A DGPS point collection of each tree within the polygon would represent the distribution and density information in a better way. For a detailed calibration an analysis on this basis, preferably in combination with density estimation of the individuals, would be advisable.

6.2.3 High Atlas



The surface heterogeneity of the mountain area made a separation into two more homogenous (see subsection 6.1.1) sub-regions necessary. The result of the differentiation of the (sub-) sub-region is indicated on the left (blue color) and is based on the principle of PMU mapping according to Daels and Antrop (1977), as described in section 2.1. The high remaining background variability made the use of six background endmembers necessary (see Hill, 2000) and hampered the differentiation of the background information on level four of the classification scheme (see Table 3.1). The background was thus classified on hierarchy level three as 3320 (bare surfaces). The normalised differenced snow index (NDSI) (see e.g. Riggs et al., 1994; Romanov et al., 2000) is by the usage of LANDSAT ETM+ data defined as:

$$NDSI = \frac{Band4 - Band2}{Band4 + Band2},$$

where Band2 and Band4 denote the LANDSAT ETM+ spectral bands 2 and 4 (NASA, 2001). The NDSI was used to generate a snow mask above values of $NDSI > 0.4$. Figure 6.23 shows the rules applied for the class differentiation. The validation resulted in an overall accuracy of 92.43% with Kappa coefficient of 0.898. The confusion matrix is shown in Table 6.6.

The region of the High Atlas, as described in section 2.1 is characterised by high elevations and elevation differences, resulting in different illumination conditions. This different illuminations can potentially be corrected with a decent DEM in combination with an illumination correction (see section 5.4). This can potentially improve the classification result and the possibility to differentiate classes better.

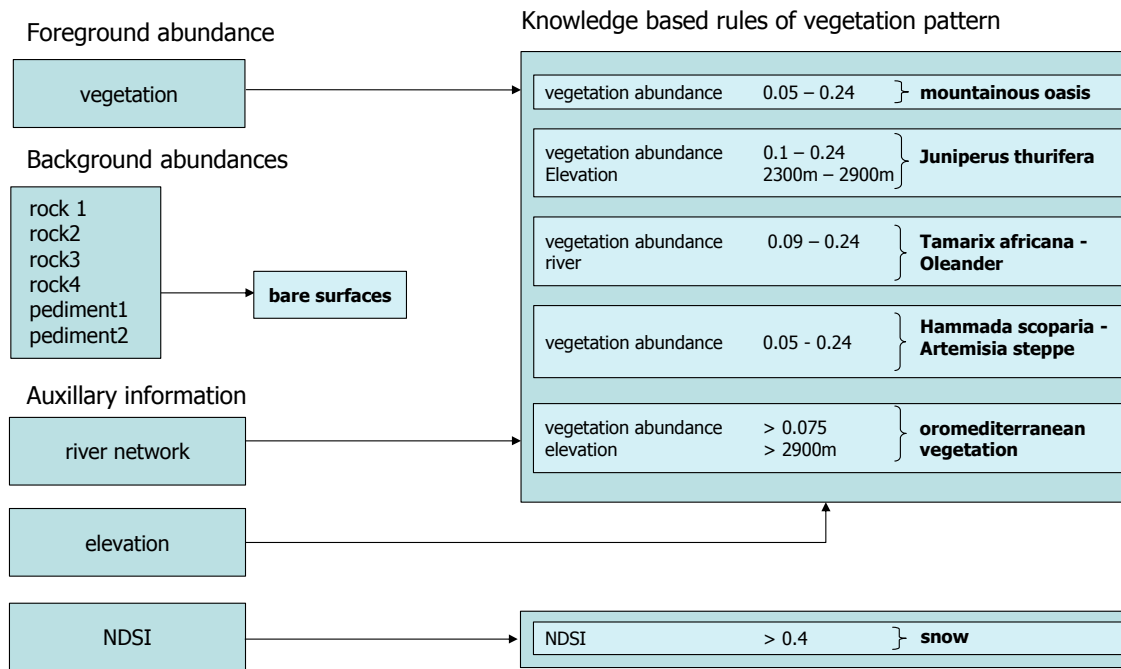


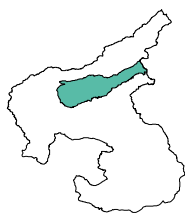
Figure 6.23: Flow chart of the land cover classification decision rules for the High Atlas

Table 6.6: Land cover classification accuracies of the High Atlas with 6 validated classes (next page)

Ground Truth (Percent)							
Class	3320	3251	4132	2342	3242	3221	Total
Uncl.	0	0	0	0	0	0	0
3320	98.28	10.1	0	0	1.02	0	9.41
3251	1.72	89.5	8	0	14.32	9.18	29.12
4132	0	0	92	1.26	0	0	3.01
2342	0	0	0	98.74	0	0	34.97
3242	0	0.4	0	0	84.65	0	18.54
3221	0	0	0	0	0	90.82	4.96
Total	100	100	100	100	100	100	100

Ground Truth (Pixels)							
Class	3320	3251	4132	2342	3242	3221	Total
Uncl.	0	0	0	0	0	0	0
3320	114	51	0	0	4	0	169
3251	2	452	4	0	56	9	523
4132	0	0	46	8	0	0	54
2342	0	0	0	628	0	0	628
3242	0	2	0	0	331	0	333
3221	0	0	0	0	0	89	89
Total	116	505	50	636	391	98	1796

6.2.4 Basin of Ouarzazate



The heterogeneous source material from the High Atlas mountains contributes to a complex mixture of background materials so for this reason five background endmembers were utilised in the spectral unmixing. The abundance information of which resulted in the differentiation of four background classes. Figure 6.24 shows the decision rules and the classification procedure in this region. The differentiation of the three rangeland vegetation classes was achieved by SAM. The 1120 (class discontinuous urban fabric) was derived with 17 reference spectral signatures due to the SAM with low angles Θ (less than

0.03). According to the validation data the overall classification accuracy is 96.8% with a Kappa coefficient of 0.958.

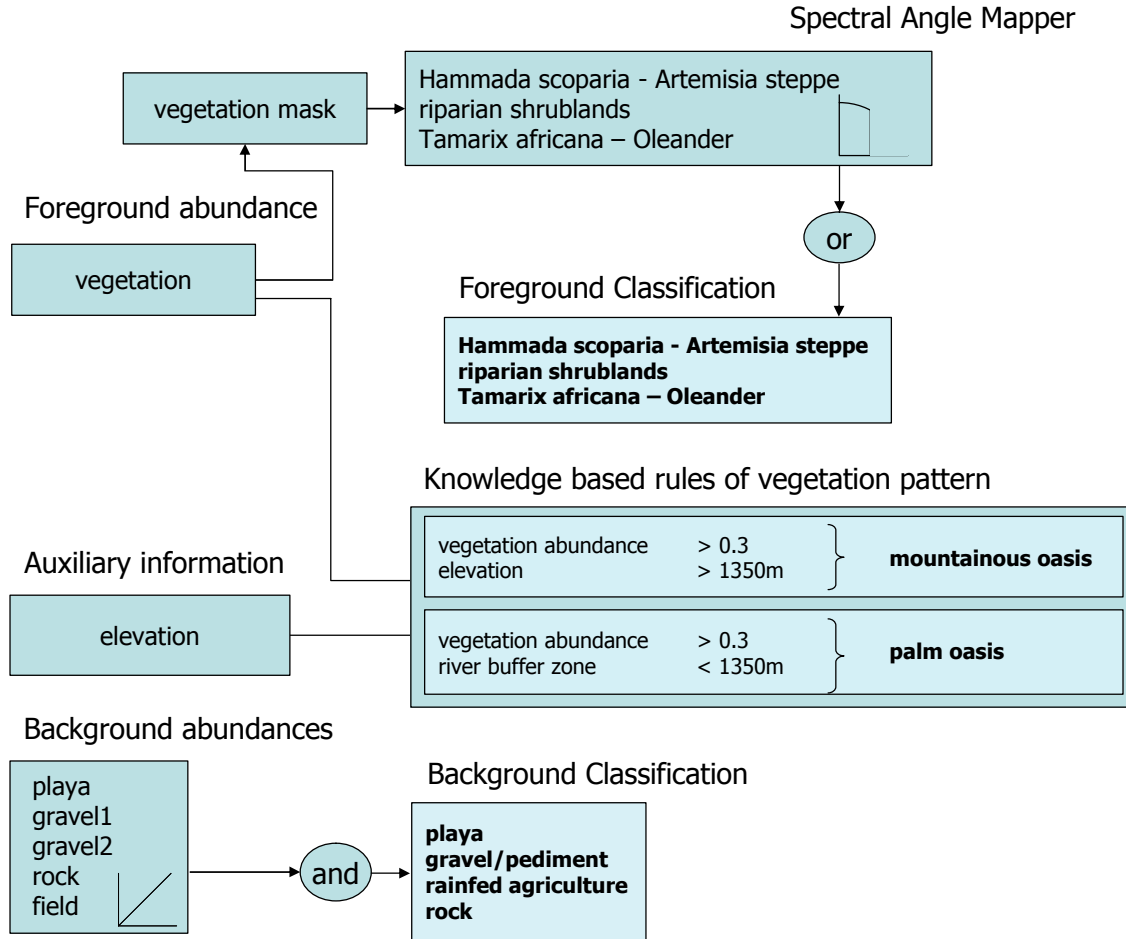


Figure 6.24: Flow chart of the land cover classification decision rules for the Basin of Quarzazate

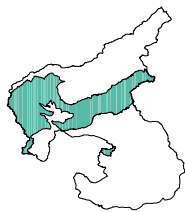
The actual and detectable vegetation distribution of the LSU above a vegetation abundance threshold of 0.025 was determined and differentiated. From a botanic point of view, the bare surfaces would also be attributed with names of vegetation associations, such as 3251 (Hammada scoparia - Artemisia steppe) (M. Finckh, pers comm.). In the terminology of the classification scheme and from the remote sensing point of view, these areas are assigned to non-vegetated classes. Class information in combination with the sub-region can account for further information of the vegetation associations. Table 6.7 shows the confusion matrix of the validation procedure.

Table 6.7: Land cover classification accuracies of the Basin of Ouarzazate with 9 validated classes

Class	Ground Truth (Percent)									Total
	3321	2111	4133	3251	2341	4132	1420	1111	2342	
Uncl.	0	0	0	0	0	0	0	0	0	0
3321	98.72	0	0	1.3	0	0	0	0.47	0	19.44
2111	0	93.55	0	0	0	0	0	0	0	4.18
4133	0.55	0	97.06	2.6	0	4.55	3.72	0	0.2	2.95
3251	0.73	0	2.94	96.1	0	2.27	0.45	0	0	3.06
2341	0	0	0	0	95.38	0	1	0	0.59	4.97
4132	0	0	0	0	0	93.18	0	0	0	1.48
1420	0	0	0	0	0	0	94.83	0	0	37.65
1111	0	0	0	0	0	0	0	99.53	0	7.56
2342	0	6.45	0	0	4.62	0	0	0	99.22	18.72
Total	100	100	100	100	100	100	100	100	100	100

Class	Ground Truth (Pixels)									Total
	3321	2111	4133	3251	2341	4132	1420	1111	2342	
Uncl.	0	0	0	0	0	0	0	0	0	0
3321	538	0	0	1	0	0	0	1	0	540
2111	0	116	0	0	0	0	0	0	0	116
4133	3	0	33	2	0	2	41	0	1	82
3251	4	0	1	74	0	1	5	0	0	85
2341	0	0	0	0	124	0	11	0	3	138
4132	0	0	0	0	0	41	0	0	0	41
1420	0	0	0	0	0	0	1046	0	0	1046
1111	0	0	0	0	0	0	0	210	0	210
2342	0	8	0	0	6	0	0	0	506	520
Total	545	124	34	77	130	44	1103	211	510	2778

6.2.5 Crystalline Anti-Atlas



The Crystalline Anti-Atlas is also a high mountain area with elevations of more than 3000m. The complex mixture of rock and soil made the use of five background endmembers necessary and hampered a further background differentiation, except of the ploughed fields which could be differentiated as rainfed agriculture. Figure 6.25 shows the applied classification rules. On the southern slopes on high elevated areas species of *Juniperus phoeniceae* and *Buxus balearica* were identified growing locally in reasonable

amounts and density. The growth area seems to be determined by areas with a surplus of orographic precipitation (M. Finck, 2001 pers. comm.). The area was identified according to field observations by IMPETUS botanists and supplied as a polygon layer. The differentiation between the classes 3243 (*Buxus balearica*) and 3242 (*Juniperus phoeniceae* shrubland) is possible as the class 3243 (*Buxus balearica*) is located in shaded areas, for the description of which the RMS error of the LSU was utilised (see Roberts et al., 1998). Figure 6.25 shows the classification rule applied within this sub-region.

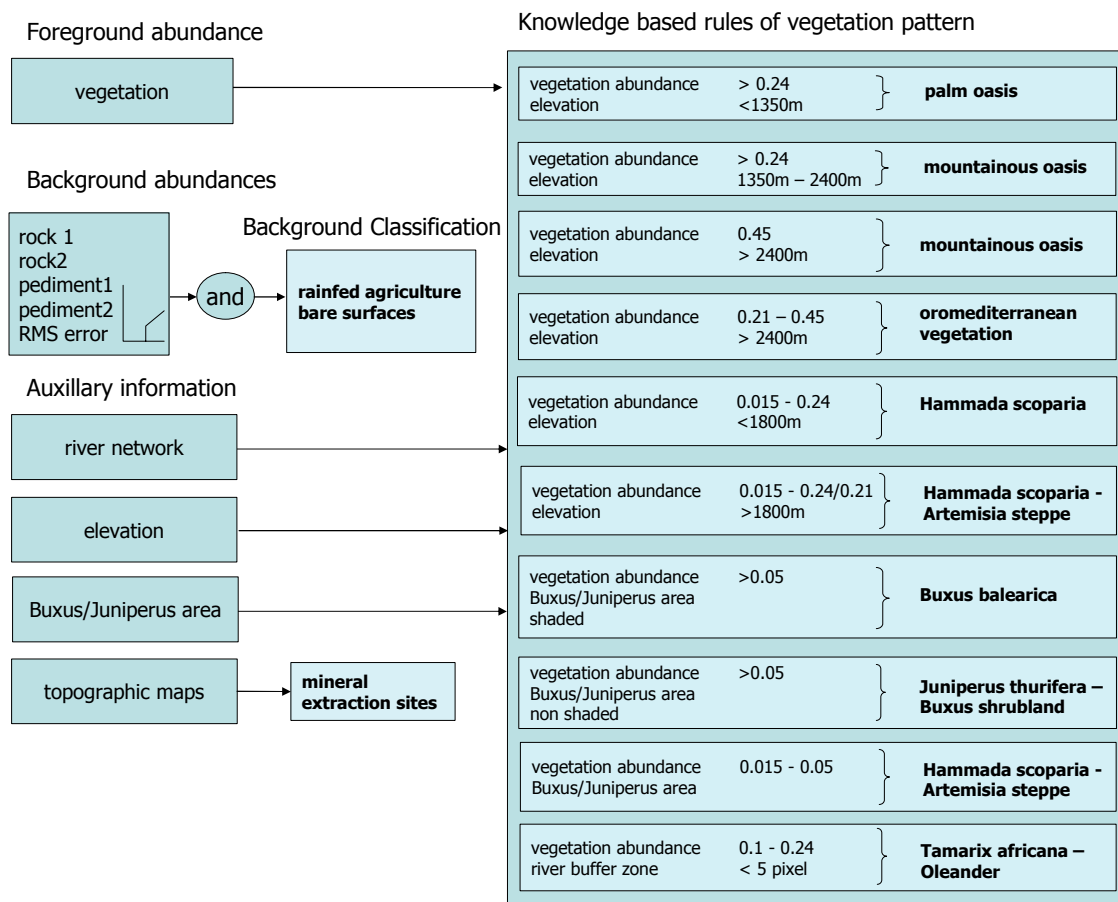


Figure 6.25: Flow chart of the land cover classification decision rules for the Crystalline Anti-Atlas

The class 1310 (mineral extraction sites) were identified either during field campaigns or extracted from topographic maps (see section 2.1). The overall accuracy is 89.89% with Kappa coefficient 0.879.

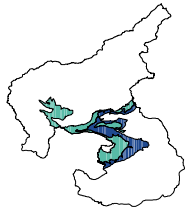
Table 6.8: Land cover classification accuracies of the Crystallin Anti-Atlas with 8 validated classes

Class	Ground Truth (Percent)								Total
	3320	3257	3251	4132	2341	3221	2111	2342	
Uncl.	0	0	0	0	0	0	0	0	0
3320	100	13.51	0.55	0	0	0	0	0	10.76
3257	0	86.49	13.66	2.63	1.53	0	3.82	0	7.52
3251	0	0	76.78	1.75	0	5.17	0	0	22.63
4132	0	0	0.27	81.58	0	0	0	1.42	7.59
2341	0	0	0	4.39	98.47	0	0	0	20.81
3221	0	0	0.27	0	0	93.1	0	0.71	4.43
2111	0	0	0	0	0	0	96.18	0	11.95
2342	0	0	8.47	9.65	0	1.72	0	97.87	14.32
Total	100	100	100	100	100	100	100	100	100

Class	Ground Truth (Pixels)								Total
	3320	3257	3251	4132	2341	3221	2111	2342	
Uncl.	0	0	0	0	0	0	0	0	0
3320	129	5	2	0	0	0	0	0	136
3257	0	32	50	3	4	0	6	0	95
3251	0	0	281	2	0	3	0	0	286
4132	0	0	1	93	0	0	0	2	96
2341	0	0	0	5	258	0	0	0	263
3221	0	0	1	0	0	54	0	1	56
2111	0	0	0	0	0	0	151	0	151
2342	0	0	31	11	0	1	0	138	181
Total	129	37	366	114	262	58	157	141	1264

The classes 3243 (*Buxus balearica*) and 3242 (*Juniperus phoeniceae* shrubland) could not be validated due to a very low number of validation data. The subsequent field campaigns will reveal the quality of the classification these two classes.

6.2.6 Sedimentary Anti Atlas



High background heterogeneity resulted in the separate treatment of two units of reduced variability. This (sub-) sub-regions are indicated on the left and were mapped according to the PMU concept (see section 2.1). The difficult to access mountainous areas were classified with limited terrain knowledge and low amount of validation data (see the confusion matrix in pixels). In spite of the small amount of validation data a land cover classification was performed.

Although the classification accuracy within this region is of less importance for the IMPETUS project, a visit of this region for further validation is highly advisable. Four background and one vegetation endmember was used in the LSU. Figure 6.26 shows the flow chart of the applied classification rules.

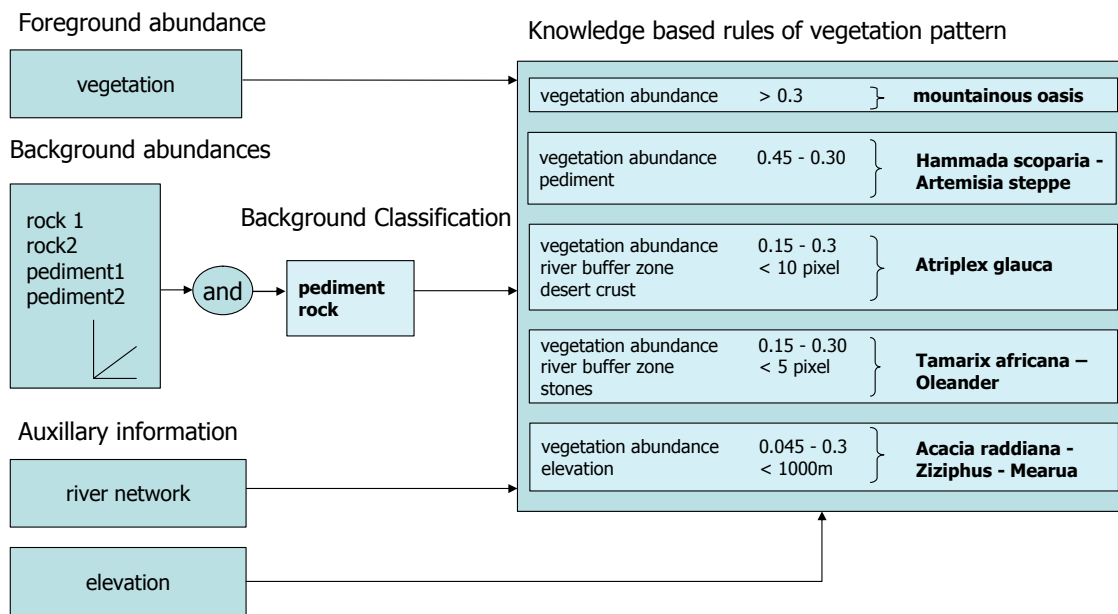


Figure 6.26: Flow chart of the land cover classification decision rules for the Sedimentary Anti-Atlas

The background information was differentiated in two classes, which were filtered with a 3×3 majority filter to improve spatial consistency. The overall accuracy for this sub-region is 89.19% with Kappa coefficient of 0.870. The confusion matrix for pixels and in percent is shown in Table 6.9.

Table 6.9: Land cover classification accuracies of the Sedimentary Anti-Altas with 6 validated classes

Class	Ground Truth (Percent)						Total
	3321	3322	3254	2342	3251	2341	
Uncl.	0	0	0	0	0	0	0
3321	100	0	0	0	0	0	20.27
3322	0	100	14.29	0	0	0	18.92
3254	0	0	64.29	0	25	0	16.22
2342	0	0	0	100	0	0	14.86
3251	0	0	21.43	0	75	0	16.22
2341	0	0	0	0	0	100	13.51
Total	100	100	100	100	100	100	100

Class	Ground Truth (Pixels)						Total
	3321	3322	3254	2342	3251	2341	
Uncl.	0	0	0	0	0	0	0
3321	15	0	0	0	0	0	15
3322	0	12	2	0	0	0	14
3254	0	0	9	0	3	0	12
2342	0	0	0	11	0	0	11
3251	0	0	3	0	9	0	12
2341	0	0	0	0	0	10	10
Total	15	12	14	11	12	10	74

6.3 Discussion and outlook

Image decomposition by spectral unmixing techniques transform multispectral information in membership grades of endmember spectra. The membership grades were interpreted as fuzzy sets which allows the interpretation of the inherent information in the satellite image in a more physically related sense than dimensionless DN_s. The differentiation of foreground vegetation and background soil information appeared to be very useful. Knowledge, based on field observations, of the growing conditions of vegetation associations related to these physical properties, could be formulated as decision rules. By incorporating auxiliary information in the sense of a hybrid classifier and knowledge based decision rules of fuzzy sets an expert classification system was implemented in IDL program codes within ENVI. The classification rules were formulated on the basis of the classification scheme (see Table 3.1) for the Dra catchment. The whole catchment was classified by merging land cover map-

pings from six sub-regions differentiated according to the principle of PMU mapping (see section 2.1). The overall classification result from the six sub-catchments of the validated classes is shown in Table 9.1.

Table 6.10: Classification accuracies of the six sub-regions of the Dra catchment

	Overall accuracy [%]	Kappa coefficient	Nr. of classes	Size [km ²]
High Atlas	92.4	0.898	6	4642.5
Basin of Ouarzazate	96.8	0.958	9	2651.1
Crystallin Anti Atlas	89.9	0.879	8	7213.8
Sedimentary Anti Atlas	89.2	0.870	6	3706.1
Basin of Tazenakht	96.5	0.951	8	919.7
Dra valley	82.2	0.795	18	9286.0

The classification approach is more successful in the basin areas: the Dra valley, the Basin of Tazenakht and the Basin of Ouarzazate compared to the mountainous areas. Within these areas the background information is better distinguished compared to the (complex) geology in the mountainous regions. Problems arise if the background heterogeneity is too high. This resulted in a reduced number of differentiable (background) classes or even class assignment on the hierarchy level three as in the High Atlas and the Crystalline Anti-Atlas. Regardless of these difficulties, the vegetation abundance was less background influenced than the NDVI. Within the land cover classification the actual vegetation coverage is represented, which is the parameter of relevance for the derivation of biophysical parameters and the data integration into meteorological models, as required by the IMPETUS project. The classification accuracy in the Dra valley was improved by merging two classes contain *Acacia raddiana* (3261 and 3263) and by removing errors due to false ground truth data collection to 93.1% with Kappa coefficient of 0.918.

Further improvement might be possible by incorporating a dry biomass endmember as proposed by Roberts et al. (1998); Hill (2000) potentially on smaller areas, with less heterogeneity and more ground measurements. This could lead to an end-member combination with different, potentially improved interpretation and classification possibilities. Especially the difficult to detect *Acacia raddiana* classes 3261, 3262 and 3263 will most probably improve. Improvements of this approach are most likely by the use of this classification approach with satellite data in higher spectral resolution, such as ASTER. Potentially within soil information the degree of salinity can be estimated.

The classification detail and accuracy are very high for a land cover map derived with LANDSAT data, especially with regard to the large catchment area. For the mapping with a sub-pixel approach of this large catchment, including five LANDSAT ETM+ scenes, the use of a radiometrically corrected image mosaic of high quality was crucial. The status and the density of the vegetation is always dependent on the image acquisition time and growth status within the phenological cycle of the plants. The image mosaic was generated from five almost cloud-free LANDSAT ETM+ images recorded within the same month. The vegetation growth state is however different in the lower elevated regions than in the mountainous areas and might also differ due to localised precipitation events.

In theory the presented classification results can also be achieved with classical classification approaches, such as the MLC. But to achieve a land cover classification in comparable detail and quality an enormous amount of training and test pixels would be necessary, not only due to the normal distribution constraint of training pixels, but also to differentiate between the often similar (vegetation-) class spectra. During this work, especially with regard to the size and complexity of the region, this was impossible. This drives also the concept of remote sensing *ad absurdum*, therefore, that if during the ground truth campaigns almost the whole area needs to be sampled or mapped.

One draw-back of the approach of using only relatively normalised data is that the thresholds within the decision rules are only transferable to data normalised to the data of this study. Since no atmospheric correction was performed, all thresholds are based on relative abundances, such that the same thresholds need modification if they are to be adapted to other regions. On the other hand the creation of a spectral library requires a perfect atmospheric correction, which is currently not available from any existing algorithm.

It could be argued that a more suitable result of the spectral decomposition would be the abundance layers of the endmembers. These could then be used, by applying user specified decision rules, to serve for a dynamic generation of products. In theory, this concept would be more flexible, but every mapping product is usually derived with a certain (main-) focus and only within that focus will the best or most reliable results be achieved. Nevertheless, an interpretative potential within the abundance channels that can be utilised for a variety of analysis and interpretations has been achieved/developed. The approach to incorporate all potential layers of information into one database would be ideal. The initiative of Africover (2003) is in fact leading

in this direction.

6.4 Conclusion

A map of the actual vegetation/land-cover of the Dra catchment was successfully generated and merged of the sub-region classifications and is enclosed as addendum. A classification approach was presented that produces remarkably good results, as judged by comparison with the validation dataset. The outlined analysis of the sub-pixel information above seems suitable for classification purposes in the project region. The number of classes within the sub-regions is dependant on factors such as the terrain knowledge, the unmixing quality and the surface heterogeneity.

Apart from adequate terrain and vegetation knowledge as a prerequisite for this approach, no assumptions are made that limit this approach to the described project region. For the LSU and SAM no assumption on normal distribution of training pixels is required, decreasing the number of pixels that are required for the classification. The classification approach is based on the decomposition of a remote sensing image in abundance information that can be more easily interpreted and classified, even by non remote sensing experts. The approach is deterministic, repeatable, and offers other differentiation capabilities than conventional hard classifiers. Integration of data with different resolutions for validation purposes, is only possible with appropriately geometrically corrected images.

The implementation of an expert classification system requires the knowledge and understanding of the eco-physical environment and the complex regulation pattern. A recommendation is therefore that remote sensing should not stand at the beginning of a research project and be designed to purely deliver e.g. NDVI data for potential users. The amount of information that can be extracted from the data is much higher if additional ground knowledge is incorporated, as the presented work has demonstrated. The applied methodology can generally be extrapolated to other regions of the world with similar environmental conditions.

7 Change Detection: what to detect?

”Change is the only constant”

T. McVicar, 2003

Land cover change refers to changes in the attributes of the land surface. Since in several regions around the world land cover changes occur rapidly, remote sensing provides a valuable source of information to detect changes, due to the repeating data recording and the synoptic view of areas (Singh, 1989). A prerequisite to detect land cover changes by the use of remote sensing data and methods is, that the changes in land cover result in changes in the surface spectral properties. These changes must be significantly larger than data noise, such as those induced by the recording platform or differing atmospheric influences (Mas, 1999). Donoghue (1999) states that: ”At a global or regional scale remote sensing offers the only practical method of change detection.”. With regard to historic data archives remote sensing data are often the only source of information for detecting long term changes. With the release of data from the first CORONA missions, satellite data are available to the public since 1960 (Ruffner, 1995). Multispectral data from the first LANDSAT missions start in 1972. The comparison of the historic data with recent or actual data is challenging, not only due to the changed sensor characteristics. Examples of satellite based change detection applications are reviewed by e.g. Singh (1989) and Lunetta and Elvidge (1998); Mas (1999).

The assessment and/or quantification of changes in land cover is an important task, not only in modelling and forecasting studies, but also for the identification of problematic zones for resource management plans or decision making support.

The task of quantifying changes requires that data are suitable to show the changed objects and need to be pre-processed in a manner that the data are comparable. Singh (1989) sees as a major problem in change detection studies the accurate

image (co-) registration. Verbyla and Boles (2000) calculated errors in change detection studies due to mis-registration. Their investigation showed, that a false change identification due to mis-registration rises with the number of classes within a classified image and with land cover heterogeneity. This implies that either a careful pre-processing or methods with less sensitivity to mis-registration are necessary (Singh, 1989).

Different methods of change detection and their specific advantages and problems are outlined, with reference to the data, application, and purpose.

7.1 Data

For change detection applications using data from different origins and view geometry, such as analog CORONA and digital IKONOS-2, the image characteristics require special attention (see chapter 4 and subsection 7.2.3). Due to the differing view geometry, image displacements can become considerable (see chapter 4). The comparison of multispectral and panchromatic data requires additionally knowledge of the objects of interest.

Spectral characteristics of data recorded from the same satellite program, such as SPOT or LANDSAT, changed during the operation time and need consideration in comparisons. Starting with the MSS sensor, LANDSAT data were recorded in 4 spectral channels with a spatial pixel resolution of $79m \times 56m$. From 1984 onwards the TM sensor obtained images in 7 spectral bands with a spatial resolution of $28.5m \times 28.5m$. Due to a shift in the spectral range of the recorded bands the comparison is not a straightforward process. The characteristics for the multispectral data of ETM+, operating since 1999, are mostly the same as for TM. In order to compare ETM+ and TM data radiometric normalisation techniques, either relative or absolute, are common (section 5.3). In the case of an MSS to TM/ETM+ comparison, the spectral bands, and thus also the ratios of the bands or common indices like the NDVI, are not directly comparable. A solution to these problems usually involve atmospheric corrections or post classification change detection methods (Singh, 1989). Often information about historic atmospheric conditions and land cover/land use for an image classification at the time of the image acquisition is difficult or even impossible to obtain. In these cases robust change detection methods that overcome these difficulties are needed.

7.2 Methods and results

In the following sections several change detection methods are outlined. At this stage of the work methods were identified and evaluated as case studies at "hot spots" of change to identify methods to apply potentially for the whole catchment or certain sub-regions. The applied methods were case dependent to satisfy the given application.

7.2.1 Visual interpretation and object digitalisation

LANDSAT

Certain changes and processes can be visualised simply by the generation of colour composites and their interpretations. The representations of 1) colour, 2) patterns and c) texture as described in section 2.1 and the knowledge about reflectance properties help the observer to identify objects and interpret satellite data. The inspection of FCCs is usually the first approach to identify and analyse multi-temporal data and changes. Figure 7.1 shows an example of the region around the Lac Iriki.

The red colours represent in both images photosynthetically active vegetation due to the spectral band combination. The visual analysis, in conjunction with historic data and actual ground truth data can serve to aid understanding and analysis of environmental changes. Figure 7.2 shows photos of the Lac Iriki in 1969 filled with water during a wet period in the late 1960s (Hnichi, 1989) and with riparian vegetation (*Tamarix africana*).

This vegetation seems to have completely vanished in the image recorded in 2000. A major cause for this change is the dam built upstream near Ouarzazate in 1972 (see section 2.1). From that time onwards water regulation prevented spring floods or runoff from heavy rainfall events in the High Atlas mountains from reaching this area frequently (Hnichi, 1989). The rare local precipitation events are usually insufficient to contribute to plant existence. An enormous rainfall event in spring 1989 filled the dam so completely that surface water was draining directly through the Oued Dra in such an amount, that even surface water drained into the Atlantic ocean. During the 20 years of water absence the natural water course to the Lac Iriki was filled with sand so that flood water could no longer reach this area. Figure 7.3 shows the actual vegetation situation.

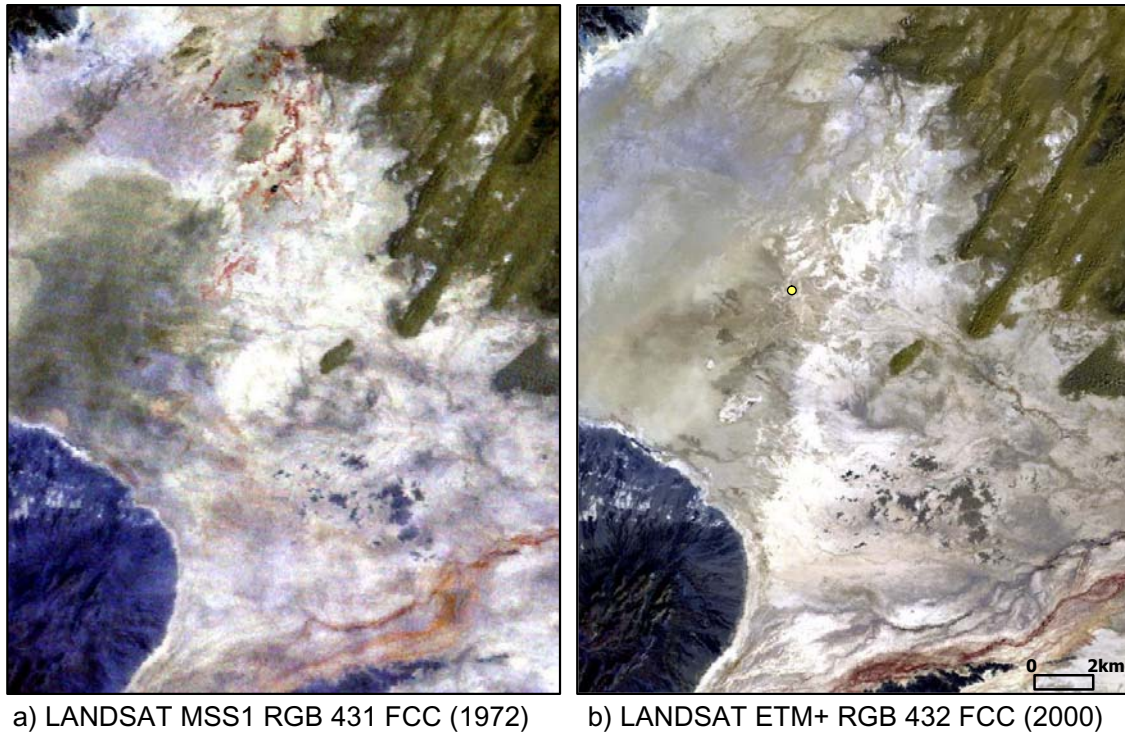


Figure 7.1: LANDSAT MSS and ETM+ RGB image subsets of the region around the Lac Iriki, in a) September 8, 1972 and b) October 25, 2000 (indicated is the area of the photo in Figure 7.3 with UTM coordinates 744299/3300598)

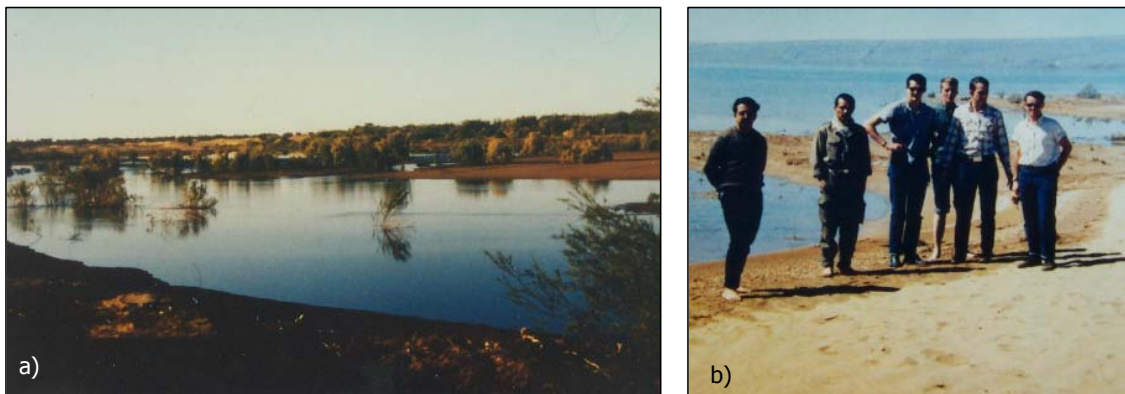


Figure 7.2: Photos of the region around the Lac Iriki in 1969, source: O. Abdellaoui

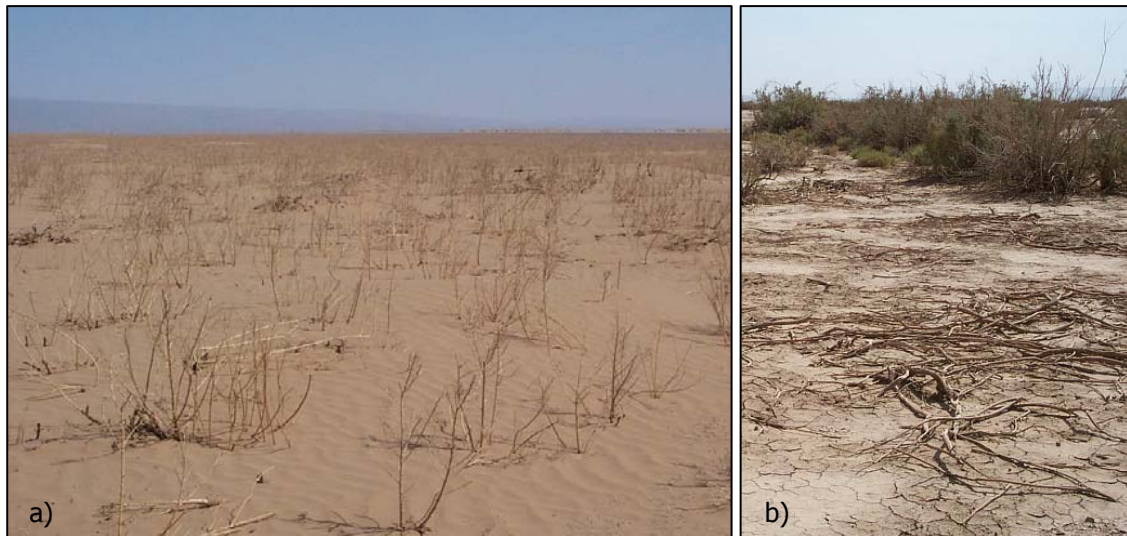


Figure 7.3: Photos of the region around the Lac Iriki in 2000, source: M. Schmidt

Attempts to reactivate the ancient riverbed and the initiative to create a national park of this area were not supported by the Moroccan government.

CORONA-IKONOS

For certain analysis, especially with very high resolution data, a visual image interpretation might be sufficient. For example by object identification for military purposes or if the data quality is too low for automated analysis. As with any subjective interpretation method, an interpretation key must be defined to avoid misinterpretations. For the purpose of visual change identification, data from IKONOS-2 and CORONA were used from 1972 and 2001. As an example the town of M'hamid was chosen to display the change of the extent of the desert town. The IKONOS-2 multispectral bands were fused with the panchromatic band (see Table 5.1, for the spectral characteristics) with the Brovey method to obtain an (almost) true colour composite with 1m resolution (RSI, 2002; Canty, 2002). The fused bands \overline{DN}_i are generated as follows:

$$\overline{DN}_i = DN_{highres} \cdot \frac{DN_i}{\sum_{i=1}^n DN_i}$$

where n is the number of bands used, $DN_{highres}$ denotes the higher resolution band while DN_i are the multispectral bands. The spectral range of the bands in this approach is assumed to sum up to the high resolution band range. For

this purpose, calibrated IKONOS-2 bands 1,2 and 3 were used to generate a color composite of the first three fused bands ($n=3$) in $1m$ resolution. With this rather simple fusion method, colour images in high resolution can be generated, with some loss of spectral information. These data were used in combination with co-registered CORONA data for a visual change identification. The town of M'hamid is located within the CORONA KH4B from mission DS-1117 from 1972 (see chapter 4) at the fringe of the recorded image strip and inherits large distortions and a decreased spatial resolution (see Figure 7.4). The CORONA KH4A data were supplied by the University of Gent, Belgium, where the data on film strips were photographically enlarged (by a factor of 10) and scanned (at 400 dpi). The extension of the town M'hamid was digitised in three time steps according to 1) dominating tonality or colour, 2) patterns (dots, lines, patches etc.) and c) texture following the concept of PMUs (see section 2.1, (Daels and Antrop, 1977)). The town of M'hamid grew enormously within the 37 years, similar to the towns of Ouarzazate and Zagora. To show the changes in Figure 7.4 on the basis of very high resolution satellite images, a vector layer with the extent of the town in 2001, was overlaid on the images from 1972 and 1964.

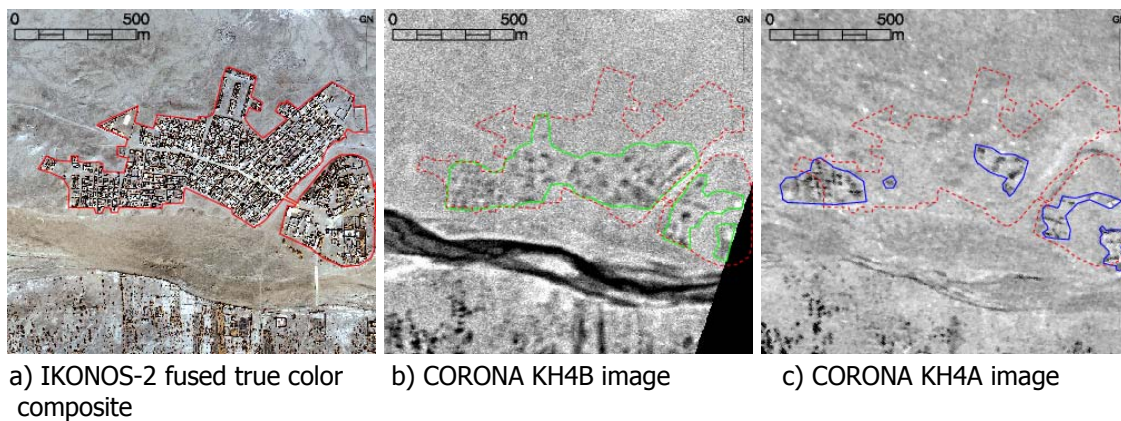


Figure 7.4: The size of the town M'hamid in a) 2001 (red), b) 1972 (green) and c) 1964 (blue)

Beside population growth, a reason for this general tendency in the Oasis systems of Morocco is that people tend to live in modern stone houses rather than in the traditional Ksars or Kasbah (Ait-Hamza, 1997). Although the sealed road ends in M'hamid, the town recently became attractive for the growing desert tourism as a starting point for desert trips (Popp, 2000). The size of the town M'hamid was,

according to the digitised polygons, in 2001 53.1ha, 25.7ha in 1972 and 10.8ha in 1964 (see Figure 7.4). This implies a growth in area by a factor of 4.9. The left polygon in Figure 7.4 c) might be part of the town in 1964, but more probably was an agricultural area. In this case, by excluding this polygon, the size of the town was only 6.1ha corresponding to a growth factor of 8.7.

7.2.2 Analysis of multitemporal NDVI data

This study aims to investigate if changes in the rangeland vegetation coverage are potentially detectable with LANDSAT data and the NDVI. Four LANDSAT TM5 image subsets (280×232 pixel) from the local project partner ORMVAO were co-registered with an RMS error of less than 0.5 pixel. Three subsets from LANDSAT data, as described in chapter 5, were included to build a time series with seven LANDSAT scenes in total with of 28.5m pixel size. The time series of LANDSAT TM5/ETM+ data were relatively radiometrically normalised to the "master" scene dating from May, 2 in 2000 as described in section 5.3. The area of observation is a test plantation with species such as *Artemisia herba-alba*, *Anabasis articulata* etc. (see Ouaskioud, 1999, for further details) of the ORMVAO, initiated in 1979, when fences were built to exclude nomadic grazing. In 1982, a controlled grazing program was initiated (Ouaskioud, 1999). Figure 7.5 shows the area of the test plantation in the basin of Ouarzazate (center coordinates: 794940/3475809).

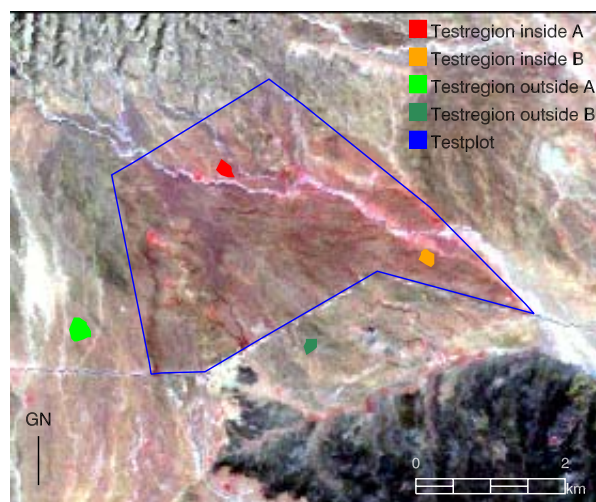


Figure 7.5: Test area of the ORMVAO, displayed in a LANDSAT ETM+ RGB 423 FCC subset of November 24, 1999

The NDVI time series represents an increasing NDVI trend during the time and generally a higher signal in the inner plot than outside at all time steps. The subregions A and B in Figure 7.5a) represent areas with similar soil type and vegetation coverage inside and outside the ORMVAO testplot. The image dating from 1999 is the only scene from winter, showing in this year relatively wet conditions, resulting in the peak in NDVI.

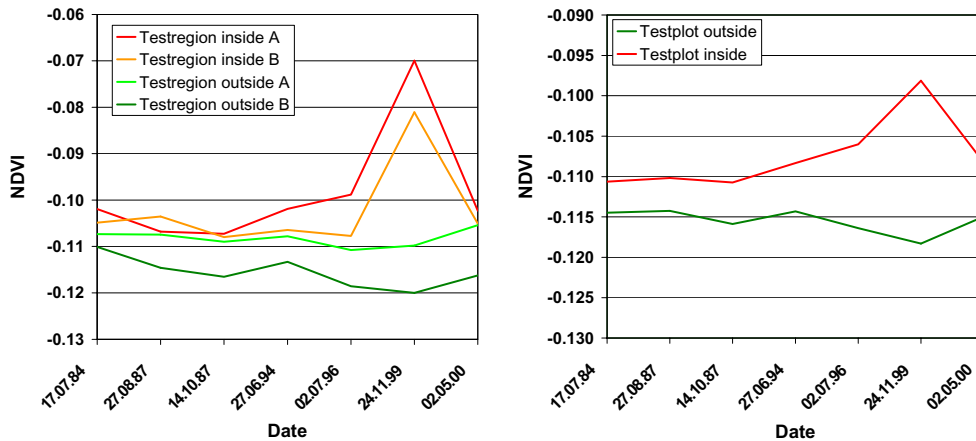


Figure 7.6: Comparison of NDVI values inside and outside the testplot at different time steps. a) shows regions inside and outside the test plot with similar soil coverage, while b) displays the mean values inside and outside.

This long term vegetation monitoring shows that the exclusion of certain surfaces for grazing has an effect on the vegetation cover and that the system generally seems to have the potential to recover and regrow in undisturbed conditions. The test plot was given up in 2000 and grazing started again (M. Finckh, pers. comm).

The comparison of image ratios, differences and indices is possible due to the image normalisation. As shown in section 5.3 the effect of illumination differences on non-shaded surfaces is reduced due to the relative radiometric normalisation.

7.2.3 Post classification change detection

7.2.3.1 Long term change detection with very high resolution data

Background and motivation

Overgrazing or inappropriate land use, together with periods of drought and climatic changes, threaten to destroy the natural resources in south Morocco in an

irreversible manner. The German Ministry of Economic Cooperation assists the Moroccan government in the implementation of the project "Combat Desertification in the Dra Valley". Part of the project is special attention to protect the oasis of M'hamid, a component which is co-financed by a micro-project of the Global Environment Facility. One aim of this project is to stop or at least to slow down the desertification process on a regional basis. This study can be seen in the framework of the United Nations Convention to Combat Desertification, which is signed and ratified by the Moroccan and German governments. The objectives in the M'hamid region are twofold: on one hand to improve the irrigation system of the oasis in order to protect the oasis from inside and on the other to protect tamarisk plants nearby the oasis in order to prevent the oasis from mobile sands. The latter objective is followed within this study and described in the following section. Figure 7.7 shows an example of attempts to fix mobile sands that move into a palm oasis. It is especially important to understand the ecosystem as a whole and to know whether changes in vegetation cover are due to human actions or due to hydrologic changes as a consequence of the dam construction further upstream near the town of Ouarzazate in 1972.

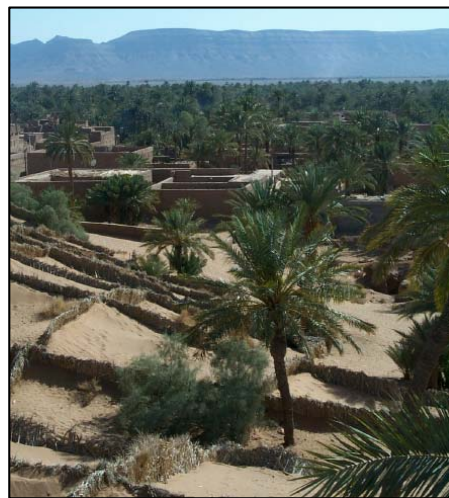


Figure 7.7: Example of an oasis protection against mobile sand, south of Zagora
Photo: M. Schmidt, 2001

Approach

The approach chosen includes mappings on the basis of high resolution satellite data. Due to the location of the study area close to the Algerian border ($\approx 2km$)

aerial photographs are difficult or impossible to access. Until recently the number of applications dealing with very high resolution datasets is still low. One reason for this is that IKONOS data have only been available since 1999, but also because these data have inherent problems due to the oblique viewing angle and the resulting image displacements (Baltasavias et al., 2001). Hence, very high resolution data need special attention (Schmidt et al., 2003a) in order to map in real-world coordinates and integrate the results in a GIS. The aim of this study is to investigate changes in a natural forest of *Tamarix aphylla* and *Tamarix africana* in the northern fringes of the Sahara in South Morocco (see subsection 6.2.2). To some extent halophytic tamarisks tolerate a soil salinity of up to 2-3% and accumulate sand in little hills of clay, sand and nutrients. These trees are growing in extreme ecosystems and fix not only mobile sand, but also are a rare habitat for the almost extinct local fauna, e.g. the desert fox. Very high resolution satellite data were chosen to achieve the individual mapping of the trees. Historic CORONA data with a nominal ground resolution of 1.8m (see subsection 4.2.1) were used in combination with recent IKONOS-2 data with a ground resolution of 4m in the multispectral channels (see subsection 6.2.2). The geometric data properties of the two datasets are discussed briefly in order to understand and interpret the displayed changes in vegetation cover.

The IKONOS image used in this application was recorded with a satellite view angle of 21.8°. Due to the flat surrounding terrain only the object displacements of the tamarisk hills need consideration. Object displacements can be expressed as a function of the view angle and the object height (see chapter 4 for further details), e.g. a 10m object leads to a displacement of 4m at a view angle of 21.8° (Figure 7.8).

In the case of CORONA data the image displacements are smaller due to the lower view angle. The CORONA data were recorded stereoscopically and thus the image with the best geometric characteristics can be used. Ideally, the approach would be to record GCPs for a photogrammetrical restitution and the generation of an orthophoto map. In the sandy terrain with no infrastructure lines, the identification of GCPs is difficult. The meta-information of the CORONA and the IKONOS data are shown in Table 7.1.

The CORONA data of the DS-1117 mission have a collection azimuth angle of approximately 350° in the afterwards image, which corresponds well with the values of the IKONOS scene. This means that by the use of the afterwards image the objects are displaced in the same direction.

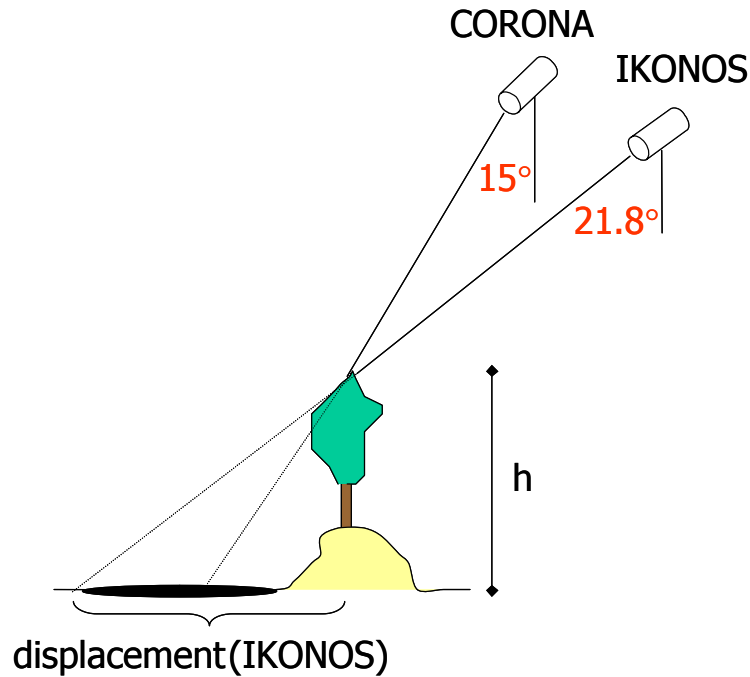


Figure 7.8: Image displacements by CORONA and IKONOS satellite viewing geometry, adapted from Schmidt et al. (2002)

Table 7.1: Meta information of CORONA KH4B (26.05.1972) and IKONOS-2 (23.11.2001) data used in this study

Satellite	IKONOS-2	CORONA	CORONA
Image mode	oblique	forward	afterward
Collection Azimuth	347.2°	$\approx 170^\circ$	$\approx 350^\circ$
View angle	21.9°	15°	15°
Date of Acquisition	26.11.2002	26.05.2001	26.05.2001
Sun azimuth	164.3°	$\approx 160^\circ$	$\approx 160^\circ$
Sun elevation	38.4°	$\approx 70^\circ$	$\approx 70^\circ$

The darker pixels in the CORONA image represent the objects (tamarisk and the hill) plus the object shadow (see Figure 7.8). The sun elevation of approximately 70° in May is equivalent to an illumination angle of 20° . This means that the shadow of the object on the flat terrain has a larger extent than the object displacement resulting from the 15° view angle. The sun azimuth angle of approximately 160° results in

an object shadow in the direction of the image displacements. Thus, the dark pixel can be interpreted as objects plus their own shadow. The view angle of the IKONOS sensor is 21.8° at an collection azimuth of 347.2° , which results in object displacements in the same magnitude as derived from the CORONA images (Table 7.1). (The and sun azimuth angle of 164.3° of the IKONOS-2 data accounts for the situation that the IKONOS-2 objects are displaced above the shadow.) Thus, spatial comparisons between the polygons calculated from NDVI values of the IKONOS-2 data (see subsection 6.2.2) and the tamarisk hills derived from the CORONA image are possible (Figure 7.9). This is important to recognise because otherwise changes could not be detected accurately. The classified polygons of the IKONOS-2 data were (see subsection 6.2.2) used in comparison with polygons of vegetation coverage derived by an image threshold of the CORONA data. Polygons covering areas smaller than one pixel were ignored. The vector layers were analysed in ArcView. Figure 7.9 shows the two vegetation layers from 1972 and 2001.

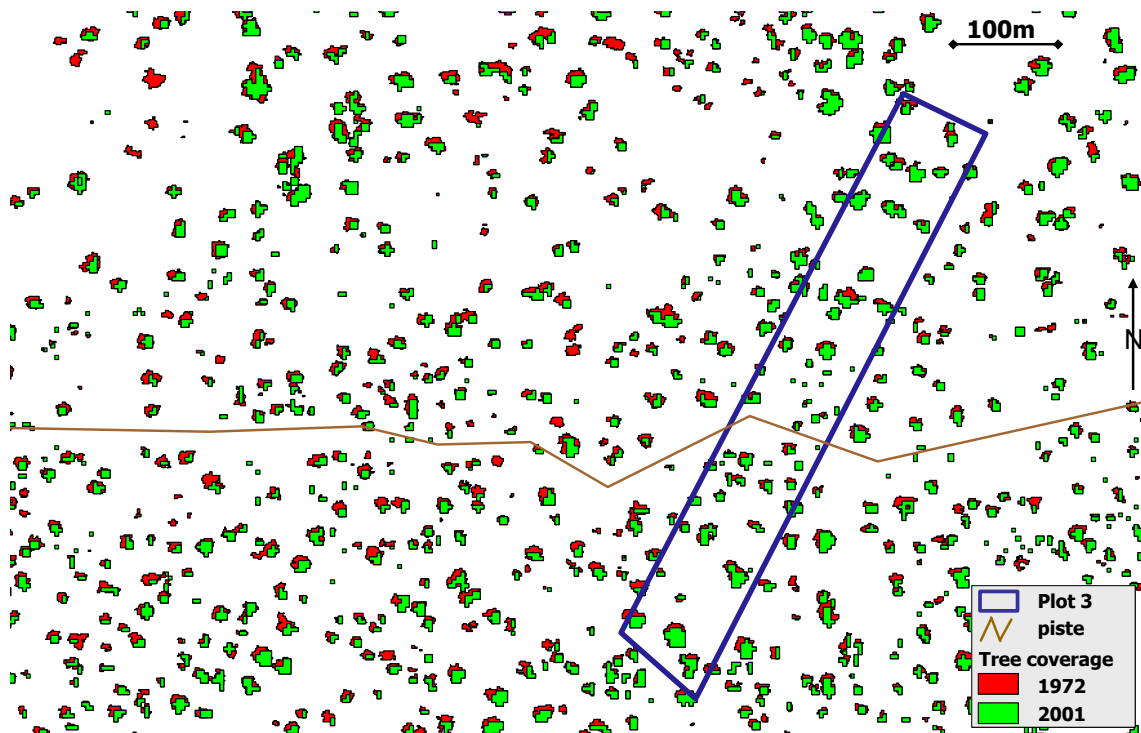


Figure 7.9: Example of the tamarisk coverage of 1972 (red) and superimposed in 2001 (green) as derived from CORONA and IKONOS-2 data

The tamarisk coverage as obtained in 2001 is shown in the green polygons, while

the distribution in 1972 is displayed in a red layer underneath. Thus areas appearing in red show tamarisks existing in 1972 but not in 2001. The difference in the shape of the polygons can be explained by the different spatial pixel resolution: 4m in the case of the IKONOS data, while the CORONA data are displayed in 1m resolution (although the ground resolution is around 1.8m). In this representative area near Plot 3 (see subsection 6.2.2) only small changes in the total number of the tamarisks occurred, as shown in Table 7.2.

A slight decrease in spatial coverage with tamarisks happened in Plots 1-4. Although the total number of tamarisks did not change drastically during the 30 years of investigation, the total area covered by tamarisk trees in Plot 5 changed enormously. This is due to the growth of the individual tamarisks. Changes in the hydrological cycle did not lead to a general and dramatic reduction of the number of tamarisks. In Plot 5 the number and the total coverage of tamarisk trees even increased.

Table 7.2: Land cover changes as mapped with CORONA KH4B (1972) IKONOS-2 (2001) data in representative test plots (see also subsection 6.2.2)

Plot	Satellite	Nr. of trees	coverage [%]	cover change [%]
1/2	IKONOS	31	0.087	-0.83
	CORONA	33	0.088	
3	IKONOS	60	0.086	-8.70
	CORONA	61	0.094	
4	IKONOS	79	0.041	-4.54
	CORONA	81	0.043	
5	IKONOS	48	0.039	98.82
	CORONA	43	0.020	

7.2.3.2 Case study of multispectral long term change detection of the palm oasis near Zagora

In order to overcome the problems of different sensor radiometry, a method is proposed that uses a LSU approach by categorising the surface in temporally invariant features as image derived end-member spectra (see subsection 6.1.2).

Data spanning over three decades of the LANDSAT program, MSS1, TM5 and

ETM+ of the years 1974, 1984 and 1999 were chosen from a similar time of the year to have similar vegetation growth states and illumination conditions. The data were geo-corrected as described in subsection 5.2.1. The LANDSAT MSS image was resampled to the same spatial resolution of 28.5 meters as TM and ETM+ data. In order to monitor the changes in land use/land cover a LSU was applied to derive classifications of the three times by the use of 4 image-derived endmember spectra (chapter 6). The endmember spectra were chosen as proxies to describe the ground variability (Adams et al., 1995). Features were selected that could well be identified in all the images: rock, playa, sand and vegetation. Figure 7.10 shows the spectra of the image derived endmembers of the LANDSAT TM scene. An LSU was applied to all three images with the same set of spectra. The endmember spectra vegetation was taken from densely vegetated palm oasis with high NDVI values in each image. The variations of the other three endmembers was assumed to be low over time and were taken from the same location in all the other images.

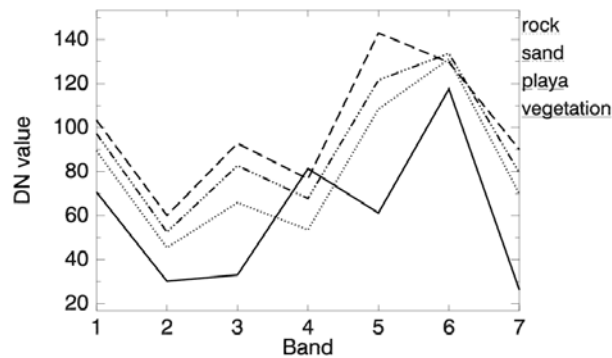


Figure 7.10: Endmember spectra used in the LSU approach in the case of the LANDSAT TM data

The class 2342 (palm oasis) was derived by identifying a threshold value of the vegetation abundance channel with the same threshold in every image. Pixels with more than 30% of vegetation abundance were classified as 2342 (palm oasis) areas (Figure 7.11). Additionally the abundance information was used as density information of the class to describe the inner-class changes.

For the class 2342 (palm oasis) several pixels were identified in advance, in order to compile the endmember spectrum for the LSU and additionally reference pixel for the class-validation. For the validation, pixels of the scene dating from December 19, 1999, and ground truth data from October 2000 were used, assuming that no major changes occurred in the intervening period. For the historic data (1974) a validation

7 Change Detection: what to detect?

with independent data is more difficult. "Validation" pixels were identified visually within the images prior to the classification and a cross check was made with local authorities (O. Abellaoui, pers. comm.). This was the only possible approach to obtain historic information. This method is only possible due to the distinct differences between the desert and a palm oasis. With this approach only the very dense vegetated areas were identified explaining the high validation accuracies.

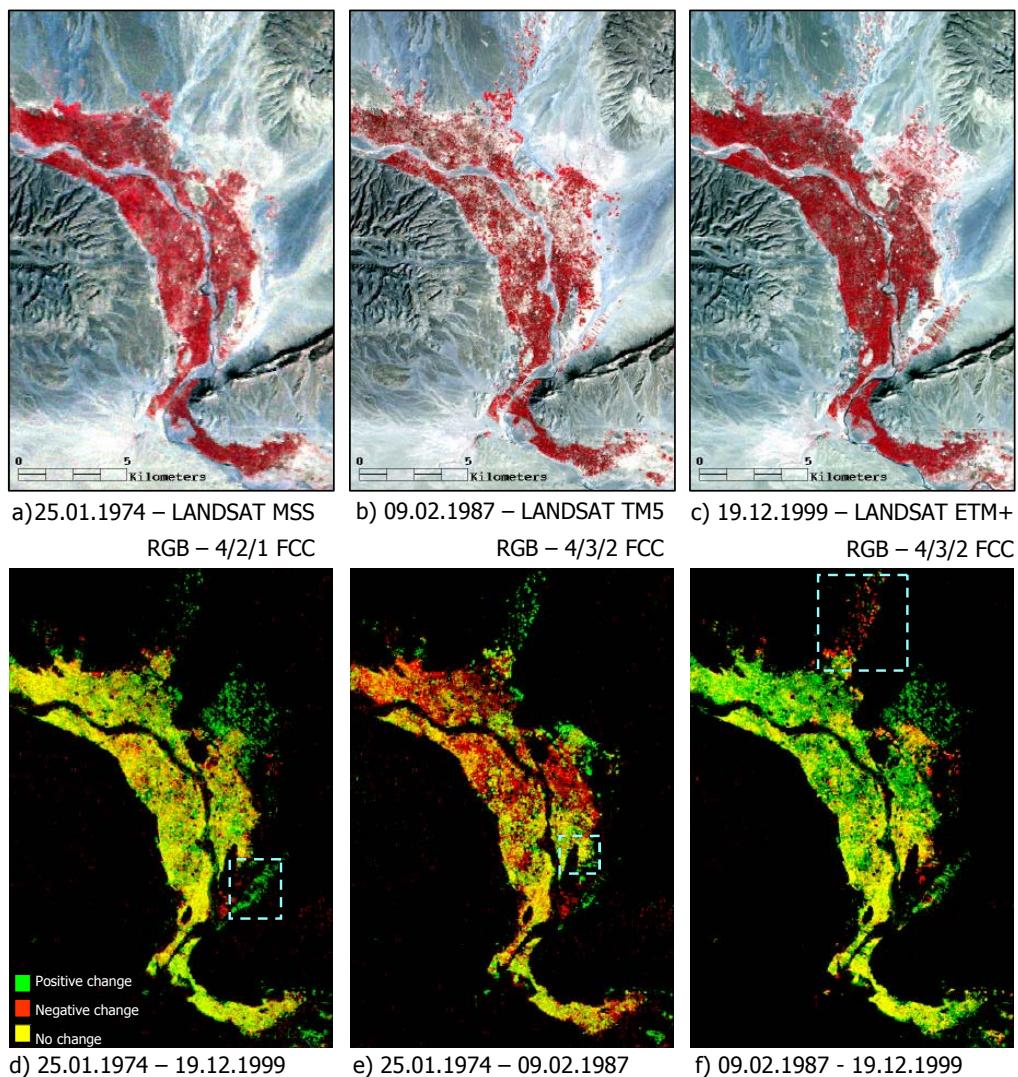


Figure 7.11: Visualisation of change in the vegetation abundance (with more than 30 % of spectral abundance), displayed in a FCC RGB - image1/image2/zero composition; three example areas of change are marked (explanation in the text)

Table 7.3: Accuracy assessment for the three classification time steps

class ID	3251	3312	3322
Year	1974	1987	1999
Nr. of training pixels	74	39	111
Nr. of validation pixels	412	71	152
Overall accuracy	100	100	99.2

The validation results are shown in Table 7.3. In 1974 16.7 % of the observed area was covered with the class 2342 (palm oasis), in 1987 11.6 % and in 1999, after two successful agricultural years 18.8 % (Figure 7.11). During the drought in the 1980s (Figure 2.2) production was only possible in areas with deep wells and diesel-pumps (O. Abellaoi, pers. comm.). Extensions of the traditional palm oasis started when working emigrants returned from Europe with enough money for diesel-pumps and wells (marked area in Figure 7.11 e), f)). In the early 1970's a sedentisation process of nomads began due to population growth and social changes (Ait-Hamza, 1997). Former pasture land became farm land, e.g. the marked area in Figure 7.11 e). Especially in this area many new farms appear 1987. Figure 7.11 f) displays a negative trend compared to 1999. This is, as discussions with local authorities revealed, the result of the lowering ground-water level, mainly due to intensive irrigation by the use of diesel-pumps. Hence many farms had to be given up again after only a couple of years. For more detailed interpretations the abundance values of the class 2342 (palm oasis) were used to indicate a density information of this class. Figure 7.12 a) shows some representative abundance values for parts of a dense oasis where the vegetation density was always high through the three time steps.

Figure 7.12 b) shows some abundance values of the indicated area in Figure 7.11 e), where the above mentioned processes can be shown: recently founded farms usually work with diesel-pumps on former pasture land, where no big palm trees exist. The irrigation often results in salinisation effects and after a couple of years this leads to the negative change when comparing 1987 to 1999 in areas of poor drainage. The corresponding abundances to the area marked in Figure 7.11 f) are displayed in Figure 7.12 c), where in 1974 no vegetation existed and during the following 3 decades a large area of irrigation extension was created (Figure 7.13).

7 Change Detection: what to detect?

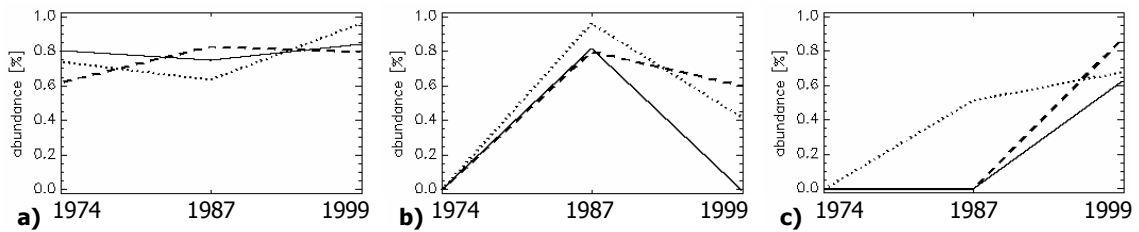


Figure 7.12: Representative vegetation abundance values of the three time steps of investigation a), b), c) for the region marked in Figure 7.11 d), e), f)



Figure 7.13: Irrigation area (see Figure 7.11 c), f)) near the town of Zagora (Photo: M. Schmidt, 2000 - view direction: North/East)

The transfer of this method to the sparsely vegetated rangelands needs further research and potentially better validation data, especially if LANDSAT MSS data are incorporated in a change detection study.

7.2.3.3 Case study of operational high resolution post classification change detection in the Basin of Tazenakht

The aim of this study was to analyse the feasibility of a classification for a sub-region (see chapter 2) at an historic time step without operator interference with the same decision rule and abundance thresholds as described in chapter 6. A LANDSAT5 TM scene obtained on April 5, 1987 was geometrically corrected as discussed in subsection 5.2.1 with a pixel size of $28.5m$ and relative radiometric normalised to the master scene from May 2, 2000. The regression coefficients of the relative radiometrically normalisation were calculated with 5600 no-change test pixel of the MAD algorithm and are shown in Table 7.4.

Table 7.4: Slope (a), intercept (c) and the correlations of the relative radiometric normalisation of LANDSAT TM5, April 1987 towards LANDSAT ETM+, May 2000

channel	a	c	correlation
1	0.759	20.106	0.979
2	1.387	22.877	0.984
3	1.225	35.356	0.986
4	0.791	18.999	0.989
5	0.603	16.813	0.988
6	0.685	59.471	0.796
7	0.822	18.184	0.988

The endmember spectra used in the classification of the May 2000 image as described in subsection 6.2.1, were extracted and stored in a spectral library. The LSU of the normalised scene from April 1987 used the spectra from the existing library only. The identical decision rules and auxiliary data of the classification from the ETM+ dataset, as described in subsection 6.2.1, were applied. Figure 7.14 shows a flow chart of the proposed method.

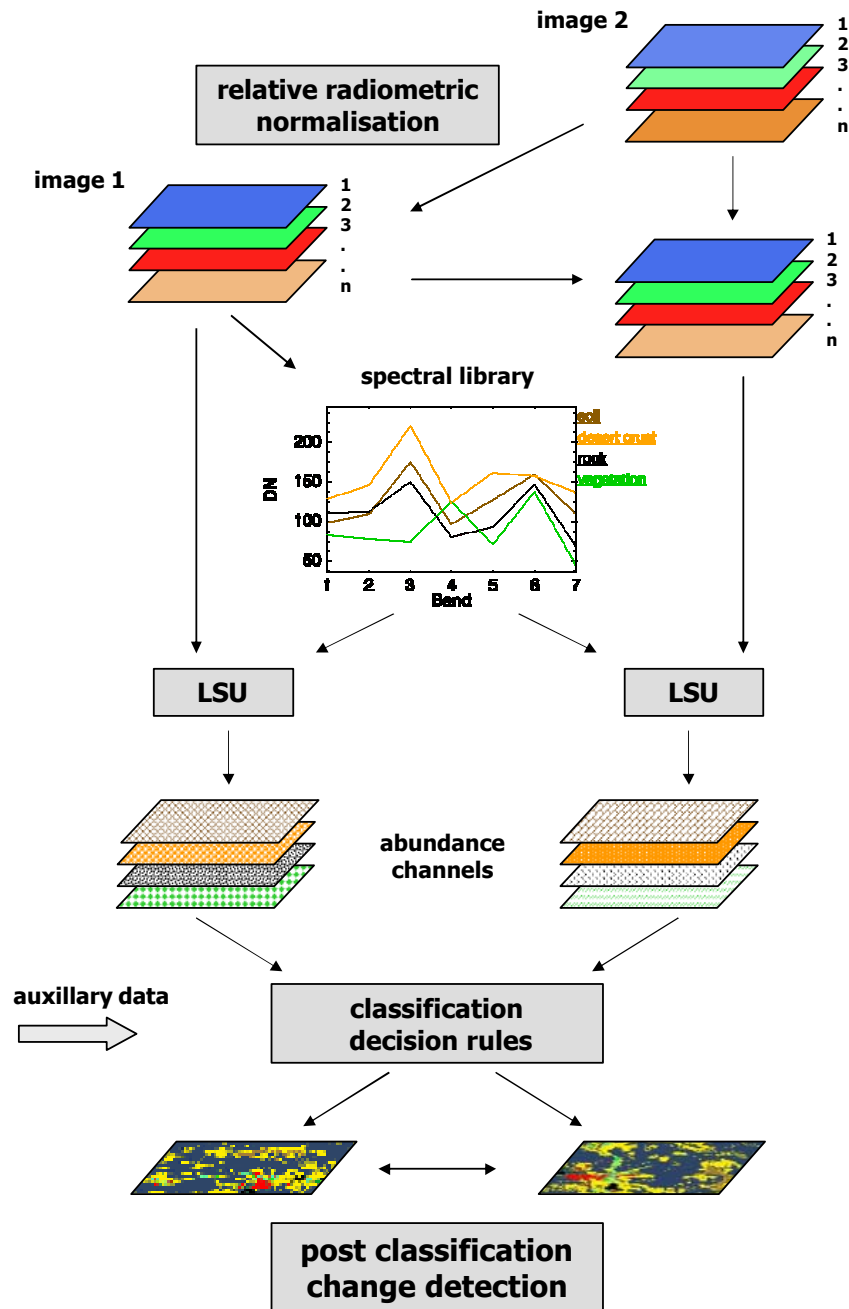


Figure 7.14: Flow chart of the post classification change detection approach (for geometrically corrected images)

Figure 7.15 shows the fully automated classification result for the Basin of Tazenakht of April 1987, based on LANDSAT TM5 data.

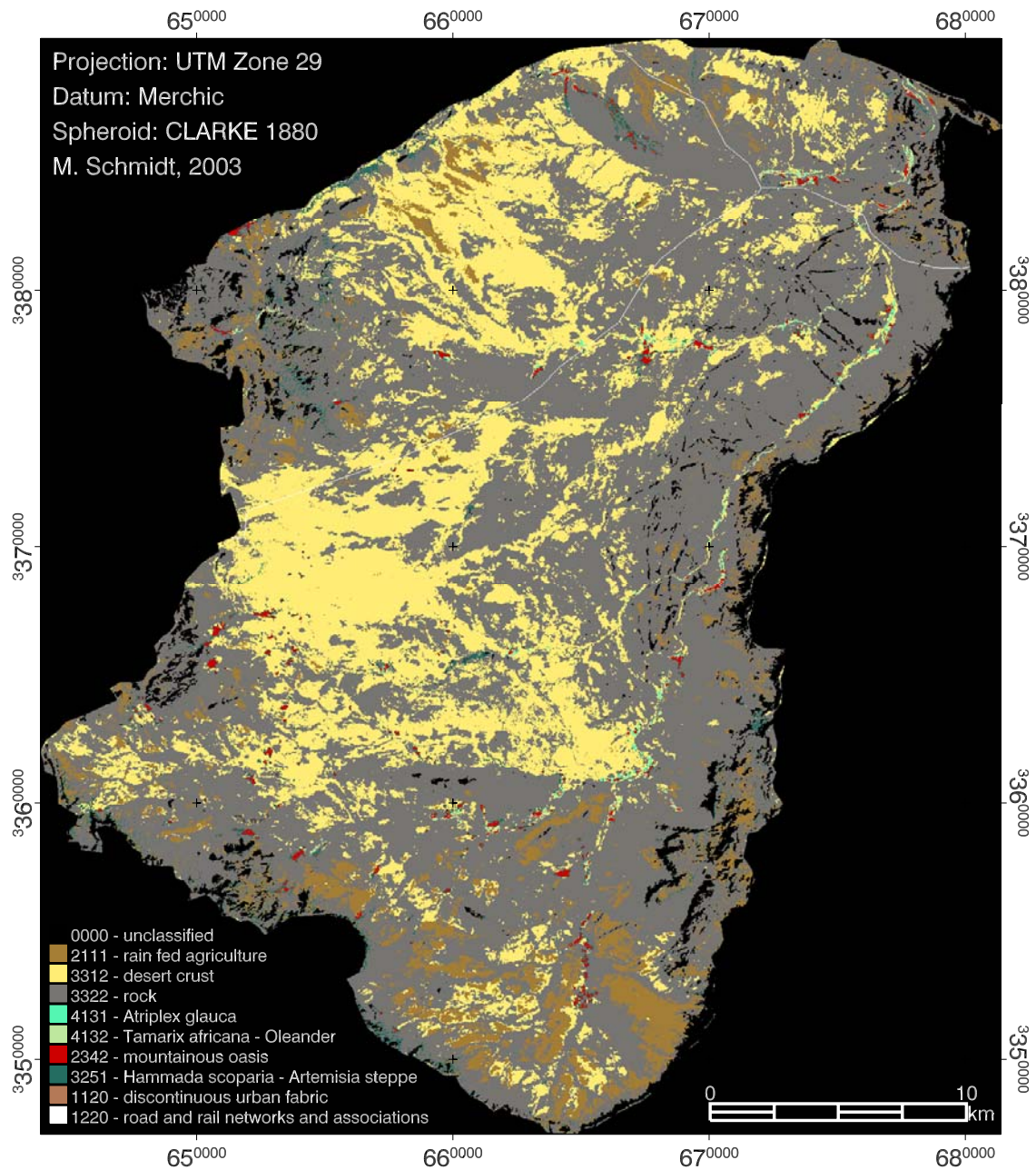


Figure 7.15: Classification of the Basin of Tazenakht from LANDSAT TM5 data, April 1987 (for comparison see Figure 6.12)

Figure 6.12 shows the classification result from May 2000 for comparison. Main surface features remained generally within the 13 years, so that the same classification scheme was used as in the classification of 2000 (see subsection 6.2.1). For a good change detection analysis historic ground truth data would be necessary.

Historic data on land use/land cover might be partly available from regional administration, potentially photos from tourists might also serve as source of information. Regardless of the lack of a "hard" validation an example of the two classifications is shown in Figure 7.16 (center coordinates: 665025/3352118).

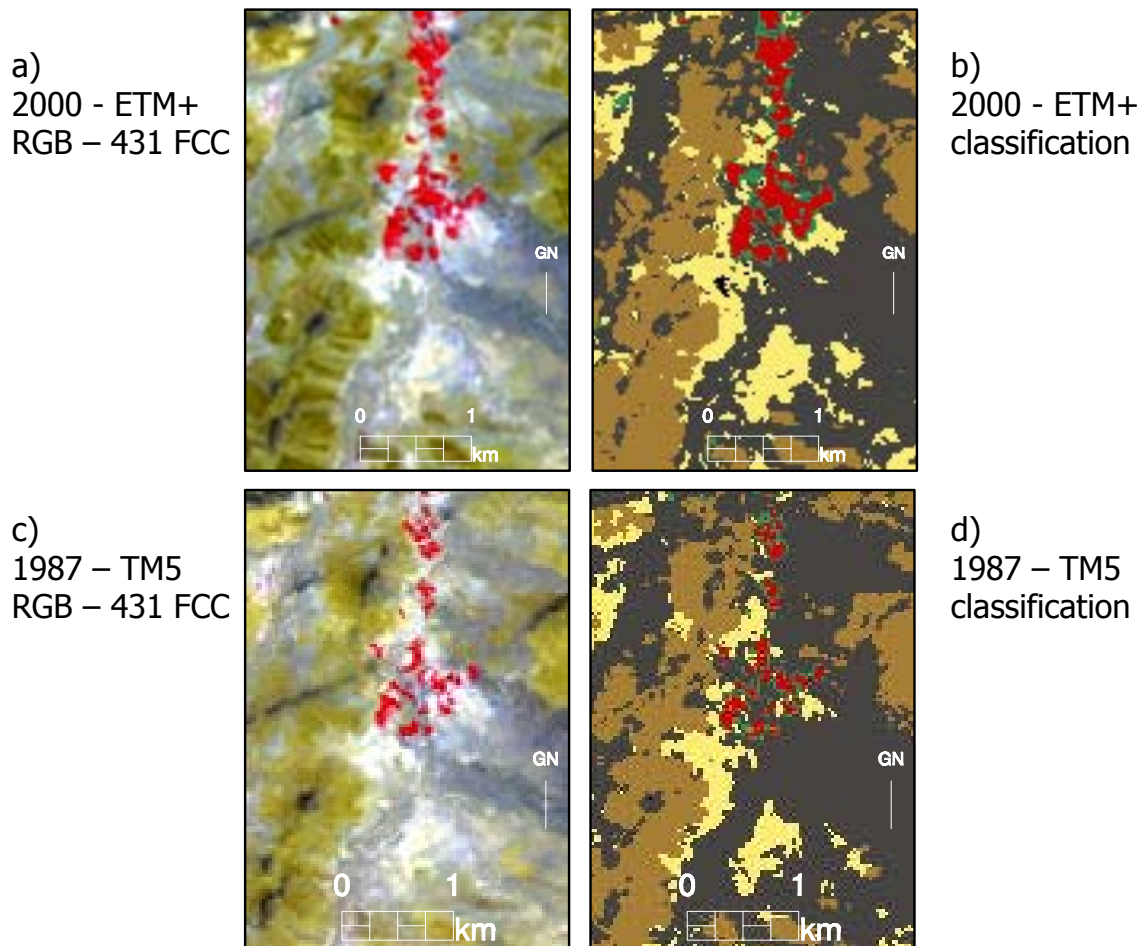


Figure 7.16: RGB FCC and classification example of the Basin of Tazenakht, from May 2000 and April 1987

Visual interpretation shows a good representation of the surface coverage in both time steps. As a threshold dependent discrete decision assigns pixels to either one or another class, some changes may only be due to slight differences in the abundance values. A description of land cover in terms of membership fractions might overcome this situation. The representation of the surface in the classified images from both time steps seem plausible although the LANDSAT ETM+ data were delivered as

recorded in 25m pixel resolution and the LANDSAT TM5 data at 28.5m. The results nevertheless are comparable due to the rather homogeneous and expanded surface features.

The class coverage of the region as a result of the two classifications is shown in Table 7.5.

Table 7.5: Class coverages [%] of 1987 and 2000 of the Basin of Tazenakht, according to the post classification

class id	Name	1987	2000
	unclassified	44.8488	44.4570
2111	rainfed agriculture	3.9105	5.4147
3312	desert crust	14.2844	13.9107
3322	rock	35.5239	32.4688
4131	<i>Atriplex glauca</i>	0.1002	0.1546
4133	<i>Tamarix africana</i> - Oleander	0.2012	0.2732
2352	mountaneous oasis	0.3063	0.7890
3251	<i>Hammada scoparia</i> - <i>Artemisia</i> steppes	0.7571	2.4541
1120	discontinuous urban fabric	0.0005	0.0189
1221	roads	0.0673	0.0591

An increase in all vegetation classes is evident from Table 7.5, which coincides with a phase of drought during the 1980s and a more humid period during the 1990s. The unclassified area changed due to different shade masks and differing amount of supersaturated pixels in channel three (see chapter 6). It is obvious that the class 2111 (rainfed agriculture) increased towards 2000, corresponding to increases in land use due to population growth. An example of the spatial occurrence of the class 2352 (mountainous oasis) is visible in Figure 7.16.

Assumptions for this method are, that the thresholds and auxiliary data do not change and that changes between the scenes due to distortions as atmospheric or sensor noise can be minimised by the relative radiometric normalisation (see chapter 5).

Further studies (potentially) with improved ground truth would be helpful to evaluate this method exactly. As the aim of this work was to establish a land cover map with the best possible result, the decision was taken to map the area with the

highest possible spatial resolution of $25m$ (see chapter 6). The Basin of Tazenakht is relatively homogeneous at the resolutions used in each classification, rather than being dominated by large discrete objects, allowing valid comparison between the classifications made at different spatial resolutions. The aim was to outline the possibilities of a post classification approach, which seem more than promising.

7.2.4 Multivariate Alternate Detection

The MAD method as change detection procedure was introduced in section 5.3 for the identification of no-change pixels. The original application of the method is to analyse areas of change (Nielsen et al., 1998). Since the MAD components are approximately normal distributed about zero and uncorrelated threshold for change or no change pixels can be set in terms of standard deviations about the mean (Canty, 2002). Figure 7.17 b) shows an example of the first three MAD components as calculated from co-registered images of May 2, 2000 and April 5, 1987 of the sensors ETM+ and TM in $28.5m$ pixels size in RGB space. Two standard deviations of each MAD component $\pm\sigma_{MAD_i}$ $i=1..7$ about the mean were set to the mean value (appearing as grey values) and were interpreted as areas of no change.

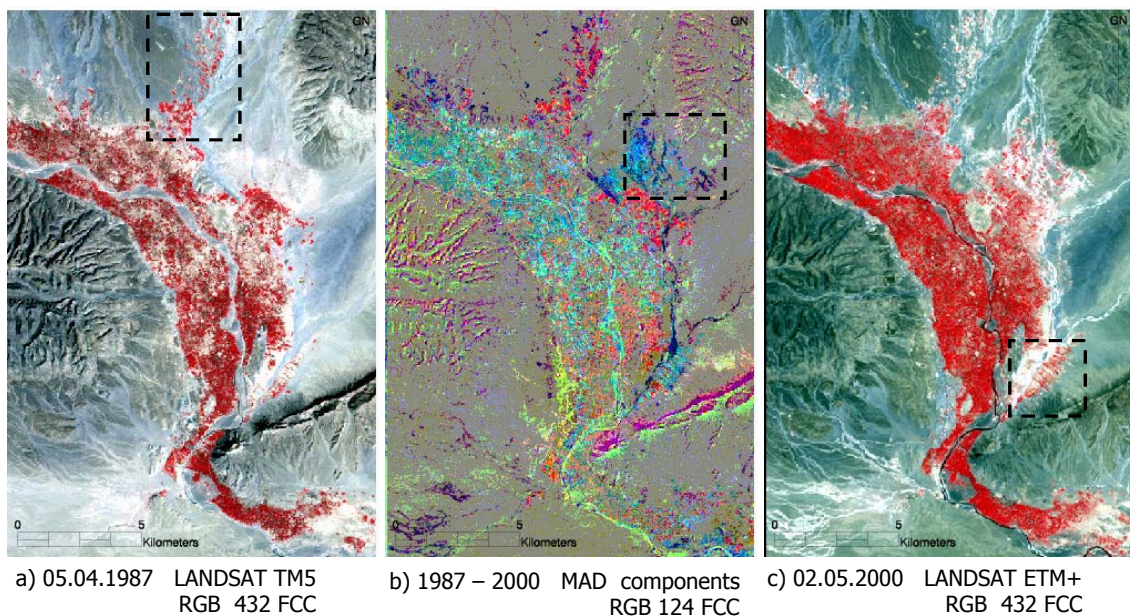


Figure 7.17: MAD based changes April 1987 - May 2000 (the marked areas are discussed in the text)

Within the marked regions in Figure 7.17 a), b) and c) areas of change are indicated. The red coloured pixels in Figure 7.17 b) can be interpreted as negative vegetation change while the positive vegetation change is expressed in light blue tones. If the changes within the image resulted solely from vegetation changes high correlation of the change pixel with the original bands 3 and 4 would be expected (Nielsen et al., 1998). The correlations of image 1 (May 2000) and image 2 (April 1987) with the MAD components are shown in Table 7.6. For the change pixels, positive correlations with band 3 and higher correlations in band 7 and band 2 are displayed. Since band 7 records radiation in the near thermal infrared, it can be stated that those changes are not related to vegetation changes. These areas of change indicated are more probably due to reflection changes of bare surfaces. The difference in shaded pixels is also recorded as areas of change, which can potentially be minimised with an illumination correction (see section 5.4).

Table 7.6: Correlation coefficients for the MADs of the change pixels and the image DNs

ETM+ 2000	1	2	3	4	5	6	7
1	0.08	-0.36	0.39	-0.15	-0.07	0.00	0.76
2	0.09	-0.40	0.41	-0.17	-0.01	0.01	0.68
3	0.14	-0.47	0.40	-0.20	0.04	0.06	0.61
4	-0.14	-0.23	0.20	-0.01	-0.10	-0.06	0.68
5	0.12	-0.51	0.27	-0.11	0.04	0.02	0.66
6	0.05	-0.25	0.33	-0.08	-0.29	0.00	0.85
7	0.19	-0.55	0.27	-0.18	0.07	-0.01	0.61
TM5 1987	1	2	3	4	5	6	7
1	-0.33	0.46	-0.17	0.19	-0.01	-0.10	-0.21
2	-0.33	0.52	-0.18	0.13	0.11	-0.02	-0.08
3	-0.33	0.55	-0.10	0.23	0.15	-0.19	-0.06
4	0.17	0.35	-0.05	-0.01	0.29	0.10	-0.12
5	-0.32	0.56	0.04	-0.06	0.14	-0.06	-0.21
6	-0.30	0.25	-0.05	0.06	0.46	0.04	-0.37
7	-0.40	0.53	0.11	0.22	0.12	0.05	-0.19

The marked regions in Figure 7.17 b) and c) indicate the vegetation change areas

in the river beds as dark blue as change in surface reflectivity, that might be due to a rainfall event prior to the image acquisition. The dark blue areas in Figure 7.17 b) are potentially the result of irrigation and salinisation processes. A terrain inspection for this purpose is thus advised for a subsequent field trip.

The MAD transformation results in orthogonal MAD channels with information on changes that can be analyzed and interpreted. Cluster analysis can be used for the verification of areas of changes e.g. in the form of a supervised classification. A quantification of this change requires a calibration of the MAD bands in each image and would imply further ground data are required. The identification of historical records is necessary in this case.

The advantage of the MAD is that it is fully automatic and parameter free. The method is independent to linear changes, such as gain settings and reveals in combination with an actual classification, areas and classes in which changes occurred. An advantage of the method is that different categories of changes are sorted in the MAD components e.g. anthropogenic and climatologically induced changes can be identified as different categories in differing MAD components (Canty, 2002).

7.3 Discussion and conclusion

In some occasions visual interpretations and manual polygon derivations are the most effective and precise tools in a change analysis, especially if the data quality is not sufficient for a descent statistical analysis. This approach is reasonable if the study area is well known, not too large and the objects of interest are easy to visually distinguish. This is certainly the case with very high resolution data. Generally special attention must be paid to the sensor and satellite geometry of very high resolution data in order to map the desired objects and to interpret changes. If this step is performed, these data may reveal great mapping accuracy potential.

The LSU with only four endmember spectra works independent of data calibration so that the historic data of the LANDSAT MSS sensor could be used in a long term change detection analysis. The extraction of a reliable vegetation coverage is a very useful application of this method (subsection 6.2.2). For a more detailed analysis and the application to a larger area the information content may not be high enough. A possible way to overcome this might be a data fusion with the historic CORONA ortho-images and co registered LANDSAT MSS data both dating from

1972 e.g. with wavelet transformation Canty (2002), to a spatial resolution similar to LANDSAT TM/ETM+ potentially. This might reveal more precise land cover information than treating the two datasets separately.

The MAD method has the advantage of being completely automatic and user independent. Areas of (potential) change are displayed and can be inspected on the images. For mapping purposes, the follow-up step of assigning and interpreting changes to (physical) surface elements and the identification of proper thresholds is time consuming. This process requires considerable terrain knowledge. An assumption of this approach is that the atmospheric conditions differ only in a linear manner.

Due to the reliable relative normalisation, simple change detection methods, such as image differencing or change vector analysis are potentially possible. Also the analysis of time series becomes feasible and reliable.

An autonomous classification of historic data could be applied to a region where no further ground spectra were required. This is a great advantage for the establishment of an operational change detection application with satellite data. This method can potentially be applied for the remaining sub-regions. In some classes the adjustment of threshold and decision rules would be necessary, especially if non linear external image distortions exist, e.g. resulting from atmospheric influences. For more problematic classes a classification scheme on a lower level of detail may be more favorable. The quality of this approach needs to be validated, potentially in a long term project, including repeated compilation of validation data. The potential errors in change detection quantification need careful and systematic attention and should be the focus of further studies aiming to quantify changes. The overall conclusion remains that with this method a (semi) automatic post classification change detection in real time, without a loss in classification detail, is feasible if the classification rules and thresholds are implemented.

8 Biophysical analysis and land use derivation

”After all it is land cover that can be sensed remotely, not land use, which can only be inferred by the interpreter.”

Hung and Ridd, 2002

8.1 Biophysical analysis

Vegetation indices are not a direct measure of biomass or net primary productivity, but are correlated with variables such as the leaf area index (LAI) or plant biomass (Todd et al., 1998). The LAI can be described as the projected leaf area per unit ground surface area and is a key variable in biophysical models used to describe parameters, such as land surface photosynthesis, transpiration, carbon absorption and energy balance (Baret and Guyot, 1991; Bonan, 1995; Chen and Josef, 1996; Jensen, 2000). Satellite remote sensing offers e.g. by the formulation of a VI LAI relationship, the possibility of deriving LAI values for large areas. Although land surface observations by satellite data become more and more routine the derivation of biophysical parameters, such as the LAI, is still in its infancy (Qi et al., 2000; Gilabert et al., 2000).

Green leaves are selective absorbers of radiation and, in comparison with non-vegetated areas, absorb more visible and less near infrared radiation (Chen and Josef, 1996). Reflectance in red and near infrared wavelengths have been used to formulate VIs (see section 3.2). Numerous studies to relate VIs to LAI have been performed with differing focus (Baret and Guyot, 1991; Bonan, 1995; Asner, 1998; Asner et al., 2000). For example Chen and Josef (1996) used high resolution LANDSAT data to derive LAI in Conifer forests, Turner et al. (1999) used the same sensor for LAI estimation studies in three different climatic zones. Diaz and Blackburn (2003) discuss the influence of background influenced VIs on the calculation of LAI in

Mangrove areas. In other studies results from spectral unmixing are related to LAI values. Gilabert et al. (2000) postulates that vegetation abundances from LSU outputs in the form of vegetation fraction maps should not be the final output, but rather ecological variables as vegetation cover or LAI should be generated. For example Asner et al. (2000) proposed non linear mixture models to account for the complex multiple scattering of plant canopies. Gilabert et al. (2000) state that unmixing canopy and soil spectra tend more to a linear mixture and that leaf spectra within a canopy are to be modelled as behaving in a non-linear manner.

In this study, multispectral very high resolution data (IKONOS-2) were used to map individual trees and to derive LAI values per individual tree. The results, on a scale on which objects can be directly assessed, were transferred to LANDSAT ETM+ data with which a linear unmixing was performed to account for the objects sub-pixel size. With very high resolution data an analysis based on single objects could be performed, while with the coarser resolution data analysis is only possible on plant associations. Neither applications relating LAI to very high resolution satellite data nor the fusion of this outcome to high resolution satellite data have been described in the scientific literature, making this a new approach.

8.1.1 Leaf area index derivation from IKONOS-2 data

Field measured LAI values from a hand-held CID digital plant canopy imager (CI-110) device were used to identify a relationship between NDVI values derived from the IKONOS-2 data. This approach was chosen, because the area of investigation comprises relatively uniform soil materials (mostly clay and sand) and the object size is in the order of a pixel ($4m \times 4m$) or higher. The trees are located on hills of varying size consisting of a mixture of sand, clay and nutrients (see subsection 7.2.3). To reduce LAI measurement errors five measurements of each tamarisk hill were performed: north, west, south, east facing and one in the center. In five representative test plots (see Figure 6.13) 32 LAI measurements (each as a mean of 5 single measurements) were used for a regression of the mean NDVI values of the corresponding tamarisk polygon. The NDVI was calculated with IKONOS-2 data calibrated to at-sensor reflectances (see subsection 6.2.2). A logarithmic regression resulted in a best fit with correlation coefficient $r^2 = 0.78$ (see Figure 8.1). Analysis of e.g. Chen and Josef (1996); Turner et al. (1999) with LANDSAT data described the relationship between the LAI and NDVI similarly with a logarithmic behavior.

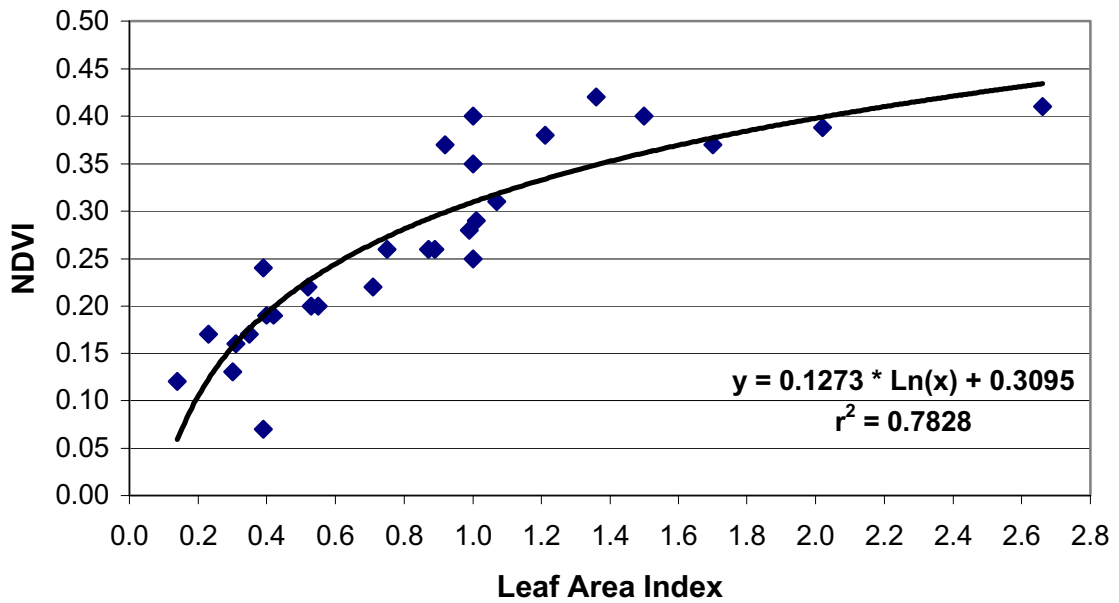


Figure 8.1: Regression between field measured LAI and NDVI values derived from IKONOS-2 data

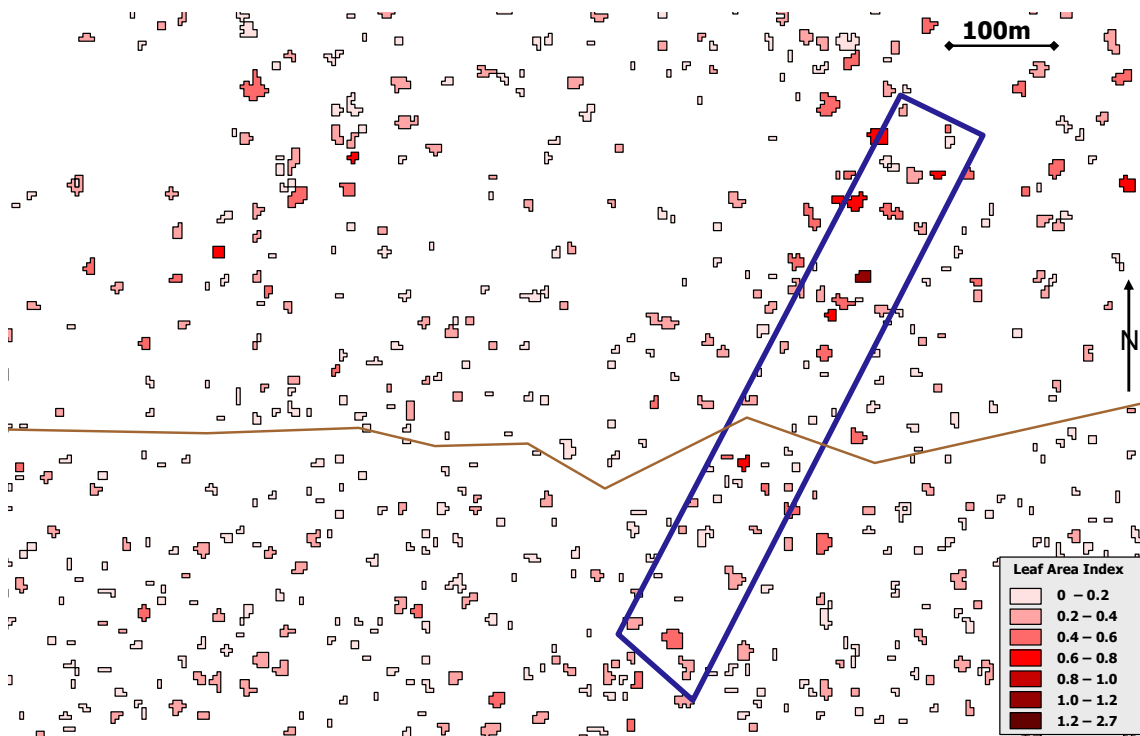


Figure 8.2: LAI values as derived from IKONOS-2 data in the area of Plot 3 (in blue). The piste is displayed in brown.

Gilabert et al. (2000) describe that in an LAI and NDVI relation the LAI becomes almost constant at values between 3 and 4. They explain this is due to the saturation of NDVI at high NDVI values (see also Jensen, 2000, for further discussion). This general behavior is also visible in Figure 8.1, but with the maximum recorded LAI value 2.66 a saturation level was not faced. The functional LAI-NDVI relationship was transferred to tamarisk trees as classified in subsection 6.2.2 by applying Equation 8.1.

$$LAI = e^{\frac{NDVI-0.3095}{0.1273}} \quad (8.1)$$

The LAI density information is graphically shown in the area around Plot 3 in Figure 8.2.

8.1.2 Interpretations of the LAI density information

One aim of this study was to investigate if human induced forcing of the natural ecosystem contributed to a decrease in the forest density, e.g. by extracting firewood. In subsection 7.2.3 it was shown that the total number of trees was not significantly reduced. It was hypothesised that the LAI, as a density measure of the tamarisk trees, would be related to the distance to the town M'hamid and the distance to the piste (indicators for potential human interference)(pers. comm. K. Goldnick, GTZ Zagora). Along the piste, people have easy access to the forest. Figure 8.3 shows two common examples of human influence in the area: in a) the vegetation cover was removed almost completely so that sand became mobile while in b) only the big stems are cut but the remaining smaller branches left so that the sand is still fixed.

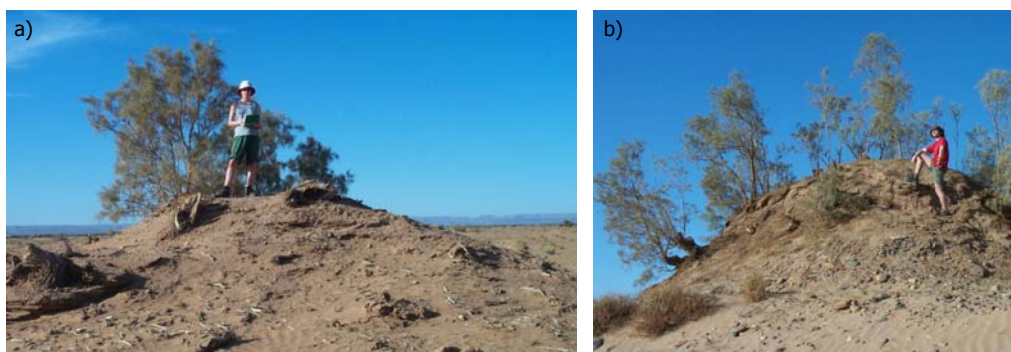


Figure 8.3: Example of disturbed tamarisk trees, (Photos: B. Ostwald, C. Lauber, 2002)

Figure 8.2 generally confirms the speculation, that the density of the tamarisk trees is dependent on the distance from the pistes. Another explanation is that in the recent years more and more tourists drive through this remote area, which is a challenging route for 4 wheel drivers due to the high amount of sand, collecting firewood for their camp-fires. In order to assess the degree of human interference a description of this parameter was categorized by a fuzzy description in 5 groups: very high, high, medium, low and very low.

Changes in the vegetation coverage (as described in Table 7.2) and the mean LAI value as an indicator of the vegetation density within the five test plots are shown in Table 8.1.

Table 8.1: Land cover changes (as described in Table 7.2) and LAI values mapped with CORONA KH4B (1972) and IKONOS-2 (2001) data in five representative test plots

Plot	year	Nr. of trees	coverage [%]	cover change [%]	Mean LAI	Human interference
1/2	2001	31	0.087	-0.83	0.25	high
	1972	33	0.088			
3	2001	60	0.086	-8.70	0.29	very high
	1972	61	0.094			
4	2001	79	0.041	-4.54	0.32	medium
	1972	81	0.043			
5	2001	48	0.039	98.82	0.73	very low
	1972	43	0.020			

The tamarisk coverage in the five representative test plots, analysed in subsection 7.2.3, resulted in a minor change in the coverage within Plot 1 and 2, a coverage change of -8.7% in Plot 3, a decrease of -4.5 % in Plot 4 and a very high increase in Plot 5 (see Table 8.1).

In Plots 1 and 2 a high human impact is recorded and coincides with low mean LAI values. The impact in Plot 3 is more tremendous and rigorous as the total coverage also decreased between 1972 and 2001. The description of degree of human interference by comparing the mean LAI values within the test plots coincides, so that the low mean LAI values can at least be partly explained by wood extraction.

The upper piste is only a couple of years old (pers. comm. K. Goldnick , GTZ, Zagora; Lahbib Naamani, Hotel Sahara, M'hamid) which might explain why the mean LAI is (still) relatively high. Plot 5 has no direct access by a piste. The doubling of the tamarisk coverage with almost no visible human interference on the tamarisks observed supports the conclusion that the human impact is responsible for the decrease in the areas closer to human influenced areas.

To analyse the relationship between the distance to the piste and the density of the LAI values, the LAI values of all tamarisks in the mapped area were correlated with the distance to a piste. The dry river bed of the Dra was in this case also interpreted as an access to the tamarisks, as it is a route frequently used by nomads. Correlations with the tamarisk distance to the pistes and the corresponding LAI values were analysed and were low (0.135). In a second correlation the new upper piste was neglected and the correlation increased to 0.337. Consequently the hypothesis that the distance to the piste is dependent on the degree of human influence can not be directly verified with this method. The absolute value of this statistic is in this case not a fair indicator, therefore that the tamarisks are inhomogeneously distributed in the terrain due to natural factors. So a relationship between these two variables exists which seems to be worth monitoring, in our opinion.

In order to display areas of dense and potentially undisturbed tamarisks the LAI point data were spatially interpolated with an ordinary Kriging method (see Armstrong, 1998) as implemented within ArcMap (ESRI, 2003). The interpolated LAI values can be interpreted as proxy information and where they are large are most likely areas with potentially less disturbed or undisturbed individuals. The graphic representation is shown in Figure 8.4.

The tamarisk forest retains sand from the oasis. If this sand becomes mobile it would endanger the agricultural areas within the oasis (see Figure 7.7) and would force even more farmers to abandon their fields. Measurements on the tamarisk hills were conducted to estimate the amount of sand that potentially can become mobile if the complete tamarisk coverage were removed. Ground measured parameters of height, length and width of 83 tamarisk hills served as a basis for a first estimation of the total amount of sand that is fixed by the tamarisk hills within the study area. The estimation is based on two assumptions: first that the shape of the hills can be described by an ellipsoid and second, that the 83 measurements of the 5 test plots are representative for the whole forest. The volume V of the tamarisk hills was calculated as follows:

$$V = \frac{2}{3}\pi \times \frac{\text{length}}{2} \times \frac{\text{width}}{2} \times \text{height}$$

This resulted in a mean volume of $18m^3$ per tamarisk hill. A total of 23438 tamarisk polygons were calculated resulting in an estimation of the total amount of about $420000m^3$ of sand fixed by tamarisks.

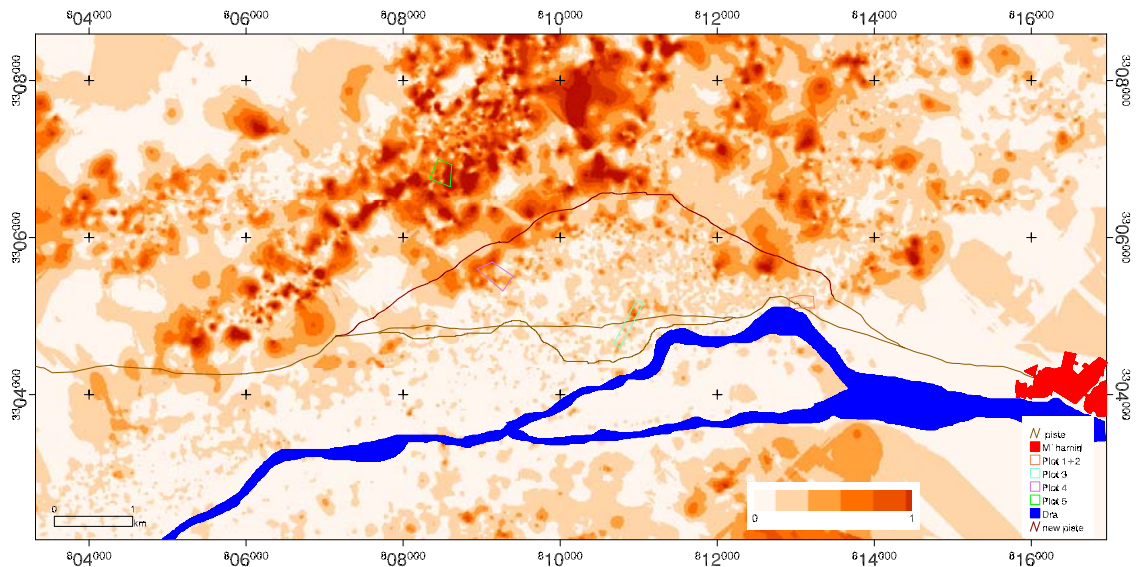


Figure 8.4: Interpolated LAI values derived from IKONOS-2 data, the values close to 1 represent areas with potentially less disturber or undisturbed individuals (explanation see text)

It seems that changes in hydrology had a minor influence on the growth of the tamarisk trees in the area. The major influence results from the land use of the local inhabitants. Local people use the tamarisk forest not only for collecting firewood, but also as grazing ground for camels and goats. The density of the single tamarisk hills decreased due to this behaviour in the accessible regions. In remote or difficult to access regions, the number of tamarisks increased, as in Plot 5. If only the big stems are taken from the hills and the other branches remain, then at least the sand is still fixed and the system remains stable.

8.1.3 Transfer of LAI measurements

Due to the large number of vegetation cover classes within the Dra catchment, an intensive investigation was performed on only one class in a detailed study. The aim

was to transfer this locally derived relationship to the land cover classification on the basis of high resolution data: LANDSAT ETM+. The vegetation abundance information, as obtained from the LSU for the Dra valley, described in subsection 6.1.2, was related to IKONOS-2 derived polygons using LAI values. To ensure that the tamarisks were mapped by the abundance information of the LSU, tamarisk polygons that are spatially of the same order of a LANDSAT ETM+ pixel ($25m \times 25m$) were chosen. Polygons with an area of larger than ($24m \times 24m =$) $576m^2$ were selected and the LAI values were regressed with the abundance values from the LANDSAT ETM+ data. Figure 8.5 shows the results of this analysis, with a correlation coefficient of $r^2 = 0.60$.

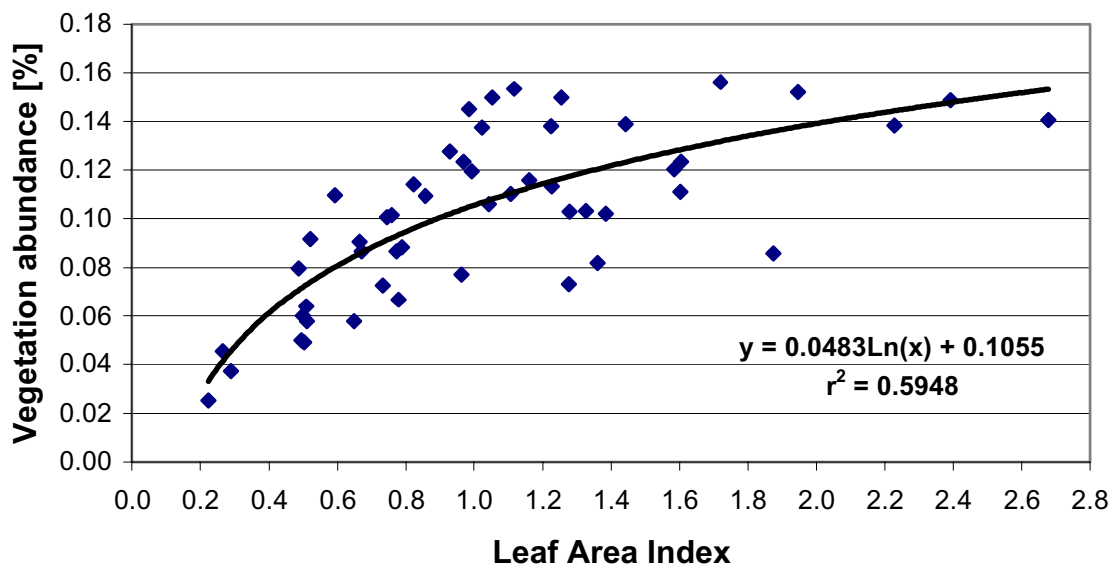


Figure 8.5: Regression between field measured LAI and vegetation abundance values from LSU with LANDSAT ETM+ data (May 2000)

The IKONOS-2 data, dating from November 23, 2001, were recorded in autumn, while the LANDSAT data were recorded in May 2, 2000 at the beginning of the hot and dry season. The comparison of the data from the two dates is feasible due to the low seasonal variability of the evergreen *Tamarix aphylla*. The locally derived relationship between the vegetation abundance and the LAI incorporates uncertainties, but might serve as a first approximation of the LAI for the class 3264 (*Tamarix aphylla*) in the Dra valley. So that Equation 8.2 was applied to the vegetation abundance (VA) values for class 3264:

$$LAI = e^{\frac{VA-0.1055}{0.0483}} \quad (8.2)$$

8.2 An integrated approach: the Basin of Fezuata

Remote sensing data and techniques can potentially assist with describing the physical properties of the earth's surface and to group clusters of similar spectral response to certain land cover classes (Richards and Jia, 1999). The term land use refers to an interpretation of the thematic information. Within this section an example is shown where multitemporal land cover information can, by the incorporation of terrain knowledge, be transferred to land use information.

This section represents a summary of a collaboration with J. Werner from GTZ Zagora (Schmidt and Werner, 2003).

Motivation for the study in the region of Fezuata

Changes in land use due to population pressure and changes in the socio-economic situation of the population are characteristic for most developing countries. Since pastoral land use was the traditional economic strategy in arid regions, change in land use increases the potential for social conflict. These sensitive ecosystems are especially affected by climatic variations, desertification processes and land use transformations. The complex structure and dependencies of the problems is outlined in this section.

The basin of Fezouata is situated near the town of Zagora (see Figure 8.6) and can be divided into two sub-units, in the areas Feija, west of the river Dra, and Tiguida east of the river Dra. Besides this, the extensive mobile pastoralism on collective land is the traditional form of land use in the areas outside of the palm oasis. The arid pastoralism has been an ecological and economically stable form of land use (Zainabi, 1989) over decades and centuries. Mayhew (1997) state, that "[.] that the pastoral nomadism, once thought to degrade the environment, may represent the best use of desert areas." The herds of mobile pastoral animals consist mainly of goats and dromedaries, and in some cases, sheep. The rare resource of freshwater is, on the one hand taken by wells directly from the groundwater, or from surface river water originating from the upstream dam near the town of Ouarzazate. The dam water is released during short periods 4-6 times per year and is primarily used in the palm oasis for agriculture. A complicated and historically developed network of

water rights regulates the water distribution (for further reading see Pletsch (1971); Hammoudi (1985); Popp (2000)).

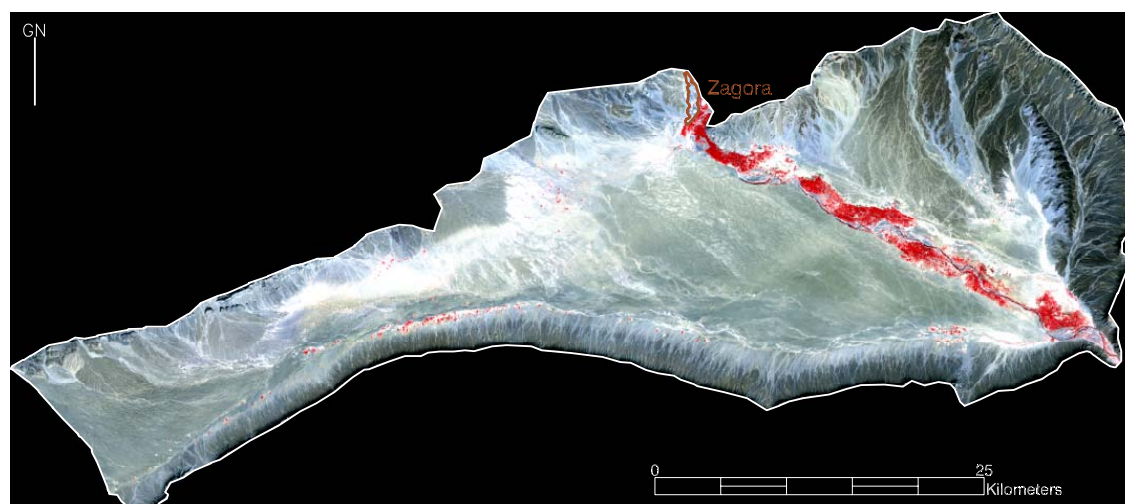


Figure 8.6: Overview of the Basin of Fezuata with a LANDSAT ETM+ RGB 432 FCC (October 2000)

During the 1970's a sedentisation process of the mobile pastoralists in the basin of Fezouata began. Due to technological improvements, in both bore well drilling and diesel pump installation, areas outside of the historical groundwater locations became attractive for agriculture and settlements. Socio-economic developments, governmental and administrative changes promoted this effect (Ormvaio, 1981). Beside the rarity of land it was initially forbidden for the Berbers (in this case the Ait Atta) to own land in the oasis (Zainabi, 1989). The oasis land was owned and cultivated by families of arabic origin and former slaves (arabic "Haratin") of either autochthonous black population or brought by caravan trade with origins in sub-Saharan Africa (Hammoudi, 1985). Historically the Berbers lived as nomads with herds of goats, sheep and camels in the rangelands surrounding the river oasis, including Fezouata. The process of change began when communal land, traditionally used by mobile pastoral people, became, according to Islamic right, property of those former nomads and other people who could afford to construct a well (Hammoudi, 1985; Zainabi, 1989). This sedentisation process and the resulting problems and conflict potentials are outlined in the following.

Approach

In this study multispectral satellite data of the LANDSAT program was used in conjunction with data on household level and ground truth data. In order to analyse the socio-economic changes at household level, 32 pastoralists and farmers were chosen as case studies. In these households an evaluation of the present situation as well as a problem analysis was realized. This contribution is addressed to display the transformation of a mobile pastoral society to sedentary agricultural level and its associated consequences.

LANDSAT ETM+ data WRS2 path/row 200/39 and 201/39 from October 18 and October 25 in 2000 with a ground resolution of $28.5m \times 28.5m$ in seven spectral bands were geometrically corrected (see subsection 5.2.1) and used for calculating an image mosaic for October 2000 according to the methods described in subsection 5.3.1.2. LANDSAT TM data from August 27, 1984 WRS2 202/39 and LANDSAT MSS data from September 9, 1972 WRS1 216/39, covering the study region by one scene, were used to assess multitemporal land cover information. The remote sensing images were chosen in late summer to avoid confusion and interferences with annual vegetation and agricultural cycles. Time invariant endmember spectra, according to the method described in subsection 7.2.3.2, were identified for a LSU approach. The land cover class 2341 (palm oasis) was derived by an vegetation abundance threshold of 30% (see subsection 7.2.3.2), so that three binary classifications could be generated, independent of interscene radiometric or atmospheric variations.

Methods and tools for data collection on household level

In order to gain insight into the situation of the recently founded farms as well as the remaining mobile pastoralists, an analysis on household level was undertaken in the selected area of the basin of Fezouata. The aim of the analysis was to understand the reasons for the transition from mobile animal husbandry towards a sedentary agricultural production in the past three decades and the resulting problems of the changes in land use. Furthermore the potential for conflicts deriving from the change, as well as already existing conflicts for reasons of natural resources scarcity have been assessed. For this purpose 16 nomadic and 16 sedentary households installed on communal pastoral land in the basin of Fezouata were selected and visited in 1998 and 2002. The households were chosen with the objective to cover as far as possible the levels of transition from mobile pastoral land use towards sedentary agricultural production. The aim was not to achieve an analysis on a statistical basis but to study

several households thoroughly as case studies. Different tools of rapid rural appraisal and participatory rural appraisal (Chambers, 1992, 1994) were used to collect data in the mobile and sedentary households. Semi-structured interviews with the different household members as well as other key persons, focussed on prevailing income sources, and changes in land and water resource use. Defining problems and problem awareness formed the main part of the analysis at the household level. Furthermore, observations during several visits as well as transects in the selected area, together with the involved households completed the analysis and enabled a cross-checking of the collected information. For the evaluation of the collected data, the data from each household was organised and thematically summarised. An overall impression of the situation of each household was written and the conditions of the different households compared.

Results

Validation results from the binary classifications from three different time steps are shown in Table 8.2 (see for a further discussion of the method and the ground truth sampling subsection 7.2.3.2).

Table 8.2: Validation of the binary classification

Image	2000	1984	1972
Overall accuracy [%]	99.5	99.4	98.8
Number of test pixels	206	182	164

In 1972 land use in the Basin of Fezuata was characterised by areas of the classical palm oasis and extensively used rangelands, which could be distinguished with the binary classification of the LANDSAT MSS image dating from 1972. In combination with the multi-temporal binary classification, at time steps of 1984 and 2000, areas as extensions of the traditional palm oasis, or as new farms, were identified. Figure 8.7 Shows the classification results and the temporal information.

The colours in the Figure Figure 8.7 represent the different classifications in an additive colour scheme: for the class palm oasis, in blue the time step of 1972, green 1984 and red the year 2000 and their mixtures (see Table 8.3).

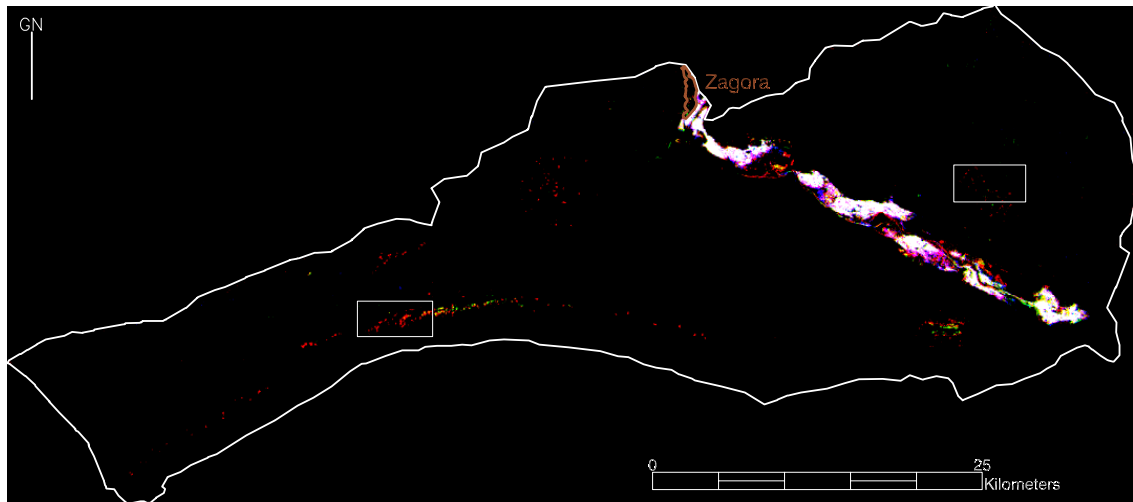


Figure 8.7: Visualisation of three binary classifications for the Basin of Fezuata in an additive colour scheme (see Table 8.3)

Table 8.3: Colour representation in the additive colour scheme

colour	2000	1984	1972
red	×		
green		×	
blue			×
cyan		×	×
magenta	×		×
yellow	×	×	
white	×	×	×

As an area with permanent vegetation, the palm oasis appears in white. Changes in the fringes of the oasis are potentially due to variations in water availability for agriculture, and the extensions of the palm oases and abandoned fields. Large parts of the traditional palm oasis remain stable over the three decades of investigation. The magenta tones represent areas with less agricultural production in 1984 due to a dry period (see Figure 2.2).

Changes in the rangeland areas are displayed in the sense that in the regions of Feija and Tiguida spots with high vegetation abundance occurred in 1984 and 2000.

These areas were classified in a mono-temporal classification as palm oasis (2342) and are totally absent in 1972. In 1984 these spots appear and increase significantly by the year 2000.

Ground observations revealed that these areas represent new founded farms within the former rangelands. The overall changes can be expressed in the absolute numbers, that in 1972 31.16 km^2 of the observed area (1483.67 km^2) were covered by the class palm oasis/agriculture, 1984 32.36 km^2 and in 2000 39.94 km^2 . Population data for this region shows a parallel evolution, where in 1972 approximately 20 people lived in Feija, the population increased to 1187 people in 1997 (Proludra, 1998). This population development is far above the regional and national average population increase. Data from Proludra (1998) report new farm foundations as 78 in the time interval 1971 to 1985 and 169 new farms by 1997 in Feija. A similar trend, but with a later initiation phase, is described for Tiguida.

The trend to found new farms and settlements on the rangelands can be explained by several interconnected processes. The interviews at the household level revealed that mostly former mobile pastoral people became sedentary and founded farms on the collective rangelands. Reasons for this process are manifold. One reason can be seen in the lack of a functioning pastoral land management in combination with the disappearance of the nomadic pastoral management tradition (see also Bencherifa, 1990). Because of the lack of grazing management, pastoralists from regions up to 1000 km away bring their herds, after a rainfall, to the study area by vehicle (K. Goldnick, GTZ, Zagora, pers. comm.). This leads to an increased pressure on the collective land and thus reduced forage availability. As a result of the overgrazing of the collective land, a large part of the mobile pastoralists in the present situation cannot ensure the survival of their household by the income of mobile animal production and are forced to find other income sources. The interviews revealed that farming seems to be the only possible alternative. Often the poorer pastoralists can not afford vehicular transport of their herd to other distant regions with rainfall events. These people are usually the first pastoralists to settle on the collective land. Severe droughts during the last two decades accelerated this sedentisation process. The settlement itself is managed by the different ethnic groups: it is preserved to the respective ethnic group claiming their collective land by habitual rights (Zainabi, 1989). Lack of acceptance and consideration of mobile pastoralists in the national Moroccan legislation and rural policies as well as on international donor level in the past additionally impeded the mobility of the

pastoralists (Thomas and Middleton, 1994).

In cases of farms with enough irrigation water, farming in droughts is possible and high prices for the cultivated cash crop henna in the last five years guaranteed a more profitable income source than pastoralism. However, sedentisation does not solve the problem of overgrazing of the collective land. Indeed it aggravates the situation. The fact that mobile pastoralists settle on farms on the collective land does not mean that they will abandon their herds. Generally the herds will graze in the neighbourhood of the newly installed farm. This means, because of the reduced mobility, that the pasture land around the farms is heavily overgrazed, as ground truth data revealed. The farm land of the former collective pastoral land is not private land, but is rather cultivated according to the Islamic law referred to as called "melk". This means that the person cultivating the land also owns the land, with the result that large surfaces are ploughed in order to mark off the property. In most cases however, only small parts of the ploughed surface can be cultivated afterwards because of limited irrigation water availability. Large surfaces are thus left without any vegetation and are prone to erosion, especially during the frequently occurring sand storms. Furthermore the farmers explained that they use the practice of ploughing several meters around the cultivated fields with the aim that sand will be stopped by the rough soil of the ploughed surface and thus will not reach the cultivated crops (see Figure 8.8 a)). This practice however, further increases wind erosion because the ploughed surfaces, meant to protect the cultivated crops, are left without any vegetation either.

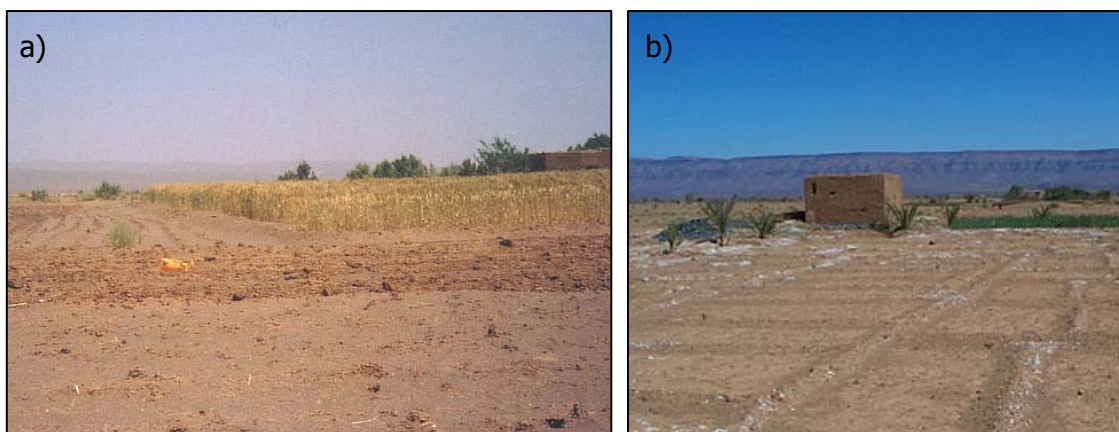


Figure 8.8: Examples of a cultivated a) and saline field b) (Photos, J. Werner, 2001 and M. Schmidt 2000)

Farmers reported that the scarcity of irrigation water also had the effect that after some years, several farmers had to deepen their wells. In years of drought, cultivation in some cases is no longer possible and farms have had to be abandoned (see also Schmidt et al., 2003b). The farms are installed on the most fertile parts of the collective pasture land, which means those closest to the groundwater aquifer. These surfaces, which are also preferred grazing grounds, are thus no longer available for the remaining mobile pastoralists. From this scenario it becomes obvious that conflicts between farmers and pastoralists are frequent and sometimes even violent (Thomas and Middleton, 1994). In most cases, people prefer the nomadic way of life, even if this does imply a lower standard of living. Generally it is only the economic necessity that has forced them to give up mobile pastoralism and to do sedentary farming. The described vicious circle of problems caused by overgrazing and farming in this area is graphically shown in Figure 8.9.

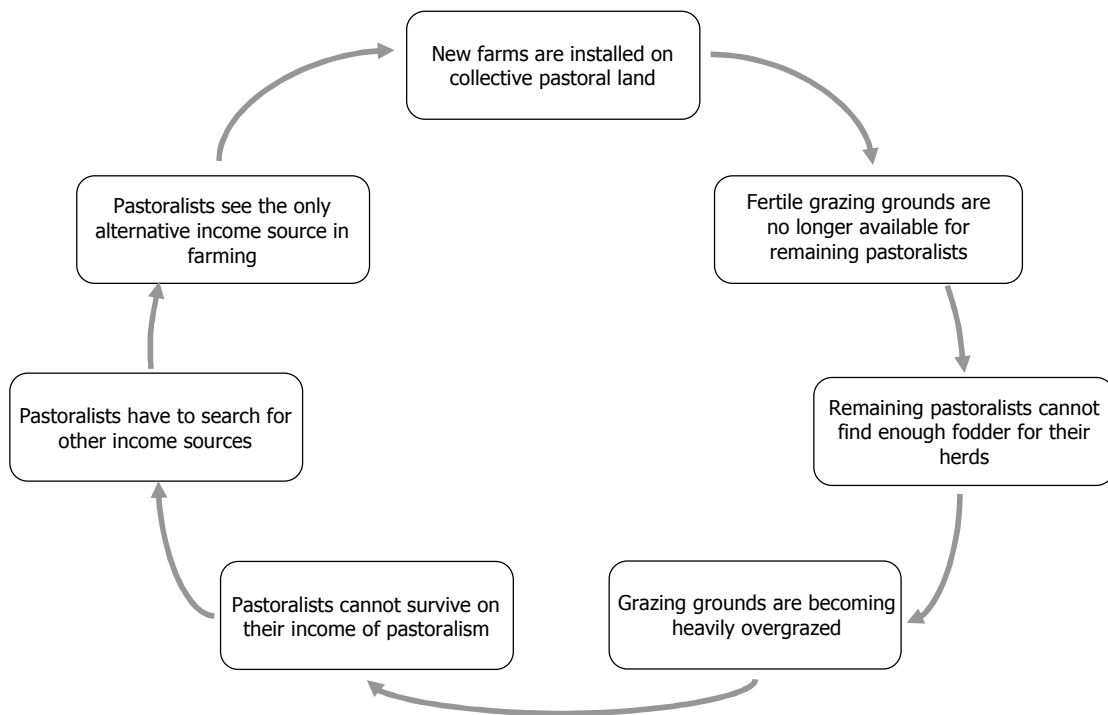


Figure 8.9: Vicious circle of nomadic people in the Basin of Fezuata

The heavily increased construction of wells on the pastoral land further leads to water use discrepancies with the needs of the nearest town of Zagora with 40,000 inhabitants, where freshwater is obtained by the same aquifer, as used by farmers.

In periods of drought water limitations restrictions are imposed on the residents of Zagora, while farming still continues. A problem for the farmers on the new settlements is the high evaporation rate, as no trees prevent the plants from the direct sunshine as is common in the traditional oasis. This results in a higher water consumption which is often accompanied with problems of salinisation.

Intensity of the agriculture production as an indicator of water consumption and vitality of the farms can be estimated from the vegetation abundance values of the classification.

Figure 8.10 shows, that fields in Fejja are larger and also more intensively used for production as displayed in the more intense colours.

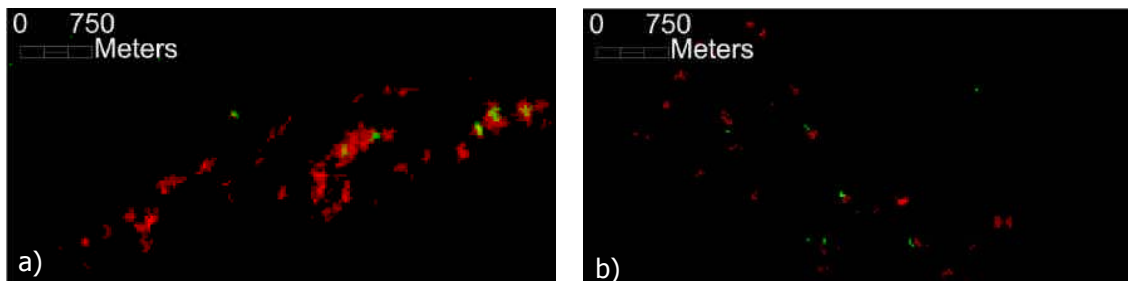


Figure 8.10: Example of field size and intensity of land use from Fejja a) and Tiguida b). Visualised through vegetation abundance information from the LSU

Similar observations were made in the field; that in Tiguida the amount of available groundwater is more limited and the production is lower. Tiguida was cultivated in the mid 1980s and after a couple of years the circle of problems as visualized in Figure 8.9 arose (see also Figure 8.8 b)) and several farms had to be given up or are used to a lesser extent. Production is only possible on small patches due to irrigation induced salinisation and lack of groundwater.

8.3 Discussion and Conclusions

The LAI and NDVI relationship reveals that very high resolution data are generally suitable for the derivation of biophysical parameters, such as the LAI. One advantage of very high resolution data is that the spatial resolution is in the order of trees and their canopy so that this data in studies on forested areas potentially delivers favorable results. Still the amount of field work for the derivation of the LAI, due

to the ground measurements is very high and as every measurement to a certain degree subjective. The incorporation of other spectral channels or eco-physical parameters might contribute to model the LAI in a less labour intensive way. The scale gap between LANDSAT and IKONOS data was bridged in the formulation of the relationship between IKONOS derived LAI values and the vegetation abundance estimation of the LSU with LANDSAT ETM+ data, so that the locally derived relationship could be transferred to the Dra catchment. Further analysis of other plant associations with the importance of the eco-system is needed to complete the description of LAI values or other biophysical parameters such as biomass or transpiration of the land cover in the Dra catchment. This approach is planned to follow in the second phase of the IMPETUS project, in collaboration with the Institute of Agricultural Chemistry at the University of Bonn.

The map product of an actual assessment of the tamarisk density and coverage in combination with a change detection application covering three decades with historic satellite data was achieved. The original idea of deriving a high resolution DEM with CORONA data and estimating the changes in the amount of sand had to be withdrawn to difficulties in the identification of suitable GCPs in the historic CORONA data in this sand dune-dominated area.

A hydrologic map and future coverage with satellite data, preferably with the IKONOS-2 sensor, could contribute to an improved and more reliable interpretation of the human impact in the study region.

The complexity of problems in the area, especially in ethnic context, can not and was not meant to be discussed completely in this contribution, but the general problems that result in the 'circle of poverty' are obvious. Results from the Basin of Fezuata demonstrate that in the long term the inhabitants are suffering from uncontrolled changes in land use. People are forced to strategies of living and survival that are logical in their situation and, in the short term, are solutions for their problems. In the long run, the displayed developments result in problems such that it can be stated that the limited resources are not used in a sustainable way. This situation might be improved by a management system, which could possibly reduce the degradation and desertification processes that have already started and might also reduce the social conflicts.

Census data and socioeconomic analysis are important sources of information to understand, describe and potentially model past and future changes within a landscape. In combination with historical remote sensing data certain land cover/land

use changes can be described, mapped and quantified. Developments, as described in the example of the Basin of Fezuata, in combination with further environmental information of the same time span, such as changes the ground water table (identified in the archives of the Service Hydrolique, Ouarzazarte) or the number of cattle, sheep, camels etc. (identified in the archives of the ORMVARO, Ouarzazate) contribute a valuable information source for further research, establishing environmental models and management plans.

9 Overall Discussion, Conclusions and Outlook

”If we knew what it was we were doing, it would not be called research, would it?”

A. Einstein, 1879-1955

The overall objective of this study was to produce an actual and detailed land cover map of the Dra catchment. This map serves to improve input parameters for meteorological models and is of fundamental importance for environmental and resource management. Vegetation has long been recognised as a major component of water balance in an ecosystem (Troll, 1939; Hill, 2000; Steffen and Tyson, 2001), so the focus within this classification approach was on the actual vegetation coverage, with the aim of describing the dominant vegetation associations, their bio-physical characteristics, and changes over time. Within this study, an excursion into digital photogrammetry led to the generation of valuable and accurate base material for environmental studies. Generally it can be stated that all activities and applications within this work focused finally on obtaining the mapped products at the highest possible level of accuracy. The identification of methods to achieve this resulted in the application of several approaches and methods. The results of these can be concluded as follows:

9.1 Conclusions

DEMs and orthophotos could be generated from historic CORONA data. Within a test area with high image contrast a DEM could be generated from scanned CORONA KH4B archive data with $1.8m$ ground resolution. Accuracy assessment of the DEM, by comparison with 146 check points, resulted in a mean height difference of $\Delta z = 3.6m$ with a standard deviation of $\sigma = 13.2m$. The photogrammetric

restitution is highly dependent on the quality of GCPs, so that better quality GCPs in this region will increase the accuracy of the DEM. In addition an ortho-photomap, as a distortion free document, could be generated on scale of 1:10000 with overlaid contour lines. The methodology due to modern photogrammetry can be applied to all kinds of non metric stereo images, including terrestrial pictures.

Image distortions of very high resolution data in a rugged terrain could be overcome as prerequisite for change detection. Very high resolution satellites such as IKONOS-2 and Quickbird-2 record images in an oblique mode. If the data are to be used for further mapping purposes or GIS analysis then the resulting object displacements must be accounted for. An applied solution was image co-registration to an orthographic map product, derived from CORONA data, which opens the opportunity for change detection over more than three decades with very high resolution satellite data.

Large area DEM and ortho-photomaps of ASTER data were generated. The launching of the TERRA satellite in 1999 with the on-board sensor ASTER opened new opportunities for remote sensing. A DEM and ortho-photomap of three adjacent ASTER images could be generated and mosaiced, for an area of 7926km^2 , roughly one fourth of the project area. The DEM accuracy in the Basin of Ouarzazate was evaluated with 1439 validation points as obtained in a small area, gridded to 5m . The mean height difference to the DEM is $\Delta z = 1.6\text{m}$ with $\sigma = 11.9\text{m}$. The ortho-photomaps were used to co-register LANDSAT data in a region where the topographic maps did not inherit sufficient accuracy or detail.

A new, reliable, stable, parameter free, fast and sensor independent relative radiometric normalisation technique was presented and applied. The MAD based automatic relative radiometric normalisation was compared with a PIF approach and was preferred due to the automatic applicability and the slightly better results. The normalisation algorithm was improved, as described in (Canty et al., 2003) by an orthogonal regression as a result of a collaboration with M. Canty, KFA, Jülich (Germany) and A.A. Nielson, School of Mathematics, Copenhagen (Denmark).

A radiometrically correct LANDSAT image mosaic of the catchment was produced. Five LANDSAT ETM+ scenes acquired during May 2000 were calibrated to the center image and mosaiced to one data coverage of LANDSAT data. Further classifications were generated on the image mosaic.

NOAA/AVHRR data, processed with the software package Terascan,

in the region of the Dra catchment and the given data coverage are not suitable for an analysis of the vegetation dynamics. A full automatic processing chain from raw NOAA/AVHRR data was implemented, including the storage of the meta information automatically in a relational database. The geometric errors due to the navigation and coastline matching algorithm within the software package resulted in geolocation errors about 2.5 pixels. Consequently the intended sub-pixel analysis of the vegetation dynamics was not achievable with this dataset. Improved geometric correction of NOAA/AVHRR are thus necessary, or else the use of satellite data with more precise geometric information, such as MODIS is recommended.

Fieldwork was performed by which ground truth data were obtained and organised in GIS. Fieldwork is essential in remote sensing, not only to validate the mapped products, but also to understand the environmental interplay of regulation factors. Due to intensive field campaigns ecological interdependence and potential land use/land cover classes can be identified. The obtained ground truth data and methods used were documented and stored in a GIS as a data inventory for further studies.

A hierarchical regional adjusted land cover classification scheme in the defined operational scale was generated. On the basis of field observations, in accordance with the IMPETUS project requirements, the land cover classes to be mapped were identified. A classification scheme for the heterogeneous catchment was set up on the basis of CORINE landcover, in which large parts of Morocco are already mapped. Adaptations of this classification scheme, mainly the introduction of a forth level of detail, permit the mapping on the scale of interest for the IMPETUS project. The hierarchical structure enables the fusion or reduction to a lower level to meet the standards of CORINE. The classification scheme was established in collaboration with M. Finckh and M. Staudinger, Institute of Botany, University Hamburg (Germany).

The image mosaic of the Dra catchment was segmented in six PMUs. Due to the high heterogeneity within the Dra catchment the catchment was divided into six sub-regions, according to similar geologic and ecologic constraints followed by the concept of PMU mapping (Daels and Antrop, 1977).

LSU and SAM were applied to transform spectral information into sub-pixel membership descriptions on the basis of fuzzy sets. Two supervised sub-pixel classifiers were applied to decompose the multispectral information into

membership grades of pure spectra (endmembers). The membership grades were interpreted as fuzzy sets which are more readily interpretable in a physical sense. While the approach works in (semi-) arid environments, applications have also been found in urban areas using a similar approach with a four endmember LSU model of LANDSSAT ETM+ data in the metropolitan area of Columbus, USA (Wu and Murray, 2003).

Fuzzy variables from image decomposition were used as input variables to implement knowledge based decision rules in an expert classification system. A combined classification approach incorporating auxiliary information in the sense of a hybrid classifier and knowledge based decision rules of fuzzy sets were integrated in an expert classification system. The expert system was implemented in IDL program codes within ENVI. The decision rules are adapted to the Dra catchment and the classification scheme.

A land cover map of the Dra catchment based on LANDSAT ETM+ data from May 2000 could be generated. The aim to classify the catchment as whole on the basis of one classification scheme using data obtained from the same satellite at a similar time with reported errors could be fulfilled. Before this map was created, only patches of the catchment were classified, and with varying aims and approaches. The overall classification result from the six sub-catchments of the validated classes is shown in Table 9.1.

Table 9.1: Classification accuracies of the six sub-regions of the Dra catchment

	Overall accuracy [%]	Kappa coefficient	Nr. of classes	Size [km ²]
High Atlas	92.4	0.898	6	4642.5
Basin of Ouarzazate	96.8	0.958	9	2651.1
Crystallin Anti Atlas	89.9	0.879	8	7213.8
Sedimentary Anti Atlas	89.2	0.870	6	3706.1
Basin of Tazenakht	96.5	0.951	8	919.7
Dra valley	82.2	0.795	18	9286.0

The classification accuracy in the Dra valley was improved by merging two classes contain *Acacia raddiana* (3261 and 3263) and by removing errors due to false ground truth data collection to 93.1% with Kappa coefficient of 0.918.

Classification results from different image resolutions could be merged. Classification results from IKONOS-2 mapping in 4m pixel size could be merged to the validation data-set of the LANDSAT ETM+ land cover classification.

Land cover data for the input of a regional meteorological model could be supplied. The achieved land cover information was supplied for updating the land cover information as input for the non-hydrostatic mesoscale model FOOT3DK (Flow Over Orographically structured Terrain, 3 Dimensional, Cologne Version) for the simulation of evapotranspiration for the Dra valley. Results of this collaboration with H. Hübner, University Cologne (Germany) were presented at the EGS-AGU-EUG Joint Assembly, April 2003 (Hübener et al., 2003).

The bio-physical parameter LAI could be derived from IKONOS-2 data and validated with ground truth measurements. LAI measurements during an intensive field measurement campaign were regressed with NDVI values of an IKONOS-2 image of November 2001 for the class 3264 (Tamarix aphylla). The logarithmic regression resulted in a LAI NDVI relationship with a correlation coefficient of $r^2 = 0.78$.

Very high resolution LAI values were used to transfer the results to high resolution abundance information for the Dra catchment. LAI values of IKONOS-2 derived polygons with an area of the order of a LANDSAT ETM+ pixel or larger were regressed with the abundance values of the LANDSAT ETM+ LSU for the class 3264 (Tamarix aphylla). The correlation coefficient of this regression is $r^2 = 0.60$. This was used to derive LAI values for the class 3264 (Tamarix aphylla) for the whole catchment.

A (semi)- automated post classification change detection was applied to the Basin of Tazenakht without loss of detail. Change detection techniques were discussed to identify, purpose dependent, an appropriate change detection technique. For a post classification change detection of LANDSAT TM and ETM+ data the expert classifier with the same decision rules and thresholds was applied to a relative radiometrically normalised image from April, 1987. Endmembers were used from a spectral library containing the endmembers from the classification of the image of May, 2000.

A time series of (inter-) calibrated high resolution satellite data could be generated and analysed. A NDVI time series of almost two decades of LANDSAT data could be generated and trends in the NDVI trajectory could be interpreted and related to ground descriptions.

Interpretation of land use information by the integration of a multi-sensoral time series of more than three decades in high resolution was performed. The LSU analysis with four time invariant endmembers of LANDSAT

data, recorded by the three different sensors MSS, TM and ETM+ permitted the description of changes in land-cover pattern during three decades. The transition from pastoral land use to agricultural irrigation could be mapped, interpreted and explained due to collaborative work with J. Werner, GTZ Zagora (Morocco) at the household level (Schmidt and Werner, 2003).

9.2 Outlook and recommendations for further research

In 2000, as the IMPETUS projet started, LANDSAT ETM+ and NOAA/AVHRR data were the available data for land cover mapping and the analysis of vegetation dynamics. During the first IMPETUS phase MODIS and ASTER data became available. Data from the two sensors are interesting for comparison studies and potentially improve some of the shown results. MODIS with 250m pixel size and the highly accurate geometric correction of about 50m at nadir (Wolfe et al., 2002) will especially enable or improve the desired study of vegetation dynamics.

ASTER, with 14 spectral bands, offers impressive opportunities for image classification and surface differentiation. The fusion of the higher spatial resolution data to the 15m resolution with an appropriate image fusion technique might be challenging task. For assessing the process and the dynamics of soil salinisation, which could only discussed marginally in this work, ASTER seems to be a very useful data source as outlined by Goossens et al. (2002b). The monitoring of this process with radar data, potentially in combination with optical data might be an approach worth considering. The understanding and potential modelling or forecasting of soil salinity is of crucial importance for agricultural production as this process is not reversible.

The generation of a DEM on the basis of ASTER data for the whole Dra catchment is approved for the second phase of the IMPETUS project, with reference to results of the present study. The improvement of terrain or illumination correction algorithms for an operational data processing of high resolution data and the integration and mapping of the masked, shades areas, are possible. The DEM will also enable differentiation of more vegetation classes, especially in the mountainous areas as more dedicated decision rules including geo-mophometric relief parameters can be formulated. Further field work for the class identification and ground truth data

will be necessary for this purpose.

An LAI vegetation abundance relation was derived for one important vegetation class in the catchment. Further ground measurement on other vegetation associations will contribute to the formulation of other relationships. Plant-physical parameters were measured during the first IMPETUS phase within the sub-projet B3 by agro-engineers (IMPETUS, 2001). The field and laboratory data can, in the second IMPETUS phase, be extrapolated for bio-physical parameterisation on the basis of the image classification and the vegetation abundance information.

With the launch of IKONOS-2 and TERRA in 1999, remote sensing seemed to enter a new phase after a decade of stagnation. New sensors open new opportunities but also bring new problems. With increasing resolution, the potential geometric errors due to the image recording increase, so that slight changes in the satellite view geometry result in image distortions that are no longer negligible compared with data with larger pixels. This increases the demand for the remote sensing community to understand and apply methods of modern photogrammetry for the data pre-processing as was, for example, identified at the conference of the International Society for Photogrammetry and Remote Sensing (ISPRS) 2001 in Hannover with the topic: "High resolution mapping from space". In our opinion it is especially in this field where the two subjects of remote sensing and photogrammetry overlap that there exists a great demand for further research. So is, for example with the shuttle radar topograph mission (SRTM) in 2000 the demand for the generation of DEMs not satisfied. Most of the modern very high resolution data, such as Quickbird, IKONOS or SPOT5 have the capability to record images stereoscopically, with pixel resolution that obviously promises higher DEM resolution than the SRTM mission can provide. Optical data have the additional advantage of generating orthophotos as cartographic products. With the integration of co-registering or image matching algorithms for the multispectral channels, potentially of fused datasets, then also the display of orthophotos in true colours is possible. Co-registered multispectral bands would also immediately allow work to start with multispectral image interpretations of highly accurate datasets. It is probably an academic discussion if photogrammetry and remote sensing should merge again, but it would definitely be an advantage if certain data processing components of both disciplines could be integrated in one software package. Trends in this direction are underway, as recently ERDAS imagine announced the toolkit Orthobase Pro and RSI also produced an ASTER stereo module for ENVI. Results of the close collaboration with Prof. Goossens, University

Gent (Belgium) in the subject of 3D remote sensing contributed to an initiative, that recently became recognised by the European remote sensing community, by setting up a special interest group within the European Association of Remote Sensing Laboratories (EARSeL). The first joint ISPRS/EARSeL workshop on 3D remote sensing will be held in October 2003 at the University of Hannover (Germany).

To build up routines for the generation of consistent time series of very high resolution data, potentially from satellite missions providing differing view angles, is a challenge for the future. Potential applications for these data sets include crop monitoring and precision farming. The recently launched MISR sensor, for example, views the earth simultaneously at nine different view angles. "MISR provides new types of information for scientists studying Earth's climate, such as the partitioning of energy and carbon between the land surface and the atmosphere, and the regional and global impacts of different types of atmospheric particles and clouds on climate. The change in reflection at different view angles affords the means to distinguish different types of atmospheric particles (aerosols), cloud forms, and land surface covers. Combined with stereoscopic techniques, this enables construction of 3-D models and estimation of the total amount of sunlight reflected by Earth's diverse environments." (NASA, 2003a).

Despite the improved spatial and spectral capabilities of recent and forthcoming satellites, the temporal aspect of archived data is also a source of highly valuable information. NOAA/AVHRR has recorded data since the early 1980's with high temporal resolution. LANDSAT satellites have operated for more than three decades, including nearly 20 years at high resolution with the advent of the TM sensor in 1984. CORONA data are available since the first successful mission in 1960 in very high resolution. These historic satellite data promise a huge, but as yet hardly used potential, for surface monitoring especially in combination with long term ground and/or atmospheric data, and for environmental monitoring, modelling and decision support systems for sustainable management.

Since the adoption of the Agenda 21 in Rio de Janeiro more than a decade ago, the scientific community has increased the knowledge of the driving forces of global change and contributed to sustainable development. The IMPETUS project is aiming to develop strategies for a sustainable and efficient use of freshwater in two catchments north and south of the Sahara. The regionally obtained knowledge of land cover and relevant parameters in this, and other sub-projects, is highly detailed. With integration in environmental models, especially in combination with informa-

tion from different time steps, these approaches can potentially be transferred to the whole of North-West Africa or to comparable regions of the world. This work is contributing to this ambitious goal with accurate information of the actual land cover and the detection of changes within the last three decades.

Bibliography

- Abdeljali, M., Marcais, M., Choubert, M., and Fallot, M. (1959). Service de la Carte- Geologique Royaume du Maroc. In *Feuille Ouarzazate, 1:500000*, Rabat, Morocco. Ministere de de l'Economie Nationale. 17, 19, 117
- Adams, J. B., Sabol, D. E., Kapos, V., Filho, R. A., Roberts, D. A., Smith, M. O., and Gillspie, A. R. (1995). Classification of multispectral images based on fractions of endmembers: Application to land-cover change in the Brazilian Amazon. *Remote Sensing of Environment*, 52:137–154. 93, 97, 153
- Adams, J. B., Smith, M. O., and Johnson, P. E. (1986). Spectral mixture modelling: A new analysis of rock and soil types at the Viking Lander 1 Site. *Journal of Geophysical Research*, 91(B8):8098–8112. 93, 96, 97
- Addink, E. A. and Stein, A. (1999). A comparison of conventional and geostatistical methods to replace cloud pixels in NOAA-AVHRR images. *International Journal of Remote Sensing*, 20(5):961–977. 30
- Africover (2003). Internet: <http://www.africover.org>, (11.03.2003). 35, 138
- Ait-Hamza, M. (1997). Auswirkungen der Arbeitsmigration auf die Oasen in Südmarokko. *Geographische Rundschau*, 49:82–88. 145, 155
- Amstrong, M. (1998). *Basic Linear Geostatistics*. Springer, Berlin-Heidelberg, Germany. 171
- Anderson, J. R., Hardy, E. E., Roach, J., and Witmer, R. (1976). A land use and land cover classification system for use with remote sensor data. Geological Survey Professional Paper 964. Washington, page 28. 34

- Andresen, T., Mott, C., Zimmermann, S., and Schneider, T. (2001). Monitoring of reed populations on bavarian lakes with high-resolution satellite data. In *High resolution mapping from space*, E-proceedings of ISPRS workshop. Hannover, Germany. 42
- Asner, G., Wessman, C. A., Bateson, A., and Privette, J. L. (2000). Impact of tissue, canopy, and landscape factors on the hyperspectral reflectance variability of arid ecosystems. *Remote Sensing of Environment*, 74:69–84. 166, 167
- Asner, G. P. (1998). Biophysical and biochemical sources of variability in canopy reflectance. *Remote Sensing of Environment*, 64:234–253. 166
- Atkinson, P. M. and Curran, P. J. (1997). Choosing an appropriate spatial resolution for remote sensing investigations. *Photogrammetric Engineering and Remote Sensing*, 63(12):1245–1351. 30, 31
- Baltsavias, E., Gaschen, S., Li, H., and Sinning, M. (1996). DTM generation with the Leica/Helava DSW 770 and Virtuozo digital photogrammetric systems. The International Conference on Geoinformatics and Socioinformatics 1996 Wuhan, China, pages 10–17. 51, 52
- Baltsavias, E., Pateraki, M., and Zhang, L. (2001). Radiometric and geometric evaluation of IKONOS GEO images and their use for 3D building modelling. In *High resolution mapping from space*, E-proceedings of ISPRS workshop. Hannover, Germany. 64, 149
- Baltsavias, E. P. (1996). Digital ortho-images - a powerful toll for the extraction of spatial- and geo-information. *Journal of Photogrammetry and Remote Sensing*, 51:63–77. 46
- Banko, G. (1997). Waldoptimierte Korrektur von geländebedingten Beleuchtungssunterschieden in LANDSAT-TM-Daten. *Salzburger Geographische Materialien*, 26:1–10. 87
- Baret, F. and Guyot, G. (1991). Potentials and limits of vegetation indices for LAI and APAR assessment. *Remote Sensing of Environment*, 35:161–173. 166
- Bateson, A. and Curtiss, B. (1996). A method for manual endmember selection and spectral unmixing. *Remote Sensing of Environment*, 55:229–243. 98

- Belward, A. S., Estes, J. E., and Kline, K. D. (1999). The IGBP-DIS global 1-km land-cover data set discover: A project overview. *Potogrammetric Engineering and Remote Sensing*, 65(69):1013–1020. 34
- Bencherifa, A. (1990). Die Oasenwirtschaft der Maghrebländer: Tradition und Wandel. *Geographische Rundschau*, 42(2):82–87. 14, 179
- Bennouna, T., Nejmeddine, A., Lefevre, M., Kaemmerer, M., Lacombe, J., and Revel, J. (2000). Innovative evaluation of field and spatial remote sensing data for analysis of vegetation bio-types in arid rangelands, Taznakht, Moroccan Anti-Atlas. *Arid Soil Research and Rehabilitation*, 14(69):85–94. 7, 105, 107
- Boardman, J. W., Kruse, F. A., and Green, R. O. (1995). Mapping target signatures via partial unmixing of AVIRIS data. In *Fifth JPL Airborne Earth Science Workshop*, number 95-1 in JPL Publication, pages 23–26. 98
- Bonan, G. B. (1995). Land - atmosphere interactions for climate system models: Couplin biophysical, biogeochemical, and ecosystem dynamical processes. *Remote Sensing of Environment*, 51:57–73. 166
- Botkin, D. B., Estes, J., MacDonald, R., and Wilson, M. (1984). Studying the earth's vegetation from space. *BioScience*, 34(4):508–514. 3
- Braun, G. (1996). Vegetationsgeographische Untersuchungen im NW-Karakorum (Pakistan). Number 93 in *Bonner Geographische Abhandlungen*, page 156. 33
- Campbell, J. B. (1996). *Introduction to remote sensing*. Taylor and Francis Ltd., London. 3, 48, 49, 91
- Canty, M., Nielsen, A., and Schmidt, M. (2003). Automatic radiometric normalization of multitemporal satellite imagery. *Remote Sensing of Environment, submitted*. 70, 77, 82, 83, 186
- Canty, M. J. (2002). Digital processing of multispectral images. In *Lecture Notes*, Center for Remote Sensing on Land Applications, University of Bonn. 65, 144, 162, 164, 165
- Chambers, R. (1992). Rural appraisal: Rapid, relaxed and participatory. In *Discussion paper 311*, Institute of development studies, Brighton, UK. 177

- Chambers, R. (1994). The origins and practice of participatory rural appraisal. *World development*, 22(7):953–969. 177
- Chen, J. M. and Josef, C. (1996). Retrieving leaf area index of voral conifer forests using Landsat TM images. *Remote Sensing of Environment*, 55:183–162. 166, 167
- Cihlar, J. (2000). Land cover mapping of large areas from satellites: status and research priorities. *International Journal of Remote Sensing*, 21:1093–1114. 28, 29, 31, 32
- Cihlar, J., Latifovic, R., Chen, J., Beaubien, J., Li, Z., and Magnussen, S. (2000). Selecting representative high resolution sample images for land cover studies. Part 2: Application to estimating land cover composition. *Remote Sensing of Environment*, 72:127–138. 28
- Civco, D. L. (1989). Topographic normalization of LANDSAT Thematic Mapper digital imagery. *Photogrammetric Engineering and Remote Sensing*, 55(9):1303–1309. 87, 88
- Cracknell, A. P. (1997). *The Advanced Very High Resolution Radiometer*. Taylor and Francis, London. 67
- Crist, E. and Cicone, R. (1984). Application of the tasseled cap concept to simulated thematic mapper data. *Photogrammetric Engeneering and Remote Sensing*, 50(3):343–352. 69
- Crossley, J., Plocher, J., Cox, P., Gedney, N., and Planton, S. (2000). Uncertainties linked to land-surface processes in climate change simulations. *Climate Dynamics*, (16):949–961. 2
- Daels, L. and Antrop, M. (1977). The extraction of of soil infomation from remote sensing documents. *Pedologie*, 27(2):123–190. 15, 128, 145, 187
- Dech, S. (1997). Anwendung der Satellitenfernerkundung. In *Von der geowissenschaftlichen Forschung zum operationellen Einsatz*, DLR, Oberpfaffenhofen. 67, 83
- Deering, D. W. (1989). *Theory and Applications of Optical Remote Sensing*, chapter Fiel Measurements of Bidirectional Reflectance, pages 336–428. John Wigley and Sons, New York. 87

- Definiens (2002). *User Guide*. Internet: <http://www.definiens-imaging.com>, (17.12.2002). 103, 123
- Diaz, B. and Blackburn, G. (2003). Remote sensing of mangrove biophysical properties: evidence from a laboratory simulation of the possible effects of background variation on spectral indices. *International Journal of Remote Sensing*, 24(1):53–73. 166
- Donoghue, D. N. M. (1999). Remote sensing. *Progress in Physical Geography*, 23(2):271–281. 140
- Du, Y., Teillet, P. M., and Cihlar, J. (2002). Radiometric normalization of multitemporal high-resolution images with quality control for land cover change detection. *Remote Sensing of Environment*, 82(1):123–134. 68
- Eastman, J. R. and Laney, R. M. (2002). Bayesian soft classification for sub-pixel analysis: A critical evaluation. *Photogrammetric Engineering and Remote Sensing*, 68(11):1149–1154. 92, 97
- El-Addouni, M. (1989). Contribution à l'étude de l'écologie et de la dynamique des peuplements naturels de *Tamarix aphylla* karst dans la basse vallée du Dra. *Institut agronomique et vétérinaire Hassan II*. 119
- Elmore, A. J., Mustard, J. F., Manning, S. J., and Lobell, D. B. (2000). Quantifying vegetation change in semiarid environments: Precision and accuracy of spectral mixture analysis and the normalized difference vegetation index. *Remote Sensing of Environment*, 73:87–102. 97
- Emberger, L. (1939). Aperçu général sur la végétation du Maroc. In *Ergebnisse der Internationalen Pflanzengeographischen Exkursion durch Marokko und Westalgerien 1936*, Veroeff. Geobot. Inst. Ruebel, pages 40–157. 16
- Emran, A., Hakdaoui, M., and Chorowicz, J. (1996). Anomalies on geological maps from multispectral and textural classification: The Bleida mining district (Morocco). *Remote Sensing of Environment*, 57:13–21. 18
- ESRI (2003). *ArcMap*. Internet: <http://www.esri.com/software/arcgis/>, (30.04.2003). 171

-
- Fahsi, A., Tsegaye, T., and W. Tadesse, T. C. (2000). Incorporation of digital elevation models with LANDSAT-TM data to improve land cover classification accuracy. *Forest Ecology and Management*, 128:57–64. 87
- Fennane, M. and Tattou, M. (1998). Catalogue des plantes vasculaires rares, menacées ou endémiques du Maroc. *Bocconea*, 8:5–243+ addenda. 16
- Finckh, M. and Staudinger, M. (2002). Mikro- und Makroskalige Ansätze zu einer Vegetationsgliederung des Draa-Einzugsgebietes (Südmarokko). *Ber. d. Reinh. Tüxen-Ges.*, 14:81–92. 12, 22, 103
- Fischer, G. (1986). *Lineare Algebra*. Vieweg, Braunschweig. 100
- Fleming, D. (2001). IKONOS DN value conversion to planetary reflectance values. In *CRESS Project*, University of Maryland. 80, 82
- Fogarty, P., Francis, J., and Wild, B. (1993). How severe is your discharge area. In *Dryland Salinity*, Department of Land and Water Conservation, Australia. 22
- Foody, G. M. (2002). Status of land cover classification accuracy assessment. *Remote Sensing of Environment*, 80:185–201. 29, 103
- Forman, R. T. T. and Godron, M. (1986). *Landscape Ecology*. Wiley and Sons, New York. 33
- Froitzheim, N., Stets, J., and Wurster, P. (1988). Aspects of Western High Atlas tectonics. pages 219–245. 17
- Furby, S. and Campbell, N. (2001). Calibrating images from different dates to 'like-value' digital counts. *Remote Sensing of Environment*, 77:186–196. 67, 68
- Garmin (1999). *GPS III plus Owner's Manual and Reference*. Garmin Cooperation, Kansas, USA. 24
- Gilabert, M., Garcia-Haro, F., and Melia, J. (2000). Mixture modelling approach to estimate vegetation parameters for heterogeneous canopies in remote sensing. *Remote Sensing of Environment*, 72:328–345. 97, 166, 167, 169
- GLOWA (2002). *German Programme on Global Change in the Hydrological Cycle (Phase I, 2000 - 2003)*, chapter Status Report 2002. 4

- Goossens, R. (2002). Fotogrammetrische restutie. In *Lecture Notes*, Vakgroep Geografie, Universiteit Gent. 41, 42, 44
- Goossens, R., Schmidt, M., and Devriendt, D. (2002a). 3D remote sensing and the generation of low cost high accuracy DEMs and ortho-photomaps. Proceedings of the 2nd EARSel Workshop on Remote Sensing in Developing Countries, Bonn, Germany. 43
- Goossens, R., Schmidt, M., and Menz, G. (2003). High resolution DEM and ortho-photomap generation from TERRA-ASTER data - case study of Morocco. In Bénes, T., editor, *Geoinformation for European wide integration*, pages 19–25. Millpress. 49
- Goossens, R., Vliegheer, B. D., and Dapper, M. D. (2002b). The use of aster data for the mapping of soil salinity. In *Proceedings of the 2nd EARSel Workshop on Remote Sensing in Developing Countries, Bonn, Germany*, Proceedings of the 2nd EARSel Workshop on Remote Sensing in Developing Countries, Bonn, Germany. 190
- Graetz, R. D. (1987). Satellite remote sensing of Australian rangelands. *Remote Sensing of Environment*, 52:313–331. 11, 32
- Gu, D. and Gillespie, A. (1998). Topographic normalization of Landsat TM Images of forest based on subpixel sun-canopy-sensor geometry. *Remote Sensing of Environment*, 64:166–175. 87, 89
- Hall, F., Strebel, D. E., Nickeson, J. E., and Goetz, S. J. (1991). Radiometric rectification: toward a common radiometric response among multidecade, multisensor images. *Remote Sensing of Environment*, 35:11–27. 68, 69
- Hammoudi, A. (1985). *Property, Social Structure, and Law in the Modern Middle East*, chapter Substance and Relation: Water Rights and Water Distribution in the Dra Valley, pages 27 – 57. SUNY Press, New York. 15, 175
- Heipke, C. (1996). Overview of image matching techniques. OEEPE Workshop on the Application of Digital Photogrammetric Workstations, Lausanne (Switzerland). 46

- Heipke, C. (1997). Automation of interior, relative, and absolute orientation. *Journal of Photogrammetry and Remote Sensing*, 52:1–19. 44
- Herold, M., Muenschen, B., Müller, A., and Klenke, M. (2000). Zur radiometrischen Reliefkorrektur von Fernerkundungsdaten. *Photogrammetrie Fernerkundung Geoinformation*, 4:347–354. 87
- Hill, J. (1998). Neue Wege zur geowissenschaftlichen Auswertung multispektraler Fernerkundungsdaten. *Geographische Rundschau*, 50(2):113–119. 95, 97, 99
- Hill, J. (2000). Assessment of semiarid lands: Monitoring dryland ecosystems through remote sensing. In Meyers, R., editor, *Encyclopedia of Analytical chemistry - Instrumentation and Applications*, pages 8769–8794. John Wiley and Sons. 11, 29, 91, 93, 96, 97, 98, 128, 137, 185
- Hill, J., Mégier, J., and Mehl, W. (1994). Land degradation, soil erosion and desertification monitoring in mediterranean ecosystems. *Remote Sensing Reviews*, 12:101–130. 98
- Hnichi, M. (1989). Un parc national en perspective. *Le Matin du Maghreb, October 10*. 12, 142
- Houérou, H. N. L. (2001). Biogeography of the arid steppeland north of the sahara. *Journal of Arid Environments*, 48:103–128. 11, 12, 15, 17, 107
- Houghton, J. (1997). *Globale Erwärmung*. Springer Verlag, Berlin, Heidelberg. 2
- Hübener, H., Schmidt, M., Sogalla, M., and Kerschgens, M. (2003). Simulating evapotranspiration in semi-arid environment: Influence of land cover data quality and resolution. In *Abstract, EGS-AGU-EUG Joint Assembly*. Nice, France, 06 - 11 April, 2003. 189
- Hulme, M. (2000). Global warming. *Progress in Physical Geography*, 24(4):591–599. 1
- Hung, M.-C. and Ridd, M. K. (2002). A subpixel classifier for urban land-cover mapping based on a maximum-likelihood approach and expert system rules. *Photogrammetric Engineering and Remote Sensing*, 68(11):1173–1180. 7, 92, 93, 97

- Hurcom, S. J. and Harrison, A. R. (1998). The NDVI and spectral decomposition for semi-arid vegetation abundance estimation. *International Journal of Remote Sensing*, 19(16):3109–3125. 91
- Hutchinson, G. E. (1957). Concluding remarks. In *Cold Spring Harbor Symposia on Quantitative Biology*, 22, pages 415–427. 33
- IMPETUS (2001). Integratives Management-Projekt für einen Effizienten und Tragfähigen Umgang mit Süßwasser in Westafrika: Fallstudien für ausgewählte Flusseinzugsgebiete in unterschiedlichen Klimazonen. Erster Zwischenbericht. Unpublished project Report. 5, 12, 17, 18, 22, 63, 191
- IMPETUS (2003). Internet: <http://www.uni-koeln.de/globaler-wandel/impetus>, (04.05.2003). 3, 4, 6
- IPCC (2001). *Climate change 2001: Impacts, Adaption and Vulnerability*. Contribution of Working Group II to the Third Assessment Report. 1, 4
- Iqbal, M. (1983). *An Introduction to Solar Radiation*. Academic Press, Toronto/New York/London. 82
- Ivits, E. and Koch, B. (2002). Object-oriented remote sensing tools for biodiversity assessment: A european approach. In Bénes, T., editor, *Geoinformation for European wide integration*, pages 465–472. Millpress. 103
- Jacobsen, K. (2001). Exterior orientation parameters. *Photogrammetric Engineering and Remote Sensing*, 67(12). 47
- Jensen, J. (1996a). *Introductory Digital Image Processing. A Remote Sensing Perspective*. Prentice Hall, New Jersey, USA, 2. edition. 21, 28, 35, 92
- Jensen, J. (2000). *Remote Sensing of the Environment*. Prentice-Hall, London, GB. 3, 32, 92, 166, 169
- Jensen, J. R. (1996b). *Digital Photogrammetry - An Abbandum to the Manual of Photogrammetry*, chapter Confluence of Mapping and Ressource Management, pages 167 – 179. ASPRS, USA. 43, 60, 64, 102, 111
- Kabat, P., Hoff, H., and Luetkemeier, S. (2002). Bahc: Biospheric aspects of the hydrological cycle. *IGBP Global Change Newsletter*. 2

- Katyal, J. and Vleck, P. (2000). Desertification - concepts, causes and amelioration. ZEF - Discussion Papers, Number 33. 33
- Kaufmann, Y. J. (1989). *Theory and Applications of Optical Remote Sensing*, chapter The Atmospheric Effect on Remote Sensing and its Correction, pages 336–428. John Wiley & Sons, New York. 67, 80
- Kim, J.-R. and Muller, J.-P. (2001). Assessment of automated techniques for extracting vegetation and buildings from 1m stereo+ multi-spectral IKONOS and 1m pan-sharpened IKONOS coupled with scanning laser altimetry. In *High resolution mapping from space*, E-proceedings of ISPRS workshop. Hannover, Germany. 42
- Klaus, D. (1994). *Dynamik der globalen Tragfähigkeit*, chapter Beiträge zu globalen Umweltproblemen, pages 28 – 50. Number 2. Akademie der Wissenschaften und der Literatur. 1
- Klaus, D. (1999). Neue Ansätze und Erkenntnisse in der Klimaforschung. *Geographische Rundschau*, 51(9):448—453. 2
- Klaus, D., Poth, A., and U.M.Voss (1994). Konsequenzen des Schmetterlingseffektes für die Klimaprognose. *Mannheimer Berichte*, 44:41—53. 2
- Konecny, G. (1999). Mapping from space. In *Sensors and Mapping from Space*, ISPRS Joint Workshop. Hannover. 28, 43
- Konecny, G. (2001). High resolution mapping from space 2001. In *High resolution mapping from space*, E-proceedings of ISPRS workshop. Hannover, Germany. 42
- Kruse, F. A., Lefkoff, A. B., Boardman, J. B., Heidebrecht, K. B., Shapiro, A. T., Barloon, P. J., and Goetz, A. F. H. (1993). The spectral image processing system (SIPS) - interactive visualization and analysis of imaging spectrometer data. *Remote Sensing of Environment*, 44:145–163. 100
- Kruse, R. (1993). *Fuzzy Systeme*. Teubner, Stuttgart. 101
- Leroy, M. and Roujean, J.-L. (1994). Sun and view angle corrections on reflectances derived from NOAA/AVHRR data. *IEEE Transactions on Geoscience and Remote Sensing*, 32(3):31–49. 86

- Leser, H. (1991). *Landschaftsökologie*. UTB, Stuttgart, 3 edition. 33
- Li, H., Manjunath, B. S., and Mitre, S. K. (1997). A contour-based approach to multisensor image registration. *IEEE Transactions on Image Processing*, 4(3):321–334. 46, 65
- Lillesand, T. M. and Kiefer, R. W. (2000). *Remote Sensing and Image Interpretation*. John Wiley and Sons, Inc., New York, Chichester, Weinheim, Brisbane, Singapore, Toronto, 4th edition. 21, 28, 29, 34, 45, 64, 79, 81, 92, 115
- Lohmann, P. (2001). Land cover classification using high resolution IKONOS data. In *High resolution mapping from space*, E-proceedings of ISPRS workshop. Hannover, Germany. 42
- Lorenz, E. (1963). Deterministic non-periodic flow. *Journal of Atmospheric sciences*, 20:130–141. 2
- Loveland, T. R., Reed, B. C., Brown, J. F., Ohlenc, D. O., Zhu, Z., Yang, L., and Merchant, J. W. (2000). Development of a global land cover characteristics database and IGBP DISCover from 1km AVHRR data. *International Journal of Remote Sensing*, 21(6):1303–1330. 28
- Lunetta, R. S. and Elvidge, C. D. (1998). *Remote Sensing Change Detection. Environmental Monitoring Methods and Applications*. Ann Arbor Press. 140
- MacDonald, R. (1995). CORONA: success for space reconnaissance, a look into the cold war and a revolution for intelligence. *Photogrammetric Engineering and Remote Sensing*, 61:689–720. 49
- Mas, J.-F. (1999). Monitoring land-cover changes: a comparison of change detection techniques. *International Journal of Remote Sensing*, 20(1):139–152. 140
- Maselli, F., Rudolfi, A., and Conese, C. (1996). Fuzzy classification of spatially degraded Thematic Mapper data for the estimation of subpixel components. *International Journal of Remote Sensing*, 17(3):537–551. 92
- Mather, P. M. (1999). *Computer Processing of Remotely-Sensed Images - An Introduction*. John Wiley and Sons Ltd., Chichester, GB, 2 edition. 31, 60, 87

- Mayhew, S. (1997). *Dictionary of Geography*. Oxford University Press, Oxford, New York, 2 edition. 174
- McGlone, C. (1996). *Digital Photogrammetry - An Abbendum to the Manual of Photogrammetry*, chapter Sensor Modelling and Image Registration, pages 115 – 124. ASPRS, USA. 44, 46
- Messerli, B. (1967). Die eiszeitliche und die gegenwärtige Vergletscherung im Mittelmeerraum. Separatdruck aus Geographica Helvetica. 12
- Metternicht, G. (2001). Assessing temporal and spatial changes of salinity using fuzzy logic, remote sensing and GIS. foundations of an expert system. *Ecological Modelling*, 144:163–179. 93
- Mikhail, E. M., Bethel, J. S., and McGlone, J. C. (2001). *Introduction to Modern Photogrammetry*. John Wiley and Sons, New York. 41, 44, 45, 46, 47, 52
- Mitchell, R. and O'Brien, D. (1993). Correction of AVHRR shortwave channels for the effects of atmospheric scattering and absorption. *Remote Sensing of Environment*, 46:129–145. 67
- Moran, M. S., Jackson, R. D., Clarke, T. R., Qi, J., Cabot, F., Thome, K. J., and Markham, B. L. (1995). Reflectance factor retrieval from Landsat TM and SPOT HRV data for bright and dark targets. *Remote Sensing of Environment*, 52:218–230. 68
- Mueller, M. and Segl, K. (1999). Object recognition based on high spatial resolution panchromatic satellite imagery. In *Sensors and Mapping from Space*, ISPRS Joint Workshop. Hannover. 58
- Mugnier, C. J. (1999). Grids and Datums: The Kingdom of Morocco. *Photogrammetric Engineering and Remote Sensing*, pages 657–658. 63
- Müller-Hohenstein, K. (1997). Die Dattelpalme. *Geographische Rundschau*, 42:104–108. 14, 113
- Nagendra, H. (2002). Using remote sensing to access biodiversity. *International Journal of Remote Sensing*, 22(12):2377–2400. 30, 31

- NASA (2001). *Landsat 7 Science Data Users Handbook*. Internet: <http://ltpwww.gsfc.nasa.gov/IAS/handbook/handbooktoc.html>, (11.02.2003). 61, 80, 81, 82, 128
- NASA (2002a). *ASTER*. Internet: <http://eosps0.gsfc.nasa.gov/atbd/astertables.html>, (24-05-2002). 48
- NASA (2002b). *Earth Observing System Data Gateway*. Internet: <http://redhook.gsfc.nasa.gov/imswww/pub/imswelcome/plain.html>, (22-01-2002). 61, 84
- NASA (2003a). *MISR*. Internet: <http://www-misr.jpl.nasa.gov/>, (05.05.2003). 192
- NASA (2003b). *MODIS Reprojection Tool Distribution Page*. Internet: <http://edcdaac.usgs.gov/tools/modis/>, (11-05-2003). 61, 84
- Naveh, Z. and Liebermann, A. S. (1984). *Landscape Ecology - Theory and Application*. Springer series on Environmental Management, New York, Berlin, Heidelberg, Tokyo. 33
- Nicholson, S. E., Tucker, C. J., and Ba, M. B. (1998). Desertification, drought and surface vegetation: An example from the West African Sahel. *Bulletin of the American Meteorological Society*, 79(5):815–829. 33
- Nielsen, A. A., Conradsen, K., and Simpson, J. J. (1998). Multivariate alteration detection (MAD) and MAF processing in multispectral, bitemporal image data: New approaches to change detection studies. *Remote Sensing of Environment*, 64:1–19. 70, 162, 163
- Ormva0 (1981). *Reconnaissance hydrogéologique Complémentaire de la Feija de Zagora par 10 sondages l'air et propositions pour une mise en valeur agricole immédiate*. ORMVAO, Ouarzazate, Morocco. 175
- Ouaskioud, D. (1999). *Contribution à l'étude de la dynamique de la végétation step-pique après une mise en défens de longue durée : cas de la station d'amélioration pastorale Anbad Boumalne Dades (Ouarzazate)*. Mémoire III. Cycle I.A.V. Hassan II, Rabat, Morocco. 146
- Ozenda, P. (1977). *Flore du Sahara*. Paris, France, 2 edition. 16

- Parlow, E. (1991). Einstrahlungskorrekturen - eine Anwendung für digitale Geländemodelle in der Satellitenfernerkundung. *Freiburger Geographische Hefte*, 234:111–118. 87
- Penaloza, M. and Welch, R. (1996). Feature selection for classification of polar regions using a fuzzy expert system. *Remote Sensing of Environment*, 58:81–100. 93
- Petoukhov, V., Ganopolski, A., Brovkin, V., Claussen, M., Eliseev, A., Kubatzki, C., and Rahmstorf, S. (2000). Climber-2: A climate system model of intermediate complexity. part i: Model description and performance for present climate. *Climate Dynamics*, 16:1–17. 2
- Pletsch, A. (1971). Strukturwandlungen in der Oase Dra. Untersuchungen zur Wirtschafts- und Bevölkerungsentwicklung im Oasengebiet Südmarokkos. *Marburger Geographische Schriften*, 46. 7, 12, 14, 15, 113, 119, 175
- Popp, H. (2000). Wüstentourismus in Nordafrika. *Geographische Rundschau*, 52(9):52–59. 145, 175
- Press, F. and Siever, R. (1995). *Allgemeine Geologie*. Spektrum Akademischer Verlag GmbH, Heidelberg, Berlin, Oxford. 22
- Price, J. (1994). How unique are spectral signatures? *Remote Sensing of Environment*, 49:181–186. 93
- Proludra (1998). *Feija d’Imssouffa: Elements de Comprehension*. ADEDRA/GTZ, Zagora, Morocco. 179
- Purevdorj, T., Tateishi, R., Ishiyama, T., and Honda, Y. (1998). Relationships between percent vegetation cover and vegetation indices. *International Journal of Remote Sensing*, 19(18):3519–3535. 92
- Qi, J., Kerr, Y., Moran, M., Wertz, M., Huete, A., Sorooshian, S., and Bryant, R. (2000). Leaf area index estimates using remotely sensed data and BRDF models in a semiarid region. *Remote Sensing of Environment*, 73:18–30. 166
- Rahman, H. and Dedieu, G. (1994). SMAC: a simplified method for the atmospheric correction of satellite measurements in the solar spectrum. *International Journal of Remote Sensing*. 80

- Ramankutty, N., Goldewijk, K., Leemans, R., Foley, J., and Oldfield, F. (2001). Land cover change over the last three centuries due to human activities. *IGBP Global Change Newsletter*. 1
- Ray, T. W. and Murray, B. C. (1996). Nonlinear spectral mixing in desert vegetation. *Remote Sensing of Environment*, 55:59–64. 97
- Richards, J. (1990). Land transformation. In Turner, B., Clarke, W., Kates, R., Richards, J., Mathews, J., and Meyer, W., editors, *The Earth transformed by human action*, pages 163–178. Cambridge University Press, New York, USA. 1
- Richards, J. A. and Jia, X. (1999). *Remote Sensing Digital Image Analysing*. Springer-Verlag, Heidelberg, 3. edition. 21, 30, 41, 79, 174
- Riggs, G., Hall, D., and Salomonson, V. (1994). A snow index for the landsat thematic mapper and modis. In of IGARSS '94, P., editor, *International Geoscience and Remote Sensing Seminar, Noordwijk*, The Netherlands. ESA Publications. 128
- Roberts, D. A., Batista, G. T., Pereira, J. L. G., Waller, E. K., and Nelson, B. W. (1998). Change identification using multitemporal spectral mixture analysis: Eastern Amazonia. *Remote Sensing Change Detection: Environmental Monitoring, Methods and Applications*, pages 137–161. 93, 96, 97, 133, 137
- Roberts, D. A., Green, R. O., and Adams, J. B. (1997). Temporal and spatial patterns in vegetation and atmospheric properties from AVIRIS. *Remote Sensing of Environment*, 62:223–240. 97, 99
- Romanov, P., Gutman, G., and Csiszar, I. (2000). Automated monitoring of snow cover over North America using multispectral satellite data. *Journal of Applied Meteorology*, 39:1866–1880. 128
- RSI (2002). *ENVI Online Help, Version 3.5*. Research System, Inc. (RSI), Boulder, USA. 100, 103, 144
- Ruffner, K. C. (1995). Americas first satellite program. CIA history stuff, Washington. 47, 49, 140

- Saunders, R. W. and Kriebel, K. T. (1988). An improved method for detecting clear sky and cloudy radiances from AVHRR data. *International Journal of Remote Sensing*, 9(1):123–150. 83
- Scepan, J. (1999). Thematic validation of high-resolution global land-cover data sets. *Photogrammetric Engineering and Remote Sensing*, 65:1051–1060. 34
- Schenk, A. (1996). *Digital Photogrammetry - An Appendix to the Manual of Photogrammetry*, chapter Automatic Generation of DEM's, pages 145 – 150. ASPRS, USA. 46
- Scherer, S. and Kruschke, M. (2001). Rapideye - an space based monitoring system for agriculture and cartography. In *High Resolution Mapping from Space*, ISPRS Joint Workshop. Hannover. 31
- Schmidt, M., Goldnick, K., Poete, P., and Menz, G. (2002). Long term vegetation change detection and degradation monitoring in an arid environment on the basis of very high resolution satellite data. In *Remote Sensing in developing countries.*, E-proceedings of the 2nd EARSel workshop. Bonn, Germany. 150
- Schmidt, M., Goossens, R., and Lauber, C. (2003a). CORONA - IKONOS, historical and recent high resolution satellite data for change detection applications. In Bénes, T., editor, *Geoinformation for European wide integration*, pages 127–132. Millpress. 41, 42, 43, 56, 149
- Schmidt, M., Goossens, R., and Menz, G. (2001a). Processing techniques for CORONA satellite images in order to generate high-resolution digital elevation models. In Bégni, G., editor, *Observing our environment from space: New solutions for a new millenium*, pages 191–196, The Netherlands. Lisse. 50
- Schmidt, M., Goossens, R., Menz, G., Altmaier, A., and Devriendt, D. (2001b). The use of CORONA satellite images for generating a high-resolution digital elevation model. In *Scanning the Present and Resolving the Future*, volume VII, pages 3123–3125, Sydney, Australia. IEEE International Geoscience and Remote Sensing Symposium. 50
- Schmidt, M., Thamm, H.-P., and Menz, G. (2003b). Long term vegetation change detection application in an arid environment using LANDSAT data. In Bénes, T.,

- editor, *Geoinformation for European wide integration*, pages 145–154. Millpress. 181
- Schmidt, M. and Werner, J. (2003). Transition from mobile pastoral to agricultural land-use in south morocco - discussing changes over three decades using LANDSAT data. *Journal of Arid Environments*, submitted. 174, 190
- Schmidt, U. (2003). *Modellierung des kurzwelligen solaren Strahlungshaushalts im Hochgebirge auf der Basis von digitalen Geländemodellen und Satellitendaten am Beispiel des Hunza/Karakorum/Nordpakistan*. Dissertation zur Erlangung des Doktgrades an der Universität Bonn, Bonn. 88
- Schott, J. R., Salvaggio, C., and Volchok, W. J. (1988). Radiometric scene normalization using pseudoinvariant features. *Remote Sensing of Environment*, 26:1–16. 68, 69, 73, 74
- Seaspace (2000). Terascan online documentation. Santa Barbara, USA. Seaspace. 67, 83
- Siegel, B. S. and Goetz, A. F. H. (1977). Effect of vegetation on rock and soil type discrimination. *Photogrammetric Engineering and Remote Sensing*, 43:191–196. 91
- Singh, A. (1989). Digital change detection techniques using remotely-sensed data. *International Journal of Remote Sensing*, 10(6):989–1003. 140, 141
- Smith, J. A., Tzeu, L., and Ranson, K. (1980). The lambertian assumption and Landsat data. *Photogrammetric Engineering and Remote Sensing*, 46(9):1183–1189. 87
- Smith, M. O., Ustin, S., Adams, J., and Gillespie, A. (1996). Vegetation in deserts I: A regional measure of abundance from multispectral images. *International Journal of Remote Sensing*, 17(5):1031–1058. 31, 91, 97
- Sobrino, J. and Raissouni, N. (2000). Toward remote sensing methods for land cover dynamic monitoring: application to Morocco. *International Journal of Remote Sensing*, 21(2):353–366. 83

- Song, C., Woodcock, C. E., Seto, K. C., Lenney, M. P., and Macomber, S. A. (2001). Classification and change detection using Landsat TM data: When and how to correct atmospheric effects? *Remote Sensing of Environment*, 75:230–244. 60, 67
- SpaceImaging (2002). *IKONOS*. Internet: <http://www.spaceimaging.com>, (27.06.2002). 61, 81
- Spaeth, H. J. (1997). Landuse and desertification in North and West Africa. Case studies from Morocco, Niger and Togo. *Paderborner Geographische Studien*, 6. 14
- Steffen, W. and Tyson, P. (2001). *Global Change and the Earth System: A planet under Pressure*. IGBP Science 4. 1, 2, 3, 185
- Strahler, A., Muchoney, D., Borak, J., Mark Friedl, S. G., Lambin, E., and Moody, A. (1999). Modis land cover and land-cover change. MODIS Land Cover Product Algorithm Theoretical Basis Document (ATBD) Version 5.0, page 72. Boston University. 34
- Thamm, H.-P. and Schmidt, M. (2001). Erhebung von Ground Truth mir dem GPS Link von ERDAS IMAGINE für eine Klassifizierung der Landnutzung in Benin und Marokko im Rahmen des IMPETUS Projekts. Proceedings of: Geosystems user Group meeting 2001, Germering, Germany. Geosystems. 26
- Thamm, H.-P., Schmidt, M., Guézo, M. M., and Menz, G. (2000). An integrative management project for efficient and sustainable use of fresh water in western Africa (IMPETUS). Proceedings of the 1st EARSeL Workshop on Remote Sensing in Developing Countries. Gent, Belgium. 5
- Thomas, D. and Middleton, N. (1994). *Desertification: Exploding the Myth*. John Wiley and Sohns, Chichester, UK. 33, 180, 181
- Todd, S. W., Hoffer, R. M., and Milchunas, D. G. (1998). Biomass estimation on grazed and ungrazed rangelands using spectral indices. *International Journal of Remote Sensing*, 19(3):427–438. 166
- Tompkins, S., Mustard, J. F., Pieters, C., and Forsyth, D. (1997). Optimization of endmembers for spectral mixture analysis. *Remote Sensing of Environment*, 59:472–489. 98



- Trenberth, K. E., Houghton, J. T., and Filho, L. G. M. (1996). *The climate system: an overview*. Cambridge University Press. 1
- Trimble (2003). *Pathfinder PRO XS*. Internet: www.trimble.com/pathfinderprox.html, (05.03.2003). 23, 65
- Troll, C. (1939). *Luftbildplan und ökologische Bodenforschung*. Zeitschrift der Gesellschaft für Erdkunde, Berlin, Germany. 28, 33, 185
- Turner, D. P., Cohen, W. B., Kennedy, R. E., Fassnacht, K. S., and Briggs, J. M. (1999). Relationships between leaf area index and Landsat TM spectral vegetation indices across three temperature zone sites. *Remote Sensing of Environment*, 70:52–68. 166, 167
- UN (1999). *The day of 6 billion*. Internet: <http://www.unfpa.org/modules/6billion>, (22.12.2002). 1
- UNESCO (2003). *Man and Biosphere*. Internet: <http://www.unesco.org/mab/>, (30.04.2003). 19
- USGS (2003a). *GTOPO30*. Internet: <http://edcdaac.usgs.gov/gtopo30/gtopo30.html>, (30.04.2003). 13, 61
- USGS (2003b). *The MODIS Vegetation Indices*. Internet: <http://edcdaac.usgs.gov/modis/mod13q1.html>, (30.04.2003). 61, 84
- Ustin, S. L., Hart, Q. J., Duan, L., and Scheer, G. (1996). Vegetation mapping on hardwood rangelands in California. *International Journal of Remote Sensing*, 17(15):3015–3036. 97
- Verbyla, D. and Boles, S. (2000). Bias in land cover change estimates due to mis-registration. *International Journal of Remote Sensing*, 21(18):3553–3560. 141
- Vogt, D. (2002). *Entwicklung eines operationellen Verfahrens zur Ableitung saisonaler Landbedeckungskarten für Marokko aus täglichen NOAA-AVHRR Daten unter Verwendung des Softwarepaketes Tera Scan*. Unpublished Master Thesis, University of Bonn, Germany. 84
- von Weizäcker, E., Lovins, A., and Lovins, L. (1997). *Factor 4. Doubling wealth - Halving resource use*. Allen and Unwin, St Leonards, Australia. 1

- Wang, Y. (1998). Principles and applications of structural image matching. *ISPRS Journal of Photogrammetry and Remote Sensing*, pages 154–165. 44, 46
- Wharton, S. (1994). *Theory and applications of Optical Remote Sensing*, chapter Knowledge-Based spectral classification of remotely sensed image data, pages 28 – 50. Number 2. Akademie der Wissenschaften und der Literatur, USA. 7, 93
- Wolfe, R. E., Nishihama, M., Fleig, A. J., Kuyper, J., Roy, D., Storey, J., and Patt, F. (2002). Achieving sub-pixel geolocation accuracy in support of MODIS land science. *Remote Sensing of Environment*, 83:31–49. 85, 190
- Wu, C. and Murray, A. T. (2003). Estimating impervious surface distribution by spectral mixture analysis. *Remote Sensing of Environment*, 84:493–505. 188
- Yang, X. and Lo, C. P. (2000). Relative radiometric normalization performance for change detection from multi-date satellite images. *Photogrammetric Engineering and Remote Sensing*, 66(8):967–980. 67
- Youbi, L. (1990). Hydrologie du bassin du Dades. Ministère de l’Agriculture et de la Réforme Agraire, Office Régional de Mise en Valeur Agricole de Ouarzazate. 12
- Zadeh, L. (1965). Fuzzy sets. *Information and Control*, 9:338–353. 101
- Zainabi, A. (1989). Vers une disparition rapide du nomadisme au Sahara marocain (1): Le cas du Dra moyen. In *Le nomade, l’oasis et la ville.*, Urbama., 20. 15, 174, 175, 179
- Zhang, J., Zhang, Z., Shen, W., and Wang, Z. (1996). Virtuozo digital photogrammetry system and its theoretical foundation and key algorithms. XVIII Congress of ISPRS, Vienna. 44, 46, 48, 51, 52, 53
- Zillbach, K. (1984). *Geoökologische Gefügemuster in Süd-Marokko*, volume 37. 7
- Zimmermann, H. J. (1996). *Fuzzy set theory - and its applications*. Kluwer, Boston/Dordrecht/London, 3 edition. 101, 102
- Zouri, A. (1992). *Utilisation des images SPOT pour la cartographie de la végétation steppique des zones arides. Exemple des parcours AIT ZEKERI à Ouarzazate*



Bibliography




(*Maroc*). Diplôme d'Etudes. Publié et Edité Par le Goupement de Developpement de la Télédétection Aérospatiale, Toulouse, France. 7


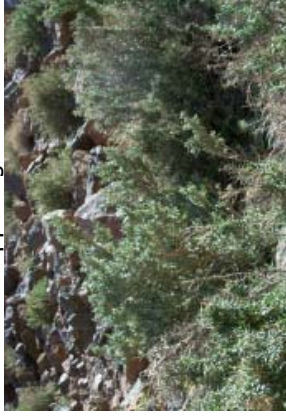

10 Appendix


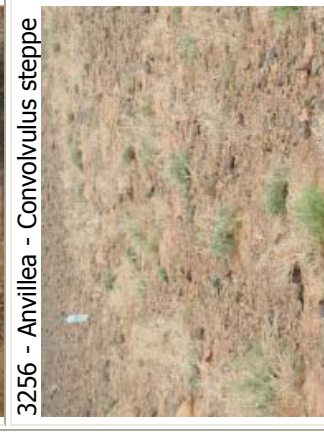

Level 1	Level 2	Level 3	Level 4	Vegetation description	
1000 - ARTIFICIAL SURFACES	1100 - urban fabric	1110 - continuous urban fabric			
		1120 - discontinuous urban fabric			
	1200 - industrial, commercial and transport sites	1210 - industrial or commercial units			
		1220 - road and rail networks and associations			
		1230 - port areas			
		1240 - airport areas			
	1300 - mine, dump and construction sites	1310 - mineral extraction sites			
		1320 - dump sites			
		1330 - construction sites			




<p>2000 - ARABLE LAND</p>	<p>2300 - heterogeneous agricultural areas</p>	<p>2340 - agro-forestry areas</p>	<p>2341 - palm oasis </p> <p>2342 - mountainous oasis </p>	<p>Ficus carica, Lawsonia inermis, Melilotus sativa, Olea europea, Phoenix dactylifera, Punica granatum, and cultivated crops (such as Zea mays, Triticum aestivum, Vitis vinifera)</p> <p>Acer monspessulanum, cultivated crops (such as Avena sativa, Daucus carota, Melilotus sativa, Raphanus sativus, Solanum tuberosum, Triticum aestivum, Zea mays), Fraxinus angustifolia, Mediterranean fruit trees (such as Ficus carica, Juglans regia, Malus domestica, Olea europea, Punica granatum, Prunus amygdalus, Prunus persica), Populus spec.</p>
	<p>2400 - pastures</p>			




3000 - FOREST AND SEMI NATURAL AREAS	3100 - forest				
	3110 - broad-leaved forest				
	3120 - coniferous forest				
	3130 - mixed forest				
	3210 - natural grassland				
		3221 - oromediterranean vegetation			Alyssum spinosum, Arenaria pungens, Artemisia atlantica, Astragalus ibrahimianus, Bupleurum spinosum, Carduncellus pinnatus, Cytisus balansae, Dactylis hispanica, Erinacea anthyllis, Festuca hystrix, Juniperus thurifera, Jurinea humilis, Ribes uva-crispa, Scorzonera pygmaea, Vella mairei
	3220 - moors and heathland				
		3230 - sclerophyllous vegetation			
	3200 - shrub and/or herbaceous vegetation				
		3241 - Juniperus thurifera - Buxus shrubland			Alyssum spinosum, Artemisia atlantica, Astragalus ibrahimianus, Bupleurum spinosum, Buxus balearica, Fraxinus xanthoxyloides, Genista scorpius, Juniperus thurifera, Ormenis scariosa, Teucrium malenconianum
		3240 - transitional woodland shrub			




<p>3000 - FOREST AND SEMI NATURAL AREAS</p>	<p>3200 - shrub and/or herbaceous vegetation</p>	<p>3240 - transitional woodland shrub</p>	<p>3242 - Juniperus phoeniceae shrubland</p>  <p>3243 - Buxus balearica</p> 	<p>Adenocarpus bacquei, Artemisia atlantica, Artemisia herba-alba, Astragalus ibrahimianus, Astragalus spinosus, Buxus balearica, Ephedra nebrodensis, Fraxinus xanthoxyloides, Genista scorpius, Hertia maroccana, Juniperus oxycedrus, Juniperus phoenicea, Juniperus thurifera, Ormenis scariosa, Pinus halepensis, Quercus rotundifolia, Stipa parviflora, Teucrium malenconianum, Thymus spec.</p> <p>Adenocarpus bacquei, Artemisia atlantica, Artemisia herba-alba, Astragalus spinosus, Buxus balearica, Genista scorpius, Hertia maroccana, Ormenis scariosa, Stipa parviflora, Stipa barbata, Thymus spec.</p>
		<p>3250 - steppe vegetation</p>	<p>3251 - Hammada scoparia - Artemisia steppe</p> 	<p>Antirrhinum ramosissimum, Artemisia herba-alba, Asphodelus tenuifolius, Astragalus spinosus, Convolvulus trabutianus, Cymbopogon schoenanthus, Farsetia hamiltonii, Genista scorpius, Hammada scoparia, Helianthemum ellipticum, Launaea arborescens, Limonium sinuatum, Marrubium desertii, Pegannum harmala, Salvia aegyptiaca, Salvia verbenaca, Stipagrostis obtusa, Stipa parviflora, Stipa retorta, Teucrium polium, Ziziphus lotus</p>



<p>3000 - FOREST AND SEMI NATURAL AREAS</p>	<p>3200 - shrub and/or herbaceous vegetation</p>	<p>3250 - steppe vegetation</p>	<p>3252 - tussock-grass steppe</p>  <p>3253 - rocksteppe vegetation</p>  <p>3254 - dwarf bush steppe</p> 	<p>Artemisia herba-alba, Helianthemum ellipticum, Salvia verbenaca, Stipa tenacissima</p> <p>Antirrhinum ramosissimum, Anvillea radiata, Artemisia herba-alba, Carthamus fruticosus, Convolvulus trautianus, Farsetia aegyptiaca, Farsetia hamiltonii, Gaillonia reboudiana, Gymnocarpus decander, Hammada scoparia, Launaea arborescens, Lavandula mairei, Marrubium desertii, Ormenis scariosa, Salvia aegyptiaca, Zilla spinosa</p> <p>Adenocarpus acquei, Carlina spec. div., Convolvulus trautianus, Genista scorpius, Launaea acanthoclada, Ormenis scariosa, Teucrium malenconianum, Withania adpressa</p>
--	--	---------------------------------	--	---

<p>3000 - FOREST AND SEMI NATURAL AREAS</p>	<p>3200 - shrub and/or herbaceous vegetation</p>	<p>3250 - steppe vegetation</p>	<p>3255 - Pulicaria steppe</p>  <p>3256 - Anvillea - Convolvulus steppe</p>  <p>3257 - Hammada scoparia steppe</p> 	<p>Anabasis articulata, Pulicaria crispa</p> <p>Anvillea radiata, Artemisia herba-alba, Convolvulus trautmanus, Cymbopogon schoenanthus, Farsetia hamiltonii, Hammada scoparia, Launaea arborescens, Marrubium desertii, Salvia aegyptiaca, Stipagrostis obtusa,</p> <p>Asphodelus tenuifolius, Hammada scoparia, Stipa retorta</p>
--	--	---------------------------------	--	---


<p>3000 - FOREST AND SEMI NATURAL AREAS</p>	<p>3200 - shrub and/or herbaceous vegetation</p>	<p>3260 - savanna vegetation</p>	<p>3261 - Acacia raddiana - Ziziphus - Mearua</p>  <p>3262 - Acacia raddiana - Retama</p>  <p>3263 - Acacia raddiana - Panicum - Zilla</p> 	<p>Acacia ehrenbergiana, Acacia raddiana, Anvillea radiata, Callotropis procera, Convolvulus trabutianus, Maerua crassifolia, Pergularia tomentosa, Pulicaria crispa, Retama monosperma, Withania adpressa, Zilla spinosa, Ziziphus lotus</p> <p>Acacia raddiana, Antirrhinum ramosissimum, Anvillea radiata, Convolvulus trabutianus, Ephedra alata, Hammada scoparia, Limoniastrum feei, Retama monosperma, Retama raelam, Rhus tripartita, Withania adpressa, Ziziphus lotus</p> <p>Acacia raddiana, Antirrhinum ramosissimum, Anvillea radiata, Ephedra alata, Fagonia zilloides, Panicum turgidum, Pennisetum dichotomum, Pergularia tomentosa, Randonia africana, Zilla spinosa, Zygophyllum gaetulum</p>
--	--	----------------------------------	--	---

<p>3000 - FOREST AND SEMI NATURAL AREAS</p>	<p>3200 - shrub and/or herbaceous vegetation</p>	<p>3260 - savanna vegetation</p>	<p>3264 - Tamarix aphylla</p> 	<p>Calligonum comosum, Callotropis procera, Cistanche violacea, Tamarix aphylla, Zygophyllum gaetulum</p>
	<p>3300 - open spaces with little or no vegetation</p>	<p>3310 - beaches, dunes and sand plains</p>	<p>3311 - sand</p> 	
			<p>3312 - desert crust</p> 	

<p>3000 - FOREST AND SEMI NATURAL AREAS</p>	<p>3300 - open spaces with little or no vegetation</p>	<p>3320 - bare surfaces</p>	<p>3321 - gravel/pecliment</p>  <p>3322 - rock</p>  <p>3323 - playa</p> 	
--	--	-----------------------------	---	--

<p>3000 - FOREST AND SEMI NATURAL AREAS</p>	<p>3300 - open spaces with little or no vegetation</p>	<p>3330 - sparsely vegetated areas</p>	<p>3331 - sanddune vegetation</p>  <p>3332 - Zygophyllum gaetulum</p> 	<p>Anabasis articulata, Caligonium spec., Nitraria retusa, Salsola tetragona , Tamarix aphylla, Ziziphus lotus</p> <p>Fagonia glutinosa, Fagonia zilloides, Kicksia sagittata, Zilla spinosa, Zygophyllum gaetulum</p>
		<p>3340 - burnt areas</p>		
		<p>3350 - glaciers and perpetual snow</p>		

	4110 - inland marshes			
	4120 - peat bogs			
			4131 - <i>Atriplex glauca</i>	<i>Atriplex glauca</i>
			4132 - <i>Tamarix africana</i> - Oleander	<i>Arundo donax</i> , <i>Nerium oleander</i> , <i>Tamarix africana</i> , <i>Vitex agnus-casti</i>
	4130 - riparian vegetation		4133 - riparian shrublands	<i>Arundo donax</i> , <i>Nerium oleander</i> , <i>Tamarix africana</i> , <i>Vitex agnus-casti</i>
		4100 - inland wetlands		

4000 - WETLANDS	4200 - coastal wetlands	4210 - salt marshes 4220 - salines 4230 - intertidal flats			
	5100 - inland waters	5110 - water courses (see 4133) 5120 - lakes			
	5000 - WATER BODIES	5200 - marine waters	5210 - coastal lagoons 5220 - estuaries 5230 - sea and ocean		